UNIVERSITY OF CALIFORNIA, SAN DIEGO

# *In Vivo* Biomechanics of Human Pulmonary Circulation

A dissertation submitted in partial satisfaction of the
requirements for the degree
Doctor of Philosophy

in

Bioengineering with specialization in Multi-Scale Biology

by

Tatsuya Arai

Committee in charge:

Professor Susan R. Hopkins, Chair
Professor Andrew D. McCulloch, Co-Chair
Professor Richard B. Buxton
Professor Geert W. Schmid-Schoenbein
Professor Rebecca J. Theilmann

2013

The dissertation of Tatsuya Arai is approved, and it is acceptable in quality and form for publication on microfilm and electronically:

_____

_____

_____

_____
Co-Chair

_____
Chair

University of California, San Diego

2013

DEDICATION

I would like to dedicate THis mANuscript to all of the people that have supported me scientifically, physically and emotionally during the last 8 years. In particular, I would liKe to thank Professor Susan R. Hopkins for her conStant availability and desiRe to answer any and every qUestIon I posed to her.

# EPIGRAPH

*For your competitiveness.*
*Winning is a reward from the past.*
*Losing is a gift to the future.*
—Erroll D. Wilmslow

EPIGRAPH

**Errol guy does not exist.**

—*Tatsuya Arai*

TABLE OF CONTENTS

LIST OF FIGURES

LIST OF TABLES

ACKNOWLEDGEMENTS

I would like to acknowledge Professor Susan R. Hopkins, my supervisor, whose attention to detail drove me to finally punctuate prose, as well as Professor Andrew D. McCulloch, Professor Richard B. Buxton, Professor Geert W. Schmid-Schoenbein, and Professor Rebecca J. Theilmann, for their support as members of my doctoral committee.

As no doctoral journey is completed alone, I would like to thank the members of the Pulmonary Imaging Laboratory for their help with my research and bringing cookies to the weekly Lung Meeting.

I also would like to acknowledge my close friends and labmates with whom I shared labored conversation about all things imaging, and all things not, over many grande burritos.

Finally, I acknowledge the patience and love of my family, for whom I am eternally grateful for their support from Japan.

Chapter 3, in part, is a reprint of the material as it appears in J Vis Exp 51, e2712, 2011. Arai TJ; Prisk GK; Holverda S; Sá RC; Theilmann RJ; Henderson AC; Cronin MV; Buxton RB; Hopkins SR. The dissertation author was the first author of this publication.

Chapter 5, in part, is a reprint of the material as it appears in J Appl Physiol 106(4), pp. 1057-64, 2009. Arai TJ; Henderson AC; Dubowitz DJ; Levin DL; Friedman PJ; Buxton RB; Prisk GK; Hopkins SR. The dissertation author was the first author of this publication.

Chapter 6, in part, uses the material, which is currently prepared for submission for publication. Arai TJ; Villongco MT; Henderson AC; Dubowitz DJ; Darquenne C; Theilmann RJ; Sá RC; Friedman PJ; Buxton RB; Prisk GK; Hopkins SR; The dissertation author is the first author of this material.

## VITA

| | |
|---|---|
| 2003 | B. Eng. in Applied Physics And Physico-Informatics, Keio University, Tokyo |
| 2004 | M. S. Eng. in Fundamental Science And Technology, Keio University, Tokyo |
| 2005-2007 | Visiting Scholar, University of California, San Diego |
| 2008 | Staff Research Associate, University of California, San Diego |
| 2008-2013 | Graduate Teaching Assistant, University of California, San Diego |
| 2013 | Ph. D. in Bioengineering with specialization in Multi-Scale Biology, University of California, San Diego |

## PUBLICATIONS

E.T. Hall, R.C. Sá, S. Holverda, T. J. Arai, D. J. Dubowitz, R. J. Theilmann, G.K. Prisk, and S.R. Hopkins. "The Effect of Supine Exercise on The Distribution of Regional Pulmonary Blood Flow Measured Using Proton MRI." Submitted to *Journal of Applied Physiology* (Under Review).

V. Tedjasaputra, R.C. Sá, T.J. Arai, S. Holverda, R.J. Theilmann, W.T. Chen, P.D. Wagner, C.K. Davis, G.K. Prisk, S.R. Hopkins. "The Heterogeneity of regional specific ventilation is unchanged following heavy exercise in athletes." *Journal of Applied Physiology*, 115(1):126 – 35, 2013.

T.J. Arai, C.T. Villongco, M.T. Villongco, S.R. Hopkins, R.J. Theilmann. "Affine Transformation Registers Small Scale Lung Deformation." *Proceedings IEEE in Engineering Medicine Biology Society*, 5298 5301, 2012.

S. Holverda, R.J. Theilmann, R.C. Sá, T.J. Arai, E.T. Hall, D.J. Dubowitz, G.K. Prisk, S.R. Hopkins. "Multi-image gradient echo quantitative MRI measures lung water with high reliability and validity". *Journal of Magnetic Resonance Imaging*, 34(1), 220 – 224, 2011.

T.J. Arai, G.K. Prisk, S. Holverda, R.C. Sá, R.J. Theilmann, A.C. Henderson, M.V. Cronin, R.B. Buxton, S.R. Hopkins. "Magnetic resonance imaging quantification of pulmonary perfusion using calibrated arterial spin labeling." *Journal of Visualized Experiments*, 51:e2712, 2011.

R.C. Sá, M.V. Cronin, A.C. Henderson, S. Holverda, R.J. Theilmann, T.J. Arai, D.J. Dubowitz, S.R. Hopkins, R.B. Buxton, G.K. Prisk. "Vertical distribution of specific ventilation in normal supine humans measured using oxygen-enhanced proton MRI." Journal of Applied Physiology, 109(6):1950 – 1959, 2010.

S.R. Hopkins, T.J. Arai, A.C. Henderson, D.L. Levin, R.B. Buxton, G.K. Prisk. "Lung volume does not alter the distribution of pulmonary perfusion in dependent lung in supine humans." *Journal of Physiology*, 588(pt 23):4759 – 4768, 2010.

G.K. Prisk, I.M. Olfert, T.J. Arai, P.D. Wagner, S.R. Hopkins. "Rapid intravenous infusion of 20 ml/kg saline does not impair resting pulmonary gas exchange in the healthy human lung." *Journal of Applied Physiology*, 108(1):53 – 59, 2010.

K.J. Burnham, T.J. Arai, D.J. Dubowitz, A.C. Henderson, S. Holverda, R.B. Buxton, G.K. Prisk GK, S.R. Hopkins. "Pulmonary perfusion heterogeneity is increased by sustained, heavy exercise in humans." *Journal of Applied Physiology*, 107(5):1559 – 1568, 2010.

R.J. Theilmann, T.J. Arai, A. Samiee, D.J. Dubowitz, S.R. Hopkins, R.B. Buxton, G.K. Prisk. "Quantitative MRI measurement of lung density must account for the change in T(2) (*) with lung inflation." *Journal of Magnetic Resonance Imaging*, 30(3), 527 – 534, 2009.

T.J. Arai, A.C. Henderson, D.J. Dubowitz, D.L. Levin, P.J. Friedman, R.B. Buxton, G.K. Prisk, S.R. Hopkins. "Hypoxic pulmonary vasoconstriction does not contribute to pulmonary blood flow heterogeneity in normoxia in normal supine humans". *Journal of Applied Physiology*, 106(4):1057 – 1064, 2008.

ABSTRACT OF THE DISSERTATION

# *In Vivo* Biomechanics of Human Pulmonary Circulation

by

Tatsuya Arai

Doctor of Philosophy in Bioengineering with specialization in Multi-Scale Biology

University of California, San Diego, 2013

Professor Susan R. Hopkins, Chair
Professor Andrew D. McCulloch, Co-Chair

Gas exchange between inhaled alveolar air and pulmonary capillary blood occurs in the lung. The relationship between ventilation and perfusion determines the global efficiency of gas exchange in the lung. The normal healthy lung maintains a regional ventilation-perfusion ratio close to unity, whereas in disease, the regional ventilation-perfusion mismatch results in inefficient gas exchange, leading to arterial hypoxemia. The original research presented in this dissertation focused on factors effecting on the regional distribution of pulmonary perfusion in supine humans, namely the effects of (1) hypoxic pulmonary vasoconstriction (HPV), and (2) lung tissue stretch due to tidal volume lung inflation. The work performed

required an understanding of pulmonary physiology, biomechanics, functional magnetic resonance imaging (MRI) and image processing.

An arterial spin labeling MR sequence, combined with pulmonary proton density imaging, was used to quantify the spatial distribution of pulmonary perfusion. The alterations in the distribution of pulmonary perfusion were induced by (1) inhalation of gases of different oxygen concentration, and (2) tidal volume lung inflation. The tidal volume lung inflation study involved MR lung images obtained at different lung volumes. A deformable image registration technique, using a piecewise polynomial interpolation method, was developed to warp acquired pulmonary perfusion images into the shape of a reference lung volume such that lung images were compared based on corresponding anatomy.

The main results of this work were: (1) mild global hypoxia and hyperoxia, induced by the inhalation of different fraction of inspired oxygen gas mixtures ($F_IO_2 = 0.125$ and 0.3, respectively) do not result in changes in the heterogeneity or redistribution of pulmonary perfusion, indicating that hypoxic pulmonary vasoconstriction is not the major contributor affecting pulmonary perfusion heterogeneity in the normal supine human lung. (2) Tidal volume lung inflation did not cause significant changes in the spatial distribution of pulmonary perfusion; however, the fractional distribution of pulmonary perfusion was redistributed away from the nondependent region of lung at the higher lung volume, indicating that the changes in the gravitational height of the lung, which result in changes in hydrostatic pressure distribution likely contribute more significantly than the overall changes in pulmonary vasculature resistance induced by lung tissue stretch.

# Chapter 1

# Biomechanics of Pulmonary Circulation

## 1.1 Abstract

This chapter introduces the background of my dissertation research. An overview of pulmonary circulation research is presented first, covering the development of mathematical pulmonary circulation models since the 1960s and recent functional imaging techniques. Following this review of the state of the art, the goals of my dissertation research are introduced, concluding the chapter and leading to the following chapters. Two previously uninvestigated pulmonary physiological topics associated with the control of pulmonary perfusion in humans were chosen for the goals of my dissertation, namely the effects of (1) hypoxic pulmonary vasoconstriction and (2) lung deformation due to breathing motion on the distribution of pulmonary perfusion. My research extends previous knowledge on these topics (chapters 5 and 6) and provides novel insights into the control of pulmonary circulation.

## 1.2 Introduction

John B. West states "The lung is for gas exchange" in the first sentence of his Respiratory Physiology textbook [48]. The lung is the blood-gas interface where the gas exchange occurs. The oxygen rich fresh air is ventilated into alveolar space and taken up by pulmonary blood perfused in capillaries in the alveolar wall. Meanwhile carbon dioxide is removed from the mixed venous blood. The relationship between ventilation and perfusion is illustrated as a simplified single compartment lung shown in Figure 1.1. For pulmonary physiology research, understanding ventilation - perfusion relationships are the fundamental basis for understanding pulmonary gas exchange.

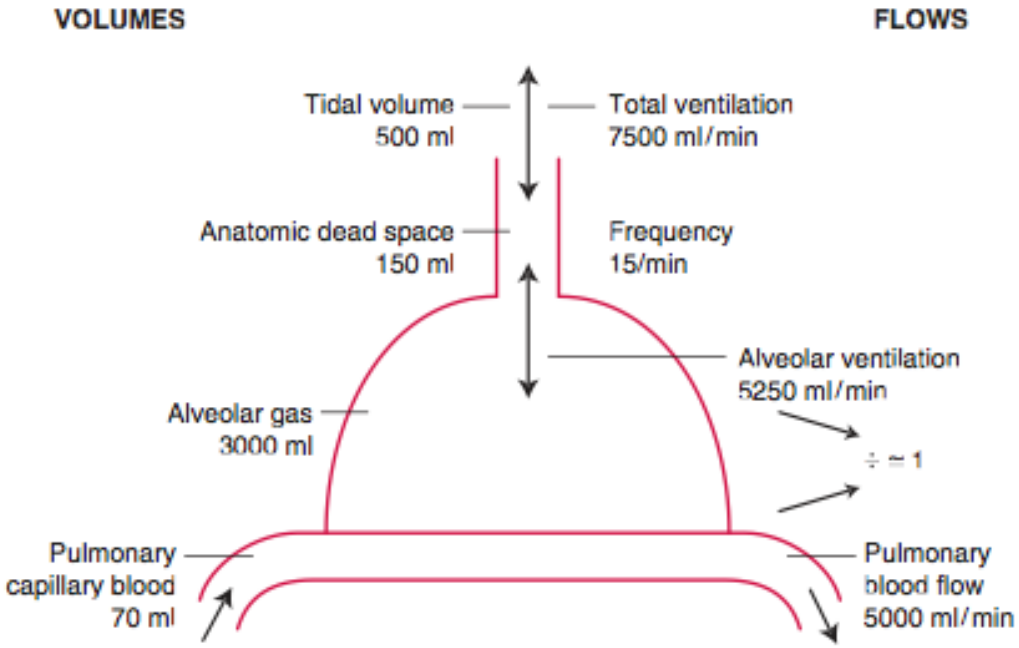


**Figure 1.1**: One compartment lung model. The diagram shows typical volumes and flows in a lung. There is considerable variation around these values.
Copyright has been obtained. *"Respiratory Physiology The Essentials"* by John B. West.

The main function of the pulmonary circulation is to move blood to and from the lung. Pulmonary circulation system carries erythrocytes (red blood cells), which mainly consist of hemoglobin where the oxygen molecule binds, directs flow

away from poorly ventilated alveoli, and regulates flow rate to give an adequate amount of time for oxygen to diffuse into erythrocytes. There are both passive and active flow controlling mechanisms implemented in the pulmonary circulation system to accomplish gas exchange.

Significant effort has been taken over the last five decades to understand the pulmonary circulation and its regulation. Before the advent of functional imaging modalities, experiments on the pulmonary circulation relied heavily on surgically removed animal lung preparations. Based on these early experimental data, several mathematical models were developed to predict the characteristics of pulmonary circulation over a wide range of vasculature branching orders. These models were simple and controlled by the minimal amount of boundary conditions; pulmonary arterial and left atrium pressures corresponded to inlet and outlet pressures respectively, while transpulmonary pressure counter-balanced the elastic recoil of lung tissue to define the lung volume. In recent years, pulmonary imaging has been gaining momentum as a new approach to study the pulmonary physiology, and extending the capabilities of these models. Due to the minimally invasive nature of imaging techniques, direct investigation of the human lung with high spatial and temporal resolutions has become more of a reality in recent years. This technology has been continuously evolving. Recently developed medical imaging modalities including functional magnetic resonance imaging (MRI) techniques enabled the quantification of the spatial distribution of pulmonary perfusion and are now an essential tool to answer some challenging questions regarding pulmonary physiology. The last five years of my thesis research work (I started to work with my collaborators at Pulmonary Imaging Laboratory, University of California, San Diego three years prior to my graduate school) builds upon the long history of pulmonary circulation research.

## 1.3 The anatomy pulmonary circulation system

The pulmonary blood vessels form a series of branching structures from pulmonary artery to the capillaries and then drain back to the pulmonary veins,

as schematically presented in Figure 1.2. Blood flows from the right ventricle to the pulmonary artery, then to capillary blood vessels, then to veins and finally to the left atrium. Initially the arteries and veins run together along the bronchi. However toward the periphery of the lung, the veins move away from the arteries to pass between lobes, while the arteries and bronchi run together down the centers of the lobes [48].

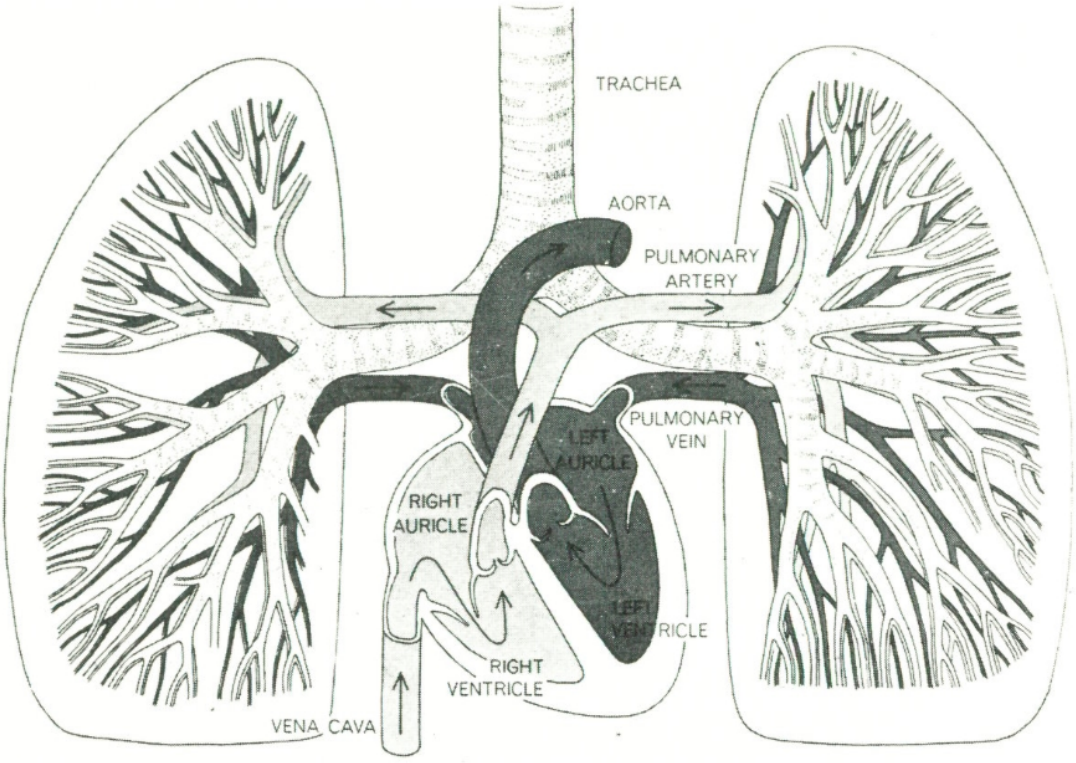


**Figure 1.2**: Relationship between the heart and the lung. Note that the pulmonary arteries lie close to the bronchi, whereas the pulmonary veins stand alone. Only the first few generations of the large pulmonary blood vessels and bronchi are shown in the figure.
Copyright has been obtained. *"Biodynamics Circulation"* by Y. C. Fung

The pulmonary vascular tree does not bifurcate symmetrically; every parent vessel does not yield two equal offspring. This bifurcation pattern is described by the branching ratio of the Strahler system [35]. The branching ratio of pulmonary vasculature tree is close to 3 [9] whereas with symmetric bifurcation the ratio is 2. Further down the branching tree when the vessel diameter is less than 100 $\mu$m,

the arterial and venous vessels are clustered separately. It appears that the region of arteries resembles isolated islands, while the region of the veins is a continuous ocean (Figure 1.3 [36]).

The capillaries consist of a dense network in the walls of the alveoli, often characterized as a sheet of fluid flowing between two membranes held apart by a number of equally spaced posts (Figure 1.4 [37]). Figure 1.5 shows the membrane known as the blood-gas barrier, which is extremely thin (less than 0.3 $\mu$m); it consists of a layer of endothelial cells, an interstitium, and a layer of epithelial cells.

Blood oxygenation is accomplished via the principle of diffusion. This requires, in addition to a thin membrane, a very large blood-gas interface area, where the blood is spread out into very thin sheets in alveoli. In an adult human lung with a pulmonary capillary blood volume of the order of 150 ml, the area of the pulmonary capillary blood-gas interface is of the order of 70 $m^2$ so that the sheet thickness of blood is approximately 4 $\mu$m [48]. Each sheet of blood forms an interalveolar septum and the smallest unit of space bounded by interalveolar septa is called the alveolus. In adult humans, there are approximately 300 million alveoli. The lung has an additional blood circulation system, the bronchial circulation, which supplies the conducting airways down to about the terminal bronchioles. Some of this blood is carried away from the lung via the pulmonary veins and some enters the systemic circulation. However, the flow through the bronchial circulation is a mere fraction of that through the pulmonary circulation.

## 1.4 Low-resistance and low-pressure pulmonary circulation system

The pulmonary blood flow must be optimized to provide an adequate transit time for the erythrocytes to complete gas exchange. Approximately 3 sec are required to move blood from the pulmonary valve to the left atrium in humans at rest. Each erythrocyte spends about 3/4 sec in the alveolar capillary network and during this time traverses two or three alveoli [48]. This brief time is sufficient to

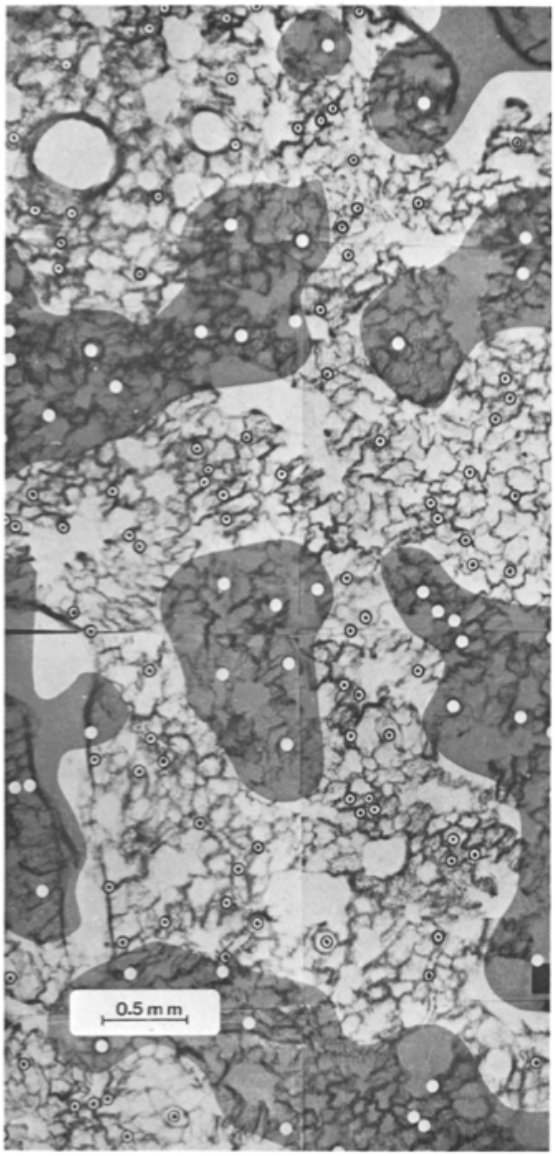


**Figure 1.3**: Histological section of cat lung. The map was made from montage of individual photomicrographs. Branches of pulmonary vessels from 15 to 100 $\mu$m diameter are individually identified. The domains of the pulmonary arteries are made darker by over lay of the area with collared film. Individual alveoli are clearly seen as well as branching vessels in the plane of the photomicrograph. The pulmonary artery domains are discontinuous and the pulmonary venous areas are continuous: the arterial areas are islands immersed in an ocean of pulmonary veins. Copyright has been obtained. *"Topology of Pulmonary Arterioles, Capillaries, and Venules in the Cat"*, 1980. by Sobin *et al.*

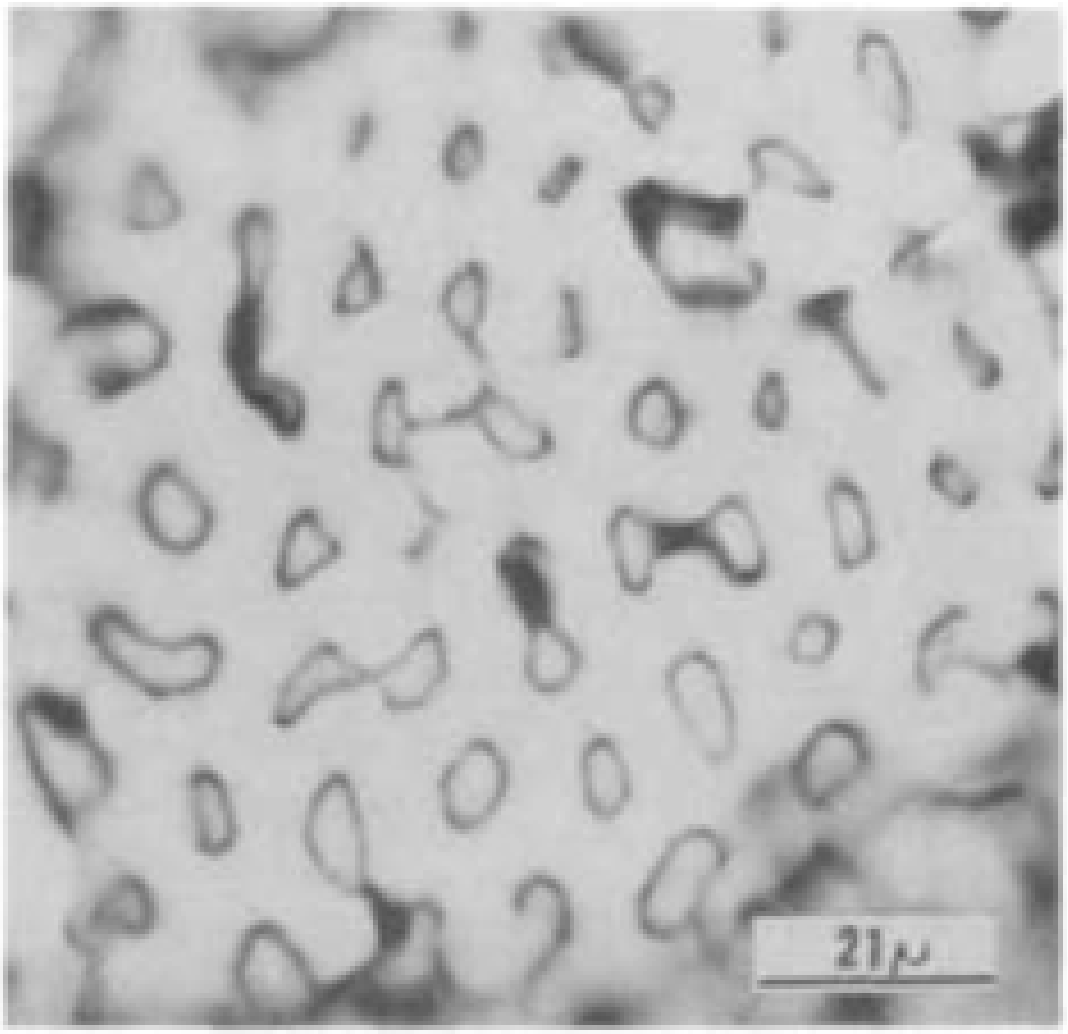


**Figure 1.4**: Flat view of interalveolar wall with the microcirculation filled with a silicone elastomer in a cat lung. It illustrates the tight mesh network of extensively filled capillary bed. The circular (or elliptical) enclosures are basement membrane and are the nonvascular posts.
Copyright has been obtained. *"Morphometric Basis of the Sheet-Flow Concept of the Pulmonary Alveolar Microcirculation in the Cat"*, 1970. by Sobin *et al.*

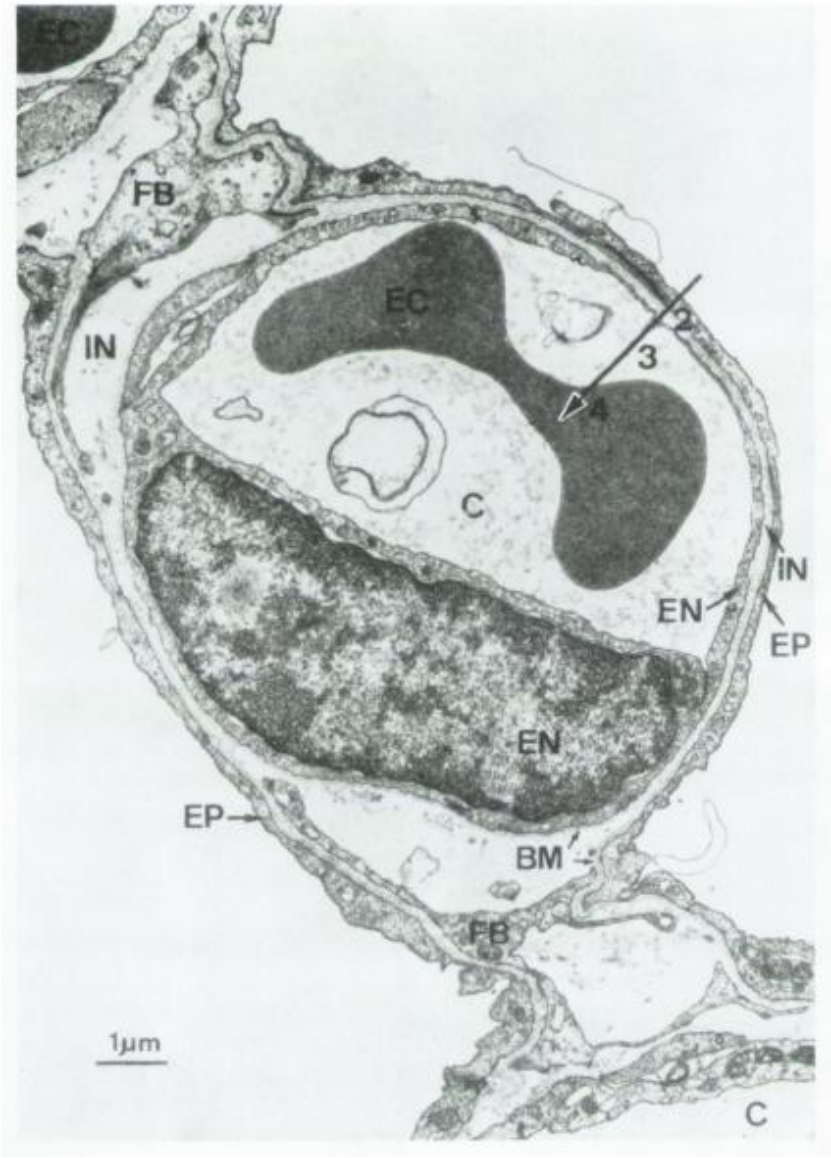


**Figure 1.5**: Electron micrograph showing a pulmonary capillary (C) in the alveolar wall. There is extremely thin blood-gas barrier of approximately 0.3 $\mu$m in some places. The large arrow indicates the diffusion path from alveolar gas to the interior of the erythrocyte (EC) and includes the layer of surfactant, alveolar epithelium (EP), interstitium (IN), capillary endothelium (EN), and plasma. Parts of structural cells called fibroblasts (FB), basement membrane (BM), and a nucleus of an endothelial cell are all seen.

accomplish the equilibration of oxygen and carbon dioxide between alveolar gas and capillary blood. In order to complete the transit of a whole cardiac output within such a short period of time, the pulmonary circulation is handled by a low-resistance system. Moreover, this low resistance system must be compliant, because the cardiac output in exercise will increase up to five fold and in this condition it is necessary to reduce the physiological stress loaded on the thin blood-gas barrier.

In addition to being low-resistance, the pulmonary vasculature is also a low-pressure system. A mean pulmonary arterial pressure oscillates around 10 cm Hg, which is required for a flow of 6 liter/min of cardiac output at rest. A low-pressure system does not require very strong vessel walls, so that the pulmonary vessel walls are thinner and flimsier than those of the systemic circulation. Therefore, the container of the pulmonary blood is quite flexible and the flow is significantly influenced by elastic deformation. The local pulmonary capillary resistance is strongly influenced by blood and air pressures, which determine transmural pressure. Pulmonary blood flow is not a linear function of the blood pressure gradient. An increase in blood pressure distends the blood vessel and reduces the flow resistance, resulting in an even greater increase in flow. The major determinations of pulmonary blood flow are (a) topology of the blood vessels, (b) the pressures of alveolar gas and blood, (c) the viscosity of blood, (d) the elasticity of blood vessels, and (e) intrapleural pressure that affects the lung volume. Among those determining parameters, the blood pressure, alveolar gas pressure, and distensibility of vascular wall are the major driving forces controlling the local pulmonary blood flow [10, 11]. The local control on the pulmonary blood flow is discussed in the next section.

## 1.5 Classic models of local pulmonary blood flow control

Before the emergence of imaging modalities, which enables the noninvasive measurement, the studies on the morphology of the pulmonary structures

and circulation system in human [17, 38] and animals [36, 37] involved surgical procedures. The basic rheological data of the blood in the microvasculature network and the mechanical properties of the pulmonary blood vessels over the wide range of branching orders were obtained using excised and perfused animal lungs [10, 11, 18, 24, 25, 34, 40, 50, 51]. Based on the early days of experimental data, several important mathematical models, which describe the local control on pulmonary circulation, were developed analytically. The results of theoretical analysis were in reasonable agreement with the data from physiological experiments [10, 11]. These models were simple, yet powerful enough to understand the complex pulmonary circulation.

The zone model that proposed by West *et al.* [46] describes the gravitational dependence of pulmonary blood flow distribution in three different zones presented in Figure 1.6. The model characterizes the blood flow in the pulmonary capillary beds by three representative pressures: alveolar air ($p_A$), arterial ($p_a$) and venous ($p_v$). (Y.C. Fung described a as arteriole (art) and v as venule (ven) to microscopically focus at the entry and exit of capillary [11]). This model assumes the alveolar air pressure is the same throughout the lung, while accounts for the linear increase in blood pressure in the gravitationally dependent direction (i.e. toward the base of the lung in upright posture) due to the hydrostatic pressure. In other words, in a static lung at end of an expiration, $p_A$ is constant and close to the atmospheric pressure, while $p_a$ varies with location within the lung, but is always bigger or equal to $p_v$. Therefore, the lung is divided into three representative zones based on the relationship among three pressure profiles. In zone 1 $p_A$ exceeds $p_a$ so that there is no capillary flow; this condition is predominantly present in the nondependent part of the lung (i.e. the apex of the lung in upright posture). In zone 2 (middle part of lung), $p_a$ exceeds $p_A$ but $p_v$ does not exceed $p_A$ so that the capillary flow depends on $p_a$ and increases linearly as the hydrostatic pressure rises along the gravitationally dependent direction. Lastly, in zone 3, both $p_a$ and $p_v$ exceed $p_A$ so that the flow is driven by the pressure difference between $p_a$ and $p_v$. As transmural pressure increases towards the bottom of zone 3, the capillaries dilate. Therefore, blood flow also increases towards the gravitationally dependent

direction. However, the change is more gradual than in zone 2.

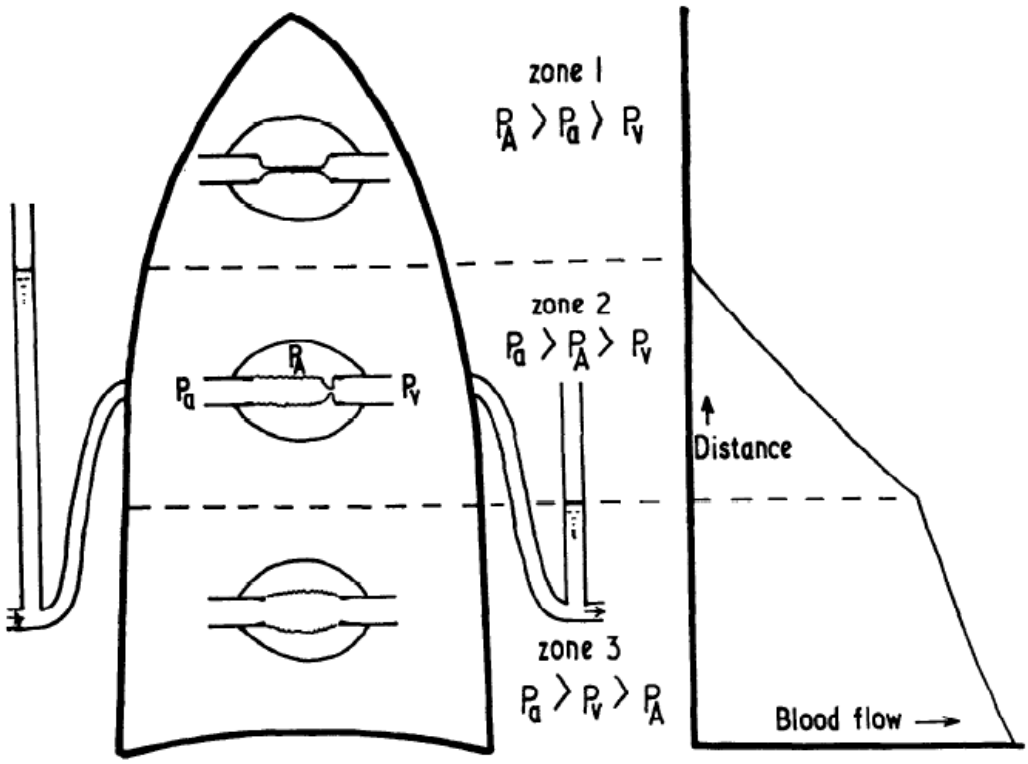


**Figure 1.6**: Uneven distribution of blood flow in the lung, based on the pressures affecting the capillaries. The lung is divided into three zones according to the relative magnitude of the pulmonary arterial ($p_a$), venous ($p_v$), and alveolar pressures ($p_A$).
Copyright has been obtained. *"Distribution of blood flow in isolated lung; relation to vascular and alveolar pressures"*, 1964. by West *et al.*

Y.C. Fung and S.S. Sobin added the concept of vessel wall dispensability onto the local pressure distribution [10]. Since the pulmonary vessel wall is elastic, the vessel diameter and cross section area are closely related to blood pressure. The geometry of the dense pulmonary capillary network in the interalveolar septa was simplified as a sheet of fluid flowing between two membranes held apart by a number of posts presented in Figure 1.7 [8]. The sheet is characterized by three parameters; the sheet height, the area of the alveolar sheet and the vascular-space-tissue ratio, which is the fraction of the alveolar sheet occupied by the blood. The sheet is elastic and the sheet height has a linear relationship with blood pressure.

Together with the equation of continuity and motion, and an experimentally verified linear relationship between local flow velocity and pressure gradient, Fung and Sobin obtained the pressure-flow relationship so called the fourth power law [10]: pulmonary capillary flow is proportional to the fourth power of blood pressure, which has a linear relationship with sheet height.

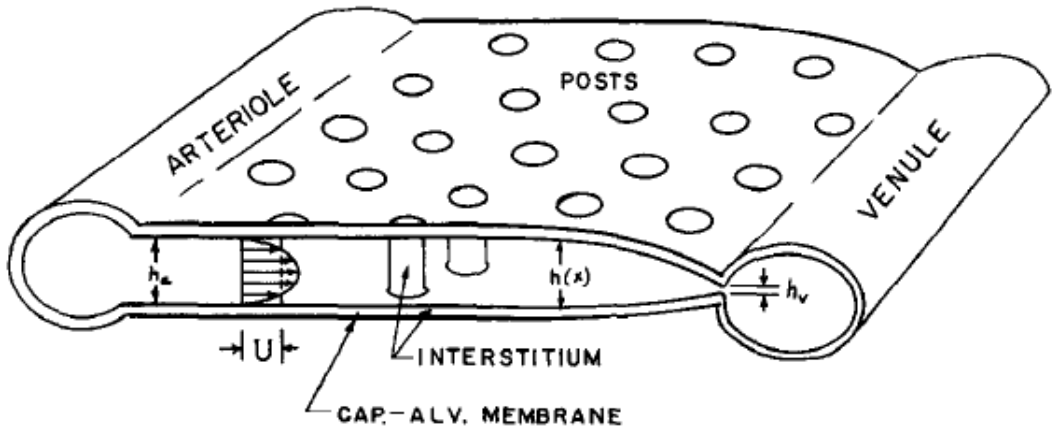


**Figure 1.7**: Schematic of an alveolar sheet. Vascular space is bounded by capillary-alveolar membranes which are connected by posts.
Copyright has been obtained. *"Fluid in the Interstitial Space of the Pulmonary Alveolar Sheet"*, 1974. by Y. C. Fung.

The blood flow in pulmonary arteries and veins was described using a different model since the geometry of this portion of the vasculature can no longer be characterized by sheet flow [50, 51]. The vessel diameter changes linearly with blood pressure. This model follows a fifth power law in which the blood flow is proportional to the fifth power of blood pressure [52]. The details of these models as well as equations are described in Appendix A. In short, the high order (fourth and fifth) relationships between these variables demonstrate that a slight change in local pulmonary blood pressure and/or vessel diameter result in a significant change in the local blood flow.

## 1.6 Recent models of the pulmonary circulation model

Basic mathematical models discussed above are still in use, but models continue to evolve [39]. Clark *et al.* developed an anatomically-based model of blood flow through the full pulmonary circuit of a single human subject combined with a parenchymal tissue mechanics model to investigate the interdependence of structure, fluid transport, and mechanical behavior in perfusion of the lung [7]. This is currently, to the best of my knowledge, the only multi-scale and multi-physics model that simultaneously includes all of the basic passive mechanisms influencing the distribution of pulmonary blood flow. The model geometry is subject-specific where the distribution of the largest blood vessels and the regional tissue density is measured from multi-row detector computed tomography [3]. A volume filling branching algorithm was used to supplement the geometry from the level at which the CT imaging resolution becomes insufficient (Figure 1.8).

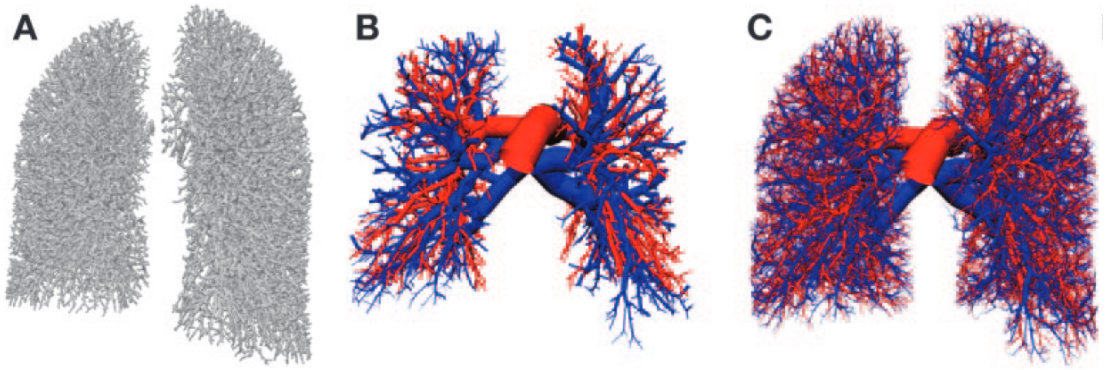


**Figure 1.8**: Subject specific pulmonary circulation model geometry. A: rendered vessels from multidetector row computed tomography (MDCT) data. B: MDCT derived arterial (red) and venous (blue) vessels. C: vessels generated into the lobar volume using the volume-filling branching algorithm.
Copyright has been obtained. *Anatomically based finite element models of the human pulmonary arterial and venous tree including supernumerary vessels*, 2005. by Burrowes *et al.*

Their microcirculatory model has a ladder structure where each rung represents alveolar septa modeled as sheet flow, one set of posts on the ladder are

arterioles, and the matching set of posts are the draining venules (Figure 1.9) [6]. The modeled acinar airways have a symmetric branching structure. Arterioles and venules are elastic vessels that follow the branching structure of the acinar airways. These vessels are assumed to be joined at each generation by capillary sheets that cover the alveoli present at that generation, forming a ladderlike structure shown in Figure 1.10C.

The structure based pulmonary circulation model is controlled by a limited number of boundary conditions such as the intrapleural pressure ($p_{pl}$), pulmonary arterial pressure ($p_a$), left atrial pressure ($p_{LA}$) and local tissue distribution. The model is solved for the distribution of local pulmonary vasculature resistance and blood flow. Therefore, it is capable of predicting the functional consequence of changes influencing local pulmonary blood flow (e.g. the effect of posture, pulmonary embolism, hypertension, etc.).

## 1.7 Noninvasive local pulmonary blood flow measurement

Testing of and progressing from the previously discussed mathematical models of pulmonary circulation require direct and noninvasive measurement of the regional distribution of pulmonary blood flow *in vivo*. West's zone model in which the hydrostatic pressure distribution is the major determining factor of pulmonary blood flow distribution has remained as the primary hypothesis for over 3 decades [39]. This was in part because of the lack of suitable techniques to directly measure the regional pulmonary blood flow distribution in humans.

Hughes *et al.* advanced the zone model in upright human lung by adding the Zone 4 condition where the pulmonary blood flow is reduced at the most dependent region of the lung. Zone 4 is believed to be created by an increase in interstitial pressure narrowing the caliber of extra-alveolar vessels in this zone [21]. Hughes *et al.* also found that the gravitational effect on the pulmonary blood flow distribution as indicated by blood flow gradients in the gravitational direction was most noticeable at total lung capacity and vanished at residual volume. However,

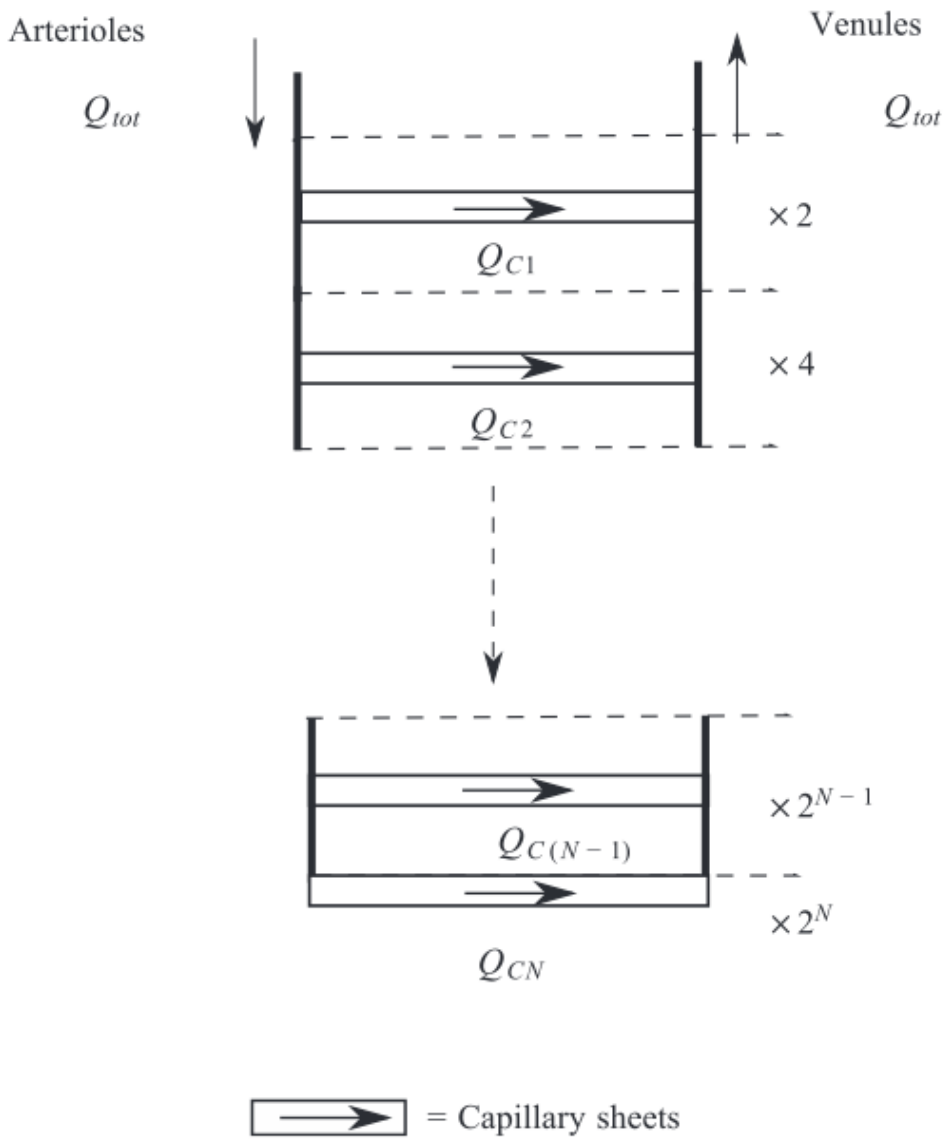


**Figure 1.9**: Ladder model: a symmetric branching srteriole/venule structure with N symmetric branches, joined by capillary sheets at each generation. Arrows show the direction of blood flow. Dashed lines represent a bifacation in the arterioles and venules and so a doubling in the number of arterioles, venules, and capillary sheets. $Q_{tot}$, total blood flow into system; $Q_C$, flow through caoillary sheet.
Copyright has been obtained. *"Anatomically based finite element models of the human pulmonary arterial and venous tree including supernumerary vessels"*, 2010. by Clark *et al.*

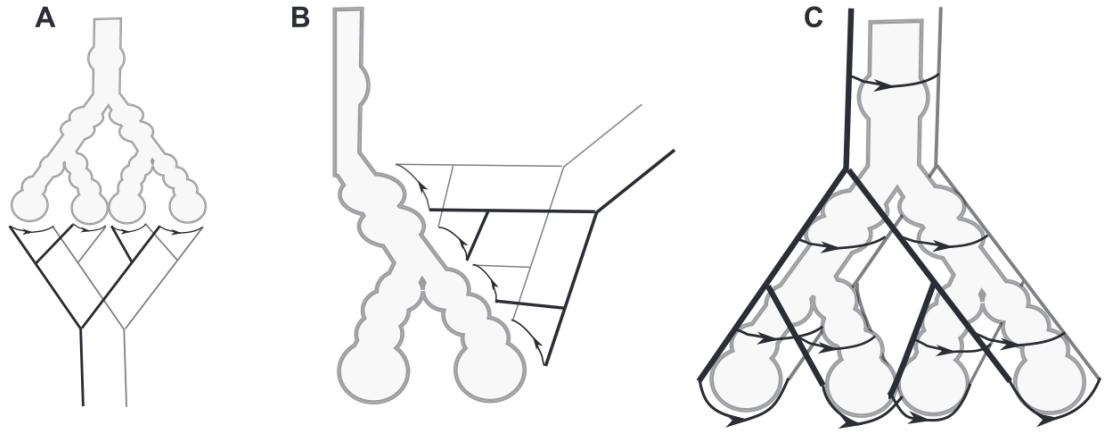


**Figure 1.10**: Model of ventilation-perfusion relationships. A: parallel ventilation/parallel perfusion. B: serial ventilation/parallel perfusion. C: Acinar geometry used to model perfusion in the acinus. Acinar units are illustrated as ducts where sacs represent alveoli. Capillary units are marked with arrows in the direction of blood flow to allow clear distinction from larger noncapillary vessels. Copyright has been obtained. *"Anatomically based finite element models of the human pulmonary arterial and venous tree including supernumerary vessels"*, 2010. by Clark *et al.*

Glenny *et al.* showed that the changes in pulmonary blood flow distribution in isolated baboon lungs with different postures were not only attributed to the zone model [13]. The pulmonary blood flow gradients in the gravitational direction were not reversible by reversing posture. Contrary to the Zone model hypothesis, Glenny *et al.* concluded that the anatomical geometry of the lung and vasculature structure are the major contributors to the regional distribution of pulmonary blood flow [14]. The relative contribution of gravity on pulmonary blood flow distribution has been subject of intense debate in recent years [15, 22].

The development of imaging modalities enabled direct and noninvasive quantification of the blood flow in the human lung [30]. Recent functional MRI studies showed the gravitational dependency of pulmonary blood flow and the parenchymal tissue distribution at high spatial resolution [20, 29]. The gravitational dependency of pulmonary blood flow is partially caused by the self-deformation of the parenchymal tissue. This is the Slinky® effect (Slinky is a registered trademark of Poof-Slinky Incorporated). The perfusion measurements

*in vivo* are influenced by density distributions and differ from isolated lungs where density gradients are reduced through excision processes. Thus, the measured pulmonary blood flow needs to account for the parenchymal tissue distribution, e.g. density normalized perfusion (in the units of milliliter of blood per unit of time per gram of lung tissue).

When combined with the conventional mathematical models, the pulmonary blood flow map obtained using functional MRI will give a more spatially detailed set of boundary conditions. Therefore, it has the potential to estimate the dynamics of pulmonary blood flow over a wider range of pulmonary vessel orders.

### 1.7.1 Slinky® Effect

The gravitational dependency of pulmonary blood flow caused by the self-deformation of the parenchymal tissue is conceptually modeled as a Slinky® spring [20]. The greater density of lung tissues in the dependent regions of the lung due to gravity is analogous to a denser distribution of coils in the dependent parts of the upright spring (Figure 1.11). The pulmonary vessels run through the coils so that a gravitational dependency in lung tissue density also reflects a vertical gradient in perfusion distribution. Therefore, externally measured pulmonary perfusion distribution must account for lung tissue distribution. Calculating density normalized perfusion (mL(blood)/min/g(tissue)) is analogous to removal of the influences of the deformation.

## 1.8 Ventilation and Perfusion Relationship

As stated in the introduction of this chapter, the relationship between ventilation and perfusion is essential for gas exchange efficiency. At the macro scale where the lung is considered to be a single compartment model as described in Figure 1.1, the ventilation to perfusion ratio ($\dot{V}_A/\dot{Q}$) is approximately unity, e.g. alveolar ventilation and cardiac output are both approximately 5000 ml/min, respectively. At the microscopic scale, the lung is comprised of numerous compartments and both ventilation and perfusion are heterogeneously distributed. However, in

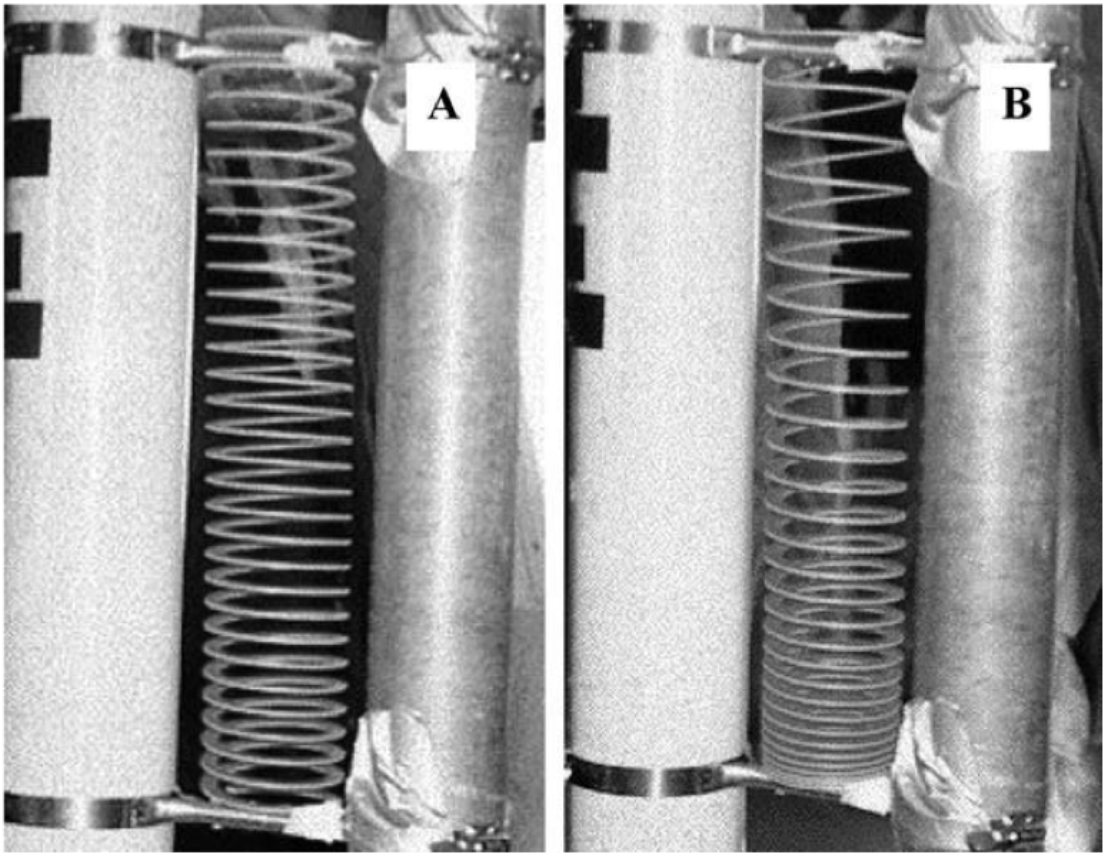


**Figure 1.11**: Deformable spring (Slinky®) during parabolic flight. In A, in the absence of gravity (0 G), the coils of spring are uniformly distributed whereas in B, under the influence of gravity 2 G, the spring deforms. The lung is modeled as a vertically oriented Slinky® where the blood flows through the coils. The greater density of lung tissue in the dependent regions of the lung is considered as a greater number of coils in the dependent parts of the spring. Calculating density normalized perfusion (mL(blood)/min/g(tissue)) is analogous to removal of the influences of the deformation.

spite of the heterogeneous distributions of underlying ventilation and perfusion, the distribution of $\dot{V}_A/\dot{Q}$ rations throughout the healthy lung is unimodal with a narrow dispersion and approximately centered around one. This narrow dispersion of the $\dot{V}_A/\dot{Q}$ distribution is essential for gas exchange efficiency. Poorly ventilated parts of the lung should be associated with low perfusion and vice versa for efficient gas exchange. The previously discussed local control of pulmonary blood flow distribution is the primary mechanism to ensure the efficiency of gas exchange. For instance, hypoxic pulmonary vasoconstriction (HPV) increases vascular resistance in regions of low alveolar ventilation, resulting in a corresponding low perfusion. The $\dot{V}_A/\dot{Q}$ distribution has been experimentally quantified using a variety of techniques. Fluorescent microsphere techniques have been used for animal experiments [5, 31], while radioactive $CO_2$ [47], positron emission tomography [41] and functional MRI [19] have been used for human experiments. The most prevailing method of measuring $\dot{V}_A/\dot{Q}$ distribution is the multiple inert gas elimination technique (MIGET). Measurements have been made on breathing air and 100 % oxygen [45], exercise at sea level and simulated high altitude [12], in patients with chronic obstructive pulmonary disease [32, 42] and in patients with asthma [2], amongst others. It should be noted that $\dot{V}_A/\dot{Q}$ dispersions measured using different techniques are not directly comparable. The $\dot{V}_A/\dot{Q}$ dispersion value depends on the scale of spatial sampling or the magnitude of smoothing factor, which are limited by the measurement techniques [5, 19].

MIGET utilizes six inert gases with different solubilities. These inert gases are dissolved in saline and infused into a subject intravenously. In equilibrium condition, the amounts of each gas retained in blood circulation and excreted with expiration are the function of $\dot{V}_A/\dot{Q}$ distribution in a lung. Therefore, a global $\dot{V}_A/\dot{Q}$ distribution is computed by solving the inverse problem with least square curve fitting [33, 43, 44]. MIGET experiments showed that the $\dot{V}_A/\dot{Q}$ distribution had little dispersion in young semirecumbent subjects (ages 21 - 24) where the 95.5 % range of both blood flow and ventilation was from $\dot{V}_A/\dot{Q}$ ratios of 0.3 - 2.1 and there was no shunt ($\dot{V}_A/\dot{Q} = 0$). On the other hand, the older subjects (ages 39 - 60) had a broader range of $\dot{V}_A/\dot{Q}$ distributions [45].

## 1.9 Ventilation - perfusion heterogeneity and underlying perfusion heterogeneity

The $\dot{V}_A/\dot{Q}$ dispersion is called ventilation  perfusion heterogeneity and conventionally expressed in logarithmic scale (i. e. $\dot{V}_A/\dot{Q} = 0.1$ and $\dot{V}_A/\dot{Q} = 10$ are equally weighted and the average of them becomes $\dot{V}_A/\dot{Q} = 1$ in the logarithmic scale). Ventilation - perfusion heterogeneity is the metric of the inefficiency of alveolar gas exchange together with the measurements of shunt ($\dot{V}_A/\dot{Q} = 0$) and dead-space ($\dot{V}_A/\dot{Q} = \infty$). Ignoring shunt and dead-space, Wilson and Beck described the relationship of $\dot{V}_A/\dot{Q}$ dispersion expressed as variance using the underlying ventilation ($\dot{V}_A$) and perfusion ($\dot{Q}$) distributions [49]:

$$\sigma^2_{\dot{V}_A/\dot{Q}} = \sigma^2_{\dot{V}_A} + \sigma^2_{\dot{Q}} - 2R\sigma_{\dot{V}_A}\sigma_{\dot{Q}} \tag{1.1}$$

where $R$ is the correlation coefficient between $\dot{V}_A$ and $\dot{Q}$ in logarithmic scale; ${\sigma_{V_A/Q}}^2$, ${\sigma_{V_A}}^2$, and ${\sigma_Q}^2$ represent $\dot{V}_A/\dot{Q}$, $\dot{V}_A$, and $\dot{Q}$ variances, respectively. The graphical interpretation of equation 1.1 in 2D scatter plot (in which x and y axes represent perfusion and ventilation, respectively) is illustrated in Appendix A as a 2D scatter plot (Figure A.1 from Appendix). In short, ventilation  perfusion heterogeneity is further divided into three terms; ventilation heterogeneity, perfusion heterogeneity and the correlation between the ventilation and perfusion data. Therefore, measuring the underlying perfusion heterogeneity covers one of three terms governing the overall extent of ventilation - perfusion heterogeneity.

## 1.10 The nature of perfusion heterogeneity

The distribution of pulmonary blood flow is spatially heterogeneous even in the normal human lung ( [20, 23, 26–28]). The nature of the observed pulmonary blood flow heterogeneity is partially due to gravitational factors [46] influenced by posture [28] and also from vascular branching structure [1, 4, 13, 14] that are partly under genetic control [16]. Lung tissue deformation, namely Slinky® effect, also affects perfusion heterogeneity in gravitational direction.

## 1.11 Specific aims of the dissertation

Two physiological questions regarding the local control of pulmonary blood flow were selected as the main goals for this dissertation: what are the effects of (1) hypoxic pulmonary vasoconstriction (HPV) and (2) what is role of tidal volume lung inflation on the spatial distribution of pulmonary blood flow.

Goal (1): Hypoxic pulmonary vasoconstriction increases pulmonary vascular resistance in regions of low alveolar ventilation, ideally resulting in a correspondingly low perfusion. Therefore, any alteration in regional alveolar $P_{O_2}$ ($P_{AO_2}$) may affect the spatial distribution of pulmonary perfusion. It was hypothesized that part of the pulmonary perfusion heterogeneity in humans is due to regional hypoxic pulmonary vasoconstriction. If this was the case, breathing a mild hyperoxic gas mixture would be expected to raise local $P_{AO_2}$ and abolish any localized hypoxic pulmonary vasoconstriction, resulting in a more uniform spatial distribution of pulmonary blood flow.

Goal (2): The well-ventilated regions of the lung must be well-perfused and vice versa in order to maintain the $\dot{V}_A/\dot{Q}$ distribution as close as unity. However, the greater lung tissue deformation due to breathing motion causes greater local vasculature stretch, resulting in a spatially heterogeneous change in pulmonary vasculature resistance and hydrostatic pressure distribution. Changes in vasculature topology due to lung inflation are expected to cause two confounding effects on the pulmonary vascular resistance. The increase in axial length is expected to linearly increase the resistance whereas the increase in vessel diameter is expected to result in a nonlinear decrease in the flow resistance due to fourth and fifth power laws. In addition, the increase in lung dimensions along the gravitational direction results in a change in the hydrostatic pressure and local blood pressure distributions. Therefore, the overall effect of lung inflation on the spatial distribution of pulmonary blood flow is unclear.

Both of the effects discussed above are linked to gas exchange efficiency since the distribution of pulmonary blood flow is influenced by local oxygenation and mechanical stretch, which are associated with the ventilation side of pulmonary function. The direct and noninvasive measurement of pulmonary blood flow us-

ing functional MRI is especially suited for the type of research proposed. For the lung inflation study, an anatomically identical lung element over two lung volumes needs to be compared. In addition, the local lung inflation, which expected to be heterogeneously distributed throughout the lung, needs to be computed. Therefore, nonlinear image registration technique is implemented to the data analysis scheme to handle the image displacement and local lung inflation.

In order to conduct my thesis research work, four specific aims were assigned.

Specific Aim 1: Development of MRI study protocols to quantify the spatial distribution of pulmonary perfusion and its heterogeneity in the human lung.

Specific Aim 2: Development of a nonlinear lung deformation analysis technique to compute the local lung volume change and tissue displacement due to breathing motion.

Specific Aim 3: Determining the effect of hypoxic pulmonary vasoconstriction (HPV) on the spatial distribution of pulmonary perfusion.

Specific Aim 4: Determining the effect of tidal breath lung inflation on the spatial distribution of pulmonary perfusion.

## 1.12 Accomplishment and outline of the dissertation

The details of each specific aim are laid out in later chapters. Chapter 2, 3 and 4 describe the methodologies: Chapter 2 provides the MRI sequences and data analysis methods behind the work of this dissertation: Chapter 3 presents the overall methods, describing how to conduct a human pulmonary study in an MRI scanner environment: Chapter 4 demonstrates the cubic polynomial interpolation method and its application to the nonlinear lung deformation analysis. These methods were used for physiology experiments discussed in chapter 5 and 6.

In addressing SA1, an MRI technique to quantify the spatial distribution of pulmonary perfusion in the human lung was developed and presented in Chapter 2 and 3. The part of work was published in *Journal of Visualized Experiments*

2011, "Magnetic resonance imaging quantification of pulmonary perfusion using calibrated arterial spin labeling".

The nonlinear image registration technique to compute the local lung volume change and tissue displacement was developed and presented in Chapter 4. A short paper published in *Conf Proc IEEE Eng Med Biol Soc* 2012, "Affine transformation registers small scale lung deformation" uses the same computational scheme to address SA2 of my dissertation research.

The results of two physiological experiments (effects of HPV and lung deformation), addressing SA3 and SA4 are discussed in Chapter 5 and Chapter 6, respectively.

The successful completion of SA3 led to the publication "Hypoxic pulmonary vasoconstriction does not contribute to pulmonary blood flow heterogeneity in normoxia in normal supine humans", *J Appl Physiol* 2009. In the extended form, this part of the work is presented in Chapter 5.

SA4 is the original work, presented here for the first time. Chapter 6 describes the effect of tidal breath lung inflation on the spatial distribution of pulmonary perfusion.

Finally, the conclusion of this dissertation is given in Chapter 7, including a discussion of potential future work. Appendices are also provided to supplement detailed information.

## 1.13 Bibliography

[1] W. A. Altemeier, S. McKinney, M. Krueger, and R. W. Glenny. Effect of posture on regional gas exchange in pigs. *Journal of applied physiology (Bethesda, Md. : 1985)*, 97(6):2104–2111, Dec 2004.

[2] E. Ballester, A. Reyes, J. Roca, R. Guitart, P. D. Wagner, and R. Rodriguez-Roisin. Ventilation-perfusion mismatching in acute severe asthma: effects of salbutamol and 100% oxygen. *Thorax*, 44(4):258–267, 1989.

[3] K. S. Burrowes, P. J. Hunter, and M. H. Tawhai. Anatomically based finite element models of the human pulmonary arterial and venous trees including supernumerary vessels. *Journal of applied physiology (Bethesda, Md. : 1985)*, 99(2):731–738, Aug 2005.

[4] K. S. Burrowes and M. H. Tawhai. Computational predictions of pulmonary blood flow gradients: gravity versus structure. *Respiratory physiology & neurobiology*, 154(3):515–523, Dec 2006.

[5] H. Chang, S. J. Lai-Fook, K. B. Domino, C. Schimmel, J. Hildebrandt, H. T. Robertson, R. W. Glenny, and M. P. Hlastala. Spatial distribution of ventilation and perfusion in anesthetized dogs in lateral postures. *Journal of Applied Physiology*, 92(2):745–762, 2002.

[6] A. R. Clark, K. S. Burrowes, and M. H. Tawhai. Contribution of serial and parallel microperfusion to spatial variability in pulmonary inter- and intra-acinar blood flow. *Journal of applied physiology (Bethesda, Md. : 1985)*, 108(5):1116–1126, May 2010.

[7] A. R. Clark, M. H. Tawhai, E. A. Hoffman, and K. S. Burrowes. The interdependent contributions of gravitational and structural features to perfusion distribution in a multiscale model of the pulmonary circulation. *Journal of applied physiology (Bethesda, Md. : 1985)*, 110(4):943–955, Apr 2011.

[8] Y. C. Fung. Fluid in the interstitial space of the pulmonary alveolar sheet. *Microvascular research*, 7(1):89–113, Jan 1974.

[9] Y. C. Fung. *Biodynamics Circulation*. Springer Verlag, 1984.

[10] Y. C. Fung and S. S. Sobin. Elasticity of the pulmonary alveolar sheet. *Circulation research*, 30(4):451–469, Apr 1972.

[11] Y. C. Fung and S. S. Sobin. Pulmonary alveolar blood flow. *Circulation research*, 30(4):470–490, Apr 1972.

[12] G. E. Gale, J. R. Torre-Bueno, R. E. Moon, H. A. Saltzman, and P. D. Wagner. Ventilation-perfusion inequality in normal humans during exercise at sea level and simulated altitude. *Journal of Applied Physiology*, 58(3):978–988, 1985.

[13] R. W. Glenny, S. Bernard, H. T. Robertson, and M. P. Hlastala. Gravity is an important but secondary determinant of regional pulmonary blood flow in upright primates. *Journal of applied physiology (Bethesda, Md. : 1985)*, 86(2):623–632, Feb 1999.

[14] R. W. Glenny, W. J. Lamm, R. K. Albert, and H. T. Robertson. Gravity is a minor determinant of pulmonary blood flow distribution. *Journal of applied physiology (Bethesda, Md. : 1985)*, 71(2):620–629, Aug 1991.

[15] R. Glenny. Counterpoint: Gravity is not the major factor determining the distribution of blood flow in the healthy human lung. *Journal of Applied Physiology*, 104(5):1533–1535, 2008.

[16] R. Glenny, S. Bernard, B. Neradilek, and N. Polissar. Quantifying the genetic influence on mammalian vascular tree structure. *Proceedings of the National Academy of Sciences of the United States of America*, 104(16):6858–6863, Apr 2007.

[17] B. Haefeli-Bleuer and E. R. Weibel. Morphometry of the human pulmonary acinus. *The Anatomical record*, 220(4):401–414, Apr 1988.

[18] T. S. Hakim, R. P. Michel, and H. K. Chang. Effect of lung inflation on pulmonary vascular resistance by arterial and venous occlusion. *Journal of applied physiology: respiratory, environmental and exercise physiology*, 53(5):1110–1115, Nov 1982.

[19] A. C. Henderson, R. C. Sá, R. J. Theilmann, R. B. Buxton, G. K. Prisk, and S. R. Hopkins. The gravitational distribution of ventilation-perfusion ratio is more uniform in prone than supine posture in the normal human lung. *Journal of applied physiology (Bethesda, Md. : 1985)*, 115(3):313–324, Aug 2013.

[20] S. R. Hopkins, A. C. Henderson, D. L. Levin, K. Yamada, T. Arai, R. B. Buxton, and G. K. Prisk. Vertical gradients in regional lung density and perfusion in the supine human lung: the slinky effect. *Journal of applied physiology (Bethesda, Md. : 1985)*, 103(1):240–248, Jul 2007.

[21] J. M. Hughes, J. B. Glazier, J. E. Maloney, and J. B. West. Effect of lung volume on the distribution of pulmonary blood flow in man. *Respiration physiology*, 4(1):58–72, Jan 1968.

[22] M. Hughes and J. B. West. Point: Counterpoint: Gravity is/is not the major factor determining the distribution of blood flow in the human lung. *Journal of Applied Physiology*, 104(5):1531–1533, 2008.

[23] A. T. Jones, D. M. Hansell, and T. W. Evans. Pulmonary perfusion in supine and prone positions: an electron-beam computed tomography study. *Journal of applied physiology (Bethesda, Md. : 1985)*, 90(4):1342–1348, Apr 2001.

[24] S. Kira and Y. Hukushima. Effect of negative-pressure inflation on pulmonary vascular flow. *Journal of applied physiology*, 25(1):42–47, Jul 1968.

[25] S. J. Lai-Fook. A continuum mechanics analysis of pulmonary vascular interdependence in isolated dog lobes. *Journal of applied physiology: respiratory, environmental and exercise physiology*, 46(3):419–429, Mar 1979.

[26] D. L. Levin, R. B. Buxton, J. P. Spiess, T. Arai, J. Balouch, and S. R. Hopkins. Effects of age on pulmonary perfusion heterogeneity measured by magnetic resonance imaging. *Journal of applied physiology (Bethesda, Md. : 1985)*, 102(5):2064–2070, May 2007.

[27] G. Musch, J. D. H. Layfield, R. S. Harris, M. F. V. Melo, T. Winkler, R. J. Callahan, A. J. Fischman, and J. G. Venegas. Topographical distribution of pulmonary perfusion and ventilation, assessed by pet in supine and prone humans. *Journal of applied physiology (Bethesda, Md. : 1985)*, 93(5):1841–1851, Nov 2002.

[28] S. Nyrén, M. Mure, H. Jacobsson, S. A. Larsson, and S. G. Lindahl. Pulmonary perfusion is more uniform in the prone than in the supine position: scintigraphy in healthy humans. *Journal of applied physiology (Bethesda, Md. : 1985)*, 86(4):1135–1141, Apr 1999.

[29] G. K. Prisk, K. Yamada, A. C. Henderson, T. J. Arai, D. L. Levin, R. B. Buxton, and S. R. Hopkins. Pulmonary perfusion in the prone and supine postures in the normal human lung. *Journal of applied physiology (Bethesda, Md. : 1985)*, 103(3):883–894, Sep 2007.

[30] H. T. Robertson and R. B. Buxton. Imaging for lung physiology: What do we wish we could measure? *Journal of Applied Physiology*, 113(2):317–327, 2012.

[31] H. T. Robertson and M. P. Hlastala. Microsphere maps of regional blood flow and regional ventilation. *Journal of Applied Physiology*, 102(3):1265–1272, 2007.

[32] J. Roca, P. D. Wagner, R. Guitart, R. Rodriguez-RoisÃ Ân, et al. Hypoxic pulmonary vasoconstriction and gas exchange during exercise in chronic obstructive pulmonary disease. *CHEST Journal*, 97(2):268–275, 1990.

[33] J. Roca and P. D. Wagner. Contribution of multiple inert gas elimination technique to pulmonary medicine. 1. principles and information content of the multiple inert gas elimination technique. *Thorax*, 49(8):815–824, 1994.

[34] A. Roos, L. J. Thomas, E. L. Nagel, and D. C. Prommas. Pulmonary vascular resistance as determined by lung inflation and vascular pressures. *Journal of applied physiology*, 16:77–84, Jan 1961.

[35] S. Singhal, R. Henderson, K. Horsfield, K. Harding, and G. Cumming. Morphometry of the human pulmonary arterial tree. *Circulation Research*, 33(2):190–197, 1973.

[36] S. S. Sobin, Y. C. Fung, R. G. Lindal, H. M. Tremer, and L. Clark. Topology of pulmonary arterioles, capillaries, and venules in the cat. *Microvascular research*, 19(2):217–233, Mar 1980.

[37] S. S. Sobin, H. M. Tremer, and Y. C. Fung. Morphometric basis of the sheet-flow concept of the pulmonary alveolar microcirculation in the cat. *Circulation research*, 26(3):397–414, Mar 1970.

[38] S. S. Sobin, Y. C. Fung, and H. M. Tremer. Collagen and elastin fibers in human pulmonary alveolar walls. *Journal of Applied Physiology*, 64(4):1659–1675, 1988.

[39] M. H. Tawhai, A. R. Clark, and K. S. Burrowes. Computational models of the pulmonary circulation: Insights and the move towards clinically directed studies. *Pulmonary circulation*, 1(2):224–238, Apr/Jun 2011.

[40] L. J. Thomas, Z. J. Griffo, and A. Roos. Effect of negative-pressure inflation of the lung on pulmonary vascular resistance. *Journal of applied physiology*, 16:451–456, May 1961.

[41] S. Treppo, S. M. Mijailovich, and J. G. Venegas. Contributions of pulmonary perfusion and ventilation to heterogeneity in v a/q measured by pet. *Journal of Applied Physiology*, 82(4):1163–1176, 1997.

[42] P. D. Wagner, D. R. Dantzker, R. Dueck, J. L. Clausen, and J. B. West. Ventilation-perfusion inequality in chronic obstructive pulmonary disease. *Journal of Clinical Investigation*, 59(2):203, 1977.

[43] P. D. Wagner, H. A. Saltzman, and J. B. West. Measurement of continuous distributions of ventilation-perfusion ratios: theory. *Journal of Applied Physiology*, 36(5):588–599, 1974.

[44] P. D. Wagner. The multiple inert gas elimination technique (MIGET). *Intensive care medicine*, 34(6):994–1001, 2008.

[45] P. D. Wagner, R. B. Laravuso, R. R. Uhi, and J. B. West. Continuous distributions of ventilation-perfusion ratios in normal subjects breathing air and 100% O2. *Journal of Clinical Investigation*, 54(1):54, 1974.

[46] J. B. West, C. T. Dollery, and A. Naimark. Distribution of blood flow in isolated lung; relation to vascular and alveolar pressures. *Journal of applied physiology*, 19:713–724, Jul 1964.

[47] J. B. West and C. T. Dollery. Distribution of blood flow and ventilation-perfusion ratio in the lung, measured with radioactive CO2. *Journal of Applied Physiology*, 15(3):405–410, 1960.

[48] J. B. West. *Respiratory Physiology The Essentials*. Lippincott Williams and Wilkins, 1974.

[49] T. A. Wilson and K. C. Beck. Contributions of ventilation and perfusion inhomogeneities to the va/q distribution. *Journal of applied physiology (Bethesda, Md. : 1985)*, 72(6):2298–2304, Jun 1992.

[50] R. T. Yen and L. Foppiano. Elasticity of small pulmonary veins in the cat. *Journal of biomechanical engineering*, 103(1):38–42, Feb 1981.

[51] R. T. Yen, Y. C. Fung, and N. Bingham. Elasticity of small pulmonary arteries in the cat. *Journal of biomechanical engineering*, 102(2):170–177, May 1980.

[52] F. Y. Zhuang, Y. C. Fung, and R. T. Yen. Analysis of blood flow in cat's lung with detailed anatomical and elasticity data. *Journal of applied physiology: respiratory, environmental and exercise physiology*, 55(4):1341–1348, Oct 1983.

# Chapter 2

# Quantification of Pulmonary Perfusion and Tissue Density Using Magnetic Resonance Imaging

## 2.1 Abstract

Imaging technology has become an essential tool for investigating human lung physiology. For my thesis research work, two magnetic resonance imaging (MRI) sequences were used to characterize pulmonary perfusion and pulmonary tissue density, respectively. An arterial spin labeling (ASL) technique was used to quantify the regional pulmonary blood flow in units of ml(blood)/min/cm$^3$(voxel). A multi-echo fast gradient echo (mGRE) was used to quantify the local pulmonary proton density as a surrogate measure of pulmonary tissue distribution in the units of g(tissue)/cm$^3$(voxel). Pulmonary blood flow and density images were co-registered and the blood flow map was divided by the density map, yielding density normalized perfusion (DNP) in the units of mL(blood)/min/g(tissue). The physiological meaning of DNP approximates the amount of perfusion per gram of lung tissue rather than per voxel (tissue + air). The obtained pulmonary perfusion

map was further processed to evaluate the pulmonary heterogeneity using three different metrics. In this chapter, the details of two MR sequences are discussed including the derivation of absolute quantification of pulmonary perfusion. In addition, three different pulmonary heterogeneity measures are also discussed.

## 2.2 Introduction

Imaging technology noninvasively visualizes the interior of human body without any surgical intervention and provides measurements of specific physiological parameters (such as perfusion and density) with physiologically relevant spatial and temporal resolution. Several imaging modalities such as X-ray computed tomography (CT), Positron emission tomography (PET) and single photon emission computed tomography (SPECT) have been experimentally and clinically utilized to elucidate human pulmonary function. Amongst functional imaging techniques, MRI has significant advantages. There is no radiation associated with MR techniques so that it is possible to measure a human subject repeatedly within a short period of time or plan for longitudinal studies. Proton MR technique utilizes the nuclear spin angular momentum of hydrogen atoms ($^1$H) which are abundant in biological specimens in the form of water $H_2O$ [12]. Consequently, it does not require the preparation of radioactive gases and particles or special equipment and facilities to produce them, which are required by other methodologies. Furthermore, the MR techniques developed with the collaborators at UCSD Pulmonary Imaging laboratory are quantitative with absolute units. These advantages mean that proton MRI is suited to conduct human physiology studies of the pulmonary circulation.

## 2.3 Magnetic Resonance Imaging

MR images are obtained using an MR scanner (Figure 2.1), a large electromagnet which is comprised of three different coil components; a main field coil, radio frequency (RF) coil, and gradient coil. As described in the prior section, hy-

drogen protons have a nuclear spin angular momentum, which causes a magnetic moment. When an object filled with plenty of protons is exposed to the static main magnetic field ($B_0$) generated by the main field coil, the magnetic moment vectors align in the direction of $B_0$ (referred to as the longitudinal direction) and sums up to a net magnetization $M_0$ which is proportional to the local proton density $\rho$, and precesses at a frequency called *Larmor* frequency. The *Larmor* frequency linearly relates to the applied magnetic field (equation 2.1). Since the $B_0$ main field needs to be homogeneous throughout the inside of MR scanner bore, a fourth kind of magnetic coil, namely shim coil, which is another gradient coil, offsets the inhomogeneity.

**Figure 2.1**: MRI Scanner at UCSD Radiology Imaging Laboratory (1.5 T GE HDx EXICITE twinspeed scanner, GE Healthcare).
http://ril.ucsd.edu/

$$\omega = \gamma B_0 \tag{2.1}$$

where $\gamma$ is gyromagnetic ratio. For $^1$H, $\gamma/2\pi = 42.58$ MHz/T. The main field of MR scanner, which is used for my dissertation research is 1.5 T. Therefore, *Larmor* frequency of $^1$H is approximately 64 MHz.

The RF transmitter coil transmits the magnetic RF pulse $B_1$, which resonates with the *Larmor* frequency. The application of RF pulse tips the magnetic moment vectors away from longitudinal direction with a flip angle and generates a vector component projected on transverse plane, which is perpendicular to the longitudinal direction. When the magnetic moment vectors precess, the transverse component of magnetization spins around the longitudinal direction and induces the alternating current, which is detected by RF receiver coil. The transverse component of magnetization decays with time constant $T_2$ (Figure 2.2). However, since the field inhomogeneity introduces space-dependent resonance, the collective transverse signal appears to decay with a time constant $T_2^*$ (faster than $T_2$) due to the dephasing effect. Spin Echo type MR imaging sequence utilizes RF refocusing pulse to realign the dephased transverse signals so that it enables the measurement of transverse signal decay with a time constant of $T_2$.

The longitudinal component regrows to $M_0$ with a time constant $T_1$ in the absence of additional RF pulse application (Figure 2.3). Those time constants have distinct values for different tissues. ($T_1$ and $T_2$ of blood are 1430 msec and 117 msec, respectively.) This is the basic of nuclear magnetic resonance phenomenon.

When the longitudinal magnetization is fully recovered to $M_0$, the state is described as relaxed. When the RF pulse is applied and the magnetic moment is flipped, the state is excited. When the net magnetization component is flipped by 90° and projected on transverse plane, leaving no longitudinal magnetization component, the state is described as saturated. Finally, when the net magnetization component is completely flipped by 180°, the state is described as inverted.

The flip angle is proportional to the magnitude of $B_1$ and the duration of RF pulse application. Repetition time (TR) and echo time (TE) represent specific timings on the course of $T_1$ and $T_2$ (or $T_2^*$) decays (Figure 2.3 and 2.2), respectively. The inversion recovery imaging sequence, a fundamental MRI technique for pulmonary perfusion imaging uses inversion time (TI), which is the duration between the application of 180° inversion RF pulse and the image acquisition. By controlling flip angle, TR, TE and TI, MRI can generate a variety of images with different contrasts.

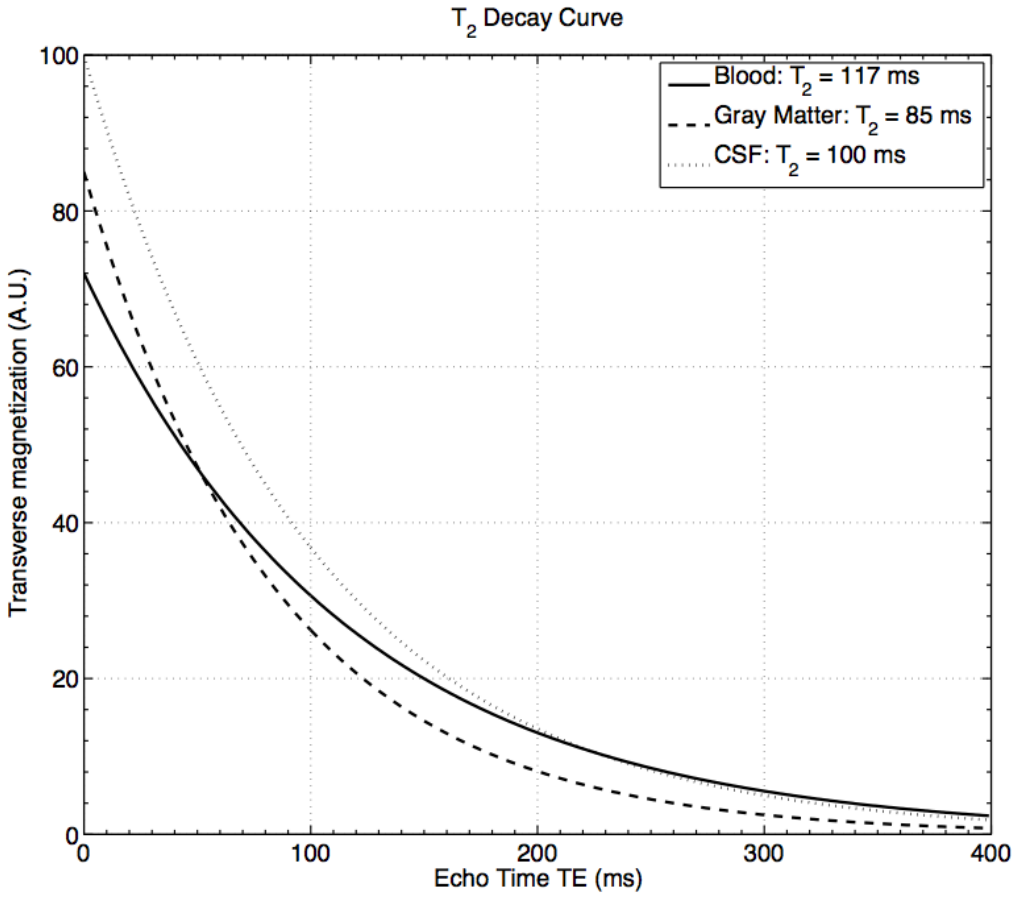


**Figure 2.2**: $T_2$ decay curve. $T_2$ decay is modeled as a exponential decay curve with a time constant of $T_2$. The decay starts from the initial magnitude of transverse magnetization and attenuates to zero.

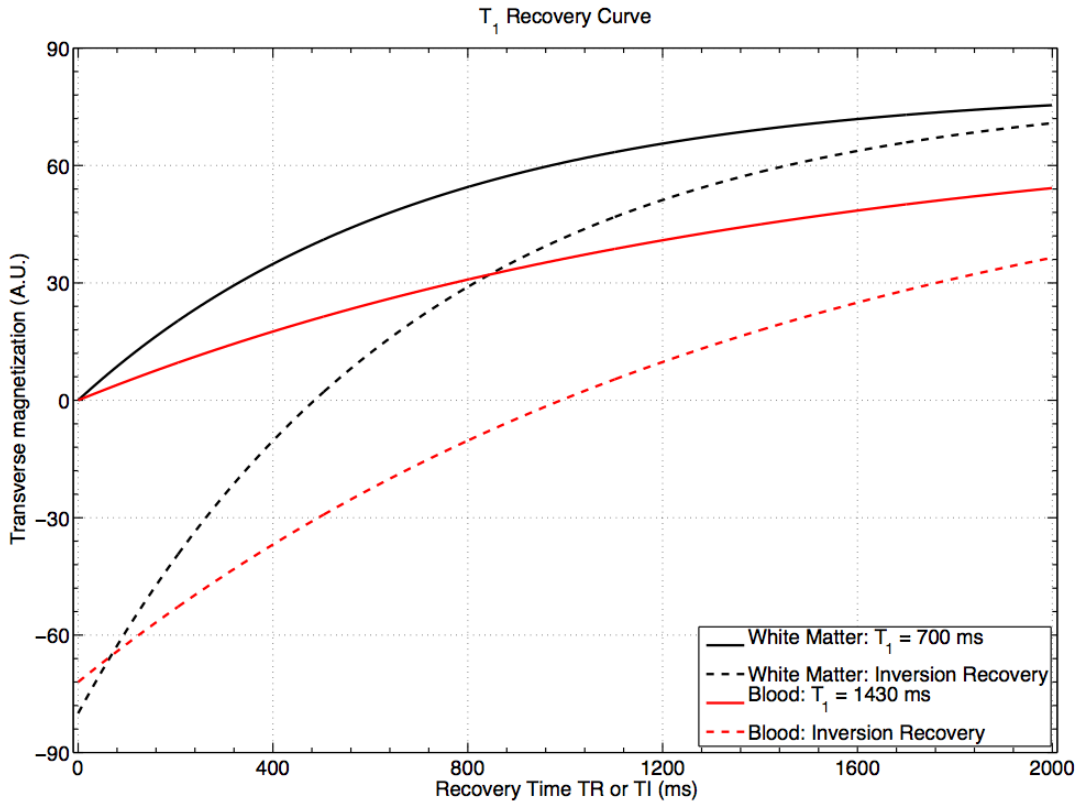


**Figure 2.3**: $T_1$ growth curve. $T_1$ growth is modeled as a exponential growth curve with a time constant of $T_1$. The growth curve starts from the initial longitudinal magnetization and exponentially approaches to the fully relaxed longitudinal magnetization $M_0$

A gradient coil adds a linear gradient magnetization to $B_0$ so that it provides a linear spatial variation in *Larmor* frequency within the object. It is crucial for location (slice) selective RF excitation, frequency encoding Fourier image reconstruction, and dephasing to cancel the transverse magnetization to prevent the residual refocusing echo on the coherent pathway from creating unwanted nuclear magnetic resonance signal.

MR signal is used to generate the Fourier representation of the object in frequency space (k-space), instead of generating a snapshot of the actual image of the object. In the basic 2D imaging, the two axes in k-space are called the frequency encoding direction and the phase encoding direction, respectively (Figure 2.4). K-space data are sampled line by line in the frequency encoding direction within approximately an echo time (TE). The line sampling is repeated every repetition time (TR) and covers every phase encoding step to fill all of k-space. The object image is then reconstructed as the Fourier transform of the k-space data.

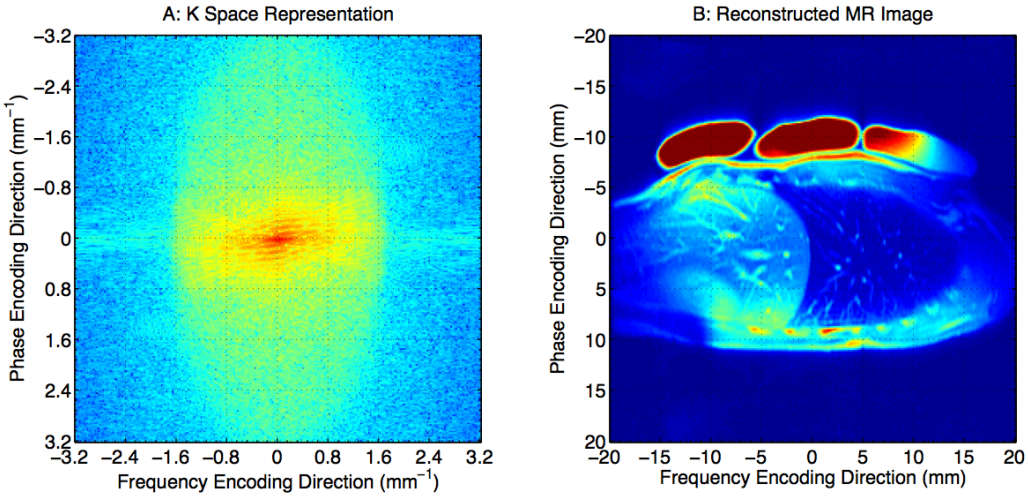


**Figure 2.4**: K-space data and MR image. MR signal generates the Fourier representation of the object in k-space. A: K space representation. X and Y axes are the frequency and phase encoding directions, respectively. K-space data are sampled line-by-line in the frequency encoding direction. The line sampling is repeated in every phase encoding direction step by step so that the entire k-space data are collected. B: Reconstructed MR Image. The image is reconstructed as the 2D Fourier transform of k-space data (A)

## 2.4 Three imaging planes

Three imaging planes are introduced in Figure 2.5. The axial plane is perpendicular to the longitudinal axis of human body and MR bore. The coronal plane passes longitudinally through the body from side to side perpendicularly to the axial plane, dividing the body into anterior and posterior parts. The sagittal plane vertically passes through, dividing the body laterally into left and right. For a pulmonary imaging study, the sagittal plane captures the gravitational dependency of self-deformation of lung, while coronal plane depicts an isogravitational picture of pulmonary physiology. The lung deformation due to breathing motion is mainly appeared in diaphragmatic direction. Both sagittal (B) and coronal (C) planes can measure lung deformation in diaphragmatic direction in-plane. Therefore these planes have been frequently chosen as imaging planes for the author's dissertation research.

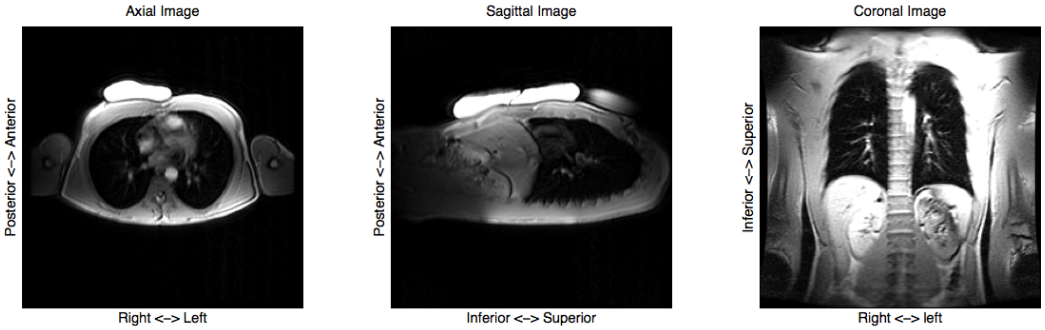


**Figure 2.5**: Three image planes. A: Axial, B: Sagittal, and C: Coronal. The axial plane is perpendicular to the longitudinal axis of human body and MR bore, which captures the cross-sectional view of torso. The sagittal plane captures the gravitational dependency of self-deformation of lung, while the coronal plane depicts the isogravitational picture of pulmonary physiology. The lung deformation due to breathing motion is mainly apparent in the diaphragmatic direction. Both sagittal (B) and coronal (C) planes can measure lung deformation in diaphragmatic direction in-plane. Therefore these planes have been frequently chosen as imaging planes for the author's dissertation research.

## 2.5 Quantified regional pulmonary blood flow using ASL-FAIRER

The type of MR sequence used to quantify pulmonary perfusion in my dissertation research is called arterial spin labeling (ASL). In particular, it is categorized as ASL with a flow-sensitive alternating inversion recovery with an extra radiofrequency pulse (ASL-FAIRER) imaging sequence and a Half Fourier Acquisition Single Shot Turbo Spin Echo (HASTE) data collection scheme [1]. In this section, the details of the ASL sequence are described first. Then, the absolute quantification of pulmonary blood flow map based on a pair of ASL images is described. Finally, the obtained blood flow map is further processed to yield a pulmonary perfusion map.

ASL utilizes an inversion recovery technique, which magnetically tags protons in blood using a 180° RF pulse and measures the amount of tagged protons delivered into a local imaging slice from outside per unit time (Figure 2.6).

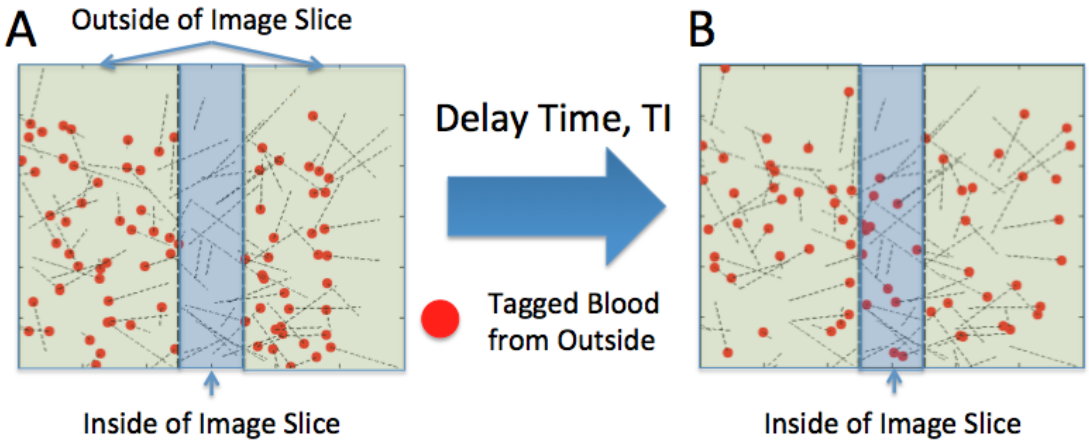


**Figure 2.6**: The basic idea of ASL-FAIRER. ASL-FAIRER measures the amount of tagged blood delivered into a imaging slice from outside per unit time. A: Protons in blood outside of image slice are tagged. B: After a delay time (TI), tagged protons are delivered into the image slice creating ASL signal. Red dots: Tagged Blood

### 2.5.1 ASL-FAIRER sequence and the HASTE image reconstruction

In FAIRER, two kinds of MR images, control and tag images are obtained during a single breath-hold, lasting approximately ten seconds. The blood signal was prepared differently in the two images (Figure 2.7A and B). Figure 2.7A shows the ASL control image where blood signal becomes bright.

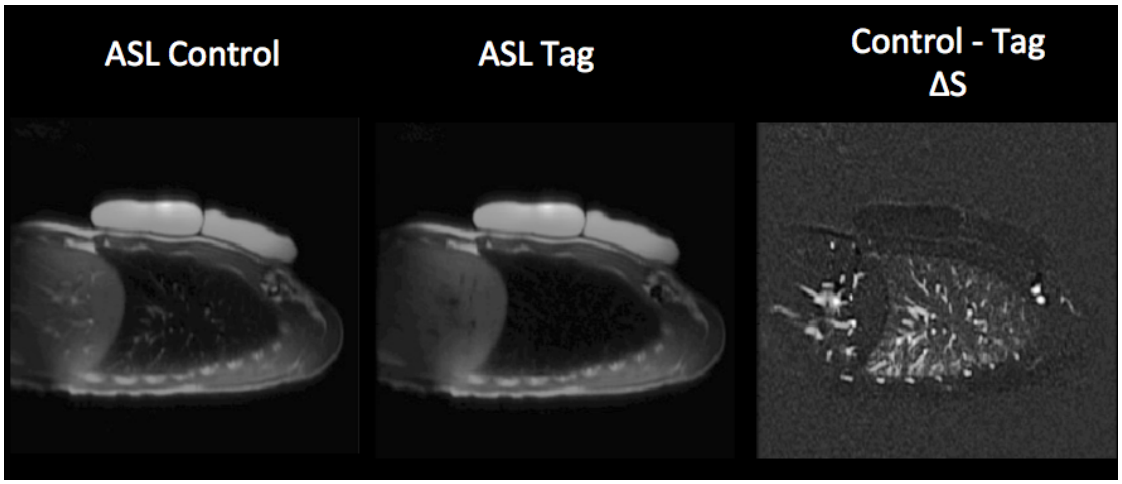


**Figure 2.7**: ASL control and tag images. There are two kinds of MR images in ASL-FAIRER; control and tag images. Blood signal is bright in ASL control image while Blood signal becomes dark in ASL tag image. The difference between control and tag images is proportional to the amount of incoming blood to the imaging slice.

The pulse sequence diagram is shown in Figure 2.8. In the ASL control image, the slice selective 180° inversion pulse, followed by an additional slice selective 90° saturation pulse and a dephasing gradient pulse, was applied during the first diastole, leaving the protons outside the slice undisturbed. An adequate delay time (TI: approximately 80% of R-R interval) allowed protons with fully relaxed longitudinal magnetization to enter the imaging slice from adjacent tissue with incoming blood while protons with recovering longitudinal magnetization are displaced out of the image slice. The image acquisition began after the delay (TI) during the second diastole, generating a strong magnetic resonance signal. The imaging slice and the inversion slice are centered on the same plane, but the width

of selective inversion slice is much wider than the imaging slice thickness to ensure that longitudinal magnetization in the imaging slice is completely inverted. The difference between the selective inversion and imaging slice widths is called a gap (Figure 2.9), which is an additional 10 mm margin on the either side of the imaging slice. The gap may be a potential source of measurement errors. In areas of low blood flow, there may not be enough time for relaxed blood to cross the gap, potentially leading to underestimation of blood flow in the ASL measurement. This is described in section 2.5.3. The addition of the extra 90° saturation pulse and dephasing gradients was required in any given voxel in the imaging slice where blood-to-tissue ratio is high [8] to prevent the lung tissue signal intensity from disappearing [7].

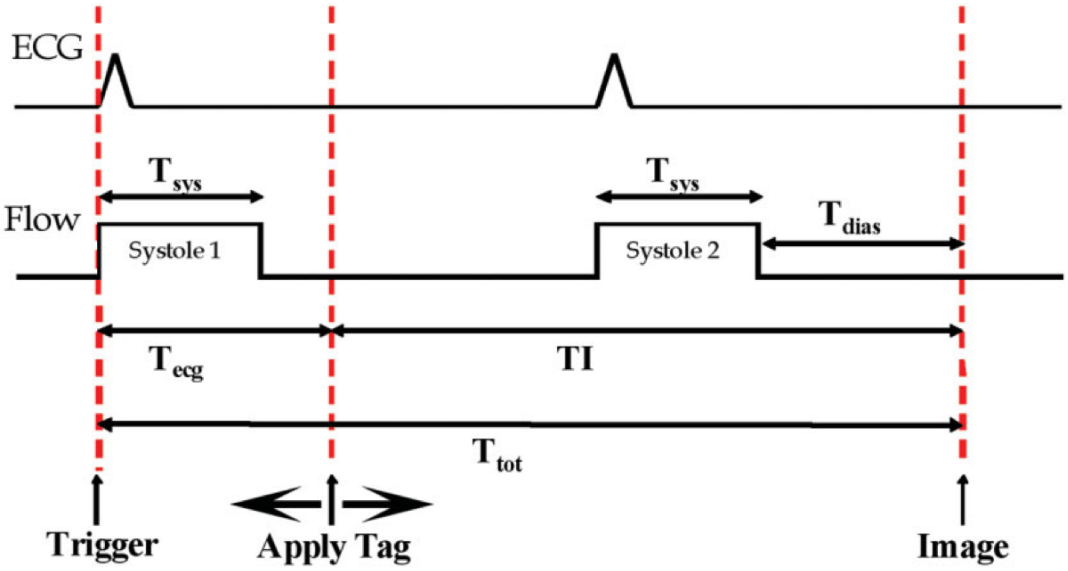


**Figure 2.8**: ASL-FAIRER pulse sequence diagram. MRI hardware triggers off the upstroke of the ECG signal to start scanning. After a delay $T_{ECG}$, the tagging pulse is applied. Another delay, TI, allows delivery of tagged blood to imaging slice. The $T_{ECG}$ and TI can be varied (horizontal arrows). $T_{ECG}$ must be greater than $T_{SYS}$ to ensure that only one systolic period (systole 2) deliveres tagged blood to the imaging plane. The imaging time must occur during the second diastolic period.
Copyright has been obtained. *"Quantification of Regional Pulmonary Blood Flow Using ASL-FAIRER"*, 2006. by Bolar *et al.*

Figure 2.7B shows the ASL tag image where blood signal becomes dark.

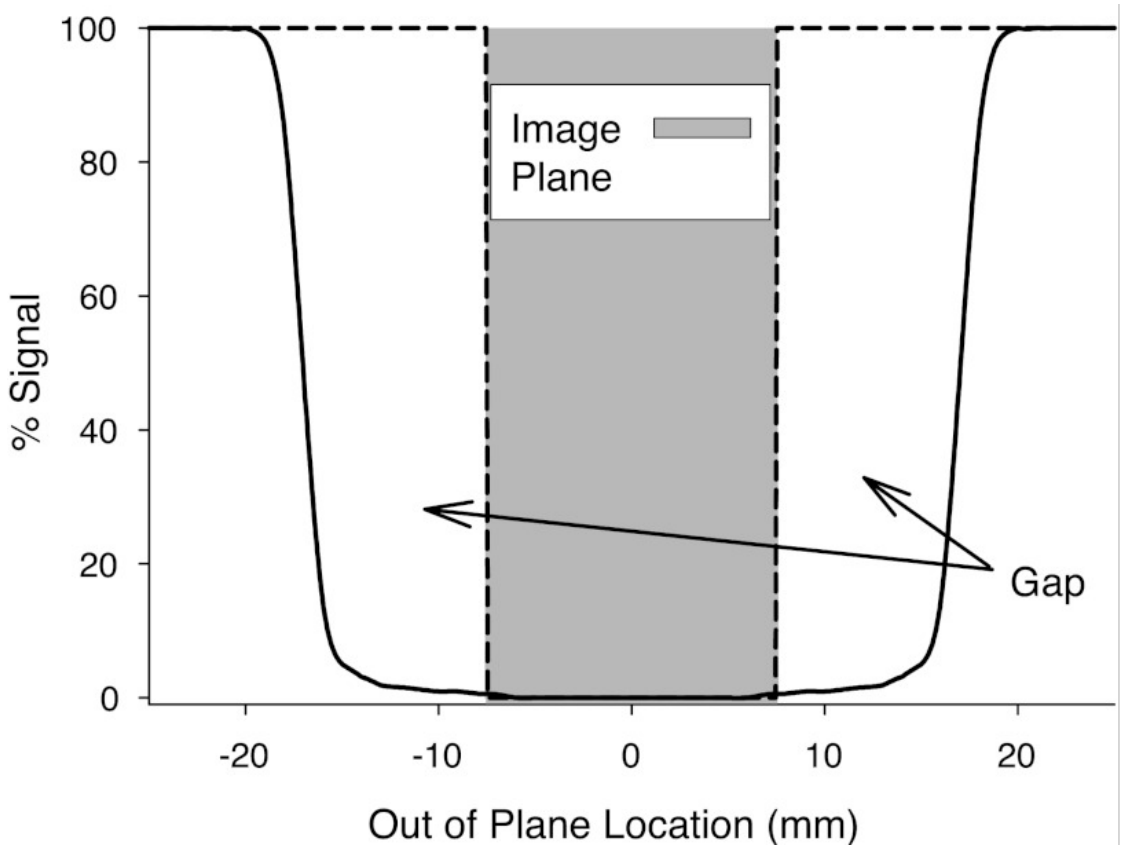


**Figure 2.9**: Characterization of the inversion profile based on a typical inversion plane taken used in an ASL experiment. Image plane is 15 mm whereas the inversion plane is wider ( 30 mm). An ideal inversion plane would exactly match the boundaries of the image plane.

In the tag image, the magnetization both inside and outside of the imaging slice (i.e. whole lung) is inverted with a spatially non-selective inversion pulse during the first diastole, followed by the additional slice selective 90° saturation pulse, as well as dephasing gradients. The image acquisition began after the same delay time (TI). Once a pair of control and tag images was obtained, the the tag image is subtracted from the control image, yielding a perfusion weighted map. The difference (i.e. ASL signal) measured for each voxel thus reflects the amount of blood delivered during one cardiac cycle and weighted by a decay factor due to the relaxation of magnetization.

Imaging sequence parameters were as follows: TI = 600 - 800 msec (based on subject heart rate), TE = 21.3 msec, field of view = 40 cm, receiver bandwidth = 125kHz, slice thickness = 15mm. The collected image matrix size was 256 × 128, and reconstructed by scanner to 256 × 256 giving voxels of 0.037 $cm^3$. The HASTE imaging sequence had an inter-echo time of 4.5 msec and 70 lines of phase encoding, resulting in a data acquisition time of 324 msec.

The phase encoding direction is subjected to a strong $T_2$ decay effect so that only 70 lines of k-space data were sampled for the image reconstruction. 64 lines covered half of k-space and the additional six lines covered additional neighboring lines from the center on the other side (Figure 2.10A). Homodyne reconstruction method was used to compensate the missing 58 lines of k-space data (Figure 2.10B).

### 2.5.2 Quantification of regional blood flow (mL/min/$cm^3$)

The difference between ASL control and tag images (ASL signal) qualitatively reflects the local pulmonary blood flow. The ASL signal is further processed in order to quantify the absolute units of pulmonary blood flow using equation 2.2. This is based upon the work of Henderson *et al.*, [5].

$$F = \frac{\Delta S}{T_{RR}} \left[ \frac{\left(1 - e^{-TI/T_{1_P}}\right) e^{-TE/T_{2_P}}}{2RS_p e^{-TI/T_{1_B}} e^{-TE/T_{2_B}}} \right] \frac{C_{torso}(x_p, y_p)}{C_{torso}(x, y)} \tag{2.2}$$

The details of derivation are described in Appendix B. The quantified pulmonary blood flow map $F$ is derived from ASL signal $\Delta S$, which is the difference between

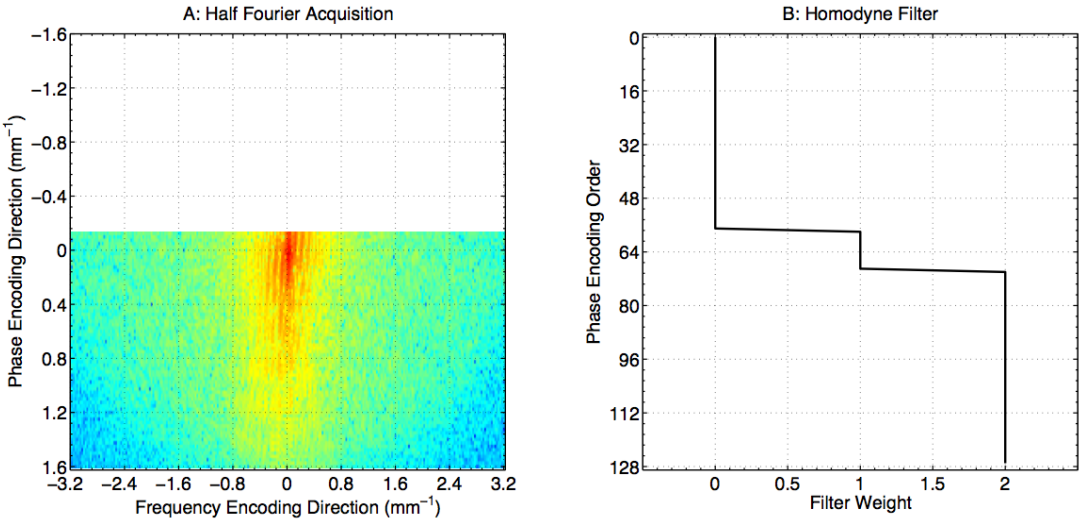


**Figure 2.10**: Half Fourier Acquisition Single Shot Turbo Spin Echo (HASTE) data collection scheme. A: 70 out of 128 lines in k-space data are sampled for the image reconstruction. 64 lines covered half of k-space and the additional six lines covered additional neighboring lines from the center on the other side. B: Homodyne reconstruction method was used to compensate the missing 58 lines of k-space data.

ASL control and tag images. Using a reference phantom we can then correlate the signal in the ASL image with quantifiable units of mL/min/cm$^3$ through equation 2.2 above. The phantom is the little circular object on the subject's chest shown in Figure 2.7). The MR signal of the phantom is denoted as $S_p$. The ratio of fully relaxed longitudinal magnetization of blood to that of the phantom is denoted as $R$, which is estimated based on previously documented [5] and experimentally measured values. $T_{1_P}$ and $T_{2_P}$ are $T_1$ and $T_2$ of phantom, which are experimentally measured in advance, whereas $T_{1_B}$ and $T_{2_B}$ are those of blood, which are previously documented values [15]. $T_{1_P}$, $T_{2_P}$, $T_{1_B}$ and $T_{2_B}$ are 859 msec, 191 msec, 1430 msec and 117 msec, respectively. TI and TE are MR timing parameters used to control the contrast of the acquired images. $C_{torso}(x_p, y_p)$ and $C_{torso}(x, y)$ represent MR signal inhomogeneity caused by the spatial sensitivity profile of the MR torso coil around phantom and lung, respectively. The sensitivity profile is discussed later in section 2.6.3.

### 2.5.3 Large vessel removal and smoothing to quantify pulmonary perfusion

At this stage pulmonary blood flow map does not directly reflect actual perfusion. The large conduit vessel flow, which does not contribute to gas exchange needs to be removed (Figure 2.11B). Voxels contained within the large conduit vessels were removed from the blood flow images since those voxels do not represent pulmonary capillary perfusion. A 35% cut-off value (35% of maximum blood flow value in ml/min/cm$^3$ within the lung) was applied to the previously computed blood flow image to distinguish voxels representing: (1) larger conduit vessels ($F$ $>$ 35% maximum in mL/min/cm$^3$) or (2) perfusion comprising smaller vessels and lung tissue ($F$ $<$ 35% maximum in mL/min/cm$^3$). The 35% cutoff value was chosen based on a computational model study of pulmonary circulation [2] where the ASL-FAIRER experiment was simulated *in silico* and the resultant ASL signal was compared with the simulated steady blood flow circulating in the model lung. The pulmonary circulation model can distinguish between perfusion and conduit vessel flow based on their anatomical domains. The model showed that the mean and standard deviation of a filtered ASL signal with 35% cutoff matched with those exclusively derived from a perfusion distribution.

As the spatial scale corresponding to functional gas exchange units in the lung is larger than that of the MR image, spatial smoothing is applied to bring the effective voxel size on the order of a few acini (Figure 2.11C). The pulmonary perfusion image is smoothed by convolution with a 2D Gaussian filter where the standard deviation of 3 voxels (0.47 cm) and full width at half maximum of 7 voxels (1.1 cm). This yields an effective spatial resolution ($10 \times 10 \times 15$ mm$^3$) to approximately the size of 5 acini. The smoothing algorithm used a lung mask, excluding voxels outside the lung and voxels identified as large conduit vessels. The Gaussian weights were adjusted to account for the removal of masked voxels. In other words, MR signals within those voxels were essentially treated as missing data.

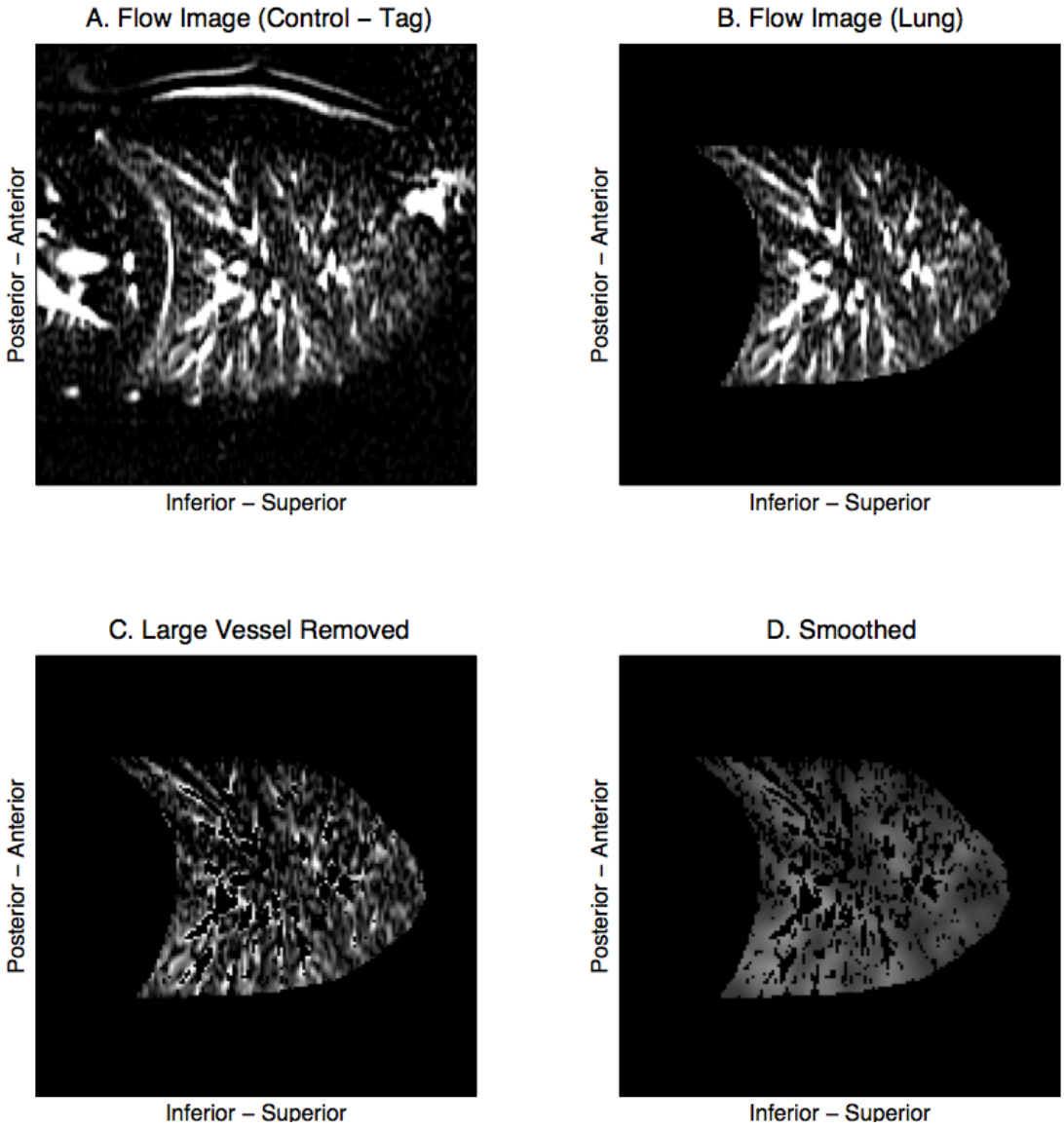


**Figure 2.11**: Large vessel removal and spatial smoothing. A: Original ASL pulmonary blood flow image. B: Pulmonary blood flow map within the lung. C: Large conduit vessel is removed from the blood flow images. D: Spatial smoothing is applied to bring the effective voxel size on the order of 5 acini

## 2.6 Lung proton density imaging using multi-echo fast gradient echo (mGRE) sequence

The gradient echo imaging technique is a suitable tool for the measurement of lung proton density $\rho$, which approximates the lung tissue distribution. However, as a result of the high magnetic susceptibility due to air-tissue interactions, $T_2^*$ of the normal human lung at functional residual capacity (FRC) lung volume is extremely short and approximately 1.7 msec [16]. As a consequence, the gradient echo sequence must deal with the rapid MR signal decay. The choice of echo time (TE) must be adequately fast to avoid MR signals to falloff below the noise level. MR signal noise is best characterized as Rician, and therefore has non-zero mean. For the high signal to noise ratio conditions (SNR $>$ 2), the Rician noise can be approximated as a Gaussian distribution so that multiple measurements can converge to the actual gradient echo signal. Therefore, the SNR limit determines the maximum TE limit, whereas the minimum TE is limited by hardware ability. $T_2^*$ also varies with lung density $\rho$ since the air-tissue interactions in the lung disturbs the local field homogeneity. Therefore, it must be measured locally. Back-extrapolation of the $T_2^*$ decay curve to the TE of zero for each voxel determines both local lung proton density $\rho$ and $T_2^*$. In order to compute two unknowns, data from two different time points ($TE_{short}$) and $TE_{long}$) on the decay curve must be obtained.

### 2.6.1 Multi-echo fast gradient echo image acquisition

Multi-echo fast gradient echo (mGRE) sequence collects 12 images alternating between two different echo times ($TE_{short}$ and $TE_{long}$) during a single breath-hold lasting approximately 10-seconds; 6 images (even images: 2, 4, 6, 8, 10 and 12) were obtained at the echo time of 1.1 msec ($TE_{short}$) while other 6 images (odd images: 1, 3, 5, 7, 9 and 11) were obtained at the echo time of 1.8 msec ($TE_{long}$). Since the repetition time (TR) is sufficiently long compared to $T_2^*$ (e.g. TR = 10 msec and $T_2^*$ 1.7msec), coherent transverse magnetization, which is magnetization carried over from one excitation to the next, will be small. Therefore, the first 4

images (out of 12) are not reached to the steady state condition of both longitudinal and transverse magnetization components and discarded. The remaining 8 images (from 5th to 12th image) are used for the lung proton density calculation.

The mGRE sequence consists of a small flip angle slice selective excitation followed by the collection of a single full line of Fourier data (Figure 2.12). The sequence begins by collecting 10 disdaqs (discarded data acquisition lines) and steps through multiple phase encoding steps at a fixed echo time (TE) and repetition time (TR) until k-space is filled for a single 2D image. The sequence then repeats by filling k-space acquired at another echo time while keeping TR constant.

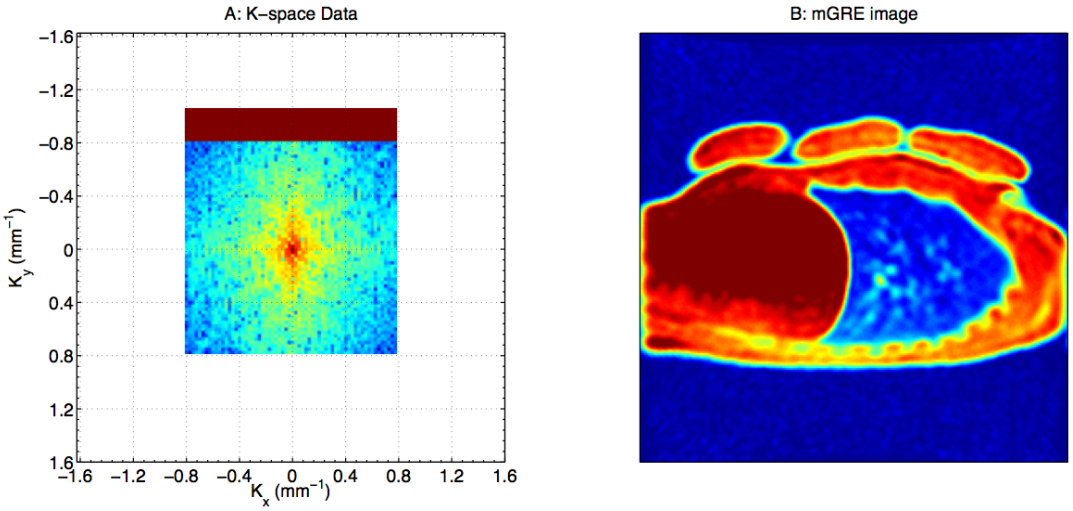


**Figure 2.12**: K-space filling in the mGRE sequence. The sequence begins by collecting 10 disdaqs (discarded data acquisition lines), and steps through multiple phase encoding steps at a fixed echo time (TE) and repetition time (TR) until k-space is filled for a single 2D image, 64 × 64.

Sequence parameters were TR = 10 msec, flip angle, $\alpha = 10°$, slice thickness = 15 mm, FOV =40 cm, receiver bandwidth = 125kHz, and a full acquisition matrix of 64 × 64. $TE_{short}$ and $TE_{long}$ are 1.1 and 1.8 msec, respectively. As TR is considerably longer than TE, this allows for collection of up to 3 separate slices within a single breath-hold by interleaving the slice acquisitions.

### 2.6.2 Quantification of local pulmonary density (g/cm$^3$)

The previously obtained 4 images with $\mathrm{TE}_{short}$ and 4 images with $\mathrm{TE}_{long}$ were averaged, respectively, yielding two gradient echo images shown in Figure 2.13 A and B. The data from the two images were fit to a single exponential decay function within each voxel to determine the image signal intensity $I_0$ at the TE of zero (equation 2.3).

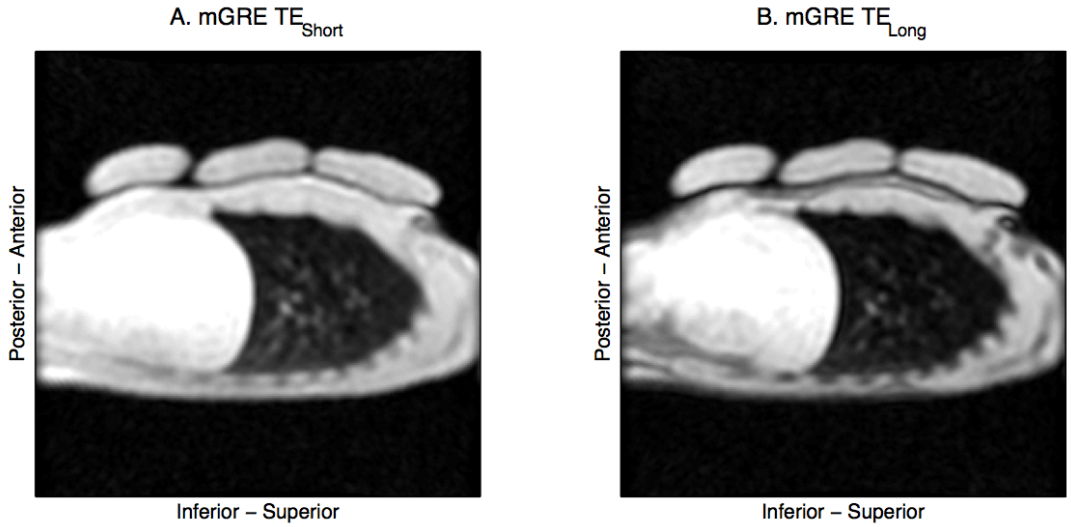


**Figure 2.13**: $\mathrm{TE}_{short}$ and $\mathrm{TE}_{long}$ images. A: The average of 4 mGRE images acquired at TE = 1.1 msec. B: The average of 4 mGRE images aquired at TR = 1.8 msec. $\mathrm{T}_2^*$ and $\rho$ are computed using two data points extrapolation.

$$I_{0k} = \frac{I_{jk}}{e_k^{TE_{jk}/T_2{}^*}} \tag{2.3}$$

where $I$ is the MR signal and the subscript j represents the image at each echo time $\mathrm{TE}_j$.The subscript k represent each voxel so that the local $T_2^*$ is denoted as $T_{2\,k}^*$, which is calculated by equation 2.4.

$$T_2{}^*{}_k = \frac{TE_{long} - TE_{short}}{ln(I_{shortk}) - ln(I_{long_k})} \tag{2.4}$$

$I_0$ is proportional to the local proton density $\rho$. Silicon phantoms with known $\mathrm{T}_1$ and $\mathrm{T}_2$ are also used as a reference for density calibration. Since the decay constants of the silicon phantom are much longer than in lung, this results in a

coherent build-up of signal in the phantom toward steady-state. The correction factor $C_p$ is used to cancel this effect ($C_p = 0.40$). $\rho$ is given as the following equation 2.5.

$$\rho = I_0/(C_p \bullet I_p) \tag{2.5}$$

where $I_p$ is the mean signal of the phantom at $TE_{short}$ and TR = 10 msec and $\rho$ is the lung proton density in the unites of g/cm$^3$(voxel).

### 2.6.3 Coil Inhomogeneity

A torso coil was used to maximize the signal-to-noise ratio in the ASL images. A torso coil has substantially higher gain than the body coil built into the scanner. However, it creates a substantially nonuniform sensitivity profile throughout the image where portions of the image close to the coil have more signal, which is shown in Figure2.14. This is called coil inhomogeneity denoted as $C_{torso}(x,y)$ in equation 2.2. In order to correct for this inhomogeneity, two mGRE images acquired using the torso coil and the body coil at the same slice location and the same echo time of 1.1 msec ($TE_{short}$) were used. Each image was smoothed in the frequency space using 2D Gaussian low pass filter with the standard deviation of 3 voxels (approximately .08 cm$^{-1}$). The two smoothed images were then divided (torso/body) to produce a coil sensitivity map. Finally, the ASL images obtained using the torso coil were divided by the coil sensitivity map and therefore it becomes independent of the spatial variation in coil sensitivity.

## 2.7 Density-normalized perfusion (mL/min/g)

Density-normalized perfusion expressed in units of mL(blood)/min/g(tissue) can be approximated by dividing the quantified perfusion image acquired by ASL technique, which has the units of mL(blood)/min/cm$^3$(voxel), by the proton density image (g/cm$^3$). A mutual information-based technique that included affine transformation was utilized to register the ASL and proton density images, and

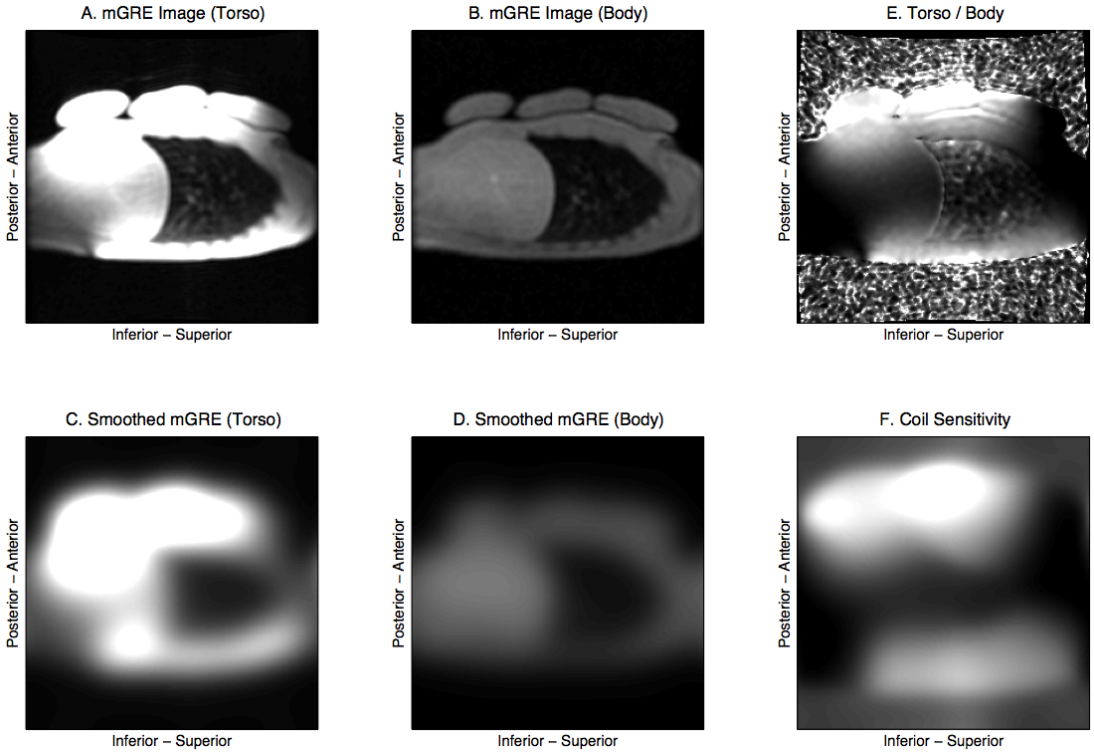


**Figure 2.14**: Sensitivity profile of torso coil. The original mGRE images acquired using A:torso coil and B:body coil. The two images were smoothed with the Gaussian low pass filter (C and D) and then divided (torso/body) to produce a coil sensitivity map (F).

then the ASL perfusion image was divided by the proton density image on a voxel-by-voxel basis. To the extent that regional lung density is reflected by the water content, density normalized perfusion then reflects perfusion in milliliters per minute per gram of lung tissue. In Chapter 5 and 6, the term perfusion refers the density normalized perfusion.

## 2.8 Estimation of perfusion heterogeneity

The perfusion heterogeneity discussed in Chapter 1 was evaluated using three different indices: relative dispersion, fractal dimension and shape parameter.

### 2.8.1 Relative dispersion

The relative dispersion (RD), also known as the coefficient of variation, is a measure of global heterogeneity defined as the ratio of the standard deviation to the mean perfusion. The larger the relative dispersion, the more heterogeneous the distribution. This statistical calculation implicitly assumes that the perfusion distribution is approximately Gaussian, when in fact it more closely resembles a lognormal distribution. However, RD has been the one of the most prevailing methods to evaluate perfusion heterogeneity [4].

### 2.8.2 Fractal Dimension

The nature of a fractal system is that the degree of irregularity remains similar through a succession of magnifications of scale. It is derived as a recursive formula relating the relative dispersion of perfusion to the measurement scale and a spatial fractal dimension $D_s$. $D_s$ is calculated from the measurements of RD made at different spatial scale, which is given by equation 2.6.

$$RD_s(v) = RD_s(v_{ref}) \left[ \frac{v}{v_{ref}} \right]^{1-D_s} \tag{2.6}$$

where $RD_s(v)$ is the measured relative dispersion when the organ is partitioned into regions of a specific spatial resolution $v$, $RD_s(v_{ref})$ is the $RD_s$ found for the

finest spatial resolution, and $D_s$ is the fractal dimension. *1-$D_s$* is given as a slope of $\log(v/v_{ref})$ versus $\log(RD_s(v))$ shown in Figure 2.15. $D_s$ varies between 1.0 (homogeneous) and 1.5 (spatially random).

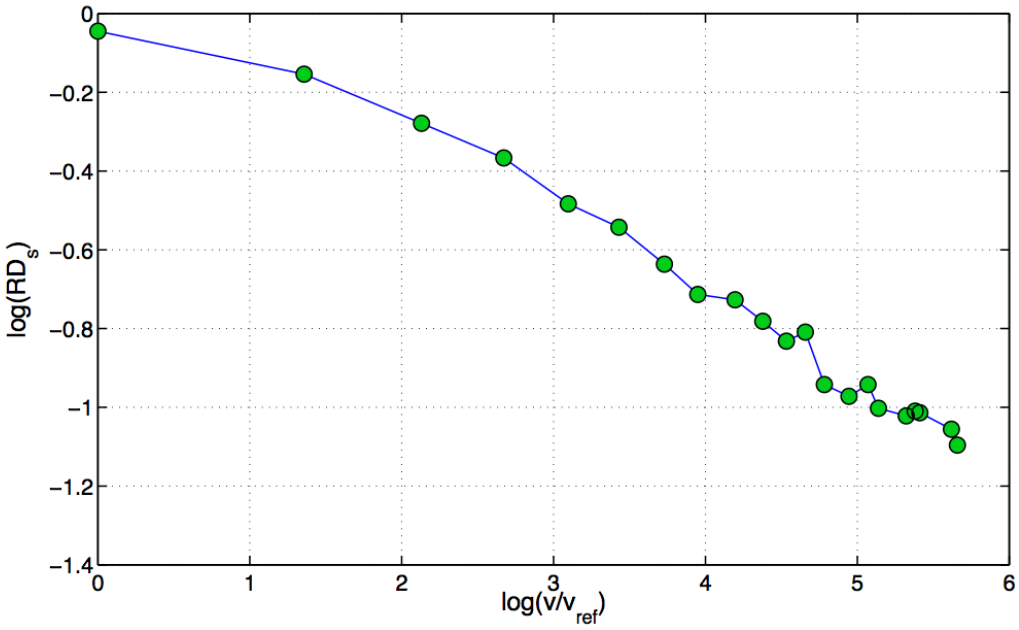


**Figure 2.15**: Fractality of pulmonary perfusion. *1-$D_s$* is given as a slop of $\log(v/v_{ref})$ versus $\log(RD_s(v))$. $D_s$: Fractal Dimension

### 2.8.3 Shape Parameter

The shape parameter is also a global measure of heterogeneity as is relative dispersion. However, it is based on lognormal model distribution given in equation 2.7.

$$p(x) = \frac{1}{x \times \sigma\sqrt{2\pi}} exp\left(\frac{-[ln(x) - \mu]^2}{2\sigma^2}\right) \tag{2.7}$$

where $p$ is probability density, $x$ is the perfusion value, $\mu$ and $\sigma$ are the scale parameter and shape parameter, respectively. From equation 2.7, $\mu$ and $\sigma$ are the mean and standard deviation of the probability density function, when the perfusion is described in a logarithmic scale. Due to the asymmetric branching at each bifurcation comprising the entire pulmonary vascular network, the nature of

the pulmonary perfusion distribution is mathematically predicted to be lognormal [3, 13]. In addition, as discussed in Chapter 1, ventilation - perfusion heterogeneity has been traditionally expressed in a logarithmic scale. Therefore, this metric is able to compare ventilation - perfusion heterogeneity with underlying perfusion heterogeneity using equation 2.7.

## 2.9 Limitation in perfusion measurements and the future direction

Pulmonary perfusion measurements using ASL-FAIRER have two main limitations. (1) ASL signal underestimates low perfusion due to the effect of the gap between the imaging slice and the inversion slice. (2) Conduit vessel removal depends on a 35% cutoff value rather than based on the actual measurements of the pulmonary vasculature structure. These limitations have been characterized by an *in silico* model prediction of the pulmonary circulation in which the model lung was lying spine [2].

### 2.9.1 The gap effect

The reduction in ASL signal due to the gap effect is predicted to be consistent across sagittal image planes from medial to lateral. The *in silico* model [2] predicted that the ASL signal was reduced to approximately 70% of the ideal gap-free value. On the other hand, there is more variability in the coronal orientation from posterior to anterior; the anterior plane loses approximately 50% of ASL signal, while the most posterior plane loses only 16% corresponding to the higher blood flow in the gravitationally dependent part of lung. The model indicated that the ASL measurement in sagittal plane is less susceptible to the gap effect than that in coronal plane.

### 2.9.2 35% cutoff

The same model predicted that the cutoff value of 35% of the image maximum intensity could reduce the contribution of conduit vessels to approximately 20% of total ASL signal. Therefore, the filtered ASL signal was dominated by perfusion and its mean and standard deviation are consistent with those of pulmonary perfusion. However, 35% cutoff is still a blunt definition. The maximum blood flow value resides on the right-tail-end of pulmonary blood flow distribution, which is lognormal distribution. Therefore, the statistical chance of which the maximum value appears in the discretized measured ASL data is very low. In addition, high ASL signal may reflect the blood volume rather than the blood flow if the voxel is filled with incoming blood and ASL signal is saturated. The maximum ASL value is susceptible to its intrinsic errors.

In the future, the large vessel removal might be improved by basing it on the actual lung anatomy or the lognormal nature of pulmonary perfusion distribution needs to be taken into account. In my dissertation study, the purpose of large vessel removal was to eliminate the pulmonary blood flow signals not contributing to the gas exchange. Therefore, the current method of threshold was the most practical method available to filter conduit vessels from the data and it does sufficiently well for the purposes of my dissertation research.

## 2.10 State of the art functional lung MR imaging

Magnetic resonance imaging and spatially selective excitation prompted by an MR scanner can be used not only for pulmonary structural images but also various forms of functional imaging. Pulmonary perfusion imaging using ASL-FAIRER used in my dissertation research is one example. Moreover, other functional pulmonary MRI technologies have been developed in recent years.

Ventilation imaging is one such functional imaging. A method to image specific ventilation ($\Delta V/V_0$, the ratio of the incoming fresh gas volume ($\Delta V$) to the end-expiratory ($V_0$)) imaging (SVI) was developed in our group [14], using the paramagnetic property of oxygen in solution in tissues. Inhaled oxygen alters

the local magnetization so that oxygen acts as a contrast agent in solution in lung tissue. A sudden change in inspired oxygen (from room air to $F_IO_2 = 1.0$) results in the regional rise in oxygen concentration in the lung, leading subsequent alterations in the MR signal. The rate of change in MR signal reflects the regional specific ventilation. SVI combined with pulmonary density image yields a regional distribution of incoming air volume per breath. Combining the spatial distribution of ventilation with that of perfusion, the ventilation-perfusion ratio ($V_A/Q$) can be visualized [6].

The viscoelasticity of pulmonary parenchymal tissue can be visualized using MR elastrography [9, 10]. The propagation of acoustic shear waves induced by a mechanical vibration is quantified by phase contrast-based MRI technique. The obtained image allows the estimation of shear modulus (kPa) of the lung parenchyma. Mechanical properties of the lung are known to be associated with local properties of the tissue, and may be a potential tool to identify pulmonary diseases. For example, emphysema causes abnormally elastic lung tissue where pulmonary fibrosis leads the increase in the parenchymal stiffness.

Conventional MR imaging utilizes the MR signal from protons (hydrogen 1 $^1$H), which are abundant in a body in form of water, fat and other organic molecules. Hyperpolarized gas MR imaging is another avenue of pulmonary MR technique, which exploits an exogenous gaseous agent such as laser-hyperpolarized $^3$He and $^1$29Xe and enables to visualize the airway side of pulmonary structure and ventilation [17]. $^3$He and $^1$29Xe gases have different physical properties; $^3$He has lower atomic mass therefore is more diffusive in air than $^1$29Xe. The high solubility of $^1$29Xe in water and chemical shifts induced when in solution are starting to be used to measure gas exchange and uptake [11].

## 2.11 Summary

1. An ASL-FAIRER technique was used to quantify regional pulmonary blood flow in units of mL(blood)/min/cm$^3$(voxel).

2. The quantified ASL map was further processed to derive a map of pulmonary

perfusion; the image voxels containing large conduit vessels were removed using a cutoff value of 35% of maximum signal intensity and remaining voxels were smoothed using a 2D Gaussian low pass filter to adjust the effective spatial resolution of 10 × 10 × 15 mm.

3. A multi-echo fast gradient echo sequence (mGRE) was used to quantify the local pulmonary tissue density in the units of g(tissue)/cm$^3$(voxel). Division of perfusion by density yielded density normalized perfusion (DNP) expressed in the unites of mL(blood)/min/g(tissue).

4. The pulmonary perfusion heterogeneity was evaluated using three indices; relative dispersion (RD), fractal dimension ($D_s$) and lognormal shape parameter ($\sigma$).

## 2.12 Bibliography

[1] D. S. Bolar, D. L. Levin, S. R. Hopkins, L. F. Frank, T. T. Liu, E. C. Wong, and R. B. Buxton. Quantification of regional pulmonary blood flow using ASL-FAIRER. *Magnetic resonance in medicine : official journal of the Society of Magnetic Resonance in Medicine / Society of Magnetic Resonance in Medicine*, 55(6):1308–1317, Jun 2006.

[2] K. S. Burrowes, R. B. Buxton, and G. K. Prisk. Assessing potential errors of MRI-based measurements of pulmonary blood flow using a detailed network flow model. *Journal of applied physiology (Bethesda, Md. : 1985)*, 113(1):130–141, Jul 2012.

[3] R. W. Glenny. Blood flow distribution in the lung. *Chest*, 114(1 Suppl):8S–16S, Jul 1998.

[4] A. C. Henderson, D. L. Levin, S. R. Hopkins, I. M. Olfert, R. B. Buxton, and G. K. Prisk. Steep head-down tilt has persisting effects on the distribution of pulmonary blood flow. *Journal of applied physiology (Bethesda, Md. : 1985)*, 101(2):583–589, Aug 2006.

[5] A. C. Henderson, G. K. Prisk, D. L. Levin, S. R. Hopkins, and R. B. Buxton. Characterizing pulmonary blood flow distribution measured using arterial spin labeling. *NMR in biomedicine*, 22(10):1025–1035, Dec 2009.

[6] A. C. Henderson, R. C. Sá, R. J. Theilmann, R. B. Buxton, G. K. Prisk, and S. R. Hopkins. The gravitational distribution of ventilation-perfusion ratio is

more uniform in prone than supine posture in the normal human lung. *Journal of applied physiology (Bethesda, Md. : 1985)*, 115(3):313–324, Aug 2013.

[7] V. M. Mai and S. S. Berr. Mr perfusion imaging of pulmonary parenchyma using pulsed arterial spin labeling techniques: FAIRER and FAIR. *Journal of magnetic resonance imaging : JMRI*, 9(3):483–487, Mar 1999.

[8] V. M. Mai, Q. Chen, A. A. Bankier, M. Zhang, K. D. Hagspiel, S. S. Berr, and R. R. Edelman. Imaging pulmonary blood flow and perfusion using phase-sensitive selective inversion recovery. *Magnetic resonance in medicine : official journal of the Society of Magnetic Resonance in Medicine / Society of Magnetic Resonance in Medicine*, 43(6):793–795, Jun 2000.

[9] Y. K. Mariappan, K. J. Glaser, D. L. Levin, R. Vassallo, R. D. Hubmayr, C. Mottram, R. L Ehman, and K. P McGee. Estimation of the absolute shear stiffness of human lung parenchyma using 1H spin echo, echo planar MR elastography. *Journal of Magnetic Resonance Imaging*, 2013.

[10] K. P. McGee, Y. K. Mariappan, R. D. Hubmayr, R. E. Carter, Z. Bao, D. L. Levin, A. Manduca, and R. L. Ehman. Magnetic resonance assessment of parenchymal elasticity in normal and edematous, ventilator-injured lung. *Journal of Applied Physiology*, 113(4):666–676, 2012.

[11] J. P. Mugler and T. A. Altes. Hyperpolarized 129Xe MRI of the human lung. *Journal of Magnetic Resonance Imaging*, 37(2):313–331, 2013.

[12] D. G. Nishimura. *Principles of Magnetic Resonance Imaging*. Self-Published, 1996.

[13] H. Q. and J. B. Bassingthwaighte. A class of flow bifurcation models with lognormal distribution and fractal dispersion. *Journal of theoretical biology*, 205(2):261–268, Jul 2000.

[14] R. C. Sá, M. V. Cronin, A. C. Henderson, S. Holverda, R. J. Theilmann, T. J. Arai, D. J. Dubowitz, S. R. Hopkins, R. B. Buxton, and G. K. Prisk. Vertical distribution of specific ventilation in normal supine humans measured by oxygen-enhanced proton MRI. *Journal of Applied Physiology*, 109(6):1950–1959, 2010.

[15] W. M. Spees, D. A. Yablonskiy, M. C. Oswood, and J. J. Ackerman. Water proton MR properties of human blood at 1.5 tesla: magnetic susceptibility, T(1), T(2), T*(2), and non-lorentzian signal behavior. *Magnetic resonance in medicine : official journal of the Society of Magnetic Resonance in Medicine / Society of Magnetic Resonance in Medicine*, 45(4):533–542, Apr 2001.

[16] R. J. Theilmann, T. J. Arai, A. Samiee, D. J. Dubowitz, S. R. Hopkins, R. B. Buxton, and G. K. Prisk. Quantitative MRI measurement of lung density must account for the change in T(2) (*) with lung inflation. *Journal of magnetic resonance imaging : JMRI*, 30(3):527–534, Sep 2009.

[17] J. M. Wild, H. Marshall, X. Xu, G. Norquay, S. R. Parnell, M. Clemence, P. D. Griffiths, and J. Parra-Robles. Simultaneous imaging of lung structure and function with triple-nuclear hybrid MR imaging. *Radiology*, 267(1):251–255, 2013.

# Chapter 3

# Conducting Pulmonary Physiology Studies in The MR Scanner Environment

## 3.1 Abstract

The experimental design (including human subject recruiting, MRI data collection and analysis) needed to be optimized to address the specific questions of this thesis research work such as the effects of inhalation of different oxygen concentration gases or tidal volume lung inflation on the distribution of pulmonary perfusion. This chapter provides the overview of experimental setups to conduct human physiology studies in magnetic resonance imaging (MRI) scanner environment. The context of chapter is partially based on the video journal in which I am the primary author [2].

The preparation for the MR imaging session and MR facility setup for the study are discussed first. Then, the limitations with current setup and future direction are mentioned.

## 3.2 Introduction

As described in the prior chapter, magnetic resonance imaging (MRI) is the research tool used in the author's dissertation research to quantify the pulmonary function within the lung. It is a powerful tool to noninvasively visualize a human anatomy and its function. However, in order to study the human lung using MRI and address the specific physiological questions of this work, the experimental design needed to be optimized. The inside of an MR scanner is a unique environment, and the inner diameter of an MR bore is approximately 60 cm, which may induce some human subjects to feel claustrophobic. It is also a loud environment, as the magnetic gradient coil generates sound. In this chapter, several key aspects of conducting pulmonary physiology research in the MR scanner environment will be discussed step by step. The design of the current MR study protocol was optimized to monitor various vital information and to reduce the subject's physical and psychological stresses during the experiment, so that collected data would represent normal physiological conditions as much as possible.

## 3.3 Preparation for the MR imaging session

Prior to the MR imaging session, participants were screened for conditions that might preclude their inclusion in the study and asked about their health status. Informed consent was provided to make sure that all participants could understand what they would be expected to do and what risks would be involved during the experiment.

### 3.3.1 Subject recruitment

Subjects were recruited by advertisement and/or word of mouth, to fit the healthy normal population demographic required for the study; specifically, we targeted lifelong nonsmokers between ages 18-45 with no history of heart or lung disease.

### 3.3.2 Informed consent and MR safety questionnaire

All subjects were informed of the potential risks of the study, e.g. exposure to strong static and rapidly changing magnetic fields and inhalation of hypoxic and hyperoxic gases, if applicable. Female subjects of childbearing age underwent a urine pregnancy test before the onset of the MR imaging session in order to rule out pregnancy. Although exposure to magnetic field is extremely unlikely to harm a developing fetus, the exact potential risk is unknown. For this reason pregnant subjects are excluded. Subjects must complete an MR safety questionnaire about items that would contraindicate magnetic resonance imaging (e.g. pacemaker, stents, tattoo, etc.). If any contraindications were found, the subject was excluded from the MR imaging session.

### 3.3.3 Physical exam

The subject was interviewed regarding their general physical health and habits, and received a brief physical examination by a licensed physician if needed. The subject's height and weight were measured. These values were used to estimate the predicted values of the pulmonary function test as well as to set the specific absorption rate (SAR: W (radio frequency power) / kg (subject's body weight)) to determine the United States Food and Drug Administration limit of radio frequency power used for the MR imaging. The radio frequency energy necessary to generate MR images has a potential risk of heating the subject's tissue. Therefore, the amount of radio frequency power administrated to a human subject is controlled by MR scanner. A radio frequency power monitor implemented in the MR scanner uses the subject's body weight as its controlling parameter.

### 3.3.4 Pulmonary function test

Pulmonary function tests followed the standard set by the American Thoracic Society / European Respiratory Society criteria [8]. The subject performed Pulmonary Function Test (PFT) by blowing into a handheld spirometer (EasyOne Spirometer, Medical Technologies Andover) in the upright posture. A nose clip

was provided so that all air would be expelled through the mouth into the device for quantification of flow + volume. Spirometry data were acquired in triplicate to ensure reliable data. Forced vital capacity (FVC [liter]) and forced expiratory volume in 1 second ($FEV_1$ [liter]) were recorded. Percentage prediction values were computed based on height, age, sex, race and weight to ensure that the human subjects were categorized as healthy normal.

### 3.3.5 Breathing maneuver training

For subjects who are first-time participants to one of the studies conducted by UCSD pulmonary imaging laboratory, this training session is crucial. MR images must be acquired at the right timing, as the subject is holding his or her breath at a certain lung volume in synchrony with image acquisition. MR scanner sounds indicate image acquisition timing. The subject was coached to synchronize breathing and breath-holding using recorded MR scanner sounds, which emulate the actual MR sequence and allow teaching outside the scanner the breathing maneuver required during the imaging session. Subjects were asked to attain a predetermined lung volume such as functional residual capacity (FRC) or end-inspiratory lung volume repeatedly during the imaging session. A training session was used to help each subject to learn hold their breath for a short period of time at the target lung volume. The typical target lung volume was FRC, which is the volume at the end of a normal relaxed exhalation, where there is no force exertion from the diaphragm or other respiratory muscles. The controlled lung inflation study utilized an air bag from which the subject inhaled. Subjects were instructed to keep their glottis open when they were holding their breath so that they would not elevate transpulmonary pressure and would avoid Valsalva maneuver [7, 10].

## 3.4 MR study room setup

Once the pre-MR procedures were completed, the subject was taken to the MRI facility. The MRI facility is physically separated into the console room and scanner room. Ferromagnetic objects are prohibited the MR scanner room, as it

could result in subject injury or death. Therefore, the subject and measurement equipment are separated between the scanner room and console room. The console room is where investigators control the MR scanner using computer hardware and software. Gas tanks, a remote inspiratory valve switch unit, a metabolic cart, a pulse oximeter, and other instruments were also placed in the console room. The scanner room is where the MR scanner is located, with a subject lying in the MR bore.

### 3.4.1 Breathing line setup

The subject's inspiration (i.e. volume and gas mixture content) was controlled and the expiration was monitored during the imaging session via an expiratory breathing line. The breathing line setup is divided into three major parts described in Figure 3.1; 1: the mask, which is the interface between the breathing setup and the human subject, 2: the inspiratory side, which allows administration of a gas mixture to a subject and 3: the expiratory side, which monitors respiratory volumes, frequency and mixed expired gas from the subject.

#### Mask

A cold-sterilized silicone mask (Figure 3.2. 7400 series Oro-Nasal Mask, Hans Rudolph) was fitted to the subject. There are six different mask sizes (petite, extra small, small, medium, large and extra large). A majority of adult subjects were fitted with small, medium or large masks. The dead space associated with the mask is approximately 100 mL [9]. The mask was attached to the subject's face covering both the nose and mouth using an overhead mesh attachment. It was equipped with a pre-sterilized non-rebreathing valve (Two-way non-rebreathing valve T-Shape$^{TM}$ configuration, 2600 Medium. 2700 Large, Hans Rudolph) to allow delivery of the inhalation gas mixtures through the inspiratory side and to monitor the exhalation gas through the expiratory side. The mask and valves were checked for leaks. Both inspiratory and expiratory ends of two-way valve were closed for a brief period by both hands, the wearer was tried to breathe in and out. If the mask was not tight fit, the wearer could sense the air leak. If there is

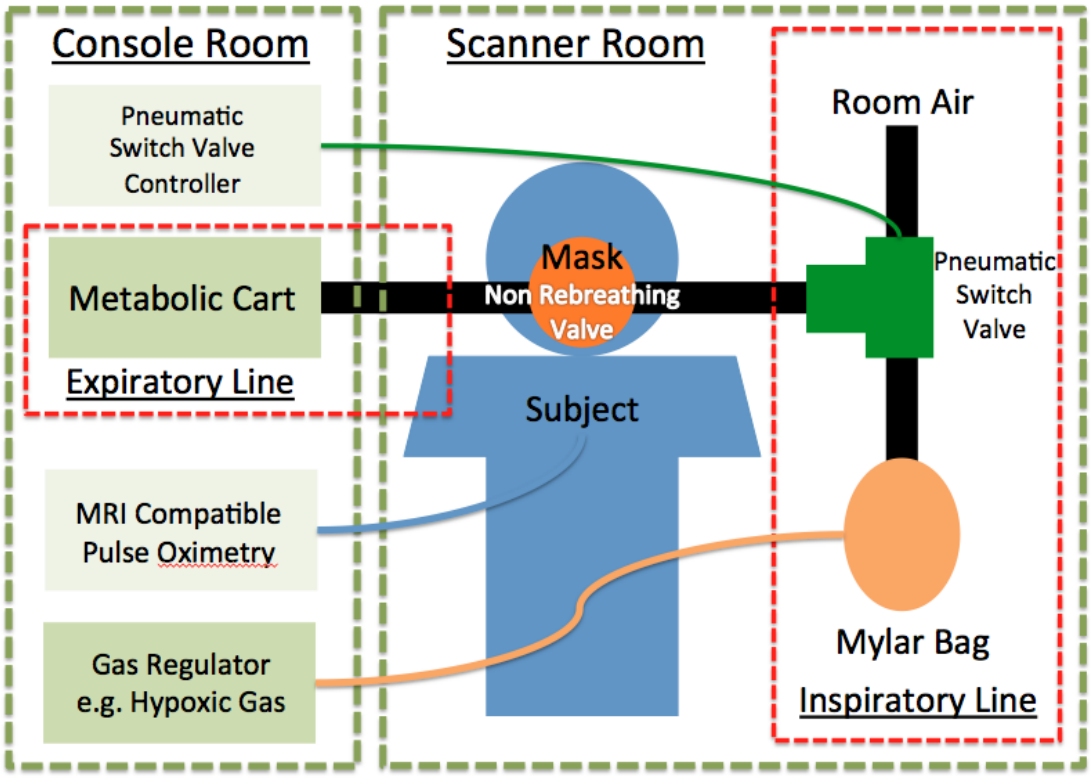


**Figure 3.1**: Breathing line setup. The breathing line setup is divided into three major parts, Mask, Inspiratory Line and Expiratory Line. A human subject is wearing a breathing mask in the MR scanner bore. Inspiratory equipment is in the MR scanner room. Expiratory gas is displaced to a metabolic cart system in MR console room through the expiratory line.

a leak, it results in underestimating the measured minute ventilation, computed oxygen consumption ($\dot{V}_{O_2}$) and carbon dioxide production ($\dot{V}_{CO_2}$) monitored at the expiratory side.


**Figure 3.2**: Breathing Mask (7400 series Oro-Nasal Mask, Hans Rudolph) + Two-way non-rebreathing valve (2600 Medium). The breathing line setup is divided into three major parts, Mask, Inspiratory Line and Expiratory Line. The human subject wears a breathing mask in the MR bore. Inspiratory equipment is in the MR scanner room. Expiratory gas is displaced to a metabolic cart system in MR console room through expiratory line.

### The inspiratory line setup

The inspiratory side of the valve was connected to a switching valve (Figure 3.3. Single-Piston Sliding-Type$^{TM}$ valve and controller 4285A, Hans Rudolph). One end of the switching valve was connected to an inspiratory Mylar gas bag (Figure 3.4. Non-diffusing gas collection bag 170 litter, Hans Rudolph) via a large bore, low resistance tube (Clean-Bor Tubing 108 1-3/8 OD fittings, VacuMed), and the other end was open to room air through another tube of the same type.

The two tubes must have an identical length in order to equalize the inspiratory flow resistance. The gas bag stayed in the MR scanner room. The valve switch was pneumatically controlled via two pressure-feed lines, which were connected to a control panel in the MR console room via a pass-through so that an investigator could remotely switch the source of the inspiratory gas mixture. For a study involving different inspiratory oxygen concentrations, a 170-liter Mylar bag was used to hold either hyperoxic or hypoxic gas mixtures [1, 2]. The bag was connected to a gas tank in the MR console room via gas regulator and long gas feed line. Gas was added to the bag by the investigator using the regulator. For the different levels of lung inflation study, a 5-liter bag was used to hold predetermined measured amount of normoxic air. A calibrated 3-liter syringe (Hans Rudolph) in the MR console room was used to standardize the volume measurement (500 mL and 1 liter), which was then administered to the bag in the MR scanner room through an air feed line.

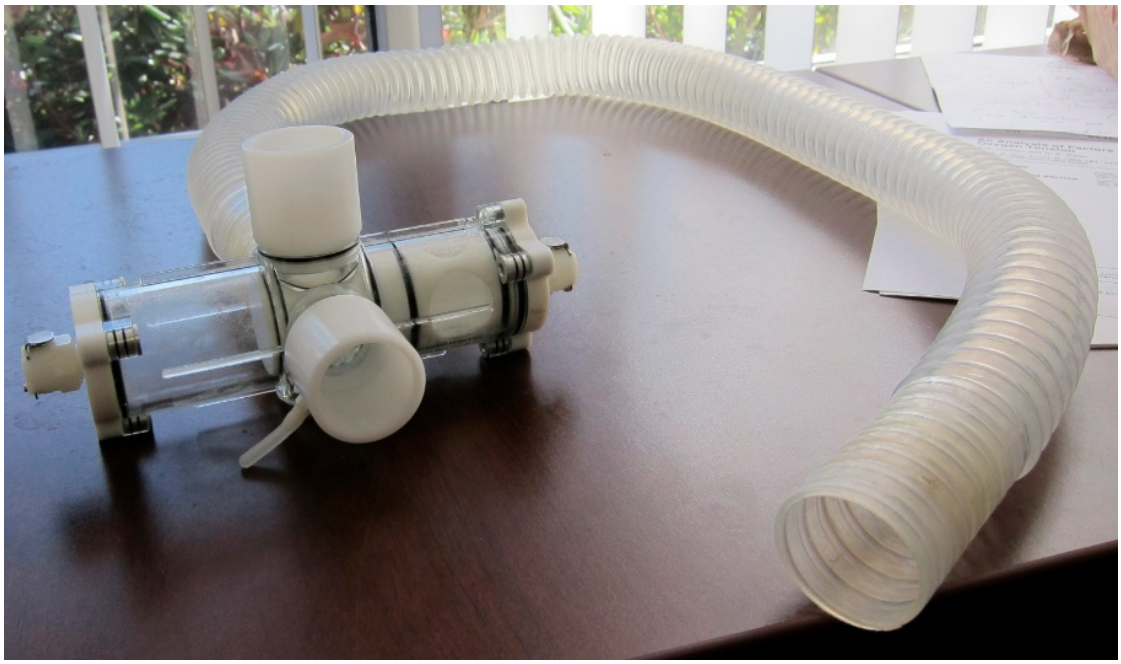

**Figure 3.3**: Switching Valve (Single-Piston Sliding-Type$^{TM}$ valve, Hans Rudolph). One end of the switching valve was connected to an inspiratory Mylar gas (Figure 3.4) and the other end was open to room air through another tube of the same type.

**Figure 3.4**: Mylar gas bag (Non-diffusing gas collection bag 170 litter, Hans Rudolph). One end of the switching valve was connected to an inspiratory Mylar gas. For a study involving different inspiratory oxygen concentrations, a 170-liter Mylar bag was used to hold either hyperoxic or hypoxic gas mixtures [1, 2].

**The expiratory line setup**

The expiratory breathing tube must be sufficiently long to connect the subject in the scanner room to the metabolic cart (TrueOne®2400, ParvoMedics) in the console room via a pass-through. The metabolic cart measures the volume of expired air per unit time as well as mixed expiratory $O_2$ and $CO_2$ concentrations. Based on these values, it also calculates various metabolic data such as the tidal volume, oxygen consumption ($\dot{V}_{O_2}$), and carbon dioxide production ($\dot{V}_{CO_2}$) as well as respiratory quotient. Continuous respiratory monitoring is not only for data collection but also for the safety of human subject. For example, when a subject is distressed in the MR bore, he or she tends to hyperventilate [6] which is observed as elevated ventilation and respiratory quotient.

The $O_2$ and $CO_2$ sensors and flow meter were calibrated before every study session by following the built-in instructions in accordance with the metabolic cart operating software. $O_2$ and $CO_2$ sensors were adjusted by a two-point calibration between the calibration gas (Typically $F_{O_2} = 0.1600$ and $F_{CO_2} = 0.0397$) and room air ($F_{O_2} = 0.2093$ and $F_{CO_2} = 0.0003$). The flow meter was also calibrated by using a standardized 3-liter syringe connected to a Hans Rudolph 2-way non-rebreathing valve and the expiratory line. The investigator pumps 3-liter volume of air (at room temperature and barometric pressure) into the metabolic cart via the expiratory breathing tube, at different flow rates. A wide range of flow rates were covered to bracket the actual expiratory flow range; this calibration was performed at least five times with peak flows ranging from 25 liter(ATPS)/min to 100 liter/min for resting measurements. The total volume of the tube and mouthpiece was calculated along with the subject's respiratory data, allowing for calculation of the delay time caused by the length of expiratory tube.

### 3.4.2 MR scanner and subject setup

The subject, having cleared all metal objects in his/her pockets, entered into the MR scanner room, and asked to lie supine on a sliding table with feet towards the scanner bore. Pillows and foam pads were used to maximize the subject's comfort. Earplugs were provided to the subject to protect them from the

loud noise produced by the scanner. A squeeze ball was positioned in the subject's hand and taped in place. As the subject wears a mask, it is not easy to communicate with the investigators in the usual way, through the microphone embedded in the MR scanner. When the subject squeezes the ball, it prompts an alarm sound in the MR console room and allows the subject to alert the investigators anytime he or she needs assistance. A fiber-optical pulse oximeter (7500 FO, Nonin) was placed on the subject's finger to monitor oxygen saturation and heart rate; this was especially important when the subject was exposed to hypoxia. An electrocardiography (ECG) electrode pad was placed on the subject's chest and connected to an In-Vivo MR-compatible monitoring device. In addition to monitoring, this allows the MR sequence to be gated using the R wave of QRS complex [3, 5]. A torso coil (8 channel receiver coil) was used to improve the signal to noise ratio of the MR image compared to the body coil by reducing the physical distance between the receiver and the subject. The torso coil induces an uneven sensitivity profile throughout the field of view and there were commonly four distinctive hot spots in an MR image around the vicinities of the coil. This sensitivity profile is called coil inhomogeneity, we correct for it, as discussed in chapter 2. A silicon phantom (Brest Implant Round 250cc, Mentor) was used for the MR signal calibration for absolute quantification. Its proton density and longitudinal and transverse relaxation times ($\rho$, $T_1$, $T_2$ and $T_2^*$) are known values. There were four phantoms used for the experiment, placed in direct contact with the subject's body within the field of view. Finally, the subject was covered with a blanket to ensure their comfort.

Once everything was in place, the sliding table was advanced and the subject was advanced into the center of the MR scanner bore. While the subject was inside of the MR bore, a scanner operator frequently talked to the subject through a microphone in the console room and associated speakers in the scanner, in order to verify that the subject was comfortable and to remind them to squeeze the squeeze ball if they needed assistance. Investigators monitored the ECG, $O_2$ saturation, tidal volume, $\dot{V}_{O_2}$, and $\dot{V}_{CO_2}$ for the first few minutes to ensure the data quality. If these numbers were in error, the metabolic cart was recalibrated, the face mask and tubes were checked for leaks, and the ECG pad and electrodes were checked

for proper engagement. Otherwise, the imaging session proceeded.

## 3.5 Limitation and future direction

The current MR pulmonary study setup was carefully designed to provide a tolerable experimental environment to the participants and to monitor their cardiopulmonary vital signals constantly throughout the imaging session. This was essential for the subject's safety and reliable physiological data acquisition. However, there is a room for the future improvement suggested below.

First, the ECG could be improved. Continuous monitoring of the R wave is essential for the cardiac gated MR sequences. The ECG signal was often disrupted by the induction current generated by the MR scanner during image acquisition as well as the subject's motion, resulting in MR sequence miss-triggering. This can be an issue in conducting exercise studies in the MR environment in which the subject's heartbeat is increased as well as body motion is involved. The inside of an MR scanner is not a suitable environment for any ferromagnetic objects and this limits the potential viability of substituting the ECG with other devices. A pulse oximetry plethysmograph, which utilizes infrared light and optical fibers, is a viable option. In this case, it is necessary to identify the signal delay between the R wave in ECG and the plethysmograph measured at the fingertip (Pulse transit time ) over a wide range of cardiac output, possibly on a subject-by-subject basis. Pulse transit time in supine posture is approximately 200 ms [4].

Second, respiratory triggering was not attainable with the current system. The respiratory gated MR sequence using respiratory chest belt will give new insight into the dynamic aspects of pulmonary physiology. The lung constantly changes its volume during breathing approximately on the order of 0.1 Hz with a normal respiratory frequency. However, these dynamics have not been well investigated using MRI. The sampling rate of MR image acquisition can be optimized to keep track of motion. A pneumotachograph attached to a breathing mask (monitoring both inspiratory and expiratory flow volumes) is another option. Respiratory information can be displayed to the subject as feedback through a projector

screen to help them control their breathing pattern to fit to a specific type of study protocol.

Third, humans spend most of their time in an upright posture. However, upright MR scanning is not a common research/clinical tool. Lastly, there is a space issue; a human subject was placed in a confined MR bore space along with a variety of other experimental instruments (e.g. mask, tubes, torso coil, ECG pad and leads, pulse oximeter probe, and calibration phantoms). These bulky devices could be miniaturized or rearranged so as not to take up as much space. Despite the fact that there is room for improving the MR study environment, the current setup was adequately optimized to conduct my thesis research work.

## 3.6 Summary

1. Subject safety was a primary concern. Pre-imaging subject screening, including informed consent and subject training, helped applicants better understand their participation in an MR pulmonary study.

2. The study setup was designed to give a sufficiently comfortable environment for a human subject and to minimize their physical and psychological stresses.

3. Continuous cardiopulmonary monitoring during the imaging session was crucial for both subject safety and reliable data collection.

## 3.7 Acknowledgement

Chapter 3, in part, is a reprint of the material as it appears in *J Vis Exp* 51, e2712, 2011. Arai TJ; Prisk GK; Holverda S; Sá RC; Theilmann RJ; Henderson AC; Cronin MV; Buxton RB; Hopkins SR. The dissertation author was the first author of this publication.

## 3.8 Bibliography

[1] T. J. Arai, A. C. Henderson, D. J. Dubowitz, D. L. Levin, P. J. Friedman, R. B. Buxton, G. K. Prisk, and S. R. Hopkins. Hypoxic pulmonary vasoconstriction does not contribute to pulmonary blood flow heterogeneity in normoxia in normal supine humans. *Journal of applied physiology (Bethesda, Md. : 1985)*, 106(4):1057–1064, Apr 2009.

[2] T. J. Arai, G. K. Prisk, S. Holverda, R. C. Sá, R. J. Theilmann, A. C. Henderson, M. V. Cronin, R. B. Buxton, and S. R. Hopkins. Magnetic resonance imaging quantification of pulmonary perfusion using calibrated arterial spin labeling. *Journal of visualized experiments : JoVE*, 51(1):2712, May 2011.

[3] D. S. Bolar, D. L. Levin, S. R. Hopkins, L. F. Frank, T. T. Liu, E. C. Wong, and R. B. Buxton. Quantification of regional pulmonary blood flow using ASL-FAIRER. *Magnetic resonance in medicine : official journal of the Society of Magnetic Resonance in Medicine / Society of Magnetic Resonance in Medicine*, 55(6):1308–1317, Jun 2006.

[4] G. SH. Chan, P. M. Middleton, and L. Wang. Change in pulse transit time and pre-ejection period during head-up tilt-induced progressive central hypovolaemia. *Journal of clinical monitoring and computing*, 21(5):283–293, 2007.

[5] A. C. Henderson, G. K. Prisk, D. L. Levin, S. R. Hopkins, and R. B. Buxton. Characterizing pulmonary blood flow distribution measured using arterial spin labeling. *NMR in biomedicine*, 22(10):1025–1035, Dec 2009.

[6] R. Ley. Blood, breath, and fears: A hyperventilation theory of panic attacks and agoraphobia. *Clinical Psychology Review*, 5(4):271 – 285, 1985.

[7] V. G. Macefield. Sustained activation of muscle sympathetic outflow during static lung inflation depends on a high intrathoracic pressure. *Journal of the autonomic nervous system*, 68(3):135–139, Feb 1998.

[8] M. R. Miller, J. Hankinson, V. Brusasco, F. Burgos, R. Casaburi, A. Coates, R. Crapo, P. Enright, C. P. M. van der Grinten, P. Gustafsson, R. Jensen, D. C. Johnson, N. MacIntyre, R. McKay, D. Navajas, O. F. Pedersen, R. Pellegrino, G. Viegi, J. Wanger, and ATS/ERS Task Force. Standardisation of spirometry. *The European respiratory journal*, 26(2):319–338, Aug 2005.

[9] R. C. Sá, M. V. Cronin, A. C. Henderson, S. Holverda, R. J. Theilmann, T. J. Arai, D. J. Dubowitz, S. R. Hopkins, R. B. Buxton, and G. K. Prisk. Vertical distribution of specific ventilation in normal supine humans measured by oxygen-enhanced proton MRI. *Journal of Applied Physiology*, 109(6):1950–1959, 2010.

[10] I. Taneja, M. S. Medow, D. A. Clarke, A. J. Ocon, and J. M. Stewart. Postural change alters autonomic responses to breath-holding. *Clinical autonomic research : official journal of the Clinical Autonomic Research Society*, 20(2):65–72, Apr 2010.

# Chapter 4

# Lung Deformation Analysis via Image Registration

## 4.1 Abstract

The motion of breathing causes lung deformation, and the shape of the lung captured in an MR image varies with the lung volume. Two MR lung images obtained at two different lung volumes are registered together so that these two lungs are comparable based on the anatomical correspondence of points in the two images. The goal of this chapter is to describe the methods to analyze lung deformation via image registration. The mathematical representation of lung deformation is introduced. The spatial pattern of deformation is modeled by a polynomial interpolation method using two different cubic polynomial interpolation functions (Hermite and B-spline). One lung image was warped into another lung image using the modeled deformation field. Meanwhile, the cost function, which quantifies the matching between two lungs within the region of interest, was recursively calculated. Therefore, the computed deformation field that gave the most optimized cost function value, was the best representation of the ground truth lung deformation. The deformable image registration technique used for my dissertation research was capable of computing not only 2 dimensional but also 3 dimensional lung deformation.

## 4.2 Introduction

Image based *in vivo* pulmonary deformation analysis enables the characterization of local lung volume change [4, 7, 9], parenchymal mechanics [8, 13, 14, 18, 21], and lung motion [5, 16] due to breathing. The local lung volume change results from local ventilation (+ dead space ventilation). The regional volumetric strain in the lung results from the spatial distribution of stress and local lung tissue mechanical properties. The estimation of lung motion throughout a breathing cycle is used for radiotherapy planning to localize the treatment volume using 4 dimensional computer tomography. Moreover, image registration is a crucial step in purpose of image processing. For instance, the current applications of functional lung MRI developed by the author's collaborators at UCSD pulmonary imaging laboratory have focused on examining the spatial distribution of specific ventilation [19] and the temporal and spatial variability of pulmonary blood flow [2]. Both applications require more than one hundred MR images acquired over 15-30 minutes. During the image acquisition, subjects are instructed to voluntarily gate their respiration approximately every 5 seconds so that images are acquired during a short breath-hold at a specified lung volume (typically functional residual capacity). This maneuver may result in registration errors potentially affecting the quality of the outcome results. Therefore, an image registration scheme needs to be implemented in post image processing [1]. In addition to the deformable image registration technique developed during my dissertation research, other methods could be used as alternatives to estimate the lung deformation. For example, the grid-tagging MR method is a hardware approach to capture an image of deformation. The spatial grid-tag is applied simultaneously with RF excitation pulse, which draws grid lines in the MR image by controlling the spatial variation of contrast. After a sufficient delay time, an MR image is acquired. The respiratory motion during the delay time distorts the grid [8, 18, 21] so that the lung deformation is visualized. However, this technique is limited to monitoring the lung deformation within a short period, which is in the order of msec. Due to the low proton density and short MR relaxation time, the grid contrast decays away quicker than the time taken for a respiratory motion. Hyperpolarized MR imaging,

where the gaseous contrast agent potentially provides high signal and long relaxation time, could be an alternative method [4]. However, it requires additional hardware such as a gas polarizer and tuned RF coil.

The other approach is elastic matching [3, 10, 14, 20], which requires prior biomechanical knowledge of the object to solve for the strain energy function. Therefore, the method relies on several assumptions such as a constitutive model, spatial distribution of stress and mechanical properties. The method of analyzing pulmonary deformation used for the author's dissertation research does not require the application of preparation RF tagging or assumptions of the spatial distribution of stress and mechanical properties in the lung. It only requires the implicit assumptions of continuum analysis.

## 4.3 Mathematical representation of deformation

When an object deforms as a result of applied force, any single material point (a small part of object) is displaced from the original location to the resultant new location. Take lung deformation in supine posture for instance: during inhalation, the diaphragm is displaced in the caudal direction, the chest wall tends to move up in the anterior direction [22] due to external intercostal muscle contraction, however the apical-dorsal part of the lung barely moves since the rib cage does not displace much in this direction. The diaphragmatic compartment is more distensible than the rib cage in normal humans in supine posture [12]. It is not trivial to keep track of every single displacement of every single material point in the lung, based on two images acquired before and after deformation. A more tractable approach is to fit a spatial model, which is sufficiently flexible to express spatially heterogeneous lung deformation.

The lung is assumed to be a continuum. The lung tissue and air are considered as lung matter expressed in units of density, g/mL. The lung matter continuously fills the lung space and the lung density distribution is expressed as a spatial function. There is a strong gravitational dependence of lung density distribution known as the Slinky$^{TM}$effect. As the lung deforms due to breathing motion, it

results in a change in lung material configuration as well as the changes in the local lung density. This change in lung material configuration can be considered as a coordinate transformation. The original configuration of material points is the original reference coordinate, which is simply expressed as Cartesian coordinate system, and the resultant configuration is the deformed coordinate system. For each axis $a_i$, the coordinate transformation, which includes both deformation and rigid body motion is expressed as equation 4.1.

$$x_i = \sum_{j=1}^{n} \frac{\partial x_i}{\partial a_j} a_j + b_i \tag{4.1}$$

where $a_j$ represents each reference coordinate axis, $x_i$ is the deformed coordinate, $\partial x_i / \partial a_j$ is the deformation gradient tensor, n represents the order of the dimension, and $b_i$ is the rigid body displacement of axis $a_i$. In 2D, there are six parameters controlling the transformation; four in the deformation gradient tensor and two in the rigid body displacement (equation 4.2 and 4.3).

$$x_1 = \frac{\partial x_1}{\partial a_1} a_1 + \frac{\partial x_1}{\partial a_2} a_2 + b_1 \tag{4.2}$$

$$x_2 = \frac{\partial x_2}{\partial a_1} a_1 + \frac{\partial x_2}{\partial a_2} a_2 + b_2 \tag{4.3}$$

In 3D, equation 4.1, 4.2, and 4.3 are extended and there are a total of twelve parameters, nine that describe the deformation gradient tensor and and three for the rigid body displacement. When these parameters are homogeneous throughout the entire function space, the deformation is called affine. However, the realistic lung deformation is regionally heterogeneous [22] and cannot be fully captured by a single affine deformation. For example, when someone breathes in, the gravitationally dependent part of the lung deforms more than the nondependent part. This is caused by the gravitational gradient in density, which places different regions of the lung in different portions of the nonlinear pressure volume curve (Figure 4.1 [22]). As can be seen from the figure, for an identical change in transpulmonary pressure (alveolar pressure - intrapleural pressure), different portions of the lung will respond with different increases in regional volume. Therefore, deformation is a

function of space, as it depends where each material point is located. It is essential to solve the deformation model with the unknown spatial function in order to correctly characterize the spatial distribution of deformation.

## 4.4 Deformation analysis using a parameterized piecewise polynomial interpolation method

A piecewise polynomial interpolation is utilized to model the unknown spatial features of lung deformation. This approach is capable of curve-fiting the complex shapes in the unknown spatial function with a high degree of continuity at the boundaries where polynomial pieces connect. Using this approach, the modeled deformed coordinate are expressed as equation 4.4.

$$\hat{x_i}(\mathbf{a}) = \sum_{\mathbf{j=1}}^{\mathbf{m}} \mathbf{p_{ij}} \mathbf{w_j}(\mathbf{a}) \tag{4.4}$$

where $\hat{x_i}$ is the function value, which describes the modeled deformed coordinate, $w_j$ is a basis function, $p_{ij}$ is a parameter representing the amplitude of the corresponding basis function, m is the number of basis function and parameter pairs, and $\mathbf{a}$ is the original coordinate. Each of the basis functions $w_j$ has the shape of a spline residing at a specific location on the reference coordinate system and the specific location is called either the node or knot point. The amplitude of the spline is defined by the corresponding $p_{ij}$. The deformed coordinate $x_i$ is approximated as the linear combination of parameters and corresponding basis functions. In other words, the complex spatial feature of coordinate transformation described in equations 4.1, 4.2 and 4.3 is modeled and parameterized using the total of m values. The more parameters are utilized, the more complex spatial feature can be accurately expressed. The region enclosed by the nearest nodes (or knot points) is called the element (or control grid); the shapes of the elements in 1D, 2D and 3D are line, rectangular, and cuboid, respectively. Therefore, there are two, four and eight nodes in 1D, 2D and 3D elements, respectively. The addition of parameters corresponds to the element grid refinement. For instance, when a single element

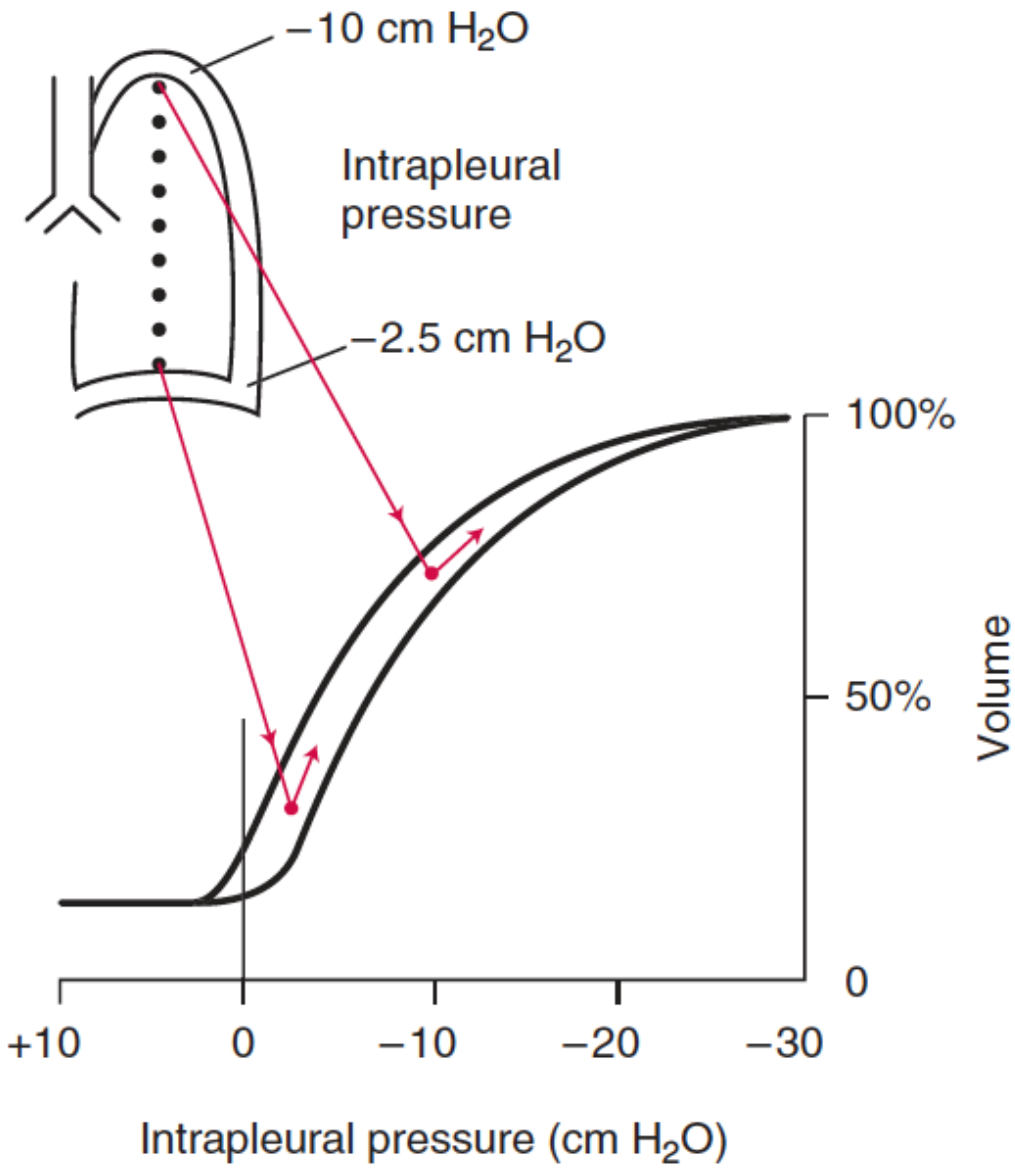


**Figure 4.1**: Pressure Volume Curve. The relationship between lung volume and intrapleural pressure is described as the pressure-volume curve relationship. For a given change in intrapleural pressure, the different portions of the lung will respond with different increases in regional volume. Transpulmonary pressure = Alveolar pressure - Intrapleural pressure.
Copyright has been obtained. *"Respiratory Physiology The Essentials"* by John B. West.

is refined into two elements, the number of nodes increases 1.5 times, resulting in the 1.5 times increase in the number of parameters. A single element allows for modeling global deformation while a finer control grid allows for modeling more localized deformations.

For my graduate research work, two different types of cubic polynomial basis functions were used: cubic B-spline and cubic Hermite basis functions. The details of these specific basis functions and their application to the general 1D and 2D functions are introduced in Appendix C.

## 4.5 Image warping and registration using parameterized deformation model

In this section, a parameterized 2D deformed coordinate model is used to demonstrate image warping. Figure 4.2 demonstrates that three deformed coordinate systems warp an original image. Conventionally, a reference image is denoted as a static image, while another image that is warped into the shape of the reference image is a moving image. Figure 4.2A shows a sagittal slice of a human right lung, X axis represents the A-P direction from left (anterior) to right (posterior) and Y axis is S-I direction from top to bottom) into three different shapes (Figure 4.2B1-3). Since these deformed coordinate systems are modeled by parameterized polynomials, different sets of parameters can warp the original image into various shapes.

In Figure 4.3, two lung images are shown: a static reference image acquired at functional residual capacity (FRC) and a moving image, which was acquired at a greater lung volume. The two lung images are overlapped for the comparison in Figure 4.3A. The goal of image registration is to match the two images by warping the moving image into a shape of reference image using a 2D parameterized deformation model. The set of parameters that approximates the model transformation is determined by an optimization process, described in the next section. Once the optimization process is complete (Figure 4.3B), the parameterized deformation model is taken to be the best approximation of the actual lung

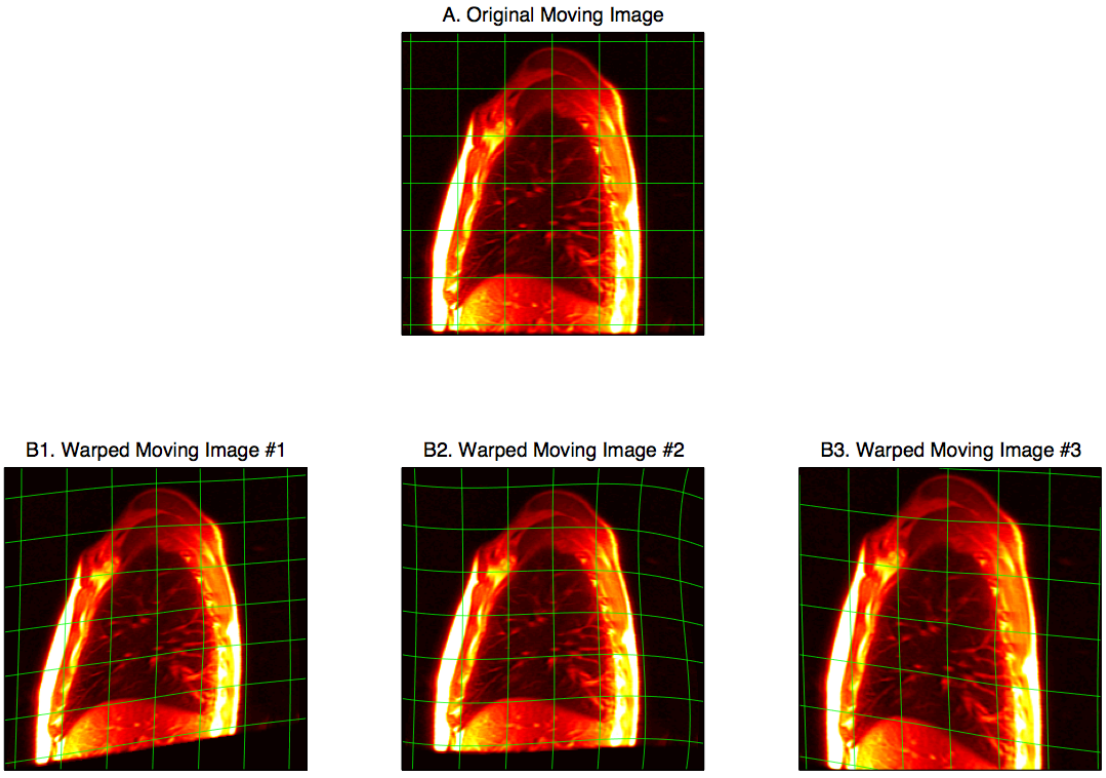


**Figure 4.2**: Image warping. Parameterized 2D deformation model warps the original image into various different shapes. A: sagittal slice of a human right lung. B1-3: Different sets of parameters can warp the original image into various shapes.

deformation between the two lung volumes captured in the two original images. This is called the kinematic approach, describing the motion of material points without the accounting for the causes of the motion. The kinematics approach has a clear advantage: it does not require to assume the spatial distribution of stress tensor and mechanical properties (*Lamé* constants) in the lung other than the implicit assumptions of continuum analysis.

Various deformation indices are computed based on the modeled deformation. The displacement field (Figure 4.3C) is described as the difference between reference coordinate system $a_i$ and the modeled deformed coordinate system $\hat{x}_i$. The local area/volume change ($V/V_ref$, V: the resultant local lung volume due to deformation, $V_ref$: the original local lung volume) is computed as the determinant of deformation tensor (Jacobian) and is show in Figure 4.3D, where the warmer color represent the greater the local are change in arbitrary unit.

The physiological meaning of the local volume change in the lung ($V/V_ref$) is associated with a regional volume of incoming air due to a respiratory motion. The regional distribution of incoming air does not directly represent the local distribution of alveolar ventilation. The unidirectional air flow in a human lung involves a dead space volume, which is a fraction of the total incoming air not contributing to the alveolar ventilation. Therefore, when combined with another imaging technique measuring the local alveolar ventilation distribution, such as specific ventilation imaging [19], the regional distribution of dead space can be visualized, i.e. dead space = regional incoming air - alveolar ventilation.

## 4.6 The cost function

The previous paragraph described how the moving image can be warped to match a reference image. In order to accomplish the image registration, the quality of the match between the warped moving image and the static image needs to be computed. Therefore, a metric is required to evaluate the similarity between warped moving and static images. The metric is also called the cost function. The image registration process consists of recursively searching for a parameter

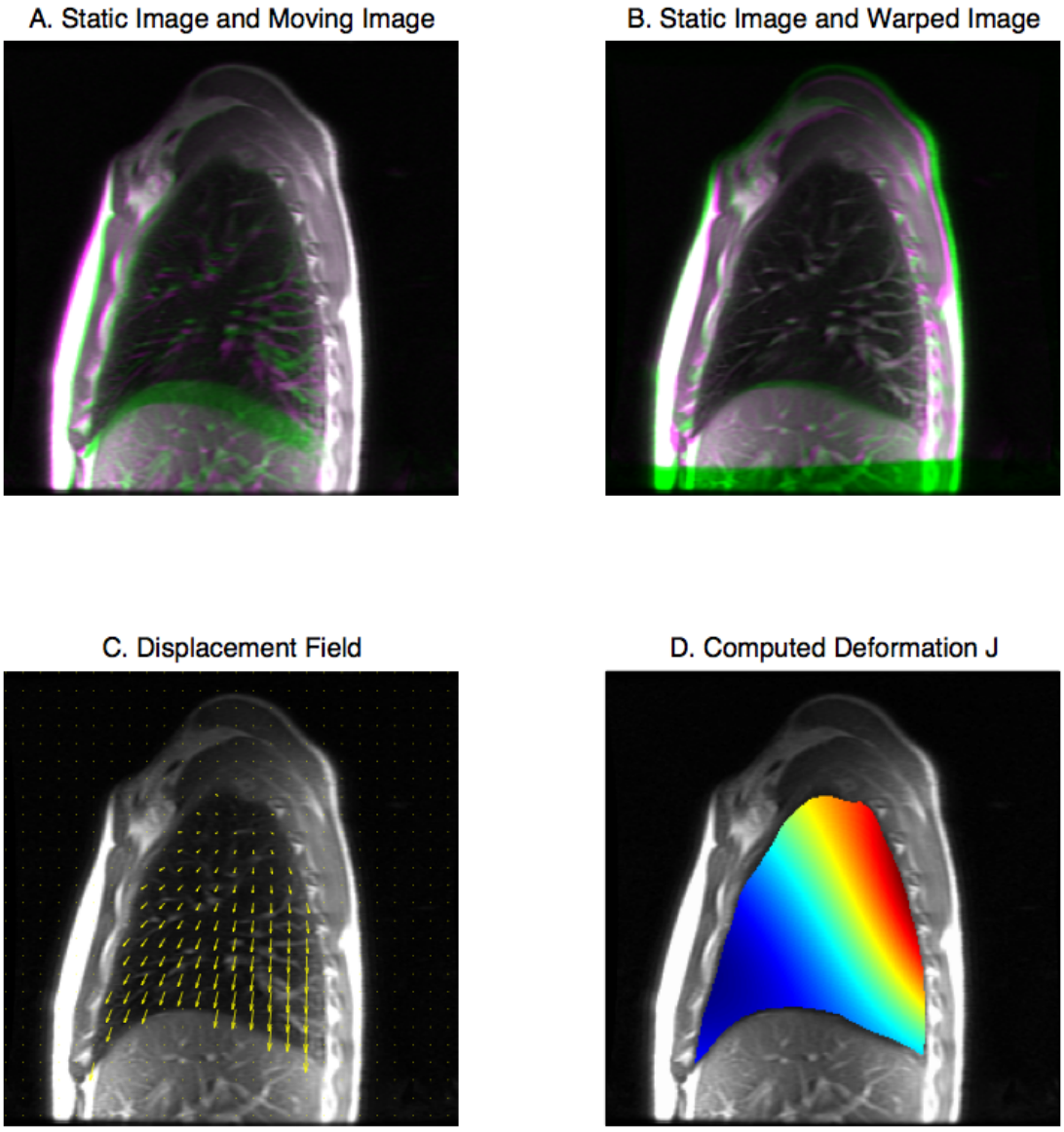


**Figure 4.3**: Deformation analysis using the computed transformation. A: static and moving images are overlapped for comparison. B: the modeled transformation warps moving image into the static image, so that the deformation model approximate the actual lung deformation between two lung volumes captured in the two original images. C: displacement field. The yellow arrows show the displacement field of lung material points between two lung volumes. D: the local area/volume change is computed as the determinant of deformation tensor.

set defining lung deformation that optimizes the cost function.

Many different functions can be used as cost functions. Typical cost functions include the normalized correlation, sum of squared differences and mutual information [17]. For example, the sum of square differences would approach to its minimum value when two images were similar and become zero when two images are completely identical. The choice of cost function is empirical. It must be chosen based on the type of images (such as density image or vasculature image) and computational power [6]. When the image contrast is similar between two images, normalized correlation and sum of squared differences method are good options, while when the image contrast is not similar such as when two images are acquired by two different imaging modalities, mutual information method is powerful option. A Nelder-Mead downhill simplex search method (implemented in MATLAB by the function fminsearch) is used for the optimization. This method searches for the local minima of the cost function for the given number of dimensions in parameter space. Because of this reason, the cost function needs to be modified such that the minimum function value represents the best alignment between two images for the given number of parameters. For example, in the case of using the normalized correlation, the search algorithm must find -1 $\times$ normalized correlation because the minimum value, which is -1 represents the perfect match between two images.

## 4.7 Image registration procedure

In the ideal situation, the image registration algorithm finds the optimal set of parameters without any initial inputs or constraints. However, it is not always the case; the algorithm may yield a set of parameters so that a moving image would be warped into the apparent wrong shape or in physiologically impossible ways. In order to avoid these pitfalls, manually selected fiducial markers assist the algorithm to find an appropriate set of parameters and to perform accurate image registration. A sensible set of constraints also helps to deduce approximate parameter values and to reduce the amount of computational time. There are

three steps for this procedure; (1) Fiducial marker selection, (2) Curve-fitting using a minimum number of parameters within a single element and (3) Element grid refinement. Steps (2) and (3) comprise an iterative process until the warped moving image is aligned onto the reference static image.

### 4.7.1 First Step: Fiducial marker selection

First, fiducial markers are manually selected on the reference image. Their corresponding displacements due to the deformation are then also manually selected on the moving image by comparing the anatomical similarity (Figure 4.4). The minimum number of fiducial markers must correspond to the number of parameters employed to describe the modeled deformation. For example, a minimum of sixteen fiducial markers are required to solve for 2D cubic B-spline and 2D cubic Hermite interpolations since these methods require at least sixteen parameters for a single rectangular element. (The details are described in Appendix C).

### 4.7.2 Second Step: Coarse approximation of modeled deformation within a single element

The selected marker displacements are curve-fitted with an initial modeled deformed coordinate system described by a single element with the minimum number of parameters. This initial model coarsely approximates the actual deformation. A set of parameters is computed using the least square (equation 4.5).

$$\mathbf{N} = (\mathbf{H}^T\mathbf{H})^{-1}\mathbf{H}^T\mathbf{X} \tag{4.5}$$

where $\mathbf{N}$ is m $\times$ n matrix describing a set of nodal parameters where m and n represent the numbers of dimensions and parameters per single dimension, respectively (i.e. m = 2 and n = 16 in 2D). $\mathbf{H}$ is a p $\times$ n matrix describing the basis function value where p represents the number of measurements (i.e. fiducial markers). $\mathbf{X}$ is a p $\times$ m matrix describing manually measured deformed coordinate based on fiducial marker locations.

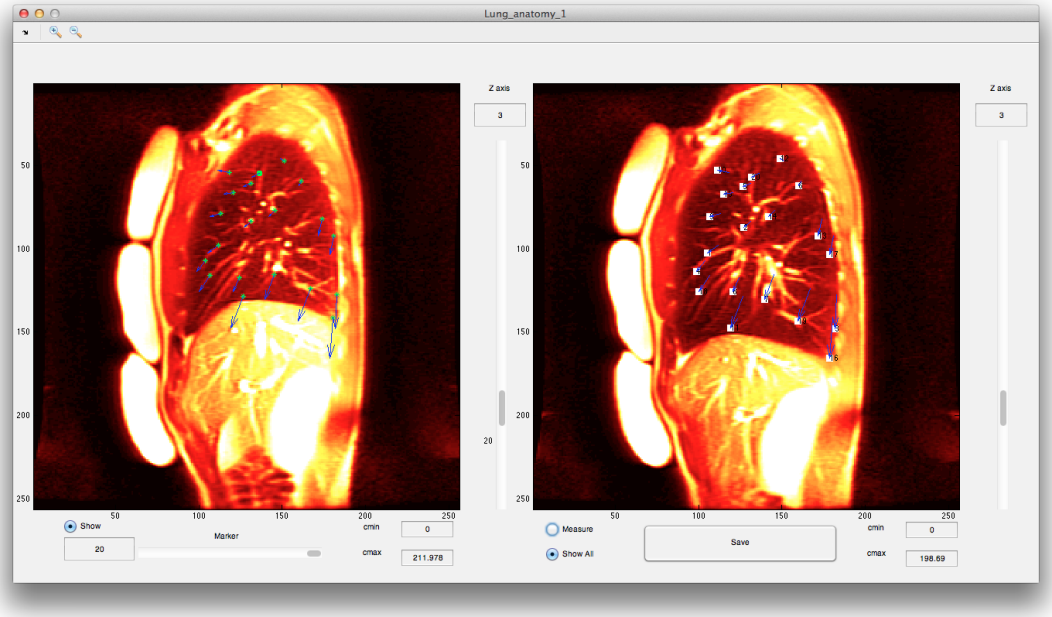


**Figure 4.4**: Manual fiducial marker selection. Left: Fiducial markers are manually selected on the reference image. Right Their corresponding displacements due to the deformation are selected on the moving image by comparing the anatomical similarity. The marker displacement field assists the image registration algorithm to deduce a transformation between reference and moving images. MATLAB®graphical user interface was developed for this task.

**N** is not the optimal set of parameters for the given degrees of freedom. Therefore, the set of parameters is used as an initial guess into the image registration algorithm and the optimization process further minimizes the cost function. Once the set of parameters is optimized, it comprises the rough 2D deformed coordinate model. This rough model is further processed with more parameters, which ensure the greater spatial complexity.

Hermite basis function was used for the second step for practical reasons. In 2D deformation, sixteen parameters are required in each dimension so that there are a total of 32 parameters. Four out of sixteen parameters represent deformed coordinate locations (i.e. function values) at each of four corners of element (nodes). In addition, four basis functions pertaining the second order derivative values have smaller impact than the rest of twelve basis functions onto the linear combination described in the equation 3. Therefore, these four parameters are negligible. There are practically $2 \times 12$ unknowns to be solved in 2D image registration and the rest of four parameters can be constrained to zero.

### 4.7.3 Third Step: Element grid refinement

More degrees of freedom are added to the previously computed rough deformed coordinate system by adding parameters and subdividing the original element into smaller elements as finer mesh grids. This process requires a sufficient computational power. For the author's dissertation research, rocce and oolite clusters at San Diego Supercomputer Center were used.

For this step, the B-spline method was used. B-spline parameters (control point) are found in the vicinity of the corresponding spline location in deformed coordinates. The image registration algorithm searches for each parameter within a given limited range. For example, the parameter displacement must be smaller than 40% of element grid size for each iteration step of the image registration algorithm to avoid the folding of the deformation field [23]. These constraints also help to reduce the computational load. In addition, B-spline ensures C2 continuity so that the modeled deformation has the second order of function continuity across the adjacent elements. On the other hand, it is less suitable to implement Hermite

method for the refinement step. The derivative values belonging to Hermite basis functions are hard to deduce since the value would be found between -$\infty$ and $\infty$. The degrees of freedom introduced by the subdivision renders Hermite parameterization superfluous for interpolating typical deformation; B-splines can adequately capture the deformation with fewer parameters. In other words, using the B-spline method it is possible to gradually increase the degrees of freedom.

The previously computed coarse scale 2D deformed coordinate model is further parameterized using a finer element grid and fit using the least square approach. The computed parameter set is introduced into the image registration algorithm and then optimized. This refinement process is repeated iteratively. The final element size is refined down to approximately 8 $\times$ 8 voxels [23], which is also approximately five folds of the size of acinus [15] and the same spatial resolution as the perfusion measurement.

## 4.8 3D deformed coordinate model and 3D image registration

In the current study setup, the sagittal plane is chosen as a target MR image slice in order to capture both diaphragmatic and gravitational motions in S-I and A-P directions, respectively. The diaphragmatic motion is the major displacement component during breathing in supine posture, while the gravitational motion captures spatially heterogeneous lung deformation due to the gravitational effect on the lung soft tissue. However, the lung actually deforms in 3D space, and 2D image registration disregards the through plane motion in L-R direction. In the work described here, the image registration method is extended to 3D. With the current MRI protocol, the in-plane resolution is approximately 1.6 mm $\times$ 1.6 mm whereas the through-plane resolution is 15 mm. A 3D volumetric lung image is expressed as a stack of 2D lung images in L-R direction. Due to the lower resolution in the third dimension (L-R) compared with other dimensions (A-P and S-I), it can be approximated adequately by fewer degrees of freedom in the L-R direction. Therefore, the linear interpolation method is used for the L-R direction (equation

4.6 and 4.7).

$$L_0(t) = 1 - t \tag{4.6}$$

$$L_1(t) = t \tag{4.7}$$

$t$ is a local coordinate within the element. $L_0$ linearly goes from 1 to 0 and $L_1$ goes from 0 to 1 between both ends of the element, respectively. A single element encompasses the L-R direction of 3D image stack. Two parameters are sufficient to determine two linear basis functions.

## 4.9 Limitation and future directions

The cubic polynomial interpolation method smoothens the computed displacement and deformation field. The interval between two adjacent nodes (or control points) is crucial to define the flexibility of the smoothed field. In my dissertation project, the interval was set to be approximately 1 cm in the in-plane direction, which results in a sample volume approximately the size of 5 acini. Choi *et al* used B-spline interpolation method to quantify the regional volumetric displacement from FRC to total lung capacity (TLC) [9]. Their interval size between adjacent control points was approximately 4 mm. The optimal interval size must be chosen based on the type of physiological question being addressed. It is also related to the computational cost; the finer the interval, the more computational time and power are required. The continuity of interpolation function might not be suited to express the deformation in the whole lung. Based on the lung anatomy, there are three and two lobes in right and left lungs, respectively. Between adjacent lobes, sliding occurs along a fissure when the lung deforms due to respiratory motion. Mathematically, the sliding is expressed as a discontinuous displacement field. Therefore, the continuous interpolation function could not fully express the discontinuity [11]. Moreover since the regional lung volume change is derived from the determinant of local deformation tensor (i.e. Jacobian), the non-continuous derivative would be computed as the abnormal deformation when the interpolation function forces to smooth out the discontinuity. In order to avoid the possible

errors from the sliding effect, the deformation was computed separately for each lobe and then combined to comprise a whole lung. This procedure may also result in another type of error; it may produce either missing or overlapping of lung matters near the fissure between lobes. My thesis research focused on the effect of pulmonary perfusion on the lung deformation. Since pulmonary vasculature is lobe specific and does not cross between lobes, pulmonary perfusion is hardly detectable near the fissure. Therefore, these effects are assumed to be negligible.

## 4.10 Summary

1. A piecewise polynomial interpolation method is used to model deformed coordinate system as a linear combination of parameters and basis functions along Cartesian coordinates.

2. The lung deformation is approximated as a continuous spatial function, computed via image registration between two lung images at two different lung volumes.

3. Basis function, cost function and element size are essential components to define the flexibility of deformed coordinate model.

## 4.11 Acknowledgement

The author acknowledges National Biomedical Computation Resource for the use of their computational resources (rocce and oolite).

## 4.12 Bibliography

[1] T. J. Arai, C. T. Villongco, M. T. Villongco, S. R. Hopkins, and R. J. Theilmann. Affine transformation registers small scale lung deformation. *Conference proceedings: Annual International Conference of the IEEE Engineering in Medicine and Biology Society. IEEE Engineering in Medicine and Biology Society. Conference*, 2012(1):5298–5301, 2012.

[2] A. K. Asadi, M. V Cronin, R. C. Sá, R. J Theilmann, S. Holverda, S. R. Hopkins, R. B. Buxton, and G. K. Prisk. Spatial-temporal dynamics of pulmonary blood flow in the healthy human lung in response to altered FIO2. *Journal of Applied Physiology*, 114(1):107–118, 2013.

[3] R. Bajcsy, R. Lieberson, and M. Reivich. A computerized system for the elastic matching of deformed radiographic images to idealized atlas images. *Journal of computer assisted tomography*, 7(4):618–625, 1983.

[4] J. Cai, T. A. Altes, G. W. Miller, K. Sheng, P. W. Read, J. F. Mata, X. Zhong, G. D. Cates, E. E. DeLange, J. P. Mugler, et. al. Mr grid-tagging using hyperpolarized helium-3 for regional quantitative assessment of pulmonary biomechanics and ventilation. *Magnetic Resonance in Medicine*, 58(2):373–380, 2007.

[5] J. Cai, K. Sheng, S. H. Benedict, P. W. Read, J. M. Larner, J. P. Mugler III, E. E. de Lange, G. D. Cates Jr, and G. W. Miller. Dynamic MRI of grid-tagged hyperpolarized helium-3 for the assessment of lung motion during breathing. *International Journal of Radiation Oncology* Biology* Physics*, 75(1):276–284, 2009.

[6] K. Cao, K. Du, K. Ding, J. M. Reinhardt, and G. E. Christensen. Regularized nonrigid registration of lung CT images by preserving tissue volume and vesselness measure. *Grand Challenges in Medical Image Analysis*, 2010.

[7] R. Castillo, E. Castillo, J. Martinez, and T. Guerrero. Ventilation from four-dimensional computed tomography: density versus jacobian methods. *Physics in medicine and biology*, 55(16):4661, 2010.

[8] Q. Chen, V. M. Mai, A. A. Bankier, V. J. Napadow, R. J. Gilbert, and R. R. Edelman. Ultrafast MR grid-tagging sequence for assessment of local mechanical properties of the lungs. *Magnetic resonance in medicine*, 45(1):24–28, 2001.

[9] S. Choi, E. A. Hoffman, S. E. Wenzel, M. H. Tawhai, Y. Yin, M. Castro, and C. L. Lin. Registration-based assessment of regional lung function via volumetric CT images of normal subjects vs. severe asthmatics. *Journal of applied physiology (Bethesda, Md. : 1985)*, 115(5):730–742, Sep 2013.

[10] T. S. Cook, N. Tustison, J. Biederer, R. Tetzlaff, and J. C. Gee. How do registration parameters affect quantitation of lung kinematics? In *Medical Image Computing and Computer-Assisted Intervention–MICCAI 2007*, pages 817–824. Springer, 2007.

[11] K. Ding, Y. Yin, K. Cao, G. E. Christensen, C. L. Lin, E. A. Hoffman, and J. M. Reinhardt. Evaluation of lobar biomechanics during respiration

using image registration. In *Medical Image Computing and Computer-Assisted Intervention–MICCAI 2009*, pages 739–746. Springer, 2009.

[12] M. Estenne, J. C. Yernault, and A. De Troyer. Rib cage and diaphragm-abdomen compliance in humans: effects of age and posture. *Journal of applied physiology (Bethesda, Md. : 1985)*, 59(6):1842–1848, Dec 1985.

[13] L. Gattinoni, E. Carlesso, and P. Caironi. Stress and strain within the lung. *Current opinion in critical care*, 18(1):42–47, 2012.

[14] J. Gee, T. Sundaram, I. Hasegawa, H. Uematsu, and H. Hatabu. Characterization of regional pulmonary mechanics from serial MRI data. In *Medical Image Computing and Computer-Assisted Intervention—MICCAI 2002*, pages 762–769. Springer, 2002.

[15] B. Haefeli-Bleuer and E. R Weibel. Morphometry of the human pulmonary acinus. *The Anatomical Record*, 220(4):401–414, 1988.

[16] X. Liu, R. R. Saboo, S. M. Pizer, and G. S. Mageras. A shape-navigated image deformation model for 4D lung respiratory motion estimation. In *Biomedical Imaging: From Nano to Macro, 2009. ISBI'09. IEEE International Symposium on*, pages 875–878. IEEE, 2009.

[17] J. B. Maintz and M. A. Viergever. A survey of medical image registration. *Medical image analysis*, 2(1):1–36, Mar 1998.

[18] V. J. Napadow, V. Mai, A. Bankier, R. J. Gilbert, R. Edelman, and Q. Chen. Determination of regional pulmonary parenchymal strain during normal respiration using spin inversion tagged magnetization MRI. *Journal of magnetic resonance imaging*, 13(3):467–474, 2001.

[19] R. C. Sá, M. V. Cronin, A. C. Henderson, S. Holverda, R. J. Theilmann, T. J. Arai, D. J. Dubowitz, S. R. Hopkins, R. B. Buxton, and G. K. Prisk. Vertical distribution of specific ventilation in normal supine humans measured by oxygen-enhanced proton MRI. *Journal of Applied Physiology*, 109(6):1950–1959, 2010.

[20] T. A. Sundaram and J. C. Gee. Towards a model of lung biomechanics: pulmonary kinematics via registration of serial lung images. *Medical image analysis*, 9(6):524–537, 2005.

[21] A. Voorhees, J. An, K. I. Berger, R. M. Goldring, and Q. Chen. Magnetic resonance imaging-based spirometry for regional assessment of pulmonary function. *Magnetic resonance in medicine*, 54(5):1146–1154, 2005.

[22] J. B. West. *Respiratory Physiology The Essentials*. Lippincott Williams and Wilkins, 1974.

[23] Y. Yin, E. A. Hoffman, and C. L. Lin. Mass preserving nonrigid registration of CT lung images using cubic b-spline. *Medical physics*, 36(9):4213–4222, Sep 2009.

# Chapter 5

# The contribution of hypoxic pulmonary vasoconstriction to pulmonary perfusion heterogeneity

## 5.1 Abstract

It was hypothesized that some of the heterogeneity of pulmonary blood flow present in the normal human lung in normoxia is due to hypoxic pulmonary vasoconstriction (HPV). If so, mild hyperoxia would decrease the heterogeneity of pulmonary perfusion since it universally dilates the pulmonary vessel, resulting in more spatially uniform pulmonary blood flow. On the other hand, HPV would be increased by mild hypoxia. To test this, 6 healthy non-smoking subjects underwent magnetic resonance imaging (MRI) during 20 minutes of breathing different oxygen concentrations through a face mask (normoxia, $F_IO_2$ = 0.21; hypoxia, $F_IO_2$ = 0.125; hyperoxia, $F_IO_2$ = 0.30), in balanced order. Data were acquired on a 1.5T MRI scanner during a short breathhold at functional residual capacity from both coronal and sagittal slices in the right lung. Arterial spin labeling was used to quantify the spatial distribution of pulmonary blood flow in ml/min/cm3 and

fast low angle shot to quantify the regional proton density, allowing perfusion to be expressed as density-normalized perfusion in ml/min/g. Neither mean proton density (hypoxia, 0.46(0.18) g(water)/cm$^3$, normoxia, 0.47(0.18) g(water)/cm$^3$, hyperoxia, 0.48(0.17) g(water)/cm$^3$, p = 0.28, mean(standard deviation)) nor mean density-normalized perfusion (hypoxia, 4.89(2.13) ml/min/g, normoxia, 4.94(1.88) ml/min/g, hyperoxia, 5.32(1.83) ml/min/g, p=0.72) was significantly different between conditions in either imaging plane. Similarly perfusion heterogeneity as measured by relative dispersion (hypoxia, 0.74(0.16), normoxia, 0.74(0.10), hyperoxia, 0.76(0.18), p = 0.97), fractal dimension (hypoxia, 1.21(0.04), normoxia, 1.19(0.03), hyperoxia, 1.20(0.04), p = 0.07), log normal shape parameter (hypoxia, 0.62(0.11), normoxia, 0.72(0.11), hyperoxia, 0.70(0.13), p = 0.07), and geometric standard deviation (hypoxia, 1.88(0.20), normoxia, 2.07(0.24), hyperoxia, 2.02(0.28), p = 0.11) were also not different. The study concluded that hypoxic pulmonary vasoconstriction does not affect pulmonary perfusion heterogeneity in normoxia in the normal supine human lung.

## 5.2 Introduction

Several studies have shown that the distribution of pulmonary blood flow is not spatially uniform even in the normal human lung [31, 33, 37, 41, 43]. The nature of the observed pulmonary blood flow heterogeneity is thought to be partially due to gravitational factors [54] influenced by posture [43] and also vascular branching structure [2, 9, 18, 19] that are partly under genetic control [22]. In dogs, Glenny *et al.* [19] estimated that contributions of posture and vascular structure to the total variability of pulmonary blood flow were 7.8±0.6% and 83.8±8.4%, respectively. In addition, dynamic factors such as hypoxic-pulmonary vasoconstriction may also contribute to heterogeneity when the spatial distribution of ventilation is nonuniform. Several animal studies using either a fine aerosol inhaled into the alveoli or computed tomography have also shown that ventilation is not spatially uniform [2, 39] and that the heterogeneity of ventilation was comparable to that described for blood flow [47]. Hypoxic pulmonary vasoconstriction

increases vascular resistance in regions of low alveolar ventilation resulting in a correspondingly low perfusion [12]. Thus, any alteration in regional vascular resistance due to hypoxic pulmonary vasoconstriction in regions of low alveolar $P_{O_2}$ ($P_{A_{O_2}}$) may affect the spatial distribution of pulmonary perfusion. Studies evaluating the effect of hypoxia on the distribution of pulmonary blood flow have shown variable results. For example, magnetic resonance imaging studies in normal human subjects exposed to normobaric hypoxia have been reported to show either increased perfusion heterogeneity [13] or no change [30]. Similarly, in animal studies using microspheres injected into the pulmonary vasculature, hypoxia results in various effects depending on species and postures. Hypoxia resulted in an increase in pulmonary perfusion heterogeneity in prone pigs and dogs [36, 49], while a decrease in heterogeneity was observed in pigs in the supine posture [29]. It was hypothesized that part of the perfusion heterogeneity observed in humans within an isogravitational lung plane is due to regional hypoxic pulmonary vasoconstriction. If this were the case, breathing a mild hyperoxic gas mixture ($F_IO_2$ = 0.3) would be expected to raise local $P_{A_{O_2}}$ and abolish any localized hypoxic pulmonary vasoconstriction resulting in a more uniform spatial distribution of pulmonary blood flow. Conversely, mild hypoxia ($F_IO_2$ = 0.125) would be expected to decrease $P_{A_{O_2}}$ throughout the lung compared to normoxia and lead to increased pulmonary blood flow heterogeneity. To test the hypothesis, the distribution of pulmonary blood flow in supine healthy subjects was measured using a functional lung magnetic resonance (MR) imaging technique known as arterial spin labeling (ASL) during normoxia ($F_IO_2$ = 0.21: room air), hypoxia ($F_IO_2$ = 0.125), and hyperoxia ($F_IO_2$ = 0.30). These oxygen concentrations were chosen because an inspired oxygen fraction of 12.5% results in an alveolar partial oxygen pressure ($P_{A_{O_2}}$) of 40-50 Torr, which is enough to induce hypoxic pulmonary vasoconstriction and increase pulmonary vascular resistance [5, 6]. Conversely, an inspired oxygen fraction of 30% results in a $P_{A_{O_2}} > 160$ Torr, which is sufficiently high to abolish the hypoxic pulmonary vasoconstriction [5, 6, 44], but is not expected to produce atelectasis [1, 52].

## 5.3 Method

### 5.3.1 Subjects

This study was approved by the Human Subjects Research Protection Program of the University of California, San Diego. Six healthy subjects (2 female, 4 male, age = 29(7) years old, height = 172(4) cm, and weight = 67(4) kg) participated after giving informed consent, and undergoing screening using pulmonary and MRI safety questionnaires, and a medical history and physical exam. Pulmonary function testing was performed using spirometry (VRS-2000, S&D Instrument Company, Doylestown, PA).

### 5.3.2 Data Collection

Each subject underwent MRI scanning using a Vision 1.5 T whole-body MR Scanner (Siemens Medical Systems, Erlangen, Germany) and the measurements of each subject were conducted within a single imaging session. All sequence parameters were kept within U.S. Food and Drug Administration guidelines for clinical magnetic resonance examinations. Subjects were positioned supine in the scanner with a phased-array torso coil over the chest, while breathing through a full face mask (7600 Series Oro-Nasal Mask7600 Series, Hans Rudolph) equipped with a non re-breathing valve (Hans Rudolph). Gases of $F_IO_2 = 0.21$ (normoxia), $F_IO_2 = 0.125$ (hypoxia), and $F_IO_2 = 0.30$ (hyperoxia) were presented in balanced order between subjects. After allowing the subject to breath a particular gas for 20 minutes to establish steady state conditions, MR measurements of perfusion, proton density and coil correction data (all described below) were acquired. We chose 20 minutes duration of exposure to the gas before imaging because the initiation of hypoxic pulmonary vasoconstriction response occurs within seconds and the response to alveolar hypoxia is near maximal within 20 minutes in the human lung [50]. For this project instead of silicon phantom, a water phantom doped with gadolinium (Berlex Imaging, Magnevist ®, 469 mg/mL gadopentetate dimeglumine, 1:5500 dilution) to $T_1$ and $T_2$ values approximating that of blood, was placed next to the subject within the field of view, for absolute quantification of pulmonary perfu-

sion and proton density (see below). A single 15 mm image slice was acquired in the right lung during an 8 second breathhold at functional residual capacity, in both the sagittal and coronal planes, for each inspired oxygen concentration. Data were acquired in triplicate for each slice and $F_IO_2$ and the results were averaged following quantification.

**Quantification of cardiac output with Cine Phase Contrast**

Cardiac output was estimated from the left ventricular output measured as volume of blood flowing in the aorta during each cardiac cycle, using through-plane velocity encoding for the data acquisition [16]. The flow volume per cardiac cycle was calculated as the mean forward velocity through a region of interest (ROI) positioned distal to the aortic valve, multiplied by the cross-sectional area of the ROI on each cine frame. This was then multiplied by the heart rate to give a cardiac output in ml per minute.

**Quantification of regional pulmonary perfusion with ASL**

Chapter 2 describes the way of measuring the regional pulmonary blood flow in unites of mL(blood)/min/$cm^3$(Voxel). ASL-FAIRER sequence with a half-Fourier acquisition single-shot turbo spin-echo (HASTE) imaging scheme was utilized. During each measurement, two cardiac-gated images of each lung slice are acquired during a single breath-hold. The signal of blood prepared in a different way in the two images.

**Quantification of regional lung density and coil sensitivity**

Proton density images were also acquired in the same image slice. In this project, Fast Low-Angle Shot (FLASH) sequence was used. In addition, coil sensitivity profile was also measured using a paired of density images acquired spatially using homogeneous body coil and inhomogeneous torso coil. Sequence parameters were repetition time TR = 6 msec, echo time TE = 0.9 msec, flip angle $\alpha = 4^\circ$, slice thickness = 15 mm, and image size 128 x 128. In each image so obtained,

the resulting signal after correcting for coil inhomogeneity in each voxel was referenced to the signal derived from the water phantom (which is by definition 100% water) to obtain regional lung proton (water) density in units of g water/cm3 lung. The resulting proton density was then calculated by correcting the signal for the rapid $T_2^*$ decay of signal from the lungs based on published values of $T_2^*$ (1.43(0.41) msec [25]). For simplicity, this proton density which reflects both tissue (and blood) is subsequently referred to in this manuscript as density.

**Density-normalized Perfusion**

Perfusion expressed in units of mL/min/g(water) can be approximated by dividing the image acquired by ASL, which has the units of mL/min/$cm^3$(lung), by the FLASH image of proton density (in g(water)/$cm^3$(lung)) to give perfusion in mL/min/g(water: tissue + blood). A mutual-information-based technique that included translation and rotation was utilized to register the two ASL and FLASH images [31, 45] and then the ASL perfusion image was divided by the FLASH proton density image on a voxel-by-voxel basis. To the extent that regional lung density is reflected by the water content, this density-normalized perfusion then reflects perfusion per gram of lung tissue. For simplicity, this density-normalized perfusion is referred to as perfusion in this manuscript.

### 5.3.3 Data Analysis

For each image acquired as described above (lung proton density and density-normalized perfusion), the data were analyzed in the following manner. For each image, mean density and density-normalized perfusion were calculated. In addition, in order to compare the effect of different inspired oxygen concentrations on perfusion heterogeneity, three different indices of perfusion heterogeneity were calculated as described in Chapter 2 in both coronal and sagittal planes. These were 1) relative dispersion (RD), also known as the coefficient of variation, a global scale of heterogeneity, defined as the ratio of the standard deviation to the mean perfusion where the larger the relative dispersion, the more heterogeneous the distribution; 2) fractal dimension, $D_s$, an index of the spatial heterogeneity which is

scale independent, where fractal dimension varies between 1.0 (homogeneous) and 1.5 (spatially random); and 3) The shape parameter $\sigma$ also global scales of heterogeneity, but based on lognormal model distribution. In addition to the shape parameter, geometric standard deviation denoted as $e^{\sigma}$ was also introduced. Shape parameter and geometric standard deviation are derived from the same lognormal model of perfusion distribution, however they are described in the different scale. In sagittal slices, the effect of different inspired oxygen concentrations on the vertical distribution of density-normalized perfusion was also measured. The lung of each subject was divided in the anterior posterior direction into three regions, dependent, middle, and non-dependent. Mean density-normalized perfusion of each region was compared for the different inspired oxygen concentrations. ANOVA (Statview, 5.0 SAS Institute Inc. Cary, North Carolina) for repeated measures was used to statistically evaluate changes in the major dependent variables over the three inspired oxygen concentrations (3 levels: hypoxia, normoxia, and hyperoxia). Dependent variables for this analysis were lung density as measured by FLASH in units of g (water)/$cm^3$ (lung), and density-normalized perfusion (mL/min/g) and associated measurements of perfusion heterogeneity. Where overall significance occurred, post hoc testing was conducted using Students t testing. All data are presented as means(SD); the null-hypothesis (no-effect) was rejected for p ¡ 0.05, two tailed.

## 5.4 Results

Six healthy subjects participated in this study (4 males, 2 females) after signing informed consent. All of the pulmonary function data were within normal limits. [forced vital capacity (FVC) = 5.0(0.8) liters, FVC % predicted = 101(8), forced expiratory volume in 1 sec ($FEV_1$) = 4.1(0.6) liters, ($FEV_1$) % predicted = 101(8), $FEV_1$/FVC = 83(4), and $FEV_1$/FVC % predicted = 98(4)). Physiological data for each inspired oxygen concentration are shown in Table 5.1. As expected, arterial oxygen saturation measured by pulse oximetry ($Sp_{O_2}$) was significantly reduced by hypoxia ($p < 0.001$), but unchanged ($p = 0.73$) by hyperoxia

**Table 5.1**: Physiological data for each inspired oxygen. Values are Mean (Standard Deviation); Significant difference from normoxia and hyperoxia. * $p<0.05$, † $p<0.001$ on post hoc test.
*Hypoxic Pulmonary Vasoconstriction Does Not Contribute to Pulmonary Blood Flow Heterogeneity in Normoxia in Normal Supine Humans*, 2009. by Arai *et al*

| | Oxygen Concentration | | | |
|---|---|---|---|---|
| | Hypoxia (12.5%) | Normoxia (21%) | Hyperoxia (30%) | Main Effect |
| $Sp_{O_2}$, % | 84.8(5.4)† | 97.3(1.2) | 97.9(0.9) | <0.001 |
| Heart rate, beats/min | 64(8)* | 58(8) | 57(7) | <0.05 |
| Cardiac output, liter/min | 6.0(0.8)* | 5.4(0.9) | 5.5(1.6) | NS |

compared with normoxia (hypoxia, 84.8(5.4)%; normoxia, 97.3(1.2)%; hyperoxia, 97.9(0.9)%). Heart rate was significantly increased during hypoxia ($p < 0.05$), but unchanged during hyperoxia ($p = 0.67$), compared with normoxia (hypoxia, 64(8); normoxia, 58(8); hyperoxia, 57(7)). Cardiac output measured by cine phase contrast showed a small increase in hypoxia compared to normoxia and hyperoxia but this was not statistically significant (hypoxia, 6.0(0.8) liter/min; normoxia, 5.4(0.9) liter/min; hyperoxia, 5.5(1.6) liter/min, $p = 0.29$).

Figure 5.1 shows the distribution of pulmonary perfusion, proton density, and density-normalized perfusion during normoxia in a sagittal (1) and coronal (2) slice from a representative subject. Images of the coronal slice are shown on the bottom and images of the sagittal slice are shown on top. Images in the first column represent a pulmonary blood flow map where the signal intensity of the images scales as a function of perfusion (ml blood/min/cm3) as measured by ASL (A1, A2). Images in the second column represent the proton density map measured by FLASH (B1, B2), with signal intensity proportional to proton density (g water/cm3). Images in the third column are density-normalized perfusion data (C1, C2), which are obtained by division of the ASL perfusion image by the FLASH proton density image (ml/min/g).

Mean density and density-normalized perfusion data are given in Figure 5.2. Mean proton density was greater in the coronal than in the sagittal plane, reflecting the dependent location of the coronal plane that was imaged. These

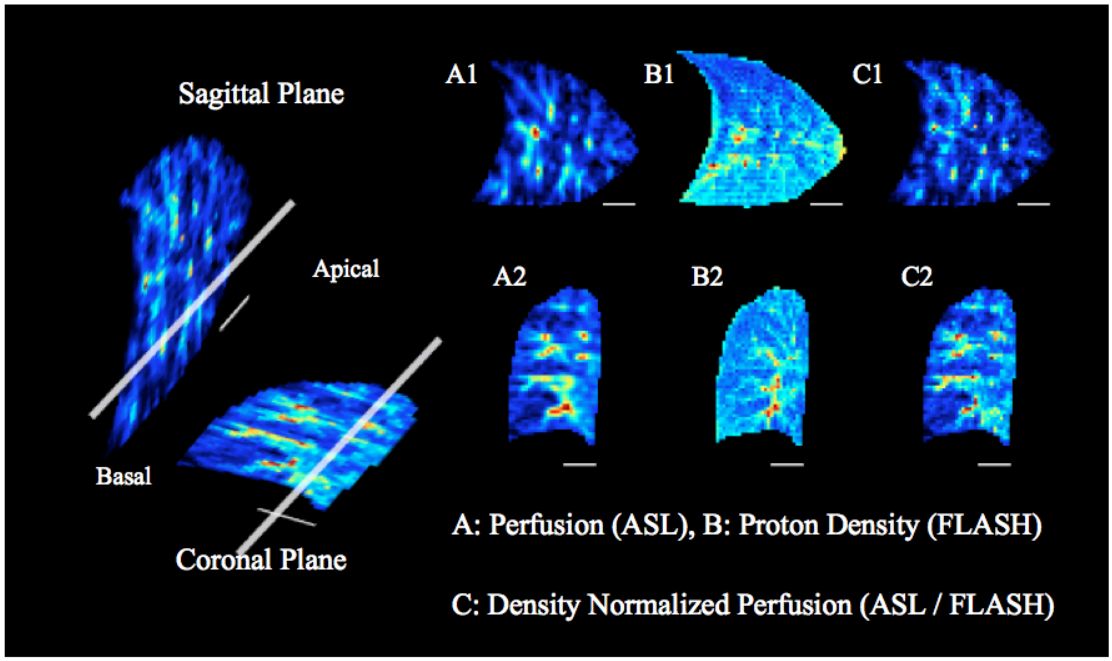


**Figure 5.1**: Representative MR lung images from the two anatomical planes (sagittal and coronal). The intersections of each plane with the other plane are indicated by the long white lines (left hand side). The short solid, white bar represents a 3 cm scale. Images of A1 and A2 represent perfusion measured by arterial spin labeling (ASL) where the signal intensity is proportional to perfusion (mL(blood)/min/cm$^3$(lung)). Images of B1 and B2 represent proton density measured by fast low angle shot (FLASH) where the signal intensity is proportional to proton density (g(water)/cm$^3$). Images of C1 and C2 are density-normalized perfusion calculated by division of the ASL image by the FLASH image (mL/min/g). Density-normalized perfusion represents the perfusion per gram of lung water, which is from tissue and blood combined. *Hypoxic Pulmonary Vasoconstriction Does Not Contribute to Pulmonary Blood Flow Heterogeneity in Normoxia in Normal Supine Humans*, 2009. by Arai *et al*

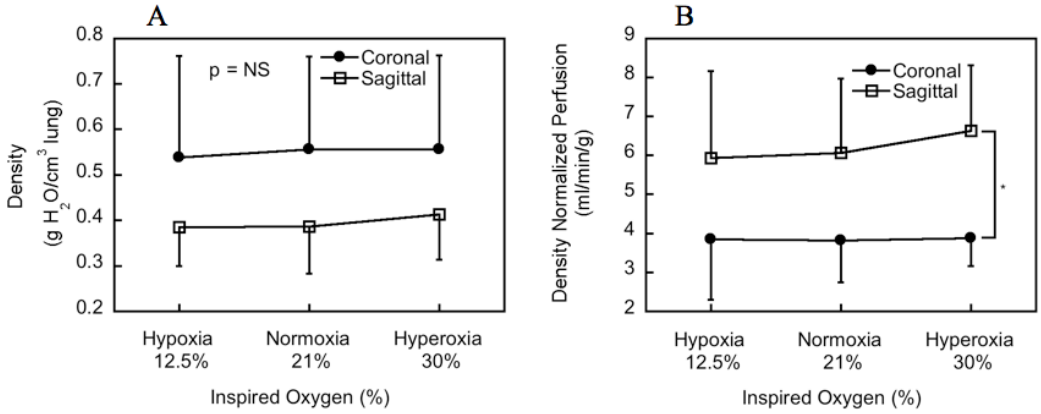


**Figure 5.2**: Effect of three different inspired oxygen concentrations on proton density (A) and density-normalized perfusion (B). Although mean proton density was greater in the coronal than the sagittal plane, reflecting the dependent location of the coronal plane, these changes did not reach statistical significance. Mean density-normalized perfusion in sagittal plane was significantly greater than in coronal plane ($p < 0.05$). Neither mean proton density (A) nor mean density-normalized perfusion (B) was significantly changed by the different concentrations of inspired oxygen.
*Hypoxic Pulmonary Vasoconstriction Does Not Contribute to Pulmonary Blood Flow Heterogeneity in Normoxia in Normal Supine Humans*, 2009. by Arai *et al*

changes did not reach statistical significance (coronal, 0.55(0.20) g water/cm$^3$, sagittal 0.40(0.09) g water/cm$^3$, p = 0.07; Figure 5.2A). The mean proton density was not altered by the different concentrations of oxygen (hypoxia, 0.46(0.18) g water/cm3, normoxia, 0.47(0.18) g water/cm3, hyperoxia, 0.48(0.17) g water/cm3, p = 0.28; Figure 5.2A). Mean density-normalized perfusion in the sagittal plane was significantly greater than in the coronal plane (coronal, 3.89(1.12) mL/min/g, sagittal, 6.21(1.86) mL/min/g, p ¡ 0.05; Figure 5.2B) and was unchanged by inspired oxygen concentration (hypoxia, 4.89(2.13) mL/min/g, normoxia, 4.94(1.88) mL/min/g, hyperoxia, 5.32(1.83) mL/min/g, p = 0.72; 5.2B).

Figure 5.3 shows the effect of different inspired oxygen concentrations and lung slice orientations on indices of pulmonary blood flow heterogeneity. The relative dispersion was not altered by orientation or oxygen concentrations, in either coronal or sagittal planes (Orientation: coronal, 0.73(0.13), sagittal, 0.77(0.16), p = 0.16; $F_IO_2$: hypoxia, 0.74(0.16), normoxia, 0.74(0.10), hyperoxia, 0.76(0.18), p = 0.97; Figure 5.3A). Similarly, the fractal dimension was not different between coronal and sagittal planes, and between inspired oxygen concentrations (Orientation: coronal, 1.19(0.04), sagittal, 1.21(0.03), p = 0.17; $F_IO_2$: hypoxia, 1.21(0.04), normoxia, 1.19(0.03), hyperoxia, 1.20(0.04), p = 0.07; Figure 5.3B). The shape parameter of lognormal model distributions and geometric standard deviation also did not show any difference between orientations or inspired oxygen concentrations (shape parameter, Orientation: coronal, 0.68(0.11), sagittal, 0.68(0.12), p = 0.98; $F_IO_2$: hypoxia, 0.62(0.11), normoxia, 0.72(0.11), hyperoxia, 0.70(0.13), p = 0.07; Figure 5.3C, and geometric standard deviation, Orientation: coronal, 1.99(0.25), sagittal, 1.99(0.25), p = 1.00; $F_IO_2$: hypoxia, 1.88(0.20), normoxia, 2.07(0.24), hyperoxia, 2.02(0.28), p = 0.11; Figure 5.3D).

Figure 5.4 shows vertical distribution of density-normalized perfusion into three regions: dependent, middle, and non-dependent (dependent, 5.21(1.86) mL per min per g, middle, 7.49(2.31) mL per min per g, non-dependent, 5.74(1.59) mL / min / g). Density-normalized perfusion in the middle region was significantly greater than in either the dependent or non-dependent region ($p < 0.05$) for all inspired oxygen concentrations. However, no significant difference was observed

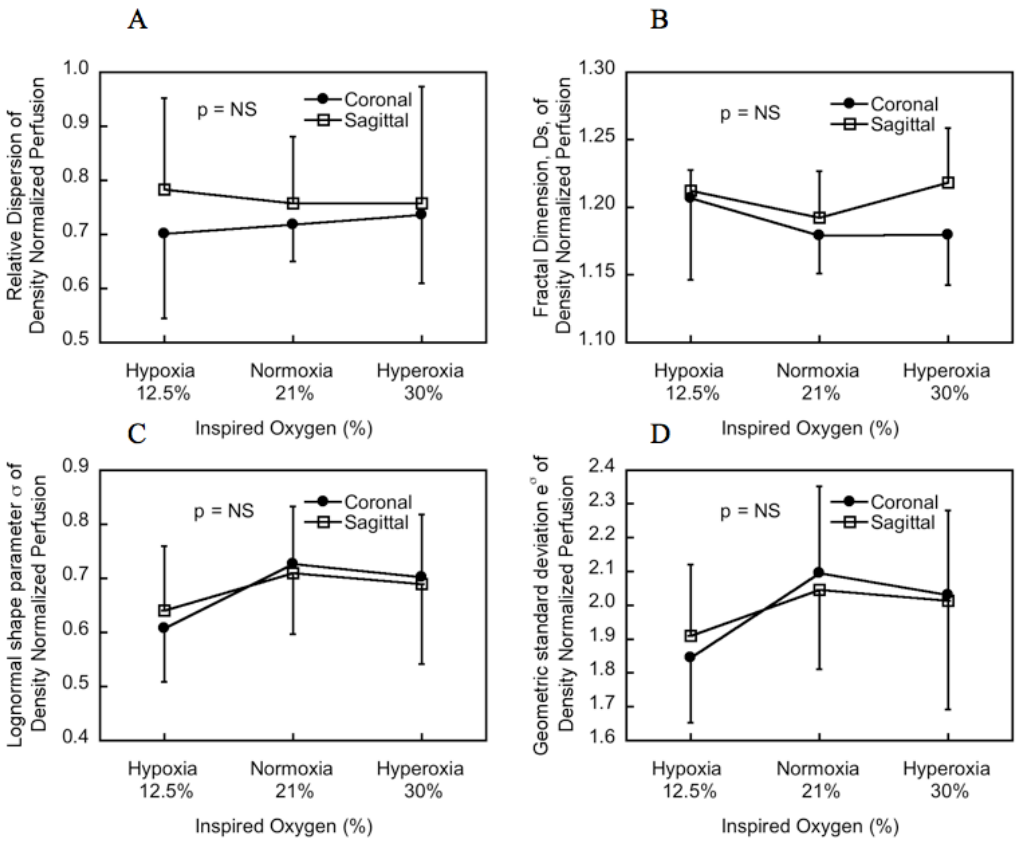


**Figure 5.3**: Effect of three different inspired oxygen concentrations on pulmonary blood flow heterogeneity. The relative dispersion (A), fractal dimension (B), and shape parameter (C) of density-normalized perfusion were not significantly different between sagittal and coronal planes and were not changed by the inspired oxygen concentrations.
*Hypoxic Pulmonary Vasoconstriction Does Not Contribute to Pulmonary Blood Flow Heterogeneity in Normoxia in Normal Supine Humans*, 2009. by Arai *et al*

between dependent and non-dependent parts of the lung (p = 0.28). Inspired oxygen concentration did not affect the vertical distribution of density-normalized perfusion (hypoxia, 5.82(2.34) mL/min/g, normoxia, 6.04(2.16) mL/min/g, hyperoxia, 6.58(1.98) mL/min/g, p = 0.39). There was also no significant interaction effect between the three regions and inspired oxygen concentration (p = 0.51).

## 5.5 Discussion

The results of this MR imaging study indicate that in normoxia, hypoxic pulmonary vasoconstriction does not have a significant effect on pulmonary blood flow heterogeneity in the healthy supine lung. In fact, contrary to the hypotheses there was a tendency for some measures of blood flow heterogeneity to be more uniform in hypoxia and unchanged in hyperoxia. These findings are in keeping with previous studies, which have suggested a predominant contribution of vascular structure to pulmonary blood flow heterogeneity both in animal [2, 18, 20, 28] and human lungs [9]. For example, microsphere studies in both supine pigs [29] and in prone dogs [36] during hyperoxia do not show significant change in perfusion heterogeneity compared to normoxia. Similarly, in a bilateral ventilation study in dogs [38] in which the left lung was ventilated with hypoxic inspiratory gas and the right lung simultaneously received hyperoxic gas, there was no alteration of regional distribution of pulmonary blood flow in hyperoxic side of lung. In keeping with the present study, Glenny and his co-workers [21] have also shown that pulmonary perfusion heterogeneity (measured as by relative dispersion) was not altered in baboon lung by administration of prostacyclin ($PGI_2$), which acts to reduce pulmonary vasomotor tone. Despite these findings, which suggest that alterations in regional vasomotor tone by hyperoxia or receptor blockade do not have a significant effect on pulmonary perfusion heterogeneity in the normal lung, there are also some evidences to the contrary. For example Melsom *et al.* [39] observed that hyperoxia ($F_IO_2 = 0.40$) altered the regional distribution of pulmonary perfusion compared with normoxia and decreased the correlation in flow between identical locations in sheep lung under the two conditions. This effect was only

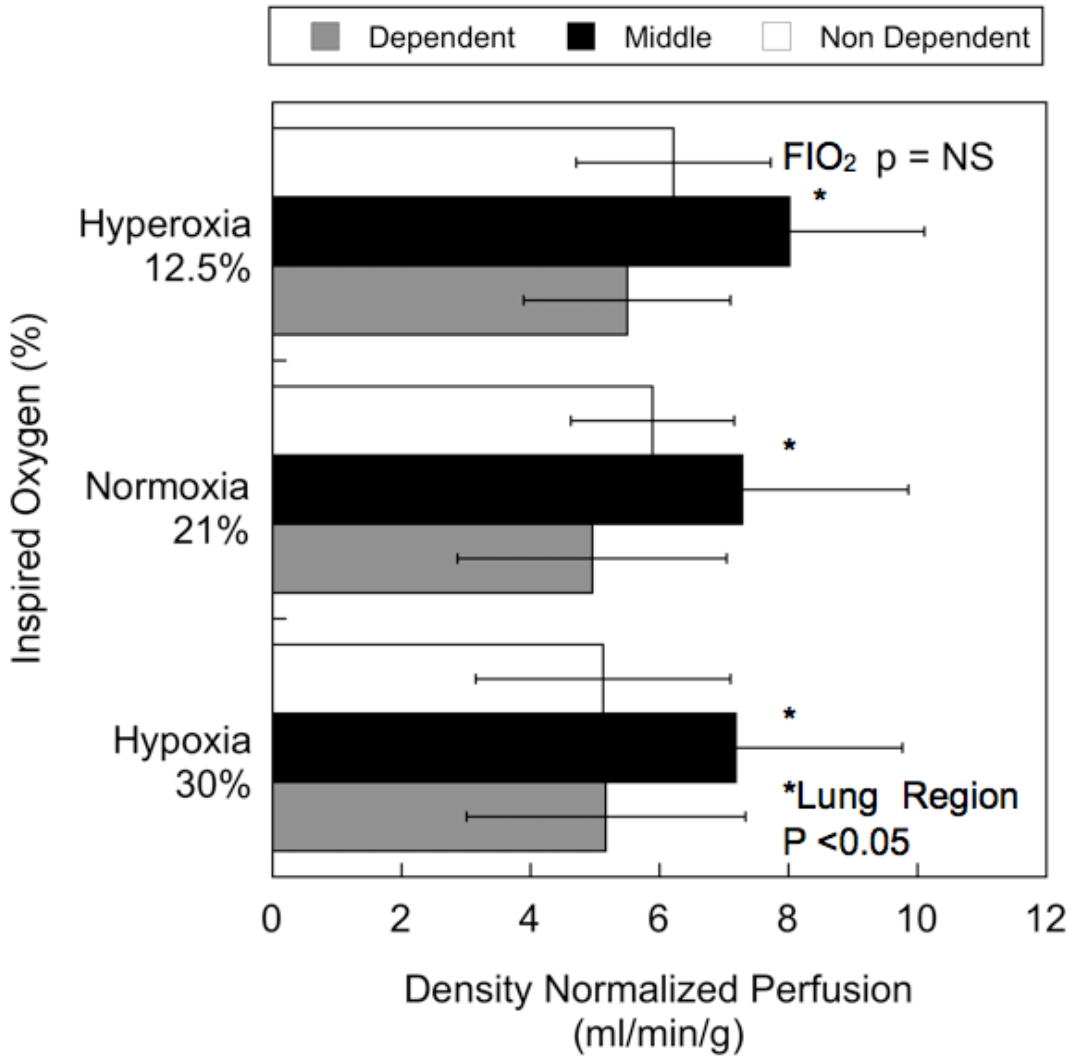


**Figure 5.4**: Effect of the different oxygen concentrations on vertical distribution of density-normalized perfusion. Density-normalized perfusion in the middle region was significantly greater than in either the dependent or non-dependent region (*$p < 0.05$) across the three different inspired oxygen concentrations. Inspired oxygen concentration did not significantly affect the vertical distribution of density-normalized perfusion, suggesting that on a gross scale the internal distribution of density-normalized perfusion was independent of inspired oxygen concentration. There was also no significant interaction effect between the three regions and inspired oxygen concentration ($p = 0.51$).
*Hypoxic Pulmonary Vasoconstriction Does Not Contribute to Pulmonary Blood Flow Heterogeneity in Normoxia in Normal Supine Humans*, 2009. by Arai *et al*

transiently observed after 10 minutes exposure to hyperoxia and disappeared by 150 minutes. In the present study, hypoxia also did not cause any alterations pulmonary blood flow heterogeneity. Importantly, these findings are consistent with the previous work done by UCSD pulmonary imaging lab where only subjects with a history of high altitude pulmonary edema (HAPE) showed significant increase in pulmonary blood flow heterogeneity in response to hypoxia [30]. In subjects without a history of HAPE, perfusion heterogeneity did not change significantly, although as with the present study there was a tendency for blood flow to become slightly more uniform in response to 12.5% oxygen [30]. However this finding is not universally reported by others [13]. The effects of hypoxia on pulmonary blood flow heterogeneity have also been investigated using animals such as pigs [29, 49], and dogs [36]. However, the different effects of hypoxia on pulmonary blood flow heterogeneity need to be evaluated considering not only the differing oxygen concentrations, but also differences in posture and species. Characteristics of both pulmonary blood flow and the response to hypoxia are known to be different between postures in humans [41, 43, 47] and animals [2, 18, 19]. For example, in pigs pulmonary blood flow heterogeneity measured by relative dispersion decreased during hypoxia [29] when the pig was supine but not in prone posture [49]. In the human lung, little difference in pulmonary blood flow heterogeneity between prone and supine posture [41, 45] has been reported although this has not always been found [43]. However, the human lung differs from animal lung in that the active posture of humans is mainly upright whereas the usual posture of most animals is prone, and this may account for some of the difference. Moreover, differences in the pulmonary vascular response of the species studied may also contribute to the differing responses between studies. The pig is well known for a brisk hypoxic response perhaps [34] because of the lack of collateral ventilation [35] and a thick pulmonary vascular smooth muscle wall [51]. By contrast, the dog is known to have a minimal pulmonary vascular response to hypoxia [51].

### 5.5.1 Re-distribution of pulmonary blood flow

One of the notable effects of hypoxia in the lung is an increase in pulmonary vascular resistance [12] and pulmonary artery pressure [14, 40] as a result of hypoxic pulmonary vasoconstriction. Because of the increase in pulmonary artery pressure and heterogeneous distribution of hypoxic pulmonary vasoconstriction throughout lung, pulmonary blood flow distribution is known to be altered on a gross scale in both animal [29, 36, 49] and HAPE-susceptible human lungs [23]. The site of redistribution and recruitment is in the capillary bed [24, 53], which acts to increase diffusing capacity [10] via an increase in the gas exchange surface area [11]. In this study, vertical redistribution of pulmonary blood flow (towards the anterior part of the lung in the supine posture) as a result of hypoxia-induced increases in pulmonary arterial pressure was not observed (Figure. 5.4). In supine posture the vertical height of lung is 15 cm and almost 50% of lung is below the left atrium [15]. Assuming the baseline pulmonary arterial pressure is 10-13 mmHg (23, 86) this leads to the conclusion that the human lung in a supine posture is almost all under zone 3 conditions [54]. Thus even if pulmonary artery pressure increased to 25 mmHg, little effect would be expected on the vertical distribution of pulmonary blood flow. Hanaoka *et al.* [23] have reported that pulmonary blood flow in the supine posture was shifted from basal to apical lung regions during hypoxia in HAPE-susceptible subjects, but not in normal subjects, consistent with data from the present study. In animal studies, Capen and Wagner [11] reported that hypoxia induced recruitment redistributed pulmonary blood flow toward upper lung in dogs, causing an increase in gas exchange surface area. A similar increase in regional pulmonary circulation to upper lung regions have also been reported in sheep [42]. Those earlier studies concluded that the increase in pulmonary artery pressure increased flow against the vertical hydrostatic pressure gradient. However, in microsphere studies of dogs and pigs, regardless of species and posture, it has been shown that hypoxia redistributes pulmonary blood flow to the dorsal caudal lung, which is the most non-dependent lung region in the normal awake quadruped posture [29, 36, 49].

### 5.5.2 Indices of pulmonary blood flow heterogeneity

Relative dispersion showed no significant change between different inspired oxygen levels (p = 0.97, Figure 5.3A), but the shape parameter showed a tendency for pulmonary perfusion to become more uniform (p = 0.07, Figure 5.3C) and the fractal dimension to be more heterogeneous during hypoxia (p = 0.07, Figure 5.3B). Although relative dispersion and shape parameter are global scales of heterogeneity of blood flow, because of the long tail characteristics of lognormal distributions, the shape parameter is relatively insensitive to high signal representing blood flow in large vessels. The tendency of the shape parameter to become somewhat more uniform in hypoxia in spite of little change in relative dispersion implies blood flow in the small vessels became more uniform during hypoxia. This would be expected from hypoxia induced vascular recruitment [24]. Moreover, unlike the spatially independent nature of the other indices, the fractal dimension, $D_s$ represents the regional self-similarity of pulmonary blood flow distribution as a function of the scale of resolution [17]. The trend of increasing fractal dimension in hypoxia implies a more random regional distribution of pulmonary blood flow. Thus, taken together, hypoxia may have caused pulmonary blood flow in poorly perfused regions to become more uniform, but spatial relocation of pulmonary blood flow may have occurred randomly.

### 5.5.3 Image planes

Although there was a trend for mean proton density to be greater in the coronal than the sagittal plane, these differences were not statistically significant (Figure 5.2A). We selected the coronal imaging slices in a plane that encompassed the posterior one-third of the aorta (see Figure 5.1), which were located in the relatively dependent part of lung where proton density is high [7, 31]. However, the sagittal plane encompasses all of the gravitational planes, and consequently the proton density, which varies with height from the most dependent lung, is averaged over the vertical height. Thus, depending on the relative dependent location of the coronal plane, density in this plane may be greater than the average of the sagittal plane. However, mean density-normalized perfusion in the sagittal plane

was significantly greater than in the coronal plane (Figure 5.2B), which also can be explained by the location of the image slices. In the most dependent part of lung, increased tissue density compresses extra-alveolar vessels resulting in increased resistance (so-called zone 4) [28, 31, 32] and reducing flow.

### 5.5.4 Critique of methods

Our study focused solely on the perfusion side of pulmonary gas exchange. Clearly gas exchange depends on both ventilation and perfusion. However, the change in distribution of ventilation due to different concentrations of oxygen is known to be much less than that of the change in perfusion [39]. One issue that needs to be addressed is whether this study had adequate statistical power to support the conclusion reached, particularly in light of the small number of subjects studied. The repeated measures design of this study, where each subject acts as their own control combined with a very high reliability of measured of perfusion heterogeneity [30] ensures excellent statistical power to detect a difference in perfusion heterogeneity with the different interventions, even if none were observed in the present study. For example, in order for the observed difference in relative dispersion of 0.74 and 0.76 between normoxia and hyperoxia to be statistically significant (if it in fact was) at p ¡ 0.05, post hoc power calculations reveal that at least 200 subjects would be required. Thus any difference is biologically very small. The arterial $CO_2$ during the study was not monitored. It might be expected to have a confounding effect since hypercapnima has a vasoconstrictive stimulus on the pulmonary circulation. However, within the physiologically appropriate range (30 - 40 mmHg) the decrease in pulmonary blood flow dur to hypercapnia is $< 5\%$ [5]. Thus, the contribution of $CO_2$ tension ($P_{CO_2}$) to hypoxic pulmonary vasoconstriction is a very minor effect compared with that of alveolar hypoxia. In addition, in a study in which subjects lay quietly supine breathing tha same gas mixture as the present study, arterial $P_{CO_2}$ ($Pa_{CO_2}$) showed minimal change. [$F_IO_2 = 0.125$, $Pa_{CO_2} = 36.4(1.7)$ mmHg; $F_IO_2 = 0.21$, $Pa_{CO_2} = 38.7(1.5)$ mmHg; $F_IO_2 = 0.30$, $Pa_{CO_2} = 38.4(2.9)$ mmHg]. Thus, the effect of the small alteration of $Pa_{CO_2}$ is physiologically unimportant in this context. This study also could have

been strengthened if measurements of pulmonary artery pressure to document the extent of hypoxic pulmonary vasoconstriction were acquired. Unfortunately the MRI techniques to measure pulmonary arterial pressure are unreliable [48] and Swan-Ganz catheters are a contraindication to MRI scanning. Non-invasive measurements such as echocardiography would require interrupting the study by taking a subject out of the scanner (and indeed out of the scanner room). Movement of the subject would risk mis-registration of the images, introducing a source of significant error. It is possible that that subjects of this study had exceptionally modest pulmonary vascular responses to hypoxia. However, since an increase in pulmonary artery pressure with alveolar hypoxia has been reported in virtually all normal subjects [14, 40], it is expected that that the subjects of this study had at least a small response to hypoxia. Another possibility is that the lack of significant findings are due to a lack of sensitivity of measurements. However, the technique has been shown in the past to be highly sensitive to interventions affecting pulmonary perfusion, thus it is expected that the lack of changes in the present study are not due to lack of sensitivity of the technique. For example, the relative dispersion has also been shown to increase with age by approximately 0.1 per decade of age [37], consistent with the well documented changes in pulmonary function with aging . Also, one hour of 30 degree head down tilt, which increases pulmonary vascular pressures also caused a significant increase in pulmonary blood flow heterogeneity measured by relative dispersion [26].

## 5.6 Limitation and Future Direction

The experimental design of this study is limited by the need to restrict subject motion during image acquisition, requiring intermittent short breath-holds at a consistent lung volume. The position of the diaphragm in each image served as a visual landmark to assess lung volume reproducibility. However, it remains possible that small misalignments between perfusion and density images may remain even after passing inspection, thus introducing a potential for error into the calculation of density-normalized perfusion (DNP). Further, it should be noted that

as the density image only measures free protons (essentially water), there is an inherent assumption that lung tissue density and lung water density are similarly distributed. Finally, all images were exclusively obtained from the right lung to avoid imaging artifacts induced by cardiac motion. The right and left lungs should behave in a similar fashion for the purposes of this study. It is not expected that the observed effects of hypoxia and hyperoxia would only appear unilaterally.

The current ASL image post processing technique involves the application of a 35 % maximum-intensity threshold mask to remove conduit vessels (those not involved in actual slice perfusion) from the blood flow image, and Gaussian spatial smoothing as described in Chapter 2. The threshold intensity value was selected based on an *in silico* pulmonary circulation model developed by Burrowes *et al.* [8], whereby voxels above the 35 % max-intensity were found to predominantly reflect blood flow in pulmonary conduit blood vessels. The spatial smoothing, on the other hand, is effectively a Gaussian lowpass filter that helps remove small mis-registration between images, and produces an effective spatial resolution on the order of approximately five acini. In the case of this particular study, neither of these post-processing techniques was applied. While the inclusion of large vessel signal has been shown to lead to overestimation of perfusion heterogeneity measured by relative dispersion [27], the calculation of geometric standard deviation and shape parameter based on a lognormal model (given in Figure 5.3C and D) is not sensitive to the presence of these vessels. Similarly, it was not necessary to spatially smooth these data as we chose to model the pulmonary vasculature as a fractal set using fractal dimension. Fractal dimension, shown in Figure 5.3B, is a metric of structural complexity by examining how the detail within the structure changes along with the scale of observation. As the pulmonary vasculature is well described as a self-similar branching tree, its fractal dimension is only minimally affected by small-scale spatial smoothing. Furthermore, although measures of relative dispersion in this study could potentially be affected by choosing to forgo both the conduit vessel masking and spatial filtering steps (leading to potential overestimation of calculated relative dispersion), it should be noted that any systematic bias would similarly affect all three different $F_IO_2$ conditions. This has the effect

of preserving the validity of comparisons between conditions subject to the same systematic bias, if indeed any were present, and therefore potential issues related to ASL image post processing are unlikely to alter the conclusions of this study in a meaningful way.

This study was first published in *Journal of Applied Physiology* 2009 [3], and was selected for an editorial [46]. The conclusion of this study, that hypoxic pulmonary vasoconstriction did not have an effect on human pulmonary blood flow, has drawn attention from the pulmonary physiology research community. Furthering this work, Asadi *et al.* studied the effect of $F_IO_2$ on temporal variability and spatial distribution of pulmonary blood flow using 100 consecutive ASL images in approximately 20 min [4]. They concluded that the temporal fluctuation of pulmonary blood flow distribution was significantly increased with hypoxic challenge, while overall spatial heterogeneity (measured by relative dispersion) was unaltered. Their study highlighted that changes in pulmonary vasomotor tone, in response to different $F_IO_2$ gasses, may induce observable spatio-temporal dynamic changes in pulmonary perfusion before gross changes in overall perfusion heterogeneity. Such dynamic vascular responses may lead to methods of early detection in cases of pulmonary disease, such as pulmonary artery hypertension (PAH). PAH is a chronic disease without any effective treatments, and the majority of PAH is diagnosed in advanced stages after irreversible pulmonary vascular remodeling has occurred. It is clear to see why PAH is a particular case in which the importance of early detection has been strongly emphasized. These kinds of experimental designs, aimed at probing pulmonary vascular reactivity and dynamic response are crucial in furthering this goal.

## 5.7 Conclusion

This study concluded that in supine normoxic humans, the heterogeneity of pulmonary blood flow observed within an isogravitational plane was not due to hypoxic pulmonary vasoconstriction and gross redistribution of pulmonary blood flow both during hypoxia and hyperoxia was also not found. Thus, the results

of this study suggest that the observed heterogeneity of pulmonary blood flow is structural or gravitational in nature. However, dynamic changes in the vascular system may not strongly manifest as changes in overall spatial heterogeneity.

## 5.8 Acknowledgements

I thank my subjects for enthusiastic participation.

This work was supported by NIH HL081171, AHA 0540002N, NIH -1F32 HL078128, and Hl080203.

Chapter 5, in part, is a reprint of the material as it appears in J Appl Physiol 106(4), pp. 1057-64, 2009. Arai TJ; Henderson AC; Dubowitz DJ; Levin DL; Friedman PJ; Buxton RB; Prisk GK; Hopkins SR. The dissertation author was the first author of this publication.

## 5.9 Bibliography

[1] O. Akça, A. Podolsky, E. Eisenhuber, O. Panzer, H. Hetz, K. Lampl, F. X. Lackner, K. Wittmann, F. Grabenwoeger, A. Kurz, A. M. Schultz, C. Negishi, and D. I. Sessler. Comparable postoperative pulmonary atelectasis in patients given 30% or 80% oxygen during and 2 hours after colon resection. *Anesthesiology*, 91(4):991–998, 1999.

[2] W. A. Altemeier, S. McKinney, M. Krueger, and R. W. Glenny. Effect of posture on regional gas exchange in pigs. *Journal of applied physiology (Bethesda, Md. : 1985)*, 97(6):2104–2111, Dec 2004.

[3] T. J. Arai, A. C. Henderson, D. J. Dubowitz, D. L. Levin, P. J. Friedman, R. B. Buxton, G. K. Prisk, and S. R. Hopkins. Hypoxic pulmonary vasoconstriction does not contribute to pulmonary blood flow heterogeneity in normoxia in normal supine humans. *Journal of applied physiology (Bethesda, Md. : 1985)*, 106(4):1057–1064, Apr 2009.

[4] A. K. Asadi, M. V. Cronin, R. Carlos. Sá, R. J. Theilmann, S. Holverda, S. R. Hopkins, R. B. Buxton, and G. K. Prisk. Spatial-temporal dynamics of pulmonary blood flow in the healthy human lung in response to altered FIO2. *Journal of Applied Physiology*, 114(1):107–118, 2013.

[5] G. R. Barer, P. Howard, and J. W. Shaw. Stimulus-response curves for the pulmonary vascular bed to hypoxia and hypercapnia. *The Journal of physiology*, 211(1):139–155, Nov 1970.

[6] S. Brimioulle, P. Lejeune, J. L. Vachiéry, M. Delcroix, R. Hallemans, M. Leeman, and R. Naeije. Stimulus-response curve of hypoxic pulmonary vasoconstriction in intact dogs: effects of asa. *Journal of applied physiology (Bethesda, Md. : 1985)*, 77(1):476–480, Jul 1994.

[7] L. H. Brudin, C. G. Rhodes, S. O. Valind, P. Wollmer, and J. M. Hughes. Regional lung density and blood volume in nonsmoking and smoking subjects measured by pet. *Journal of applied physiology (Bethesda, Md. : 1985)*, 63(4):1324–1334, Oct 1987.

[8] K. S. Burrowes, R. B. Buxton, and G. K. Prisk. Assessing potential errors of MRI-based measurements of pulmonary blood flow using a detailed network flow model. *Journal of applied physiology (Bethesda, Md. : 1985)*, 113(1):130–141, Jul 2012.

[9] K. S. Burrowes and M. H. Tawhai. Computational predictions of pulmonary blood flow gradients: gravity versus structure. *Respiratory physiology & neurobiology*, 154(3):515–523, Dec 2006.

[10] R. L. Capen, L. P. Latham, and W. W. Wagner. Diffusing capacity of the lung during hypoxia: role of capillary recruitment. *Journal of applied physiology: respiratory, environmental and exercise physiology*, 50(1):165–171, Jan 1981.

[11] R. L. Capen and W. W. Wagner. Intrapulmonary blood flow redistribution during hypoxia increases gas exchange surface area. *Journal of applied physiology: respiratory, environmental and exercise physiology*, 52(6):1575–1580, Jun 1982.

[12] C. A. Dawson. Role of pulmonary vasomotion in physiology of the lung. *Physiological reviews*, 64(2):544–616, Apr 1984.

[13] C. Dehnert, F. Risse, S. Ley, T. A. Kuder, R. Buhmann, M. Puderbach, E. Menold, D. Mereles, H. U. Kauczor, P. Bärtsch, and C. Fink. Magnetic resonance imaging of uneven pulmonary perfusion in hypoxia in humans. *American journal of respiratory and critical care medicine*, 174(10):1132–1138, Nov 2006.

[14] J. T. Doyle, J. S. Wilson, and J. V. Warren. The pulmonary vascular responses to short-term hypoxia in human subjects. *Circulation*, 5(2):263–270, 1952.

[15] P. J Friedman, R. M Peters, M. C Botkin, J. E Brimm, and R. C Meltvedt. Estimation of the volume of lung below the left atrium using computed tomography. *Critical care medicine*, 14(3):182–187, 1986.

[16] P. D. Gatehouse, J. Keegan, L. A. Crowe, S. Masood, R. H. Mohiaddin, K. F. Kreitner, and D. N. Firmin. Applications of phase-contrast flow and velocity imaging in cardiovascular MRI. *European radiology*, 15(10):2172–2184, Oct 2005.

[17] R. W. Glenny. *Complexity in Structure and Function in the lung*, chapter Heterogeneity in the lung: concepts and measures., pages 571–609. Marcel Dekker, New York, 1998.

[18] R. W. Glenny, S. Bernard, H. T. Robertson, and M. P. Hlastala. Gravity is an important but secondary determinant of regional pulmonary blood flow in upright primates. *Journal of applied physiology (Bethesda, Md. : 1985)*, 86(2):623–632, Feb 1999.

[19] R. W. Glenny, W. J. Lamm, R. K. Albert, and H. T. Robertson. Gravity is a minor determinant of pulmonary blood flow distribution. *Journal of applied physiology (Bethesda, Md. : 1985)*, 71(2):620–629, Aug 1991.

[20] R. W. Glenny, L. Polissar, and H. T. Robertson. Relative contribution of gravity to pulmonary perfusion heterogeneity. *Journal of applied physiology (Bethesda, Md. : 1985)*, 71(6):2449–2452, Dec 1991.

[21] R. W. Glenny, H. T. Robertson, and M. P. Hlastala. Vasomotor tone does not affect perfusion heterogeneity and gas exchange in normal primate lungs during normoxia. *Journal of applied physiology (Bethesda, Md. : 1985)*, 89(6):2263–2267, Dec 2000.

[22] R. Glenny, S. Bernard, B. Neradilek, and N. Polissar. Quantifying the genetic influence on mammalian vascular tree structure. *Proceedings of the National Academy of Sciences of the United States of America*, 104(16):6858–6863, Apr 2007.

[23] M. Hanaoka, M. Tanaka, R. L. Ge, Y. Droma, A. Ito, T. Miyahara, T. Koizumi, K. Fujimoto, T. Fujii, T. Kobayashi, and K. Kubo. Hypoxia-induced pulmonary blood redistribution in subjects with a history of high-altitude pulmonary edema. *Circulation*, 101(12):1418–1422, Mar 2000.

[24] W. L. Hanson, J. D. Emhardt, J. P. Bartek, L. P. Latham, L. L. Checkley, R. L. Capen, and W. W. Wagner. Site of recruitment in the pulmonary microcirculation. *Journal of applied physiology (Bethesda, Md. : 1985)*, 66(5):2079–2083, May 1989.

[25] H. Hatabu, D. C. Alsop, J. Listerud, M. Bonnet, and W. B. Gefter. T2* and proton density measurement of normal human lung parenchyma using submillisecond echo time gradient echo magnetic resonance imaging. *European journal of radiology*, 29(3):245–252, Mar 1999.

[26] A. C. Henderson, D. L. Levin, S. R. Hopkins, I. M. Olfert, R. B. Buxton, and G. K. Prisk. Steep head-down tilt has persisting effects on the distribution of pulmonary blood flow. *Journal of applied physiology (Bethesda, Md. : 1985)*, 101(2):583–589, Aug 2006.

[27] A. C. Henderson, G. K. Prisk, D. L. Levin, S. R. Hopkins, and R. B. Buxton. Characterizing pulmonary blood flow distribution measured using arterial spin labeling. *NMR in biomedicine*, 22(10):1025–1035, Dec 2009.

[28] M. P. Hlastala and R. W. Glenny. Vascular structure determines pulmonary blood flow distribution. *News in physiological sciences : an international journal of physiology produced jointly by the International Union of Physiological Sciences and the American Physiological Society*, 14:182–186, Oct 1999.

[29] M. P. Hlastala, W. J. E. Lamm, A. Karp, N. L. Polissar, I. R. Starr, and R. W. Glenny. Spatial distribution of hypoxic pulmonary vasoconstriction in the supine pig. *Journal of applied physiology (Bethesda, Md. : 1985)*, 96(5):1589–1599, May 2004.

[30] S. R. Hopkins, J. Garg, D. S. Bolar, J. Balouch, and D. L. Levin. Pulmonary blood flow heterogeneity during hypoxia and high-altitude pulmonary edema. *American journal of respiratory and critical care medicine*, 171(1):83–87, Jan 2005.

[31] S. R. Hopkins, A. C. Henderson, D. L. Levin, K. Yamada, T. Arai, R. B. Buxton, and G. Kim Prisk. Vertical gradients in regional lung density and perfusion in the supine human lung: the slinky effect. *Journal of applied physiology (Bethesda, Md. : 1985)*, 103(1):240–248, Jul 2007.

[32] J. M. Hughes, J. B. Glazier, J. E. Maloney, and J. B. West. Effect of lung volume on the distribution of pulmonary blood flow in man. *Respiration physiology*, 4(1):58–72, Jan 1968.

[33] A. T. Jones, D. M. Hansell, and T. W. Evans. Pulmonary perfusion in supine and prone positions: an electron-beam computed tomography study. *Journal of applied physiology (Bethesda, Md. : 1985)*, 90(4):1342–1348, Apr 2001.

[34] A. Kleinsasser, D. L. Levin, A. Loeckinger, and S. R. Hopkins. A pig model of high altitude pulmonary edema. *High altitude medicine & biology*, 4(4):465–474, 2003.

[35] T. Kuriyama, L. P. Latham, L. D. Horwitz, J. T. Reeves, and W. W. Wagner. Role of collateral ventilation in ventilation-perfusion balance. *Journal of applied physiology: respiratory, environmental and exercise physiology*, 56(6):1500–1506, Jun 1984.

[36] W. J. E. Lamm, I. R. Starr, B. Neradilek, N. L. Polissar, R. W. Glenny, and M. P. Hlastala. Hypoxic pulmonary vasoconstriction is heterogeneously distributed in the prone dog. *Respiratory physiology & neurobiology*, 144(2-3):281–294, Dec 2004.

[37] D. L. Levin, R. B. Buxton, J. P. Spiess, T. Arai, J. Balouch, and S. R. Hopkins. Effects of age on pulmonary perfusion heterogeneity measured by magnetic resonance imaging. *Journal of applied physiology (Bethesda, Md. : 1985)*, 102(5):2064–2070, May 2007.

[38] C. M. Mann, K. B. Domino, S. M. Walther, R. W. Glenny, N. L. Polissar, and M. P. Hlastala. Redistribution of pulmonary blood flow during unilateral hypoxia in prone and supine dogs. *Journal of applied physiology (Bethesda, Md. : 1985)*, 84(6):2010–2019, Jun 1998.

[39] M. N. Melsom, T. Flatebø, and G. Nicolaysen. Hypoxia and hyperoxia both transiently affect distribution of pulmonary perfusion but not ventilation in awake sheep. *Acta physiologica Scandinavica*, 166(2):151–158, Jun 1999.

[40] H. L. Motley and A. Cournand. The influence of short periods of induced acute anoxia upon pulmonary artery pressures in man. *The American journal of physiology*, 150(2):315–320, Aug 1947.

[41] G. Musch, J. D. H. Layfield, R. S. Harris, M. F. Vidal Melo, T. Winkler, R. J. Callahan, A. J. Fischman, and J. G. Venegas. Topographical distribution of pulmonary perfusion and ventilation, assessed by pet in supine and prone humans. *Journal of applied physiology (Bethesda, Md. : 1985)*, 93(5):1841–1851, Nov 2002.

[42] P. H. Neumann, C. M. Kivlen, A. Johnson, F. L. Minnear, and A. B. Malik. Effect of alveolar hypoxia on regional pulmonary perfusion. *Journal of applied physiology: respiratory, environmental and exercise physiology*, 56(2):338–342, Feb 1984.

[43] S. Nyrén, M. Mure, H. Jacobsson, S. A. Larsson, and S. G. Lindahl. Pulmonary perfusion is more uniform in the prone than in the supine position: scintigraphy in healthy humans. *Journal of applied physiology (Bethesda, Md. : 1985)*, 86(4):1135–1141, Apr 1999.

[44] M. D. Peake, A. L. Harabin, N. J. Brennan, and J. T. Sylvester. Steady-state vascular responses to graded hypoxia in isolated lungs of five species. *Journal of applied physiology: respiratory, environmental and exercise physiology*, 51(5):1214–1219, Nov 1981.

[45] G. K. Prisk, K. Yamada, A. C. Henderson, T. J. Arai, D. L. Levin, R. B. Buxton, and S. R. Hopkins. Pulmonary perfusion in the prone and supine

postures in the normal human lung. *Journal of applied physiology (Bethesda, Md. : 1985)*, 103(3):883–894, Sep 2007.

[46] H T. Robertson. Does hypoxic vasoconstriction influence the normal distribution of human pulmonary blood flow? *Journal of Applied Physiology*, 106(4):1034–1035, 2009.

[47] H. T. Robertson and M. P. Hlastala. Microsphere maps of regional blood flow and regional ventilation. *Journal of applied physiology (Bethesda, Md. : 1985)*, 102(3):1265–1272, Mar 2007.

[48] R. J. Roeleveld, J. T. Marcus, A. Boonstra, P. E. Postmus, K. M. Marques, J. G. F. Bronzwaer, and A. Vonk-Noordegraaf. A comparison of noninvasive MRI-based methods of estimating pulmonary artery pressure in pulmonary hypertension. *Journal of magnetic resonance imaging : JMRI*, 22(1):67–72, Jul 2005.

[49] I. R. Starr, W. J. E. Lamm, B. Neradilek, N. Polissar, R. W. Glenny, and M. P. Hlastala. Regional hypoxic pulmonary vasoconstriction in prone pigs. *Journal of applied physiology (Bethesda, Md. : 1985)*, 99(1):363–370, Jul 2005.

[50] M. Halastala, E. Swenson, and K. Domino. *Complexity in Structure and Function in the lung*, chapter Physiological effect of oxygen and carbon dioxide on VA/Q heterogeneity. Marcel Dekker, 1998.

[51] A. Tucker and J. Rhodes. Role of vascular smooth muscle in the development of high altitude pulmonary hypertension: an interspecies evaluation. *High altitude medicine & biology*, 2(2):173–189, 2001.

[52] P. D. Wagner, R. B. Laravuso, R. R. Uhl, and J. B. West. Continuous distributions of ventilation-perfusion ratios in normal subjects breathing air and 100 per cent o2. *The Journal of clinical investigation*, 54(1):54–68, Jul 1974.

[53] W. W. Wagner and L. P. Latham. Pulmonary capillary recruitment during airway hypoxia in the dog. *Journal of applied physiology*, 39(6):900–905, Dec 1975.

[54] J. B. West, C. T. Dollery, and A. Naimark. Distribution of blood flow in isolated lung; relation to vascular and alveolar pressures. *Journal of applied physiology*, 19:713–724, Jul 1964.

# Chapter 6

# The effect of lung deformation on the spatial distribution of pulmonary blood flow

## 6.1 Abstract

The pulmonary hemodynamic effects of lung inflation induced by tidal volume breaths were tested *in vivo* in the human in supine posture. Two opposing effects are at play; the radial traction induced by lung expansion decreases pulmonary vasculature resistance, whereas the axial stretch of pulmonary vessel increases the vasculature longitudinal length and decreases the vessel diameter, resulting in an increase in the vasculature resistance. It is also expected that any change in the hydrostatic pressure distribution due to a change in lung height would also contribute to the redistribution of pulmonary blood flow. The net results of these effects are unknown. To test this influence, a novel functional lung magnetic resonance imaging technique was used to measure the spatial distribution of pulmonary blood flow following lung inflation. MRI data were obtained from seven healthy nonsmoking supine subjects in sagittal slices of the right lung during a short breath-hold at three different lung volumes [functional residual capacity (FRC), FRC + 500 mL, and FRC + 1 liter in balanced order]. Each subject

inhaled a predetermined volume of air (500 mL or 1 liter) through a face mask so that the target lung volume was repeatedly achieved. Arterial spin labeling (ASL) and multi echo gradient-echo sequences were used to obtain quantified pulmonary blood flow images and proton density images, respectively. ASL images were smoothed to approximately 1 $cm^3$ resolution using a Gaussian low pass filter and combined with proton density images on a voxel by voxel basis, yielding quantitative pulmonary perfusion images expressed in milliliters (blood) per minute per gram (lung tissue). A deformable image registration technique was used to warp perfusion images at volumes above FRC into the reference FRC image. Thus, the change in the spatial distribution of pulmonary perfusion due to lung inflation was evaluated based on the anatomical correspondence between images. The results showed that + 500 mL and + 1 liter lung inflations increased the regional lung volume in the imaging slice by 22(9)% and 37(13)%, respectively, resulting in a consistent decrease in lung proton density [FRC, 0.23(0.03) $g/cm^3$; FRC + 500 mL, 0.19(0.02) $g/cm^3$; FRC + 1 liter, 0.17(0.02) $g/cm^3$; $P < 0.0001$]. Lung inflation also decreased the pulmonary perfusion measured as a density normalized perfusion (DNP: mL/min/g) in the slice although the effect was of only borderline significance [FRC, 10.0(2.5) mL/min/g; FRC + 500 mL, 8.4(1.5) mL/min /g; FRC + 1 liter, 8.8(0.8) mL/min/g; $P = 0.10$]. The lobar and gravitational perfusion redistributions, independent of the mean pulmonary perfusion change were also estimated. Fractional pulmonary perfusion was redistributed away from the nondependent part of lung at higher lung volume. However, no evidence of lobar redistribution was found. In conclusion, tidal volume lung expansion did not cause a significant change in the spatial distribution of pulmonary perfusion. However, the changes in the gravitational height of the lung, which may result in the change in hydrostatic pressure distribution, likely contributed more significantly than the overall changes in pulmonary vasculature resistance due to lung tissue stretch.

## 6.2 Introduction

Lung deformation during normal respiratory motion results in structural modifications of the pulmonary vasculature tree. It is known that the vasculature geometry is closely associated with pulmonary circulation mechanics, owing to distensibility of pulmonary vessel walls [13, 14, 40, 41] and to linkage of vascular driving pressures to hydrostatic pressure gradients in the lung [39]. Therefore, lung deformation has the potential to have a significant influence on the spatial hemodynamic pattern. In addition, local tissue stretch represents local changes in lung volume, and it is therefore associated with regional ventilation. Well-ventilated parts of lung should correspond with well-perfused part of lung or vice versa in order to ensure ventilation - perfusion matching.

Understanding the interdependence between pulmonary hemodynamics and lung deformation resulting from tidal volume breathing has the potential to give important insights for clinical practice, aiding in planning effective mechanical ventilation to maintain gas exchange in patients in intensive care. The most prevailing mechanical ventilation system utilizes positive lung inflation in which the transpulmonary pressure is elevated as the alveolar pressure increases. Several studies using perfused animal lungs have unanimously shown that positive lung inflation increased pulmonary vascular resistance via compression of pulmonary vessels [6, 16, 26, 29]. Changes in pulmonary hemodynamics lead by the elevation in pulmonary vascular resistance and vascular compression could be an underlying cause of ventilator associated complications [8, 32, 33]. In contrast, normal breathing is carried out by negative inflation, in which negative intrapleural pressure pulls the lung outwards as the lung expands. The effect of negative inflation on hemodynamics is not well known; two different types of results have been reported: Burton and Patel have shown that pulmonary vascular resistance monotonically decreased as the lung expands [6]. However, Thomas *et al.* showed a decrease in pulmonary resistance compared to completely collapsed lung with moderate inflation (corresponding to a pneumothorax lung and functional residual capacity (FRC), respectively). In addition, there was an increase on further inflation, named therefore a U-shape change in vascular resistance [37]. The de-

bate over the changes in hemodynamics due to negative lung inflation has, thus far, lasted over five decades [22, 26]. Part of the controversy could be resolved if experiments could simulate normal breathing. Moreover, the results would be more valuable if the experiment were conducted using healthy human subjects *in vivo* with minimal interventions. Throughout my dissertation research work, two techniques have been developed to study on the spatial distribution of pulmonary blood flow in the human lung. A functional MRI technique known as arterial spin labeling (ASL) measures perfusion, which when combined with tissue proton density measurements allows us to create a pulmonary perfusion map in units of mL(blood)/min/g(tissue). A deformable image registration technique enables the warping of a lung image into another reference shape so that a pulmonary perfusion map can be registered on another perfusion map acquired at a different lung volume. When combined, these techniques are especially suited to measure the changes in pulmonary hemodynamics due to lung expansion in the tidal volume range, induced by normal negative lung inflation. Pulmonary perfusion maps were obtained in supine healthy subjects within a short  15 sec breath-hold at three different lung volumes [FRC, FRC + 500 mL and FRC + 1 liter inhalation volumes]. These two inhalation volumes were chosen to encompass normal human tidal volume (approximately 500 mL in the supine posture).

## 6.3 Method

### 6.3.1 Subjects

Seven healthy subjects [3 women, 4 men: age = 27(5) years old, height = 168(12) cm, and weight = 65(12) kg] participated after giving informed consent. Each subject underwent screening for MRI safety and spirometric pulmonary function test. The basic experimental procedure was described in chapter 3.

### 6.3.2 Lung volume control

The basic setup of the breathing line in the MR scanner room was previously described in Chapter 3. A minor modification was made for this specific experiment in order to ensure that the subject would breathe in a predetermined volume of air, starting from functional residual capacity (FRC) and hold it during the MR image acquisition (Figure 6.1). All participants were coached and familiarized with the breath-holding maneuver prior to the imaging session. All subjects reported being comfortable reaching and maintaining the altered lung volume multiple times during the imaging session.

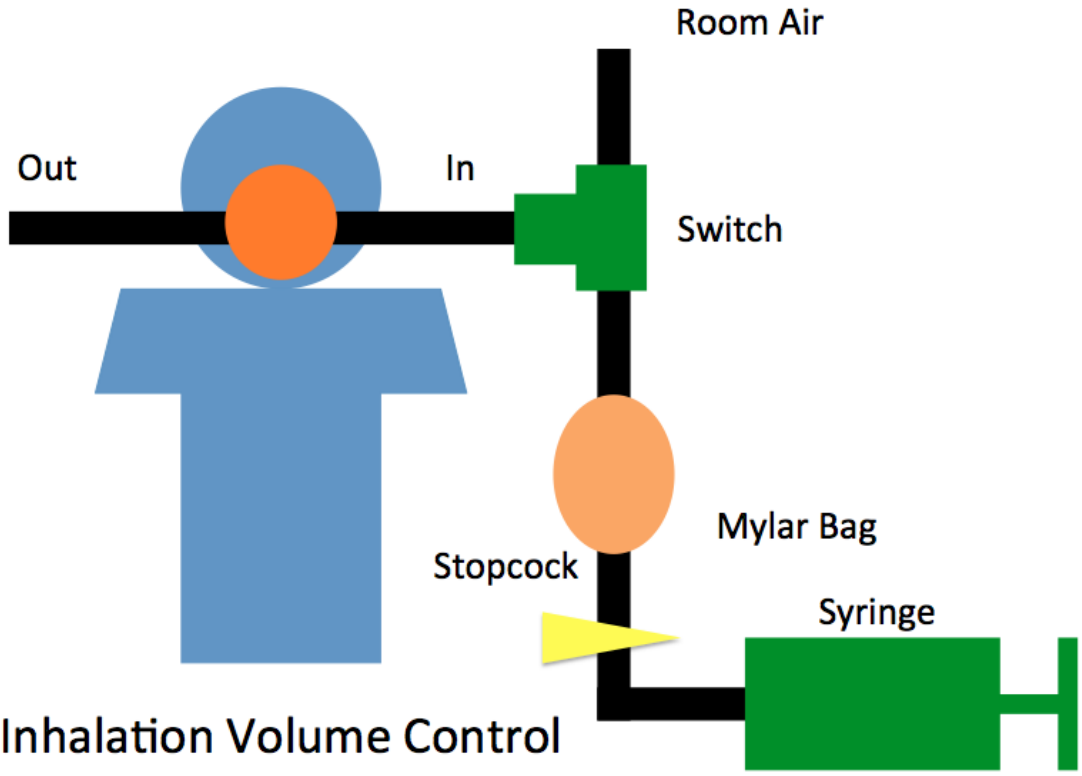


**Figure 6.1**: Breathing line setup for lung volume control. The basic setup was described in chapter 3, Figure 3.1. A minor modification was made for this specific experiment in order to ensure that the human subject would breathe-in a predetermined volume of air. The modification consists of adding a 5-liter Mylar bag, that is fed with predetermined volume of air using a3-liter syringe.

The modification consisted of connecting the inspiratory line to a 5-liter

Mylar bag via a three-way valve with switch. The other end of three-way valve was opened to room air, allowing the subject to breathe freely during the intervals between image acquisitions (Figure 6.2A). Two different inhalation volumes were chosen, close to typical tidal volume breathing; 500 mL and 1 liter. The predetermined volume of air was installed into the bag using a calibrated 3-liter syringe (Hans Rudolph). The subject was asked to hold his or her breath at FRC first. Then, the switch at three-way valve was turned allowing the subject to inhale the predetermined volume of air out of the bag (Figure 6.2B). Once the subject emptied the bag, he or she was instructed to hold his or her breath. Subjects were instructed not to forcibly expanding their chest against the empty bag in order to avoid raising intrathoracic pressure. The breath hold lasted for a maximum of 15 sec, the time it takes to perform the image acquisition. Any air leaks and/or failure in breath-holding were monitored by checking chest wall and diaphragm movement in the acquired MR image and expiratory flow detected using the pneumotachograph placed on the expiratory line.

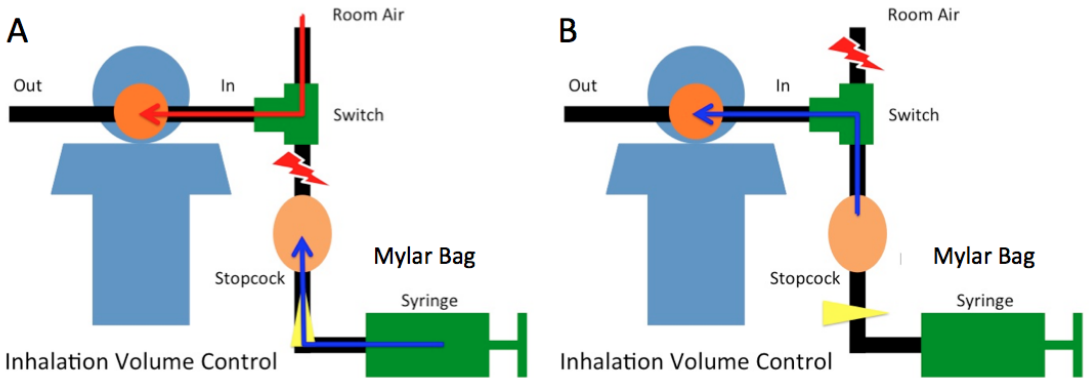


**Figure 6.2**: Lung volume control maneuver. A: At the end, inspiratory line is open to room air so that the subject is able to breathe freely during intervals between image acquisitions. Meanwhile, the predetermined volume of air (500 mL and 1 liter, respectively) is gauged and administrated into the bag using a calibrated 3-liter syringe. B: The subject holds the breath at FRC lung volume first. Then, the three-way valve is turned allowing for the subject to inhale the measured amount of air out of the bag.

### 6.3.3 Complementing ASL with a vascular structure image

The regular ASL-FAIRER consists of a pair of images as described in chapter 2. In this study, an additional inversion recovery sequence with TI = 50 msec was added after the pair of ASL-FAIRER images (Figure 6.3). Since the subject was breath-holding during the MR image acquisition for 15 sec, there was essentially no motion among the three images. In other words, these three images shared an identical physical coordinate system. The first two images were used for the absolute quantification of ASL flow map described in Chapter 2. The additional image, which highlights the vascular structure, was used for the deformation analysis by comparing it with the corresponding images at different lung volumes. Since this third image was optimized to highlight the vascular structure, it also provided clear delimitation of the boundaries between the three lobes in the right lung, since the fissures have a dark contrast boundary.

### 6.3.4 Volumetric reconstruction of the right lung

Multiple 2D sagittal ASL images at different lateral slice locations (i.e. L-R direction) were acquired to cover a part of the right lung in 3D space (Figure 6.4). This 3D volume was used for 3D lung deformation analysis described in the section 6.3.5.

The slice thickness was 15 mm and the in-plane field of view was 40cm $\times$ 40cm. The lateral slice location was shifted by 5 mm in the L-R direction so that two adjacent images overlapped by 10 mm. Nine ASL-vascular structure (ASL-VS) image sets were taken at FRC to establish a reference volumetric lung, covering 4 cm thickness of right lung in L-R direction.

For each of its altered lung volumes (FRC + 500 mL and FRC + 1 liter), five 15 mm sagittal ASL images were acquired using the same spatial overlapping scheme, covering 2 cm thickness of the right lung in L-R direction. The center image (the 3rd image) corresponded to the center of reference volume (5th image of the FRC set).

The lung density images at the three different lung volumes were also obtained at the same image locations (in scanner space) as the reference ASL images.

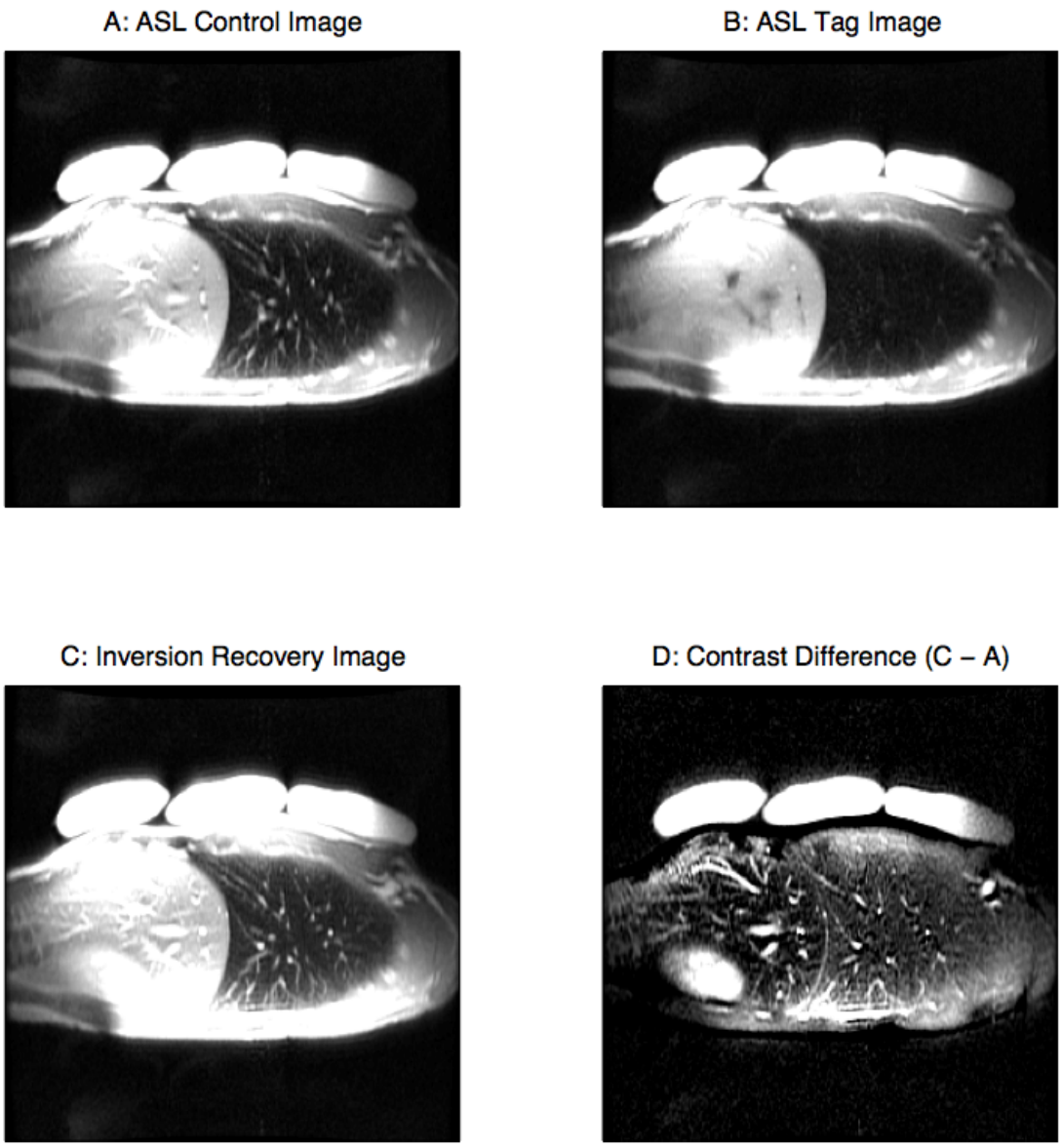


**Figure 6.3**: A pair of ASL-FAIRER images and an additional inversion recovery image. A: ASL control image. B: ASL tag image. This pair of ASL images is used for pulmonary blood flow quantification. C: This additional inversion recovery image highlights the vascular structure, which is used for deformation analysis. It also provides the clear boundaries between three lobes since the fissures have a dark contrast boundary. A map of contrast differences between inversion recovery image C and ASL control image A is shown in D.

For each slice at each lung volume, image data were acquired at least three times and one representative image was chosen to ensure that the stack of 2D images reconstructed a continuous 3D lung. The in-plane resolution of the 3D lung was approximately 1.6 mm $\times$ 1.6 mm while the through-plane resolution was 5 mm.

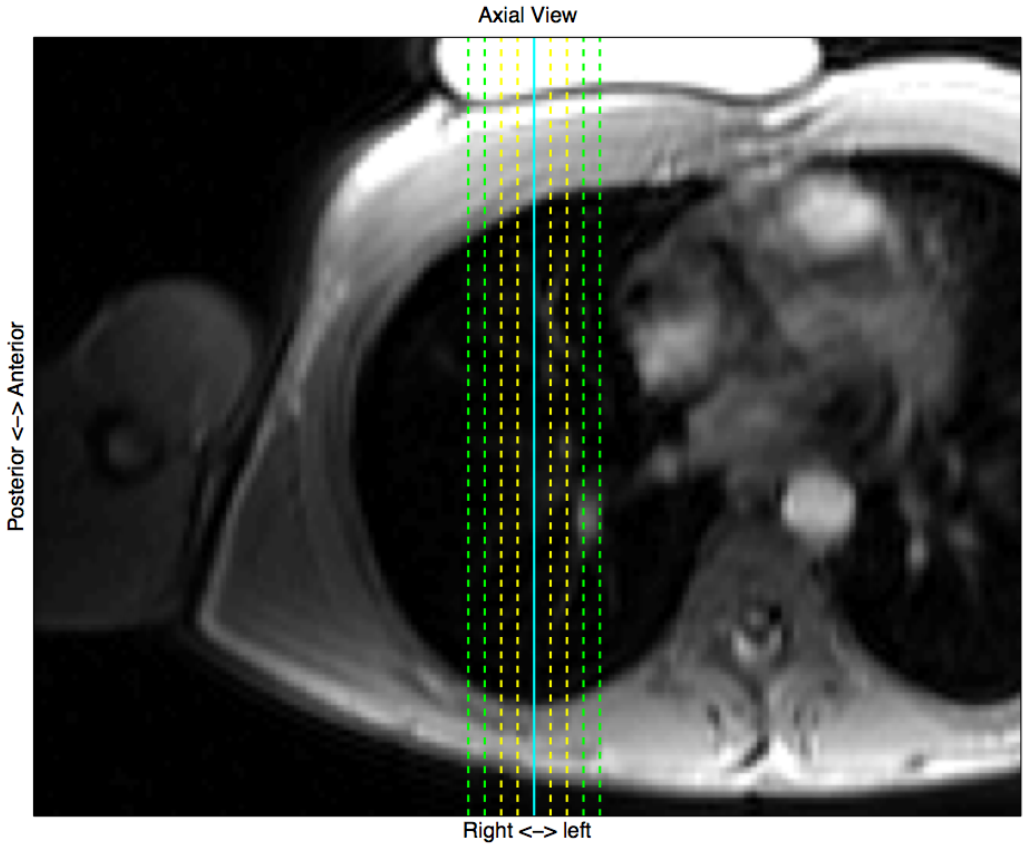


**Figure 6.4**: 3D sagittal image stack location shown in an axial view. Multiple 2D sagittal ASL images at different lateral slice locations (i.e. L-R direction) are acquired to cover a part of right lung in 3D space. Consecutive slice location is shifted by 5 mm. Nine images from nine slice locations are taken at FRC lung volume (dashed green, yellow and solid blue lines), covering 4 cm thickness of right lung. Five images from five slice locations are acquired in the same spatial overlapping scheme (dashed yellow and solid blue lines), covering 2 cm thickness of right lung. The solid blue line represents the target image slice location, selected as the image plane where anterior-posterior distance is the largest at FRC.

### 6.3.5 3D deformation analysis

The deformation between reference and deformed volumetric lungs for each subject was computed using 3D cubic-cubic-linear polynomial interpolation method described in Chapter 4. In-plane deformation was interpolated with cubic polynomials (B-spline) while through-plane deformation was interpolated with a linear interpolation method, given the lower spatial sampling in this plane. The inversion recovery vascular structure images were used for the deformation analysis. The sum of square difference was used as the cost function for image registration. Deformation was separately computed within each of the three manually segmented lobes (right lower, upper and middle lobes) in order to avoid errors induced by the continuity assumption of polynomial interpolation method, as oppose to lobar slide [9]. Thus, the output can present discontinuous displacements at the lobar border. Then, the three independently computed deformation fields were reassembled to represent the whole lung deformation. The deformation algorithm follows a stepwise approach, from a cruder to a finer scale: a single cuboid (3D rectangular) element that encompasses each lobe is used at first. This initial low-resolution element was then recursively refined in-plane until the size of refined element grid becomes approximately 8 pixels, dividing the original element into an integer number of grids.

### 6.3.6 Target slice

The center image (the 5th image) of the reference volumetric lung at FRC was selected as a target image slice (the center plane in Figure 6.4). This image goes through the portion of right lung where anterior-posterior distance is the largest, highlighting the gravitational dependency of pulmonary tissue distribution due to the Slinky® effect. It is also the image plane used in many previous studies conducted by the UCSD Pulmonary Imaging Laboratory [2–4, 19, 20, 28, 30, 35, 36]. For this study, it is expected that the Slinky® effect also influences regional tissue deformation due to breathing, making it more heterogeneous [20, 28]. In fact, specific ventilation is greater in the dependent lung than in the nondependent lung since the lung tissue in the non-dependent part is already stretched and has lesser

room for the extra expansion [30].

The quantified ASL (mL/min/cm$^3$) and density (g/cm$^3$) maps obtained at the altered lung volumes were warped into the reference FRC lung based on the 3D deformation computed using the vascular structure images. Therefore, these data were compared at the location of target slice in the reference volume. The large conduit vessel flow was removed from ASL map using a 35% maximum-intensity threshold defined by a prior simulation study [5]. ASL maps were then smoothed with a Gaussian low pass filter (full width half max = 7 voxels (1.1cm), as in previous work by our group [17]), resulting in the effective spatial resolution of perfusion map to approximately the size of 5 acini [15]. After the processing, the ASL perfusion map was divided by the density map, yielding a density normalized perfusion map (mL/min/g), which approximates perfusion per in milliliters per minute per gram of lung tissue. Voxels with negative ASL flow signal were removed since they represent inherent ASL measurement errors. In addition, voxels with the highest and lowest 5% of regional volume change were also eliminated from data to remove the occasional spurious volume changes resulting from the image registration algorithm.

### 6.3.7 Data analysis

Density(g/cm$^3$), density normalized perfusion (quantified ASL divided by density: mL/min/g), and fractional regional lung volume change (computed by the determinant of Jacobian: $V/V_0$) maps were calculated at the target slice. Lung density inherently decreases with lung inflation. Therefore, the density image at the increased lung volumes were corrected with the regional volume change map in order to capture the corresponding original lung density at FRC, yielding the deformation corrected density in units of g/cm$^{3*}$. (* indicates that MR voxel size, which is the denominator in the units, is corrected by the local lung deformation). Since this influence of voxel size change due to lung deformation is canceled by division, density normalized perfusion is insensitive to regional lung deformation. It reflects the amount of perfusion per lung tissue.

In addition to the whole right lung analysis, the lung was divided into three

parts in two different ways. (1) The lung was divided based on lobes (right lower lobe, RLL; right upper lobe, RUL; and right middle lobe, RML). (2) The lung was also divided into three equal height gravitational regions, in the posterior - anterior direction of the lung (dependent, middle and nondependent regions, respectively).

In order to study the effect of lung volume change on the redistribution of perfusion among different parts of lung, the density normalized perfusion maps were normalized by their own mean, yielding the nDNP map. The difference between two nDNP maps at an altered lung volume and at FRC reflects any perfusion redistribution (Figure 6.5) without the confounding influence of mean cardiac output change, allows the evaluation of perfusion redistribution. In other words, if there is no redistribution of perfusion and the proportion of perfusion distribution within the image plane stays the same, the difference between two nDNP maps would become zero everywhere.

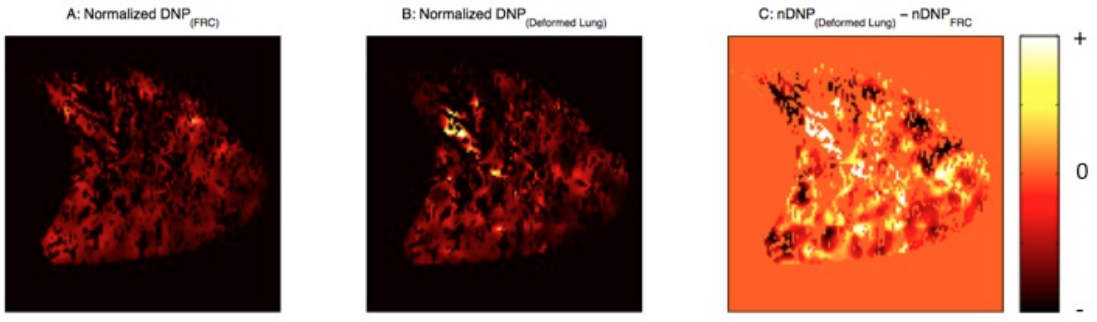


**Figure 6.5**: Redistribution of pulmonary perfusion due to lung deformation. A density normalized perfusion map is normalized by its own mean, yielding the nDNP map. The difference (C) between two nDNP maps at an altered lung volume (B) and at FRC (A) reflects the perfusion redistribution without the influence of mean cardiac output change.

ANOVA (Statview 5.0, SAS Institute, Cary, NC) for repeated measures was used to statistically evaluate changes in the major dependent variable over the three different lung volumes (3 levels: FRC, FRC + 500 ml, and FRC + 1 liter). Dependent variables for this analysis were lung density, regional lung volume change, density-normalized perfusion, and nDNP. Where overall significance occurred, post hoc testing was conducted with Students t-testing. All data are presented as mean(SD) over 7 subjects; the null hypothesis (no effect) was rejected

**Table 6.1**: Physiological data at different lung volumes. Values are mean(standard deviation); There was a borderline effect (P = 0.06) on heart rate, however the detected difference was approximately 3 bpm between the different lung volumes, therefore not likely physiologically relevant.

| | Lung Volume | | | |
|---|---|---|---|---|
| | FRC | FRC + 500 mL | FRC + 1 liter | Main Effect |
| $Sp_{O_2}$, % | 97.7(1.2) | 97.9(0.5) | 98.4(0.5) | P = 0.17 |
| Heart rate, bpm | 62(15) | 61(14) | 64(15) | P = 0.06 |

for $P < 0.05$.

## 6.4 Results

Pulmonary function data were within the normal range [forced vital capacity (FVC) = 4.4(1.1) liters, FVC % predicted = 96(8), forced expiratory volume in 1 second ($FEV_1$) = 3.5(0.8) liters, $FEV_1$ % predicted = 92(9), $FEV_1$/FVC = 0.80(0.10), and $FEV_1$/FVC % predicted = 96(7)]. Tidal volume ($VT_{STPD}$), respiratory rate (RR), and minute ventilation ($VE_{STPD}$) during the voluntary breathing (as opposed to the control breathing and breath-holding) in the MR scanner were 0.5(0.1) liter, 11(2) $min^{-1}$ and 5.0(1.0) liter/min, respectively. Other physiological data during breath-holding at different lung volumes are shown in Table 6.1. There was no overall effect (P = 0.17) on the arterial oxygen saturation measured by pulse oximetry ($Sp_{O_2}$) [FRC, 97.7(1.2)%; FRC + 500 mL, 97.9(0.5)%; FRC + 1 liter, 98.4(0.5)%]. There was a borderline effect (P = 0.06) on heart rate change, however the detected difference was small, approximately 3 bpm between the different lung volumes [FRC, 62(15)bpm; FRC + 500 mL, 61(14)bpm; FRC + 1 liter, 64(15)bpm].

Figure 6.6 shows the effect of lung deformation on mean regional lung volume change ($V/V_0$). FRC + 500 mL and FRC + 1 liter showed approximately 22(9)% and 37(13)% increase in the mean lung volume, respectively [FRC + 500 mL, 1.22(0.09); FRC + 1 liter, 1.37(0.13)]. The two increased lung volumes were significantly greater than FRC reference volume ($P < 0.0001$). The mean regional

lung volume at FRC + 1 liter was also significantly greater than that at FRC + 500 mL ($P < 0.01$).

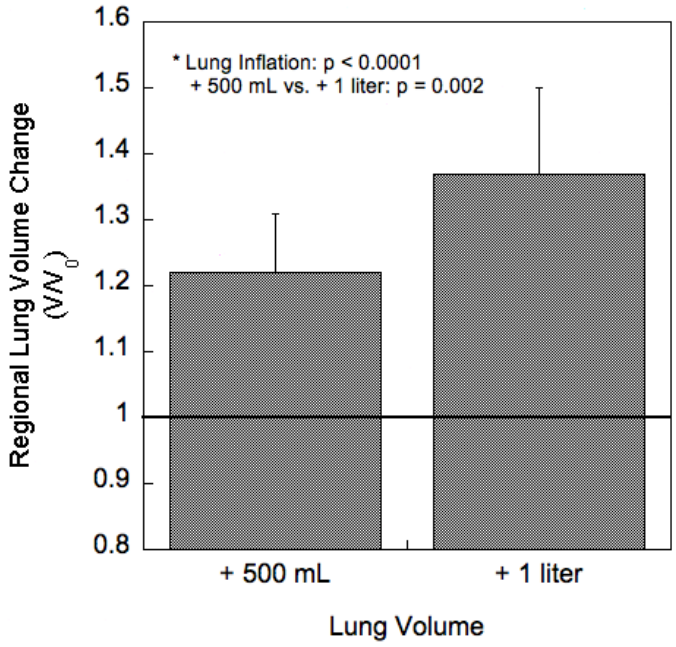


**Figure 6.6**: Effect of lung inflation on mean regional lung volume change ($V/V_0$). FRC + 500 mL and FRC + 1 liter showed approximately 22(9)% and 37(13)% increase in the mean lung volume, respectively. Both measured regional lung volumes were significantly greater than FRC (= 1: solid line) ($P < 0.0001$). The mean regional lung volume at FRC + 1 liter was also greater than that at FRC + 500 mL ($P < 0.01$).

The change in mean lung density with respect to lung deformation is given in Figure 6.7. As expected, mean lung density was greatest at FRC and decreased as lung volume increased [FRC, 0.23(0.03) g/cm$^3$; FRC + 500 mL, 0.19(0.02) g/cm$^3$; FRC + 1 liter, 0.17(0.02) g/cm$^3$; $P < 0.0001$]. The density at FRC + 500 mL was greater than that at FRC + 1 liter, however this was not a statistically significant difference based on post hoc testing ($P = 0.11$). Figure 6.8 shows the deformation corrected density. Those three numbers were nearly identical. [FRC, 0.23(0.03) g/cm$^{3*}$; FRC + 500 ml, 0.23(0.03) g/ cm$^{3*}$; FRC + 1 liter, 0.24(0.03) cm$^{3*}$; $P = 0.86$].

Figure 6.9 shows that the mean density normalized perfusion had a borderline significant declining trend with inspired lung volume, however the relationship

was not linear with the degree of lung inflation. [FRC, 10.0(2.5) mL/min/g; FRC + 500 mL, 8.4(1.5) mL/min/g; FRC + 1 liter, 8.8(0.8) mL/min/g; P = 0.10].

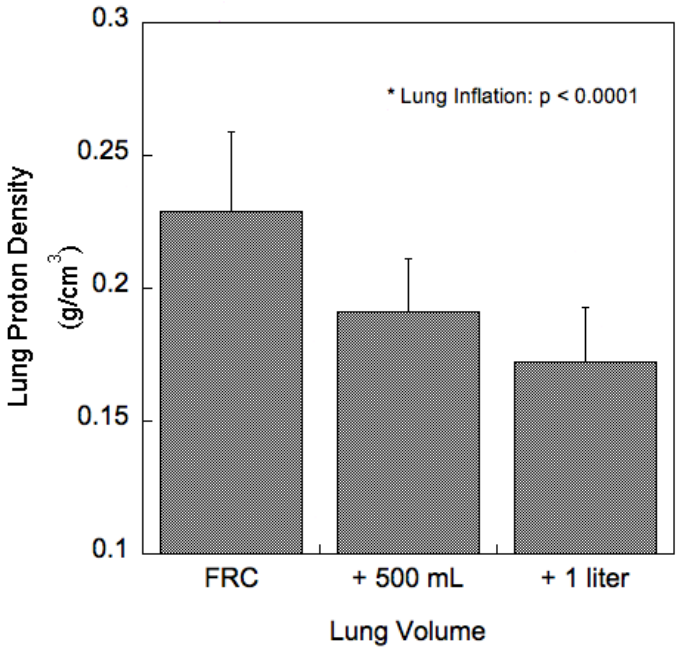


**Figure 6.7**: Effect of lung deformation on mean lung density (g/cm$^3$). The mean lung density was greatest at FRC and decreased as lung volume increased (P < 0.0001). The density at FRC + 500 ml is higher than that at FRC + 1L, however no significant difference was found based on post hoc testing (P = 0.11).

Figure6.10A and B show that the lung expands differently with respect to lobes and gravitational regions. Both regional data showed strong overall significant difference (P < 0.0001). The post hoc analysis showed that there was lobar and gravitational dependencies of lung expansion in which RLL and the dependent part showed the largest expansion [RLL: FRC + 500 mL, 1.26(0.09); FRC + 1 liter, 1.45(0.15) and dependent: FRC + 500 ml, 1.25(0.10); FRC + 1 liter, 1.45(0.13)] while RML and the nondependent part showed the smallest effect [RML: FRC + 500 mL, 1.18(0.06); FRC + 1 liter, 1.23(0.10) and nondependent: FRC + 500 mL, 1.18(0.09); FRC + 1 liter, 1.27(0.10)].

The redistribution of perfusion among three lobes and three gravitational regions measured by the difference between nDNP maps at an altered lung volume and at FRC is given in Figure 6.11A and B. The nDNP redistribution data showed

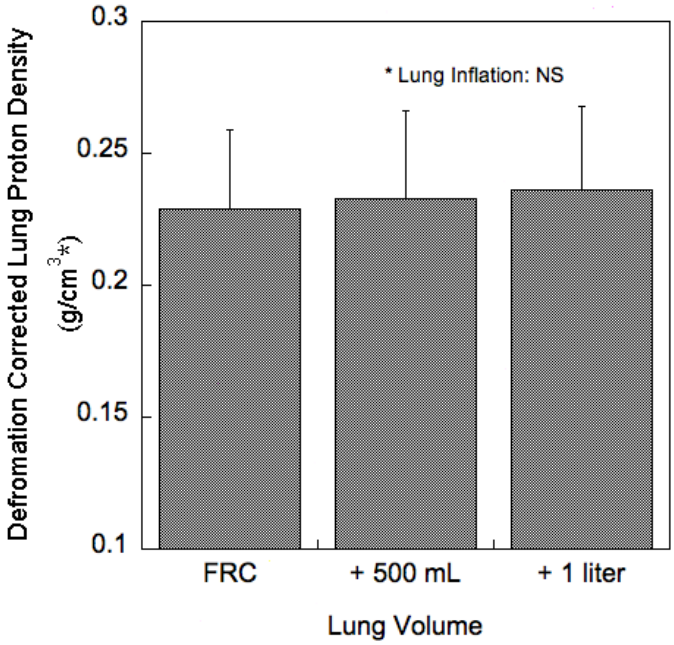


**Figure 6.8**: Deformation corrected density. Density image at increased lung volume was corrected with the regional volume change map in order to capture the original lung density at FRC. The deformation corrected density is in units of g/cm$^{3*}$ where * indicates that MR voxel size, which is the denominator in the units, is corrected by the local lung deformation. Deformation corrected density values at different lung volumes were nearly identical (P = 0.86).

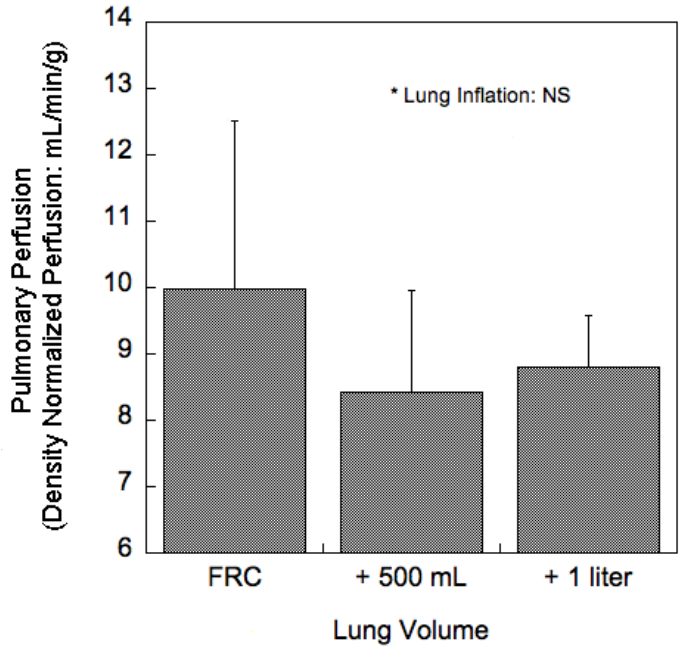


**Figure 6.9**: Effect of lung deformation on mean perfusion (mL/min/g). Mean density pulmonary perfusion had a borderline significant declining trend with inspired lung volume (P = 0.10) however the relationship was not linear with the degree of lung inflation.

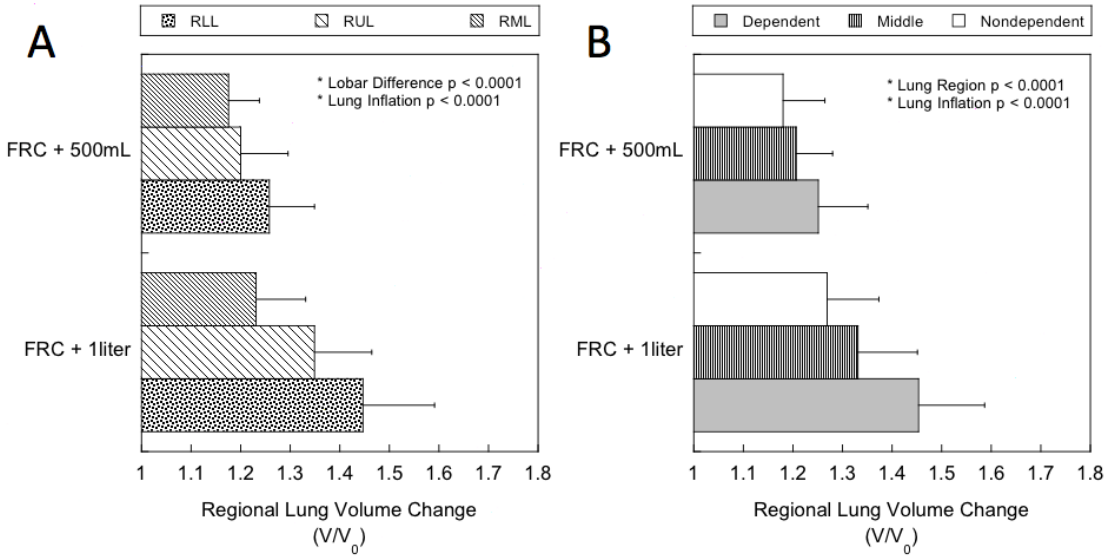


**Figure 6.10**: Lobar and gravitational dependency of regional volume change ($V/V_0$). A: lobar dependency. The result showed that each lobe expanded differently with lung inflation ($P < 0.0001$). Among the three different lobes, right lower lobe (RLL) inflated the most, while right middle lobe (RML) inflated the least. B: gravitational dependency. The result showed that the three gravitational parts (nondependent, middle, and dependent) expanded differently with lung inflation ($P < 0.0001$). The nondependent part inflated the smallest, while the dependent part inflated the largest.

there was no overall significant difference in lobar nDNP redistribution ($P < 0.89$). The gravitational nDNP redistribution data showed that there was a decreasing trend in the nondependent part and an increasing trend in the middle part of lung with lung inflation and the trends of perfusion redistribution in these two region showed a statistically significant difference ($P < 0.05$) based on the post hoc testing. However, there was no statistical difference between +500 mL inflation and + 1 liter inflation.

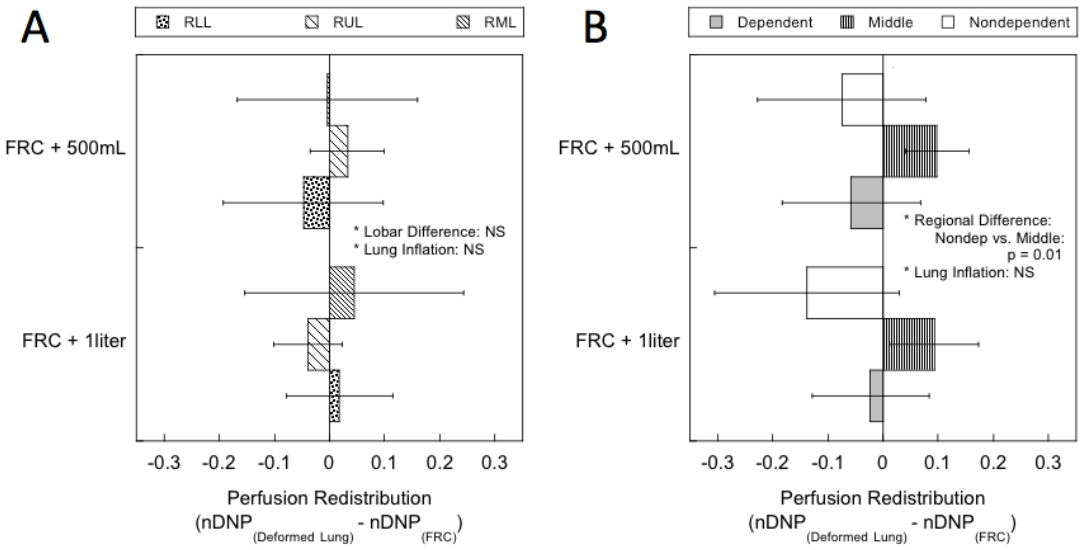


**Figure 6.11**: Lobar and gravitational redistribution of pulmonary perfusion due to lung inflation measured by lobar nDNP difference. The difference between two nDNP maps at different lung volumes reflects the perfusion redistribution without the influence of mean cardiac output change (Figure. 6.5). A: lobar redistribution. There was no overall significant difference in lobar nDNP redistribution ($P < 0.89$), despite each lobe expanded differently as shown in Figure 6.10A. B: gravitational redistribution. There were decreasing and increasing trends in nondependent and middle parts of lung with lung inflation, respectively. The difference between nondependent and middle parts were statistically significant ($P < 0.05$) based on post hoc test.

## 6.5 Discussion

The geometry of pulmonary circulation depends on mechanical deformation of the lung parenchymal tissue to which the vasculature tree is tethered. Therefore, pulmonary vasculature resistance is expected to be altered by lung inflation, inducing both radial and axial distensions in pulmonary vascular structure. According to the forth power and fifth power laws of pulmonary blood flow with respect to vascular geometry, radial distention would decrease pulmonary vasculature resistance and increase the blood flow whereas axial distension would increase the resistance and decrease the flow [13, 14]. Howell *et al.* demonstrated that pulmonary vasculature responded differently to lung inflation in excised dog lungs perfused with dextran and kerosene, respectively; kerosene has a high surface tension that prevents it from entering the smaller vessels. The result showed that the large vessels, which are embedded within and tethered to the interstitium of the lung, were expanded with inflation while smaller vessels in close association with alveoli are compressed with the lung inflation [21]. A similar effect was reported by Lai-Fook [23]. In excised dog lower lobes, the diameters of pulmonary arteries and veins (with diameters ranging from 2.5 to 7.0 cm at maximal distention) increased for any given pulmonary blood pressure. The interdependence between vessel distension and lung inflation was small at functional residual capacity, increased with lung inflation, and was greater for arteries than veins. Those findings were based on positive pressure lung inflation.

The determining factor of lung inflation is transpulmonary pressure, which is alveolar pressure minus intrapleural pressure. As transpulmonary pressure increases, the lung inflates. The positive inflation indicates the increase in alveolar pressure, which pushes out the lung from inside, whereas the negative inflation indicates the decrease in intrapleural pressure, in which the negative pressure pulls the lung outwards. (At FRC, the mean transpulmonary pressure is approximately 5 $cmH_2O$. Alveolar pressure and intrapleural pressures are 0 and -5 $cmH_2O$, respectively. The elastic recoil pressure of lung tissue counterbalances transpulmonary pressure and pulls the lung inwards towards deflation.) These two lung inflation schemes affect the pulmonary vasculature resistance differently, especially in small

vessels. The transmural pressure in small pulmonary vessels, which determines pulmonary vessel resistance via the change in vessel diameter is defined as pulmonary blood pressure minus alveolar pressure. Since positive inflation elevates the alveolar pressure, it decreases transmural pressure and increases the vessel resistance. On the contrary, the resistance would remain the same with negative inflation. Therefore, volume related changes in pulmonary vasculature resistance are similar in both positive and negative inflations, while transmural pressure related changes are different between the two lung inflations [16]. Roos *et al.* showed these two different responses using a perfused and ventilated dog lung *in vivo*. The positive pressure inflation (+7, +17 and +23 $cmH_2O$) caused a considerable rise in resistance in the left lung. The negative pressure inflation spontaneous breathing (-7 and -17 $cmH_2O$) resulted in a slight fall, followed by a small rise in resistance on further inflation (-23 $cmH_2O$) [29]. Thomas *et al.* showed that the lowest pulmonary vasculature resistance was found approximately at the half maximal lung volume (which is about the size of FRC, the lung volume where the intrapleural pressure is approximately -5 cm $H_2O$) using a negatively inflated isolated dog lung preparation. A progressive rise in resistance was found on either further inflation or deflation from the minimum resistance point at FRC i.e. the point where the intrapleural pressure was approximately -5 cm $H_2O$ [37]. This U-shape curve relationship between transpulmonary pressure and pulmonary vascular resistance has been also reported by other researchers [16, 22].

The present study showed that the pulmonary perfusion in the target sagittal image slice was reduced by 16% and 12% with +500 mL and +1 liter spontaneous negative lung inflations respectively, where despite decreasing trends were of borderline significance ($P = 0.10$, Figure. 6.9). This trend was consistent with the U-shape relationship reported by [37] where the lung inflation above FRC elevates the pulmonary vascular resistance.

The decline in perfusion can not only be attributed to the increase in vascular resistance, but also to the decline in pulmonary artery pressure and/or cardiac output. The inspiratory breath-holding with an open glottis perturbs pulmonary hemodynamics via a change in transpulmonary pressure and sympathetic nerve

activities [25, 34]. Inspiration increases the right atrial filling via reduced intrapleural pressure resulting in a brief increase in mean arterial pressure and heart rate. When the inspiration is completed, it is immediately followed by the suppression of sympathetic activity via the pulmonary stretch reflex [24], which causes bradycardia and reduction in mean arterial pressure. This reduction in the cardiac performance with inspiratory breath-holding has been commonly reported in supine [31, 34] and upright [11] postures. This change must have a corresponding change in the pulmonary circulation. There is a significant correlation between sympathetic nerve activity and pulmonary arterial pressure measured in both high altitude pulmonary edema (HAPE) susceptible and HAPE resistive human subjects [10]. Sakuma *et al.* reported the decrease in cardiac output in both aorta and pulmonary artery with inspiratory breath-holding using velocity encoded cine MRI. Taneja *et al.* showed that the reduction in the cardiac performance was subsequently followed by increased sympathetic activity [34]. Their representative data in supine posture showed that the transition between the reduction phase and the increasing phase occurred approximately 10 sec after reaching to the total lung capacity (TLC).

The change in pulmonary artery pressure with breath-holding was not measured in the present study. The breath-holding maneuver used in the present study lasted approximately 15 sec during the MR image acquisition, with the pair of ASL perfusion images obtained within the first 10 sec. Therefore, the perfusion measurement was assumed to complete during the interval corresponding to the reduction phase described by Taneja *et al.* However, those studies described above used TLC as the inspiratory lung volume, while a tidal volume inflation was chosen for the present study. Therefore, the influence of lung inflation pulmonary stretch reflex to the possible reduction in cardiac output and pulmonary artery pressure is likely much smaller in the present study. Still, it may play a role in the borderline significant reduction in mean perfusion with respect to the lung inflation (Figure. 6.9).

Figure 6.11B, the redistribution of nDNP (which offsets the change in mean cardiac output between the different imaging acquisitions) in three different grav-

itational regions indicates that the lung inflation alters the spatial distribution of pulmonary perfusion. The nondependent region of lung showed a decrease in nDNP whereas nDNP in the middle region showed an increase with the lung inflation, and the difference between those two parts was statistically significant ($P < 0.05$). Hopkins *et al.* showed a similar finding and pulmonary perfusion in nondependent region of lung was significantly reduced with a TLC lung inflation compared to FRC [19]. It should be noted that in the present study the redistribution was only seen among gravitational regions and it was not observed between the three lung lobes (Figure 6.11A). The RLL and the dependent region, RUL and the middle region, and RML and the nondependent region show similar regional lung volume changes, respectively (Figure 6.10A and B). However, the redistribution of perfusion was different based on the different types of segmentation of the lung. Therefore, these data suggest that the perfusion redistribution due to lung inflation is mainly caused by change in the hydrostatic pressure in the gravitational direction, while the change in vascular resistance due to the lung tissue stretch had a secondary effect. The reduction of pulmonary perfusion in nondependent part of the lung could be described by the increase in zone 2 regions (where alveolar pressure exceeds pulmonary venous/venule pressure), which are mainly located in the nondependent part of the lung [12]. The increase in vertical height (anterior - posterior direction) reduces the hydrostatic pressure in pulmonary blood vessels mainly in the nondependent lung so that the pulmonary venule pressure decreases and some of zone 3 regions are converted into zone 2 regions. Kira *et al.* demonstrated that the relationship between the change in the vasculature resistance due to the lung tissue stretch and the pulmonary vascular transmural pressure. When the vascular transmural pressure was approximately 5 $cmH_2O$, a low-pressure condition, the pulmonary vasculature resistance increased as the lung stretched. However, when the vascular pressure was high (11 $cmH_2O$), the transmural pressure in small vessels remained high and the vasculature cross-sectional area remained large. Therefore, the reduction in vasculature cross-sectional area due to the axial stretch was a lesser influence and the vasculature resistance was virtually unchanged [22]. Pulmonary vessels with low transmural pressures are predominantly located in

gravitationally nondependent region, while the high transmural vessels are located in gravitationally dependent region of the lung. Therefore, the nondependent part of the lung is more prone to a reduction in perfusion caused by lung expansion than the dependent part of the lung.

mGRE sequence was used to quantify the pulmonary proton density in units of $g/cm^3$. This technique was previously validated using isolated pig lungs *ex vivo* [18]. The measured proton density using the MR sequence was highly correlated with the gravimetric measurement of total water content in the pig lung at 2 levels of inflation pressure (+5 and +15 cm $H_2O$, $R^2$: 0.94 and 0.96, respectively). In the present study, the pulmonary density decreased with lung inflation (Figure 6.7). The local volume change due to lung inflation decreases the measured density, however the number of protons within the original target slice essentially remains the same. The pulmonary density map was coregistered and multiplied with the independently measured regional lung volume change map on a voxel-by-voxel basis, yielding the deformation corrected density map. Figure 6.8 showed the deformation corrected density at three lung volumes were identical. Therefore, these data support the validity of the technique used to analyze the local lung deformation.

The measured lung volume changes were + 22(9)% and + 37(13)% with + 500 mL and + 1 liter inspirations, respectively. Sá *et al.* reported the regional distribution of specific ventilation (SV: the ratio of regional ventilation ($\Delta V$) to the end-expiratory volume ($V_0$) of the region) in human subjects in the supine posture. The reported mean SV in a sagittal plane in right lung was 0.33(0.11) in a subject group with the average of 0.87(0.18) liters of expired tidal volume [30]. Prisk *et al.* reported an average SV of 0.37(0.03) in an older group of supine subjects in which the tidal volume was constrained to approximately 650 mL [27]. Those results suggest a close agreement among different techniques. It should be noted that SV and regional lung volume change have different physiological interpretations: SV is a dimensionless measure of ventilation where the measured incoming fresh air contributes to the gas exchange; on the other hand, regional lung volume change includes both ventilation and dead space volumes. Sá *et*

*al.* also reported the gravitationally dependency of SV distribution with higher values seen in dependent part of the lung. The Slinky® effect, self-deformation of lung tissue [20, 28], is the dominant effect; the nondependent part of the lung is already stretched due to the self-deformation at FRC so that the amount of fresh air displaced into the region is less than in the dependent part of the lung. The gravitational dependency in the regional lung volume change found in the present study (Figure 6.10B) was consistent with these previous findings. Moreover, the lobar dependency of regional lung volume change in the supine right lung has been reported in the literatures with RLL and RML experiencing the largest and smallest lung volume change with FRC to TLC lung expansion, respectively [1, 7]. This is also consistent with the result of present study (Figure 6.10A).

## 6.6 Limitations and the future directions

Similarly to the hypoxic pulmonary vasoconstriction project, this study could have been strengthened if the pulmonary artery pressure measurements were made at the different lung volumes. However, the reliable measurement of pulmonary artery pressure using MRI in a human subject is not yet available [38]. Moreover, the use of Swan-Ganz catheter (which directly monitors pulmonary artery pressure) is a contraindication to MRI scanning.

The present study was performed in a single sagittal plane, which was denoted as a target slice in the right lung. Even though multiple sagittal images at different lateral slice locations were obtained in 5 mm slice intervals, these extra image slices were only utilized to estimate the through-plane deformation of the target slice in the present report. It has been previously reported that this target image plane highlights the gravitationally dependent distribution of lung tissue [36] and specific ventilation [30]. Therefore, the imaging plane was suited to test the effects of various magnitudes of lung tissue stretch on pulmonary perfusion distribution. A single ASL-FAIRER acquisition is also limited within an image slice. Nonetheless, the imaging slice does not necessarily represent the whole right lung. The lung region of interest in the images for this study were

approximately 150 mL, which covers approximately 6 % of the lung.

As for lung deformation analysis using the deformable image registration technique, the accuracies in displacement field and its gradient fields have to be taken into consideration in both in-plane and through-plane directions. The accuracy in displacement field is crucial for the anatomical comparison of perfusion distribution at two different lung volumes; how the lung material points have displaced from the reference lung to the deformed lung. Ding *et al.* reported the accuracy of image registration based displacement measurement where the lung was inflated from FRC to TLC and the true displacement vectors were estimated based on the movements in vessel bifurcation landmarks. The estimated displacement error, which is the difference between the true landmark displacement and computed displacement field, was less than 1 mm. Since the in-plane resolution of pulmonary perfusion was reduced to approximately 1 cm using Gaussian low pass filter in this study and the tidal volume inhalation is much smaller compared to the full inspiration to TLC, the in-plane displacement error is expected to be negligible. Through-plane resolution of ASL-FAIRER measurement was 1.5 cm and two adjacent sagittal slices overlapped by 1.0 cm. The displacement error should be also negligible compared to the measurement scale.

The accuracy in the gradient of displacement field which comprise the deformation matrix is also essential since the regional lung volume change ($V/V_0$) was computed as the determinant of Jacobian matrix. There was an implicit assumption that lobar deformation was continuous. Lobar sliding cannot be expressed by the continuous nature of cubic polynomial curve fit. Therefore, the deformation was separately computed for each of the three lobes. The regional lung volume change (determinant of Jacobian) was calculated accordingly within each lobe and reassembled based on the boundaries between the lobar segments. Therefore, this data treatment method practically avoided including Jacobian at the location of possible discontinuous displacement field.

The linear interpolation method was applied to the through-plane direction. Linear interpolation function is fundamentally less flexible than cubic function, which was used for the in-plane curve fit. However, it was sufficient for the

current study design. According to the mean value theorem, there exist points on the function within the finite region where the gradient is equal to the slope of linear interpolation function. If the actual spatial function of deformation is quadratic or less, the linear interpolation function gives a sufficient approximation of gradient within the error of measurement. The through-plane interval, which is the difference between the most medial and lateral image planes, was 2 cm (Figure 6.4). The underlying assumption was that the polynomial order of lateral lung deformation function was less than quadratic within the 2cm interval. Therefore, the regional lung volume change in through-plane direction would be captured at the target slice, which was located at the center of image stack. The deformation corrected density data shown in Figure 6.8 supported the validity of the technique.

Pulmonary perfusion measurement using ASL-FAIRER combined with the deformable image registration technique enables the quantification of the change in the spatial distribution of pulmonary perfusion at different lung volumes. The current study elucidated the effects of tidal volume lung inflation on pulmonary hemodynamics. The quasi-static tidal volume lung inflation replicating the end-expiratory volume which was achieved by negative pressure lung inflation. Subjects inhaled a predetermined volume of air and held the elevated lung volume with open glottis during MR image acquisition. The hemodynamics effect of negative pressure lung inflation has been gaining traction [33], however little is known in *in vivo* human lung. This study will be extended in future pulmonary physiology projects. For instance, the hemodynamic effects of positive pressure lung intervention, which would result in the increase in pulmonary vasculature resistance via compressing the pulmonary vessels will be compared with negative pressure inflation. That should shed light on the possible cause of the adverse effects of mechanical ventilation utilizing positive pressure inflation. Positive end-expiratory pressure (PEEP) will be used as the experimental intervention in which a human subject wearing a breathing mask exhales against a measured hydrostatic pressure.

## 6.7 Conclusion

Although there was a tendency for tidal volume lung inflation to reduce overall pulmonary perfusion, the change was not statistically significant. The lobar and gravitational perfusion redistributions without the influence of mean cardiac output change were also compared. The pulmonary perfusion was diverted from the nondependent part of lung, however no evidence of lobar redistribution was found. In conclusion, the tidal volume lung expansion did not cause significant change in the spatial distribution of pulmonary perfusion. Changes in hydrostatic pressure distribution due to the change in lung height are likely a bigger contributor to the pulmonary perfusion redistribution than the changes in pulmonary vasculature resistance due to changes in lung tissue stretch.

## 6.8 Acknowledgement

Chapter 6, in part, uses the material, which is currently prepared for submission for publication. Arai TJ; Villongco MT; Henderson AC; Dubowitz DJ; Darquenne C; Theilmann RJ; Sá RC; Friedman PJ; Buxton RB; Prisk GK; Hopkins SR.

## 6.9 Bibliography

[1] R. Amelon, K. Cao, K. Ding, G. E. Christensen, J. M. Reinhardt, and M. L. Raghavan. Three-dimensional characterization of regional lung deformation. *Journal of biomechanics*, 44(13):2489–2495, 2011.

[2] T. J. Arai, A. C. Henderson, D. J. Dubowitz, D. L. Levin, P. J. Friedman, R. B. Buxton, G. K. Prisk, and S. R. Hopkins. Hypoxic pulmonary vasoconstriction does not contribute to pulmonary blood flow heterogeneity in normoxia in normal supine humans. *Journal of applied physiology (Bethesda, Md. : 1985)*, 106(4):1057–1064, Apr 2009.

[3] T. J. Arai, C. T. Villongco, M. T. Villongco, S. R. Hopkins, and R. J. Theilmann. Affine transformation registers small scale lung deformation. *Conference proceedings: Annual International Conference of the IEEE Engineering*

*in Medicine and Biology Society. IEEE Engineering in Medicine and Biology Society. Conference*, 2012(1):5298–5301, 2012.

[4] K. J. Burnham, T. J. Arai, D. J. Dubowitz, A. C. Henderson, S. Holverda, R. B. Buxton, G. K. Prisk, and S. R. Hopkins. Pulmonary perfusion heterogeneity is increased by sustained, heavy exercise in humans. *Journal of applied physiology (Bethesda, Md. : 1985)*, 107(5):1559–1568, Nov 2009.

[5] K. S. Burrowes, R. B. Buxton, and G. K. Prisk. Assessing potential errors of MRI-based measurements of pulmonary blood flow using a detailed network flow model. *Journal of applied physiology (Bethesda, Md. : 1985)*, 113(1):130–141, Jul 2012.

[6] A. C. Burton and D. J. Patel. Effect on pulmonary vascular resistance of inflation of the rabbit lungs. *Journal of applied physiology*, 12(2):239–246, Mar 1958.

[7] S. Choi, E. A. Hoffman, S. E. Wenzel, M. H. Tawhai, Y. Yin, M. Castro, and C. L. Lin. Registration-based assessment of regional lung function via volumetric CT images of normal subjects vs. severe asthmatics. *Journal of applied physiology (Bethesda, Md. : 1985)*, 115(5):730–742, Sep 2013.

[8] A. Corrado, M G., R. Ginanni, C. Pelagatti, G. Villella, U. Buoncristiano, F. Guidi, E. Pagni, A. Peris, and E. De Paola. Negative pressure ventilation versus conventional mechanical ventilation in the treatment of acute respiratory failure in COPD patients. *European Respiratory Journal*, 12(3):519–525, 1998.

[9] K. Ding, Y. Yin, K. Cao, G. E. Christensen, C. L. Lin, E. A. Hoffman, and J. M. Reinhardt. Evaluation of lobar biomechanics during respiration using image registration. In *Medical Image Computing and Computer-Assisted Intervention–MICCAI 2009*, pages 739–746. Springer, 2009.

[10] H. Duplain, L. Vollenweider, A. Delabays, P. Nicod, P. Bärtsch, and U. Scherrer. Augmented sympathetic activation during short-term hypoxia and high-altitude exposure in subjects susceptible to high-altitude pulmonary edema. *Circulation*, 99(13):1713–1718, 1999.

[11] M. Ferrigno, D. D. Hickey, M. H. Liner, and C. E. Lundgren. Cardiac performance in humans during breath holding. *Journal of Applied Physiology*, 60(6):1871–1877, 1986.

[12] P. J. Friedman, R. M. Peters, M. C. Botkin, J. E. Brimm, and R. C. Meltvedt. Estimation of the volume of lung below the left atrium using computed tomography. *Critical care medicine*, 14(3):182–187, 1986.

[13] Y. C. Fung and S. S. Sobin. Elasticity of the pulmonary alveolar sheet. *Circulation research*, 30(4):451–469, Apr 1972.

[14] Y. C. Fung and S. S. Sobin. Pulmonary alveolar blood flow. *Circulation research*, 30(4):470–490, Apr 1972.

[15] B. Haefeli-Bleuer and E. R. Weibel. Morphometry of the human pulmonary acinus. *The Anatomical Record*, 220(4):401–414, 1988.

[16] T. S. Hakim, R. P. Michel, and H. K. Chang. Effect of lung inflation on pulmonary vascular resistance by arterial and venous occlusion. *Journal of applied physiology: respiratory, environmental and exercise physiology*, 53(5):1110–1115, Nov 1982.

[17] A. C. Henderson, R. C. Sá, R. J. Theilmann, R. B. Buxton, G. K. Prisk, and S. R. Hopkins. The gravitational distribution of ventilation-perfusion ratio is more uniform in prone than supine posture in the normal human lung. *Journal of applied physiology (Bethesda, Md. : 1985)*, 115(3):313–324, Aug 2013.

[18] S. Holverda, R. J. Theilmann, R. C. Sá, T. J. Arai, E. T. Hall, D. J. Dubowitz, G. K. Prisk, and S. R. Hopkins. Measuring lung water: ex vivo validation of multi-image gradient echo MRI. *Journal of magnetic resonance imaging : JMRI*, 34(1):220–224, Jul 2011.

[19] S. R. Hopkins, T. J. Arai, A. C. Henderson, D. L. Levin, R. B. Buxton, and G. K. Prisk. Lung volume does not alter the distribution of pulmonary perfusion in dependent lung in supine humans. *The Journal of physiology*, 588(Pt 23):4759–4768, Dec 2010.

[20] S. R. Hopkins, A. C. Henderson, D. L. Levin, K. Yamada, T. Arai, R. B. Buxton, and G. K. Prisk. Vertical gradients in regional lung density and perfusion in the supine human lung: the slinky effect. *Journal of applied physiology (Bethesda, Md. : 1985)*, 103(1):240–248, Jul 2007.

[21] J. B. Howell, S. Permutt, D. F. Proctor, and R. L. Riley. Effect of inflation of the lung on different parts of pulmonary vascular bed. *Journal of applied physiology*, 16:71–76, Jan 1961.

[22] S. Kira and Y. Hukushima. Effect of negative-pressure inflation on pulmonary vascular flow. *Journal of applied physiology*, 25(1):42–47, Jul 1968.

[23] S. J. Lai-Fook. A continuum mechanics analysis of pulmonary vascular interdependence in isolated dog lobes. *Journal of applied physiology: respiratory, environmental and exercise physiology*, 46(3):419–429, Mar 1979.

[24] R. Looga. Reflex cardiovascular responses to lung inflation: a review. *Respiration physiology*, 109(2):95–106, 1997.

[25] V. G. Macefield. Sustained activation of muscle sympathetic outflow during static lung inflation depends on a high intrathoracic pressure. *Journal of the autonomic nervous system*, 68(3):135–139, 1998.

[26] F. Peták, G. Albu, E. Lele, Z. Hantos, D. R. Morel, F. Fontao, and W. Habre. Lung mechanical and vascular changes during positive- and negative-pressure lung inflations: importance of reference pressures in the pulmonary vasculature. *Journal of Applied Physiology*, 106(3):935–942, 2009.

[27] G K. Prisk, H. J. Guy, A. R. Elliott, M. Paiva, and J. B. West. Ventilatory inhomogeneity determined from multiple-breath washouts during sustained microgravity on spacelab SLS-1. *Journal of Applied Physiology*, 78(2):597–607, 1995.

[28] G. K. Prisk, K. Yamada, A. C. Henderson, T. J. Arai, D. L. Levin, R. B. Buxton, and S. R. Hopkins. Pulmonary perfusion in the prone and supine postures in the normal human lung. *Journal of applied physiology (Bethesda, Md. : 1985)*, 103(3):883–894, Sep 2007.

[29] A. Roos, L. J. Thomas, E. L. Nagel, and D. C. Prommas. Pulmonary vascular resistance as determined by lung inflation and vascular pressures. *Journal of applied physiology*, 16:77–84, Jan 1961.

[30] R. C. Sá, M. V. Cronin, A. C. Henderson, S. Holverda, R. J. Theilmann, T. J. Arai, D. J. Dubowitz, S. R. Hopkins, R. B. Buxton, and G. K. Prisk. Vertical distribution of specific ventilation in normal supine humans measured by oxygen-enhanced proton MRI. *Journal of Applied Physiology*, 109(6):1950–1959, 2010.

[31] H. Sakuma, N. Kawada, H. Kubo, Y. Nishide, K. Takano, N. Kato, and K. Takeda. Effect of breath holding on blood flow measurement using fast velocity encoded cine MRI. *Magnetic resonance in medicine*, 45(2):346–348, 2001.

[32] P. S. Shah, A. Ohlsson, and J. P. Shah. Continuous negative extrathoracic pressure or continuous positive airway pressure compared to conventional ventilation for acute hypoxaemic respiratory failure in children. *status and date: New search for studies and content updated (no change to conclusions), published in*, (9), 2008.

[33] L. S. Shekerdemian, I. Schulze-Neick, A. N. Redington, A. Bush, and D. J. Penny. Negative pressure ventilation as haemodynamic rescue following surgery for congenital heart disease. *Intensive care medicine*, 26(1):93–96, 2000.

[34] I. Taneja, M. S. Medow, D. A. Clarke, A. J. Ocon, and J. M. Stewart. Postural change alters autonomic responses to breath-holding. *Clinical Autonomic Research*, 20(2):65–72, 2010.

[35] V. Tedjasaputra, R. C. Sá, T. J. Arai, S. Holverda, R. J. Theilmann, W. T. Chen, P. D. Wagner, C. K. Davis, G. K. Prisk, and S. R. Hopkins. The heterogeneity of regional specific ventilation is unchanged following heavy exercise in athletes. *Journal of applied physiology (Bethesda, Md. : 1985)*, 115(1):126–135, Jul 2013.

[36] R. J. Theilmann, T. J. Arai, A. Samiee, D. J. Dubowitz, S. R. Hopkins, R. B. Buxton, and G. K. Prisk. Quantitative MRI measurement of lung density must account for the change in t(2) (*) with lung inflation. *Journal of magnetic resonance imaging : JMRI*, 30(3):527–534, Sep 2009.

[37] L. J. Thomas, Z. J. Griffo, and A. Roos. Effect of negative-pressure inflation of the lung on pulmonary vascular resistance. *Journal of applied physiology*, 16:451–456, May 1961.

[38] D. Urboniene, I. Haber, Y. H. Fang, T. Thenappan, and S. L Archer. Validation of high-resolution echocardiography and magnetic resonance imaging vs. high-fidelity catheterization in experimental pulmonary hypertension. *American Journal of Physiology-Lung Cellular and Molecular Physiology*, 299(3):L401–L412, 2010.

[39] J. B. West, C. T. Dollery, and A. Naimark. Distribution of blood flow in isolated lung; relation to vascular and alveolar pressures. *Journal of applied physiology*, 19:713–724, Jul 1964.

[40] R. T. Yen and L. Foppiano. Elasticity of small pulmonary veins in the cat. *Journal of biomechanical engineering*, 103(1):38–42, Feb 1981.

[41] R. T. Yen, Y. C. Fung, and N. Bingham. Elasticity of small pulmonary arteries in the cat. *Journal of biomechanical engineering*, 102(2):170–177, May 1980.

# Chapter 7

# Conclusion and perspectives

## 7.1 Introduction

Gas exchange between inhaled alveolar air and pulmonary capillary blood occurs in the lung. The relationship between local ventilation and local perfusion determines the global efficiency of gas exchange. The normal healthy lung maintains the regional ventilation-perfusion ratio close to one, through an interplay of regulatory mechanisms. Functional pulmonary magnetic resonance imaging technology can quantify some of these effects and help to assess their relative importance. The original research presented in this dissertation focused on the regional distribution of pulmonary perfusion in supine humans, in particular the influence of (1) hypoxic pulmonary vasoconstriction (HPV) and (2) lung tissue stretch due to tidal volume lung inflation. In this chapter, the major findings of my research work are restated, and future work is briefly presented.

## 7.2 Quantification of Pulmonary Perfusion and Tissue Density Using Magnetic Resonance Imaging

An arterial spin labeling (ASL-FAIRER) technique was used to quantify regional pulmonary blood flow in units of mL(blood)/min/cm$^3$(voxel). The quan-

tified ASL map was further processed to derive a map of pulmonary perfusion; the image voxels containing large conduit vessels were removed using a threshold value of 35% of maximum signal intensity and remaining voxels were smoothed using a 2D Gaussian low pass filter to adjust the effective spatial resolution of 10 × 10 × 15 mm.

A multi-echo fast gradient echo sequence (mGRE) was used to quantify the local pulmonary tissue density in units of g(tissue)/cm$^3$(voxel). Division of perfusion by density yielded density normalized perfusion (DNP) expressed in the units of mL(blood)/min/g(tissue). DNP reflects the amount of blood perfused into a gram of tissue within a unit of time.

Pulmonary perfusion heterogeneity was evaluated using three indices; relative dispersion (RD), fractal dimension ($D_s$) and the lognormal shape parameter ($\sigma$).

As described in Chapter 2, pulmonary perfusion measurements using ASL-FAIRER have some limitations. In particular, the removal of large conduit vessels may be improved by basing it on actual lung anatomy or the lognormal nature of pulmonary perfusion distribution rather than using a threshold value of 35% of maximum signal intensity.

## 7.3 Conducting Pulmonary Physiology Studies in The MR Scanner Environment

Magnetic resonance imaging is a powerful tool to noninvasively visualize a human anatomy and function. However, the inside of an MR scanner is a unique environment; the inner diameter of an MR bore is approximately 60 cm, which may induce some human subjects to feel claustrophobic: It is also a loud environment, as the magnetic gradient coil generates sound.

Therefore, the MRI study setup was carefully designed to provide a tolerable experimental environment to the participants. The participant's cardiopulmonary vital signals were constantly monitored throughout the imaging session. This was essential for the subject's safety and reliable physiological data acquisition.

## 7.4 Lung Deformation Analysis via Image Registration

The motion of breathing causes lung deformation, and the shape of the lung captured in an MR image varies with lung volume. Two MR lung images obtained at two different lung volumes are registered so that these two lungs are rendered based on the anatomical correspondence of points in the two images. The spatial pattern of deformation was modeled and parameterized using polynomial interpolation method. Therefore, the lung deformation was approximated as a continuous spatial function. The image registration technique used for my dissertation research allowed to compute not only 2 dimensional but also 3 dimensional lung deformation.

The type of basis function in use and the number of parameters determine the degrees of freedom of the spatial function. The optimal number of parameters must be chosen based on the spatial scale of physiological question being addressed. It is also associated with a computational cost; the more the parameters, the more computational time and power are required.

The continuity imposed in most image registration frameworks might not be suited to express the deformation in the whole lung. There are three and two lobes in the right and left lung, respectively. Between adjacent lobes, sliding may occur along a fissure when the lung deforms due to respiratory motion. The sliding is mathematically expressed as a discontinuous displacement field. However, individual lobar deformation is expected to be spatially continuous. In order to avoid the possible errors arising from lobar sliding, the deformation was computed separately for each lobe and then combined to comprise a whole lung deformation field.

## 7.5 The contribution of hypoxic pulmonary vasoconstriction to pulmonary perfusion heterogeneity

The effects of different fractions of inspired oxygen (normoxia, $F_IO_2 = 0.21$; hypoxia, $F_IO_2 = 0.125$; hyperoxia, $F_IO_2 = 0.30$) on the spatial distribution of pulmonary perfusion in supine human lungs were tested. It was hypothesized that some of the heterogeneity of pulmonary perfusion distribution present in the normal human lung in normoxia is due to hypoxic pulmonary vasoconstriction (HPV). If so, mild hyperoxia should decrease the heterogeneity since removing the hypoxic stimulus should universally dilate the pulmonary vessels, resulting in a more spatially uniform pulmonary perfusion distribution. On the other hand, HPV would be increased by mild hypoxia. Contrary to our hypothesis, this study concluded that in supine normoxic humans, the heterogeneity of pulmonary blood flow observed within an isogravitational plane was not due to hypoxic pulmonary vasoconstriction and gross redistribution of pulmonary blood flow both during hypoxia and hyperoxia was not present. Thus, the results of this study suggest that the observed heterogeneity of pulmonary blood flow is caused by other factors such as structural or gravitational in nature.

However, dynamic changes in the vascular system may not strongly manifest as changes in overall spatial heterogeneity. A more recent study from our group highlighted that changes in pulmonary vasomotor tone in response to different $F_IO_2$ induce changes in the observable spatio-temporal dynamics of pulmonary perfusion, but not gross changes in overall perfusion heterogeneity [1]. Such detectable dynamic vascular responses may lead to new methods of early detection of pulmonary disease, such as pulmonary artery hypertension (PAH). Therefore, new experimental designs, aimed at probing pulmonary vascular reactivity and dynamic response are crucial in pursuing this goal.

## 7.6 The effect of lung deformation on the spatial distribution of pulmonary blood flow

The pulmonary hemodynamic effects of lung inflation induced by tidal volume breaths (starting at functional residual capacity (FRC) and inhaling + 500 mL or + 1 liter) were tested *in vivo* in supine humans. The results show tidal volume lung inflation resulted in a small reduction in overall pulmonary perfusion, however the change was not statistically significant. The lobar and gravitational perfusion redistributions, after removal of the influence of cardiac output changes were also compared. Pulmonary perfusion was redistributed away from the non-dependent region of lung, however no evidence of lobar redistribution was found. Therefore, the study concluded that tidal volume lung expansion does not cause significant change in the spatial distribution of pulmonary perfusion. Changes in hydrostatic pressure distribution due to the change in lung height are likely a bigger contributor to the pulmonary perfusion redistribution than the changes in pulmonary vasculature resistance due to changes in lung tissue stretch.

The present study was performed in a single sagittal plane denoted as a target slice in the right lung. Even though multiple sagittal images at different lateral slice locations were obtained in 5 mm slice intervals, these extra image slices were only utilized to estimate the through-plane deformation of the target slice in the present report. The lung region covered by this a single slice was approximately 150 mL, which covers approximately 6 % of the lung. In healthy subjects the target slice is likely representative of the whole right lung; however, this is certainly not the case in a disease lung in which the dysfunctions are heterogeneously located such as asthma and chronic obstructive pulmonary disease (COPD). In the future, this study could be extended to the whole lung, so as to be applicable to patient populations. The current ASL-FAIRER acquisition is limited to a single image slice and takes approximately 5 to 10 sec to obtain one ASL image depending on the breathing maneuver. Thus, the time required to scan the entire lung increases with the number of slice. In order to reduce human subject's time spent in the MR scanner, a faster ASL acquisition would constitute a significant step forward.

Pulmonary perfusion measurement using ASL-FAIRER combined with the deformable image registration technique enabled the quantification of the change in the spatial distribution of pulmonary perfusion at different lung volumes. The quasi-static tidal volume lung inflation replicating the end-expiratory volume was achieved by negative pressure lung inflation. This study will be extended in future pulmonary physiology projects. For instance, the hemodynamic effects of positive pressure lung intervention, which would result in the increase in pulmonary vasculature resistance via compressing the pulmonary vessels will be compared with negative pressure inflation. That should shed light on the possible cause of the adverse effects of mechanical ventilation utilizing positive pressure inflation.

## 7.7 Bibliography

[1] A. K. Asadi, M. V. Cronin, R. C. Sá, R. J. Theilmann, S. Holverda, S. R. Hopkins, R. B. Buxton, and G. K. Prisk. Spatial-temporal dynamics of pulmonary blood flow in the healthy human lung in response to altered FIO2. *Journal of Applied Physiology*, 114(1):107–118, 2013.

# Appendix A

# Mathematical Models in Pulmonary Physiology

## A.1 Zone model

West *et al.* proposed the Zone model [13], which relates pulmonary capillary perfusion to the local blood (inside) pressure and alveolar air (outside) pressure. In this model, the lung is divided into three gravitational zones, with gravity affecting the hydrostatic pressure in the blood:

$$Zone\,1 \quad : p_A > p_a > p_v \tag{A.1}$$

$$Zone\,2 \quad : p_a > p_A > p_v \tag{A.2}$$

$$Zone\,3 \quad : p_a > p_v > p_A \tag{A.3}$$

where the subscripts A, and a and v stand for alveolar air, arterial blood and venous blood respectively. $p_A$ is constant throughout the lung. On the other hand, $p_a$ and $p_v$ are subjected to hydrostatic pressure so that they linearly increase towards the gravitationally dependent direction. In Zone 1, alveolar air pressure exceeds arterial pressure since pulmonary artery pressure decreases as with height from the dependent region. In this region, the pulmonary capillaries are collapsed and held closed. Therefore, there is no blood flow.

In Zone 2, the arterial pressure exceeds alveolar air pressure but the alveolar air pressure exceeds venous pressure. Under these conditions, there is a constriction at the downstream end of capillary where the pressure inside is equal to the alveolar pressure. In this case, the pressure gradient depend only on the arterial pressure since the alveolar air pressure stays constant. This is the so called waterfall effect: the flow only depends on the pressure at the upper stream.

In Zone 3, venous exceeds alveolar pressure so that pulmonary capillaries are held open. Then, the pressure gradient is determined by the difference between arterial pressure and venous pressure. The transmural pressure increases towards the bottom of Zone 3, so that capillary dilate. Therefore, the blood flow also increases. However, the change is less rapid than in Zone 2 because the pressure gradient ($p_a$ - $p_v$) stays same. There is an additional zone, namely Zone 4 in the most dependent region of lung. In Zone 4, the pulmonary blood flow is reduced in spite of higher intravascular pressure in the capillaries [12]. The cause of Zone 4 behavior is ascribed to the greater resistance in extra-alveolar vessels since the cross-section area of these vessels is narrowed by the increased interstitial pressure. In addition, the longer vascular pathways from pulmonary artery to the more peripheral region of lung are also associated to the reduction in the flow in the zone [2, 3, 11].

## A.2 Sheet model and fourth power law

Other important pulmonary circulation models were developed by Y.C. Fung and S.S. Sobin [5, 6]. In particular, the sheet model describes the pulmonary capillary blood flow. The geometry of dense pulmonary capillary network in the interalveolar septa was simplified as a sheet of fluid flowing between two membranes held apart by a number of posts. The sheet is characterized by three parameters; the sheet height, $h$, the area of alveolar sheet $A$ and the vascular-space-tissue ratio $S$, which is the fraction of the alveolar sheet occupied by the blood. The sheet is elastic so that the sheet height is a function of pressure. Experimental results in cat lungs have shown the following linear relationship.

$$h = h_0 + \alpha(p - p_A) \tag{A.4}$$

where $p$ is the blood pressure, $h_0$ is the thickness of sheet when $p = p_A$, and $\alpha$ is the compliance constant of capillary sheet. Equation A.4 is valid when $p$ - $p_A > 0$ and smaller than approximately 15 cm $H_2O$ [4, 6] beyond which $h$ becomes asymptotic. When $p$ - $p_A < 0$, the capillaries are collapsed and $h$ tends to zero. Using equation A.4 together with the equation of continuity and motion, and an experimentally verified linear relationship between local flow velocity and pressure gradient, Fung and Sobin [6] obtained the following pressure-flow relationship.

$$\dot{Q} = const[{h_{art}}^4 - {h_{ven}}^4] \tag{A.5}$$

$$= const\{[h_0 + \alpha(p_{art} - p_A)]^4 - [h_0 + \alpha(p_{ven} - p_A)]^4\} \tag{A.6}$$

where $\dot{Q}$ is the volume flow rate, $h_{art}$ and $h_{ven}$ are the sheet thicknesses at the arteriole where the blood enters into the sheet and venule where the blood exits from the sheet, respectively. And $p_{art}$ and $p_{ven}$ are the pressure at the corresponding arteriole and venule. The *const* in equations A.5 and A.6 is

$$SA/(4\mu K f \bar{L}^2 \alpha) \tag{A.7}$$

where $\mu$ is the apparent viscosity of blood in the capillary sheet, $K$ is dimensionless factor, which is a function of the ratio of the thickness to width of the capillary sheet and has a numerical value of about 12, and $f$ is a friction factor, which is a function of the ratio of post diameter to the sheet thickness and other flow parameters. $\bar{L}$ is the average length of blood pathway between the inlet and outlet. The equation A.5 is so called the fourth power law.

Further analytical discussion was done on the Zone 2 condition. When the alveolar air pressure $p_A$ is greater than venule pressure $p_{ven}$, the sheet membrane tensile stress prevents the alveolar sheet septa from completely being collapsed at the exit of one-dimensional capillary model. The membranes are curved inward if the sheets are limited in their length. Therefore, venules are kept open. The product of tension and curvature is equivalent to the pressure gradient between $p_A$

and the local blood pressure $p$. This is called the sluicing gate [7, 9]. In the three-dimensional alveoli model, the sheet height can be completely collapsed ($h = 0$) in some areas where there is no flow, while the remaining areas can handle the rest of flow. This is termed "patchy flow". In fact, the red blood cell distribution in the interalveolar septa is patchy, containing regions with cells and regions without. When the sheet is collapsed, endothelial cells on the sheet membranes adhere. Once two membranes adhere, it takes more energy to re-separate them. The experimental results suggested that the re-separation could be accomplished by raising $p_v$ to the Zone 3 condition [8].

## A.3 Fifth power law

In pulmonary arteries and veins, the vessel wall is distensible so that the diameter $D$ changes linearly with blood pressure $p$ [14, 15].

$$D = D_0 + \alpha p \tag{A.8}$$

where $D_0$ is known as the tube diameter when $p$ is zero and $\alpha$ is the compliance constant. The analytical solution for the steady flow of a viscous incompressible fluid in such a tube yields

$$\frac{640\mu\alpha L}{\pi}\dot{Q} = [D(0)]^5 - [D(L)]^5 = [D_0 + \alpha p_{entry}]^5 - [D_0 + \alpha p_{exit}]^5 \tag{A.9}$$

Equation A.9 is fifth power law. This is analogous to the forth power law from the capillary sheet model.

## A.4 Graphical representation of ventilation and perfusion relationship

In Figure A.1, equation 1.1 is explained graphically. A functional imaging modality such as MRI quantitatively measures the spatial distributions of ventilation ($\dot{V}_A$) and perfusion ($\dot{Q}$) in a lung. The two independently measured spatial

data are co-localized (registered) and the resulting spatially paired ventilation and perfusion data are plotted on log-log graph as shown in Figure A.1 where the X and Y axes represent perfusion and ventilation, respectively. In the $\dot{V}_A$ - $\dot{Q}$ log-log graph, any data points which lie on a line parallel to the identity line have the same ventilation to perfusion ratio ($\dot{V}_A/\dot{Q}$). The identity line represents all units where $\dot{V}_A/\dot{Q}$ is unity. Two broken lines in Figure A.1 represent $\dot{V}_A/\dot{Q} = 10$ and 0.1, respectively. Therefore, $\dot{V}_A/\dot{Q}$ dispersion i.e. ventilation - perfusion inequity is characterized as the standard deviation of the scattered data points in the direction perpendicular to the identity line ($\sigma_{V_A/Q}$). A more efficient lung has a smaller $\dot{V}_A/\dot{Q}$ dispersion.

As described in equation 1.1, $\sigma_{V_A/Q}$ is a function of the underlying standard deviation of ventilation ($\sigma_{V_A}$), perfusion ($\sigma_Q$), and correlation coefficient between $\dot{V}_A$ and $\dot{Q}$ ($R$), respectively. In other words, ${\sigma_{V_A/Q}}^2$ is associated with data dispersions in both the X and Y directions and the correlation between ventilation and perfusion shown in Figure A.1. The measured $\sigma_{V_A/Q}$ is also related to the spatial resolution of measurement technique. For the author's dissertation research, the spatial scale has been set to approximately 1 $cm^3$ based on a study of ventilation - perfusion matching in normal human lungs measured using MR technique [10]. However, the optimal scale for evaluating ventilation - perfusion inequity, in particular for patient with pulmonary disease, is still open for debate.

Figure A.2 shows 3 different indices of $\dot{V}_A/\dot{Q}$ dispersion. The green broken line represents $\dot{V}_A/\dot{Q}$ distribution, which is the projection of ventilation - perfusion scattered data (Figure A.1) on the line perpendicular to the identity line. Therefore, the width of distribution is closely related to $\sigma_{V_A/Q}$. The multiple inert gas elimination technique (MIGET) measures ventilation weighted $\dot{V}_A/\dot{Q}$ and perfusion weighted $\dot{V}_A/\dot{Q}$ distributions shown in the blue and red solid lines, respectively. MIGET derived parameters LogSD$\dot{V}$ and LogSD$\dot{Q}$ are equivalent to $\sigma_{V_A/Q}$ for the ventilation weighted distribution (blue solid line) and the perfusion weighted distribution (red solid line), respectively.

It must be noted that LogSD$\dot{V}$ and LogSD$\dot{Q}$ do not directly describe ventilation and perfusion abnormalities directly. Rather, their interpretation depends

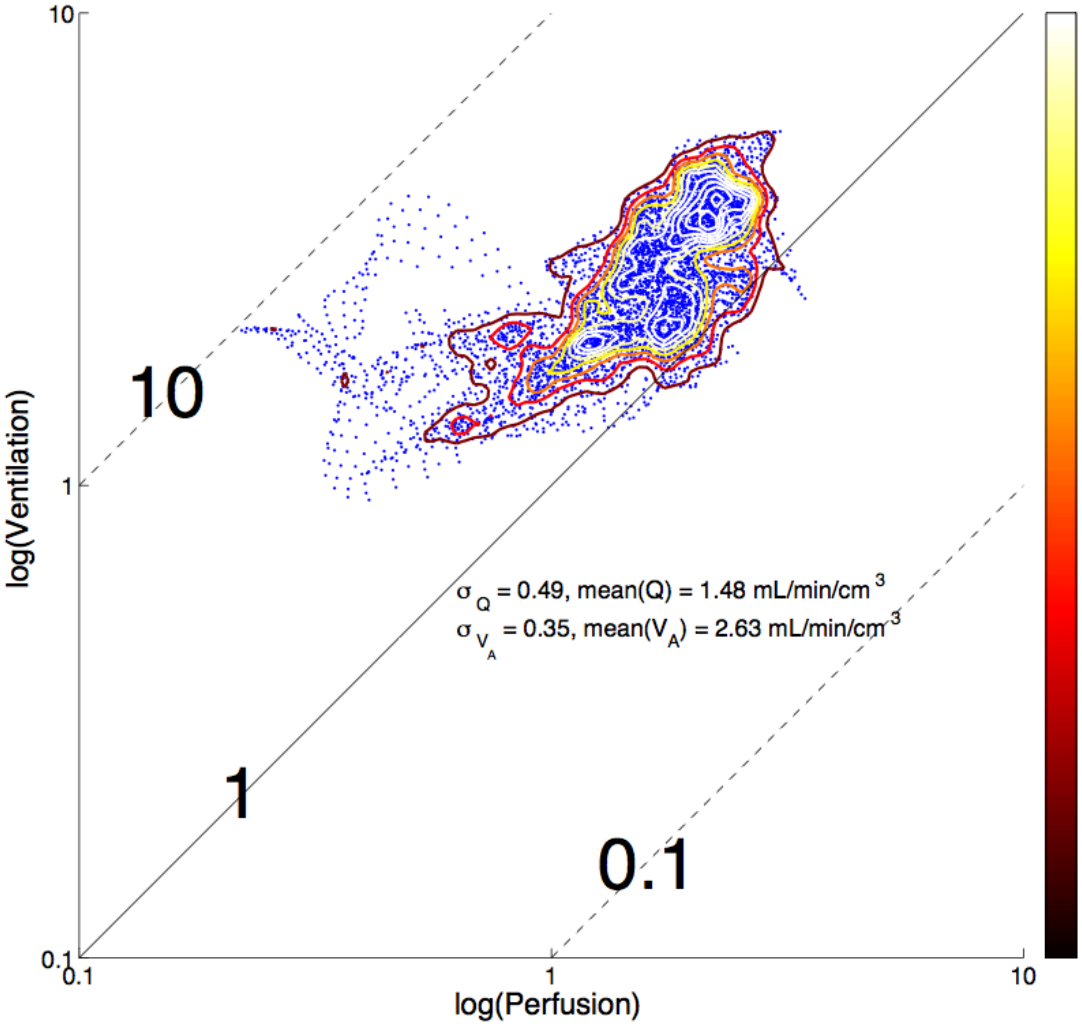


**Figure A.1**: Ventilation and perfusion relationships plotted in log-log scale. Perfusion and ventilation in supine a healthy human were measured using functional pulmonary MRI [1]. Contour lines and color bar represent the data density in the plot. The identity line represents $\dot{V}_A/\dot{Q} = 1$ while the two broken lines represent $\dot{V}_A/\dot{Q} = 10$ and 0.1, respectively. $\dot{V}_A/\dot{Q}$ dispersion is characterized as standard deviation of the scattered data in the direction perpendicular to the identity line ($\sigma_{V_A/Q}$).

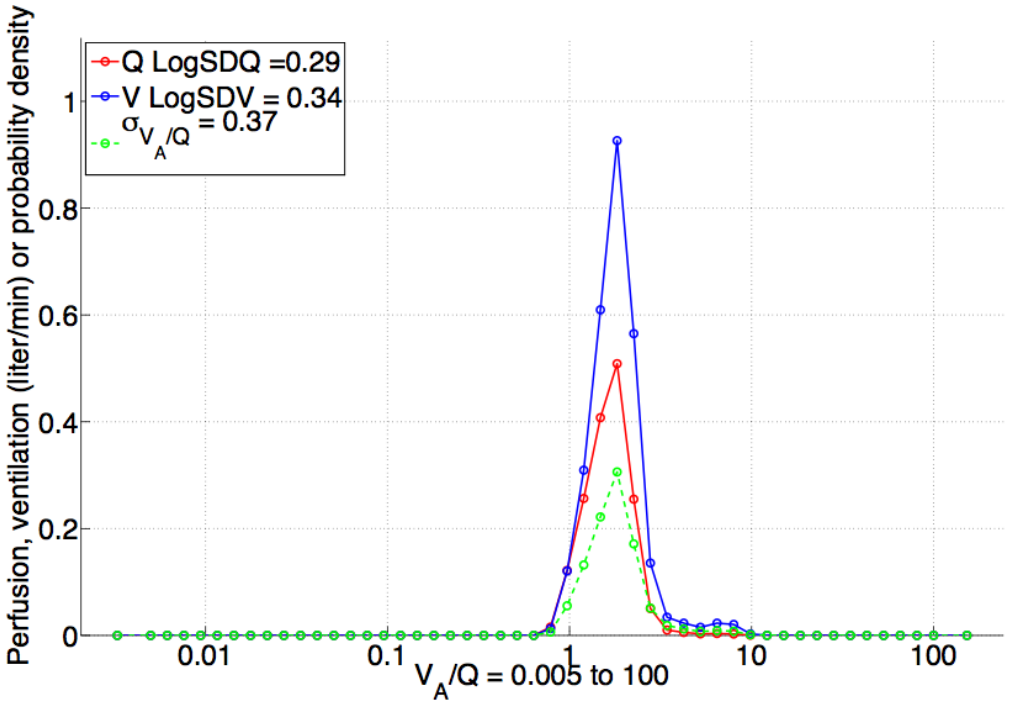


**Figure A.2**: Three different indices of $\dot{V}_A/\dot{Q}$ dispersion. $\dot{V}_A/\dot{Q}$ distribution (green broken line) is given as a projection of ventilation - perfusion data in the perpendicular direction to the identity line in the log-log graph shown in Figure A.1. Multiple inert gas elimination technique measures ventilation weighted $\dot{V}_A/\dot{Q}$ distribution (blue solid line) and perfusion weighted $\dot{V}_A/\dot{Q}$ distribution (red solid line). $\sigma_{V_A/Q}$, LogSDV and LogSDQ are associated with the width of the green broken, the blue solid, and the red solid bell-curves.

of the relationship between ventilation and perfusion heterogeneity, sometimes resulting in these indices describing pulmonary physiological and pathological event counterintuitively. For instance in the case of pulmonary embolism, which is a pulmonary circulatory abnormality, the reduction in pulmonary perfusion in the region of obstruction results in an increase in $\dot{V}_A/\dot{Q}$. It further results in the increase in the high $\dot{V}_A/\dot{Q}$ region of blue bell-curve distribution (the ventilation weighted distribution) in Figure A.2. LogSD$\dot{V}$ may also increase. However, the increase is not seen in red bell-curve distribution (the perfusion weighted distribution). The high $\dot{V}_A/\dot{Q}$ region is multiplied by the reduced perfusion, which is close to zero flow due to the embolism. In this scenario, the elevated LogSD$\dot{V}$ is an indication of a pulmonary perfusion abnormality.

## A.5 Bibliography

[1] T. J. Arai, R. C. Sá, V. Tedjasaputra, G. K. Prisk, and S. R. Hopkins. Ventilation-perfusion heterogeneity in the lung: insights from the underlying distributions of ventilation and perfusion. In *Am J Respir Crit Care Med*, volume 185, page A2684, 2012.

[2] K. S. Burrowes, P. J. Hunter, and M. H. Tawhai. Investigation of the relative effects of vascular branching structure and gravity on pulmonary arterial blood flow heterogeneity via an image-based computational modellt; sup¿ 1lt;/sup¿. *Academic radiology*, 12(11):1464–1474, 2005.

[3] K. S. Burrowes, P. J. Hunter, and M. H. Tawhai. Evaluation of the effect of postural and gravitational variations on the distribution of pulmonary blood flow via an image-based computational model. In *Engineering in Medicine and Biology Society, 2005. IEEE-EMBS 2005. 27th Annual International Conference of the*, pages 6138–6140. IEEE, 2006.

[4] A. R. Clark, K. S. Burrowes, and M. H. Tawhai. Contribution of serial and parallel microperfusion to spatial variability in pulmonary inter- and intraacinar blood flow. *Journal of applied physiology (Bethesda, Md. : 1985)*, 108(5):1116–1126, May 2010.

[5] Y. C. Fung and S. S. Sobin. Elasticity of the pulmonary alveolar sheet. *Circulation research*, 30(4):451–469, Apr 1972.

[6] Y. C. Fung and S. S. Sobin. Pulmonary alveolar blood flow. *Circulation research*, 30(4):470–490, Apr 1972.

[7] Y. C. Fung, S. S. Sobin, H. Tremer, M. R. Yen, and H. H. Ho. Patency and compliance of pulmonary veins when airway pressure exceeds blood pressure. *Journal of applied physiology: respiratory, environmental and exercise physiology*, 54(6):1538–1549, Jun 1983.

[8] Y. C. Fung and R. T. Yen. A new theory of pulmonary blood flow in zone 2 condition. *Journal of applied physiology (Bethesda, Md. : 1985)*, 60(5):1638–1650, May 1986.

[9] Y. C. Fung and F. Y. Zhuang. An analysis of the sluicing gate in pulmonary blood flow. *Journal of biomechanical engineering*, 108(2):175–182, May 1986.

[10] A. Cortney Henderson, Rui Carlos Sá, Rebecca J. Theilmann, Richard B. Buxton, G. Kim Prisk, and Susan R. Hopkins. The gravitational distribution of ventilation-perfusion ratio is more uniform in prone than supine posture in the normal human lung. *Journal of applied physiology (Bethesda, Md. : 1985)*, 115(3):313–324, Aug 2013.

[11] S. R. Hopkins, T. J. Arai, A. C. Henderson, D. L. Levin, R. B. Buxton, and G. K. Prisk. Lung volume does not alter the distribution of pulmonary perfusion in dependent lung in supine humans. *The Journal of physiology*, 588(Pt 23):4759–4768, Dec 2010.

[12] J. M. Hughes, J. B. Glazier, J. E. Maloney, and J. B. West. Effect of lung volume on the distribution of pulmonary blood flow in man. *Respiration physiology*, 4(1):58–72, Jan 1968.

[13] J. B. West, C. T. Dollery, and A. Naimark. Distribution of blood flow in isolated lung; relation to vascular and alveolar pressures. *Journal of applied physiology*, 19:713–724, Jul 1964.

[14] R. T. Yen and L. Foppiano. Elasticity of small pulmonary veins in the cat. *Journal of biomechanical engineering*, 103(1):38–42, Feb 1981.

[15] R. T. Yen, Y. C. Fung, and N. Bingham. Elasticity of small pulmonary arteries in the cat. *Journal of biomechanical engineering*, 102(2):170–177, May 1980.

# Appendix B

# ASL Appendix

The details of derivation of equation 2.2 are described in this section [1, 2]. The ASL acquisition involves the subtraction of two images. Silicone phantoms (Breast Implant Round 250cc, Mentor) with known $T_1$ and $T_2$ were placed on a human subject in the imaging field of view and used for the calibration. The volume of blood delivered to a voxel within one cardiac cycle ($V$) depends on the blood flow $F$, which is the quantified pulmonary blood flow in units of mL(blood)/min/cm$^3$(voxel). The voxel volume is denoted as $V_{voxel}$ and the R-R interval is $T_{RR}$.

$$V = FV_{voxel}T_{RR} \tag{B.1}$$

$V_{gap}$ is the volume of blood within the gap. The volume of tagged blood ($V_{ASL}$) that is delivered to the voxel during one cardiac cycle is

$$V_{ASL} = V - V_{gap} \tag{B.2}$$

The measured ASL signal, which is the difference between the control and tag images, is denoted as $\Delta S$. the fractional filling of the voxel is

$$\Delta S = \frac{V_{ASL}}{V_{voxels}} \Delta S_B \tag{B.3}$$

where $\Delta S_B$ is the ASL signal when the voxel is completely filled with the tagged blood.

In the control image, the longitudinal magnetization in the blood coming from outside the selective inversion slice is completely relaxed. On the other hand, in the tag image, the magnetization of blood outside the slice is described as inversion recovery growing from $M_{0B}$, with time constant $T_{1B}$. $\Delta S$ is also described as following.

$$\Delta S_B = {S_B}^C - {S_B}^T \tag{B.4}$$

$$= \left[M_{0B} - M_{0B}\left(1 - 2e^{\frac{-T_I}{T_{1B}}}\right)\right] e^{\frac{-T_E}{T_{2B}}} C_{torso}(x,y)k \tag{B.5}$$

$$= 2M_{0B} exp\left(-T_I/T_{1B}\right) exp\left(-T_E/T_{2B}\right) C_{torso}(x,y)k \tag{B.6}$$

where ${S_B}^C$ and ${S_B}^T$ are the blood signals in the control and tag images, respectively at the time of image acquisition. $k$ represents scanner receiver gain and $C_{torso}(x,y)$ is the sensitivity profile of the torso coil (Section 2.6.3). In both images, transverse magnetization decay $T_{2B}$ is identical. $M_{0B}$ represents the fully relaxed longitudinal magnetization of blood. TI is the time between the application of inversion RF pulse and the initiation of image acquisition, which is set to be approximately 80% of R-R interval. TE is the echo time. The signal of the phantom ($S_P$) in the control and tag image grows from zero due to the extra saturation RF pulse with the time constant $T_{1P}$.

$$S_P = M_{0P}\left[1 - exp(-T_I/T_{1P})\right] exp(-T_I/T_{2P}) C_{torso}(x_p, y_p)k \tag{B.7}$$

where $M_{0P}$ is the longitudinal magnetization of the phantom when it is fully relaxed. $T_{2P}$ is the transverse decay of phantom. The fully relaxed longitudinal magnetization of blood and the phantom is related by the following equation.

$$M_{0B} = RM_{0P} \tag{B.8}$$

where $R$ is the measured ratio of proton density of blood to the silicon phantom. This value is 0.4. Substituting $M_{0P}$ into equation B.7 for $M_{0B}$

$$\Delta S_B = 2RM_{0P} exp\left(-T_I/T_{1B}\right) exp\left(-T_E/T_{2B}\right) C_{torso}(x,y)k \tag{B.9}$$

Substituting $M_{0P}$ using equation B.8

$$\Delta S_B = 2R \left[ \frac{S_P}{\left(1 - e^{-T_I/T_{1P}}\right) e^{-T_E/T_{2P}} C_{torso}(x_p, y_p)} \right] e^{-T_I/T_{1B}} e^{-T_E/T_{2B}} C_{torso}(x, y) k \tag{B.10}$$

Using equations B.1, B.2, and B.3 to solve for blood flow as a function of $\Delta S_B$

$$F = \frac{V}{V_{voxel} T_{RR}} = \frac{V_{ASL}}{V_{voxel} T_{RR}} + \frac{V_{gap}}{V_{voxel} T_{RR}} \tag{B.11}$$

$$= \frac{\Delta S}{\Delta S_B T_{RR}} + \frac{V_{gap}}{V_{voxel} T_{RR}} \tag{B.12}$$

Substituting for $\Delta S_B$ using equation B.12

$$F = \frac{\Delta S}{T_{RR}} \left[ \frac{\left(1 - e^{-T_I/T_{1P}}\right) e^{-T_E/T_{2P}}}{2RS_p e^{-T_I/T_{1B}} e^{-T_E/T_{2B}}} \right] \frac{C_{torso}(x_p, y_p)}{C_{torso}(x, y)} + \frac{V_{gap}}{V_{voxel} T_{RR}} \tag{B.13}$$

Since $V_{gap}$ is small relative to $V$, $V_{ASL} \approx V$ and the $V_{gap}$ term in equation B.13 is negligible.

$$F = \frac{\Delta S}{T_{RR}} \left[ \frac{\left(1 - e^{-T_I/T_{1P}}\right) e^{-T_E/T_{2P}}}{2RS_p e^{-T_I/T_{1B}} e^{-T_E/T_{2B}}} \right] \frac{C_{torso}(x_p, y_p)}{C_{torso}(x, y)} \tag{B.14}$$

Therefore, the flow $F$ in units of mL/min/cm$^3$ was measured from the subtracted ASL signal and corrected to the silicon phantom signal in either control or tag image.

## B.1 Bibliography

[1] D. S. Bolar, D. L. Levin, S. R. Hopkins, L. F. Frank, T. T. Liu, E. C. Wong, and R. B. Buxton. Quantification of regional pulmonary blood flow using ASL-FAIRER. *Magnetic resonance in medicine : official journal of the Society of Magnetic Resonance in Medicine / Society of Magnetic Resonance in Medicine*, 55(6):1308–1317, Jun 2006.

[2] A. C. Henderson, G. K. Prisk, D. L. Levin, S. R. Hopkins, and R. B. Buxton. Characterizing pulmonary blood flow distribution measured using arterial spin labeling. *NMR in biomedicine*, 22(10):1025–1035, Dec 2009.

# Appendix C

# Piecewise Polynomial Interpolation

## C.1 Curve fitting using piecewise polynomial interpolation

An unknown function $x_i$ is curve-fit using piecewise polynomial interpolation method.

$$\hat{x_i}(\mathbf{a}) = \sum_{\mathbf{j=1}}^{\mathbf{m}} \mathbf{p_{ij}} \mathbf{w_j}(\mathbf{a}) \tag{C.1}$$

The basic equation of this method is described in equation C.1. $\hat{x_i}$ is a function value, which approximates the unknown function $x_i$. $w_j$ is a basis function, $p_{ij}$ is a parameter representing the amplitude of corresponding basis function, m is the number of basis function and parameter pairs, and $\mathbf{a}$ is the global coordinate system. Each of the basis functions $w_j$ forms a non-zero spline residing at a specific location on the global coordinate system $\mathbf{a}$ and the specific location is called either node or knot point. Equation C.1 shows that the original unknown function $x_i$ is approximated as the linear combination of parameters and corresponding basis functions.

There are two kinds of polynomial methods (cubic B-spline and cubic Her-

mite) introduced in my dissertation study. These basis functions ensure the function value continuity and its first order derivative continuity at the boundaries where the spline functions connect.

## C.2 Cubic B-Spline Basis Functions in 1D

There are four pieces of cubic B-spline basis functions (equation C.2-C.5. Figure C.1) [3].

$$\beta_0(t) = (-t^3 + 3t^2 - 3t + 1)/6 \tag{C.2}$$

$$\beta_1(t) = (3t^3 - 6t^2 + 4)/6 \tag{C.3}$$

$$\beta_2(t) = (-3t^3 + 3t^2 + 3t + 1)/6 \tag{C.4}$$

$$\beta_3(t) = t^3/6 \tag{C.5}$$

$t$ is a local finite element coordinate which is normalized and zero-based within a piece. These four pieces of basis functions are juxtaposed side by side and comprise a single large spline curve residing over four different segments (Figure C.1E) in the global coordinate. The boundaries between two adjacent basis functions are called knots. A single B-spline shares a single coefficient (parameter $p_{ij}$ in equation 4.4), a so-called control point, $C$.

Figure C.2 demonstrates that a set of local B-spline functions interpolates a global function, Y = 1 (Figure C.2 top row). There are six splines (Figure C.2 from the second row to the bottom row) and each of the six splines is coupled with each of the control points ($C_1$=$C_2$=$C_3$=$C_4$=$C_5$=$C_6$=1). The entire function is divided into five segments. The center of each spline is located at a knot, i.e. the center of first spline is at X = 0, the second one is at X = 20 and so on. Three colored segments, red, magenta and green are made up of the linear combination of four pieces of non-zero part of splines (equation C.6).

$$\hat{Y}(X) = \sum_{i=1}^{m} C_i \beta_i(X) \tag{C.6}$$

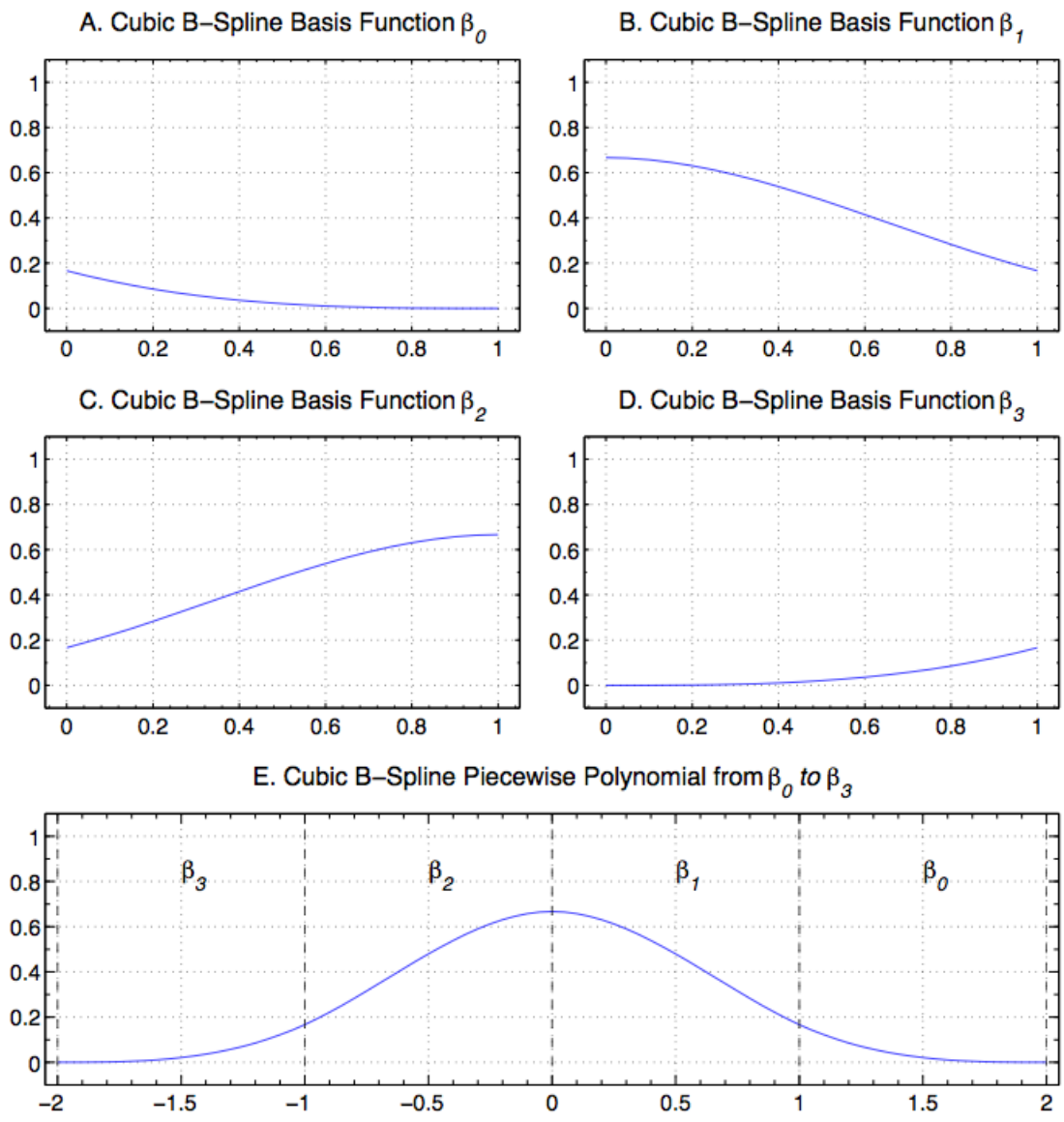


**Figure C.1**: Cubic B-spline basis functions (A-D). Four basis functions comprise a single large spline curve (E).

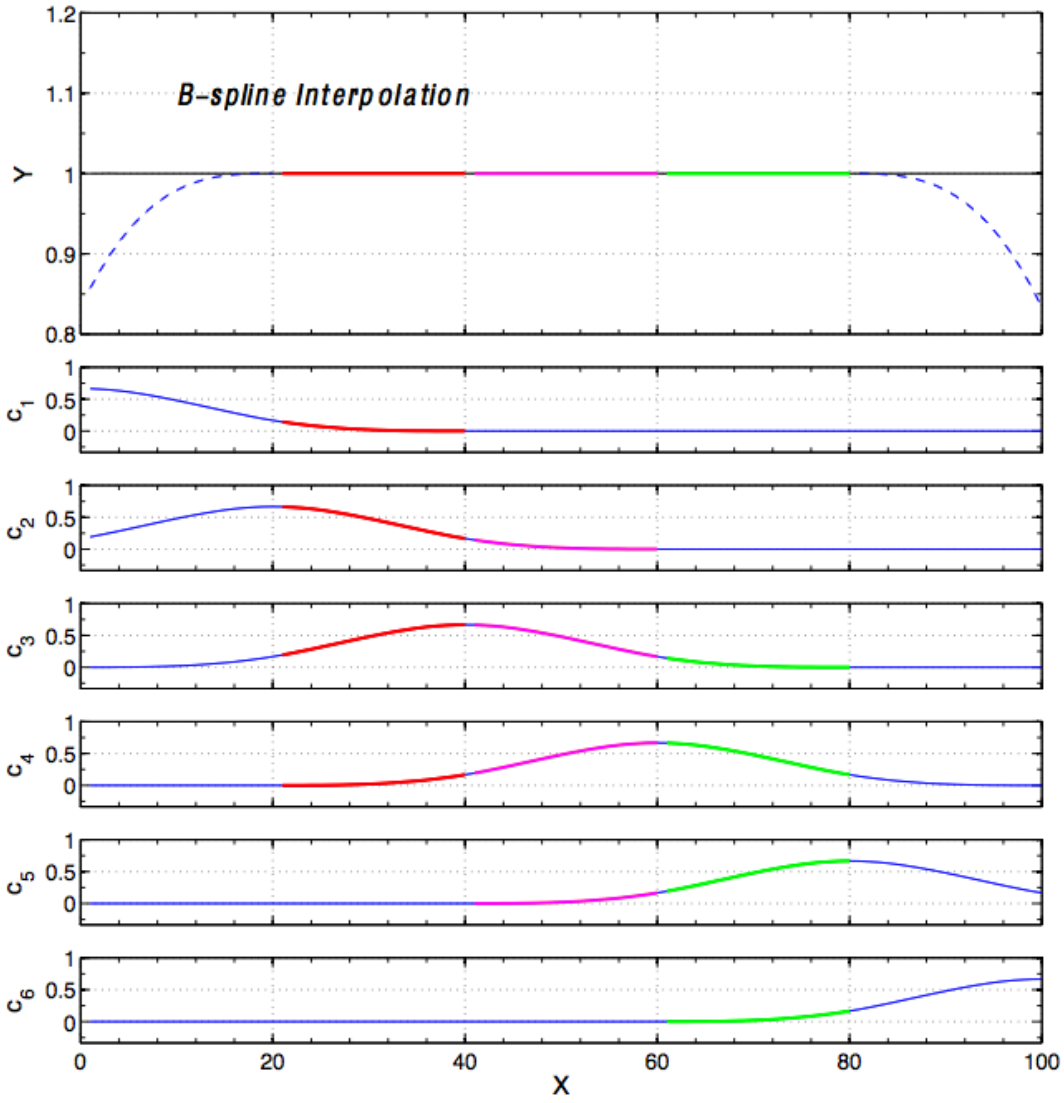


**Figure C.2**: 1D B-spline interpolation. A global function (Y = 1) is interpolated by 6 pieces of 1D cubic B-spline.

where $\hat{Y}$ is interpolation function i.e. the result of curve fit. Hence, each segment is expressed by the sum of four sets of control point and the B-spline basis function (equation C.6). If $C_2$ is changed, resulting in the change in the amplitude of second spline, the change does not affect the green segment. This is called local control. There are only three basis functions comprising both end segments. These end segments are not valid for the original function, Y = 1 as shown by a blue broken line in the top row of Figure C.2 . There are two ways to address this issue. First, two additional basis functions, $\beta_0$ and $\beta_3$, and corresponding two control points are introduced to either end to complement the fourth piece of the polynomial approach. In this case, a total of 8 splines and 8 control points are required to interpolate 5 segments of the original function ($C_1$=$C_2$=$C_3$=$C_4$=$C_5$=$C_6$=$C_7$=$C_8$=1). Second, either end of the basis functions is modified as shown in Figure C.3. Two $\beta_0$ basis functions are added on the left end of the first spline, while one $\beta_0$ basis function is subtracted from the left end of the second spline. The right end is similarly treated. Two $\beta_3$ basis function are added on the right end of the sixth spline while one $\beta_3$ basis function is subtracted from the right end of the fifth spline. In this case, there are also six splines and six control points ($C_1$=$C_2$=$C_3$=$C_4$=$C_5$=$C_6$=1).

Figure C.4 and C.5 demonstrate the B-spline curve-fit to the actual non-linear function. The original function depicted here is obtained from the Bitcoin trading price (mtgoxUSD(VWAP)) chart for 100 days from January 31st to May 10th 2013 (Figure C.4 and C.5: top row, black solid line).

This function includes one distinctive discontinuous feature, which is the major Bitcoin loss of value on April 10th 2013. The entire span is divided into 5 segments and the each segment has 20 days. The original function is interpolated by the linear combination of six control points and six corresponding splines. Figure C.4 misses the end support as shown in Figure C.2 so that only the internal three segments are valid, while in Figure C.5, splines in both ends are modified. The linear least squares between the original and interpolation functions are used to optimize a set of six control points ($C_1$= -129.6, $C_2$=58.7, $C_3$=18.7, $C_4$=105.2, $C_5$=205.9 and $C_6$=-470.2 for Figure 4 and $C_1$= 13.3, $C_2$=39.1, $C_3$=17.2, $C_4$=125.0, $C_5$=132.3 and $C_6$=-110.1 for Figure 5, respectively).

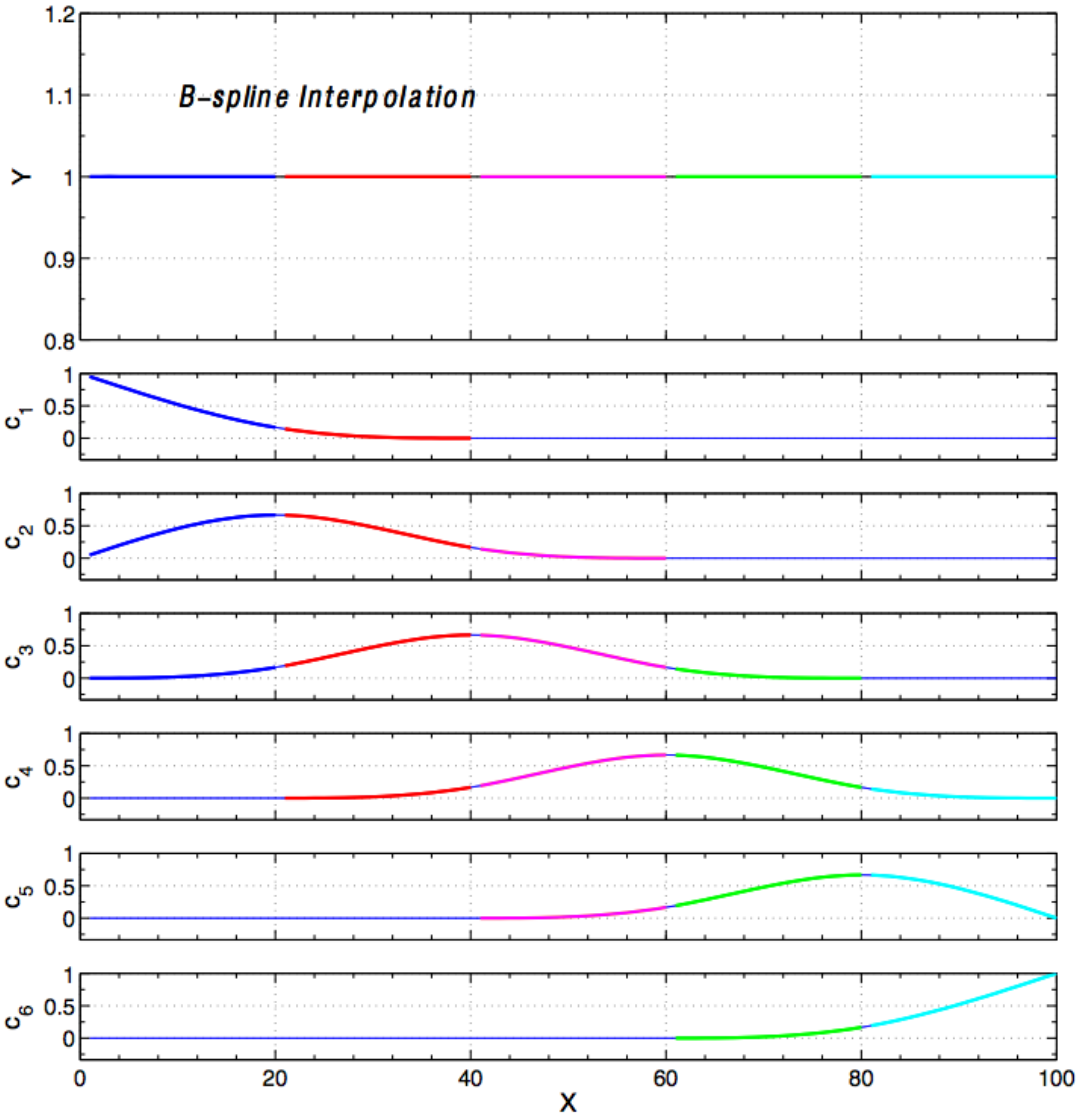


**Figure C.3**: 1D B-spline interpolation 2. A global function (Y = 1) is interpolated by 6 pieces of 1D cubic B-spline.

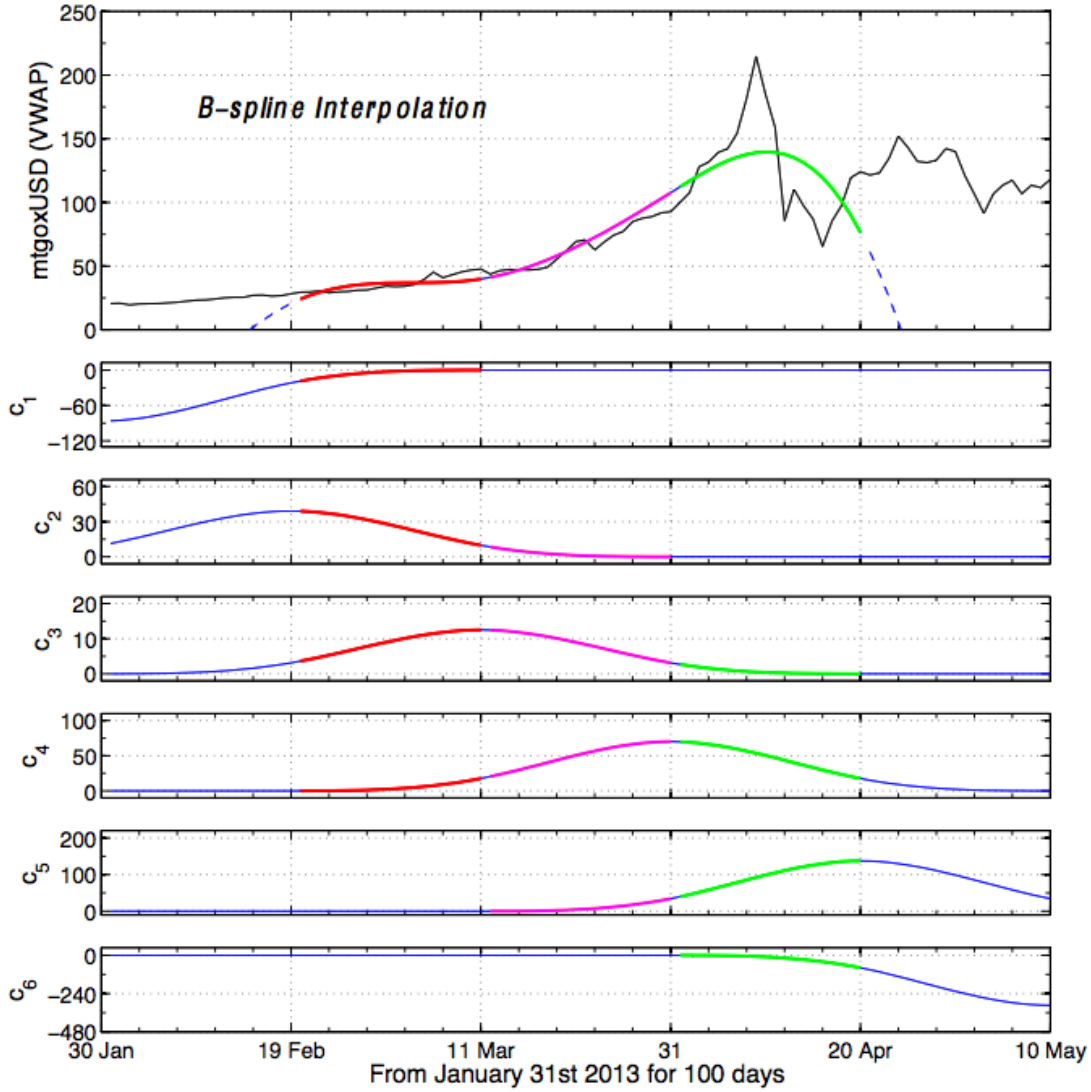


**Figure C.4**: 1D B-spline interpolation 3 (mtgoxUSD(VWAP)). A global function (Bitcoin trading price (mtgoxUSD(VWAP))) is interpolated by 6 pieces of 1D cubic B-spline.

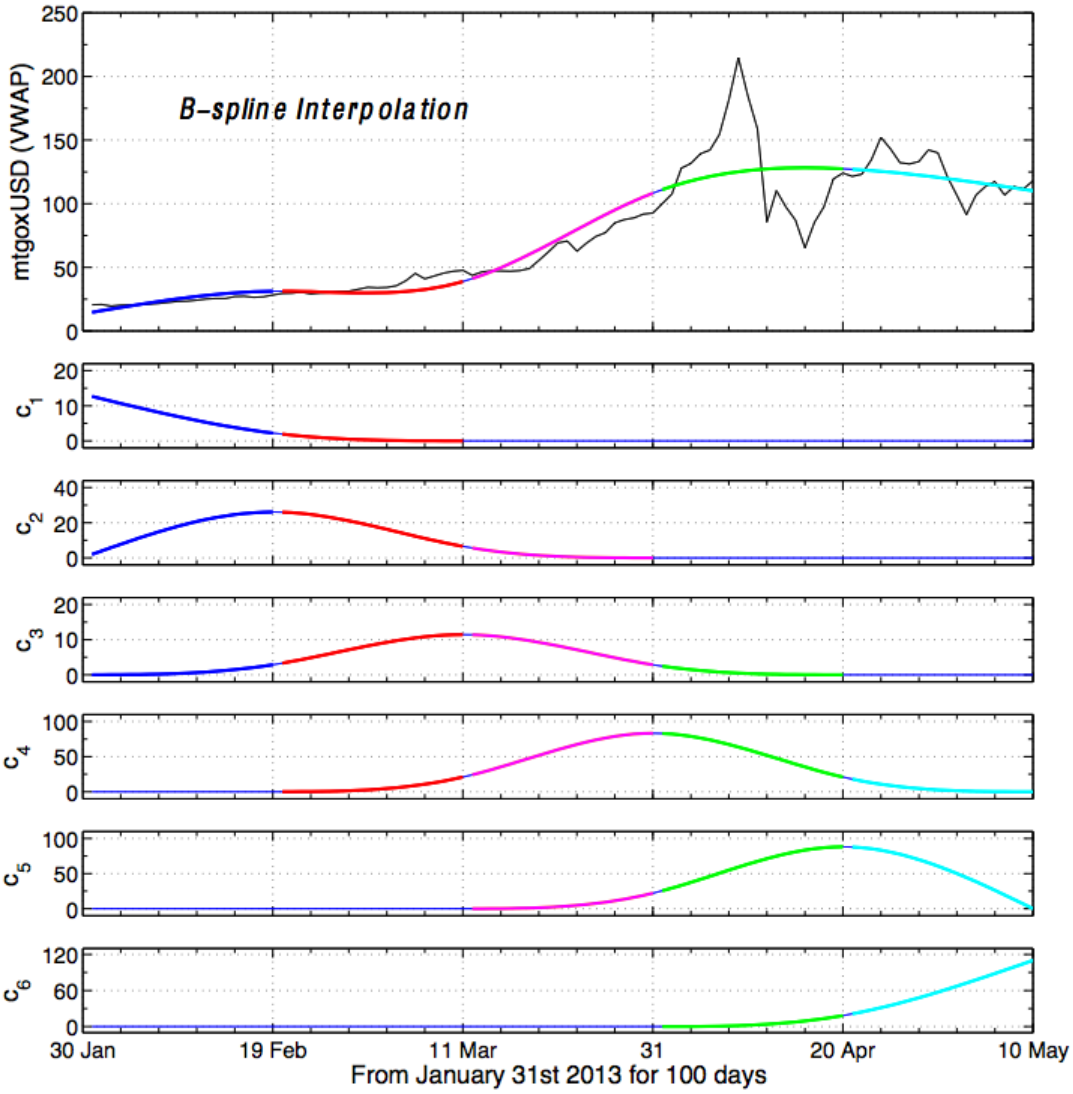


**Figure C.5**: 1D B-spline interpolation 4 (mtgoxUSD(VWAP)). A global function (Bitcoin trading price (mtgoxUSD(VWAP))) is interpolated by 6 pieces of 1D cubic B-spline.

The error (difference between data and fit) is shown in the green segment. This implies that the interpolation function is not flexible enough to fully reconstruct the original function. Increasing the number of segments and parameters ensures more degrees of freedom and reduce the amount of error. However, even though segment refinement and additional parameters reduce the error, the discontinuous feature (April 10, 2013 loss of value) in the original is smoothed and cannot be fully expressed since B-spline preserves first and second derivative continuity between two adjacent segments (C2 continuity). In summary, the original function, which is consisted of 100 discrete data points is parameterized and expressed by the linear combination of six control points and six splines in Figure C.4 and C.5.

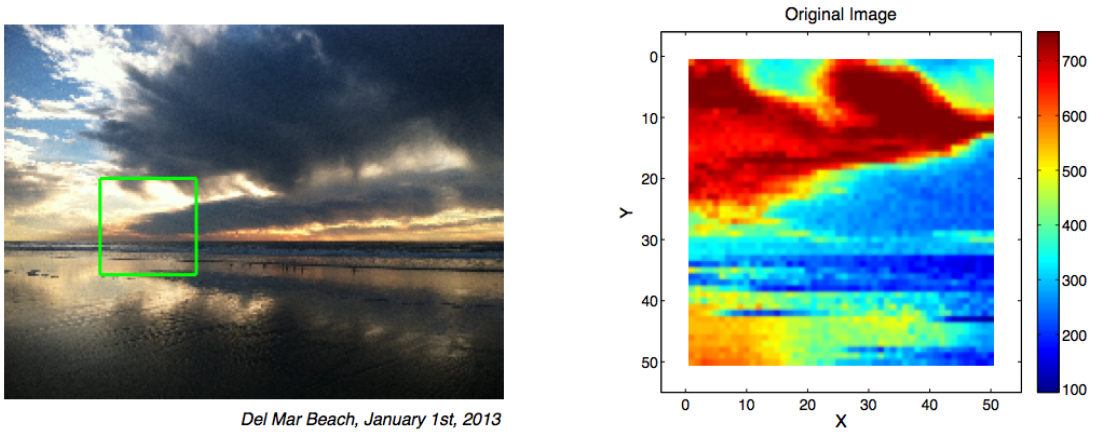


**Figure C.6**: Original image. Left: A photo of Del Mar Beach on January 31st 2013. Right: The part of the photo enclosed by a green rectangular (50 × 50 pixels) is used as the original 2D function.

## C.3 Cubic B-Spline Functions in 2D space

The B-spline interpolation technique can be extended to higher dimensions. 2D images are expressed as the linear combination of control points and 2D cubic B-spline basis functions. The left panel of Figure C.6 is the photo of Del Mar Beach on January 31st 2013. The part of the photo enclosed by a green rectangle (50 × 50 pixels) is used as the original 2D function (Figure C.6 , Right), which

contains several discontinuous features, ocean, sky, clouds, and horizon.

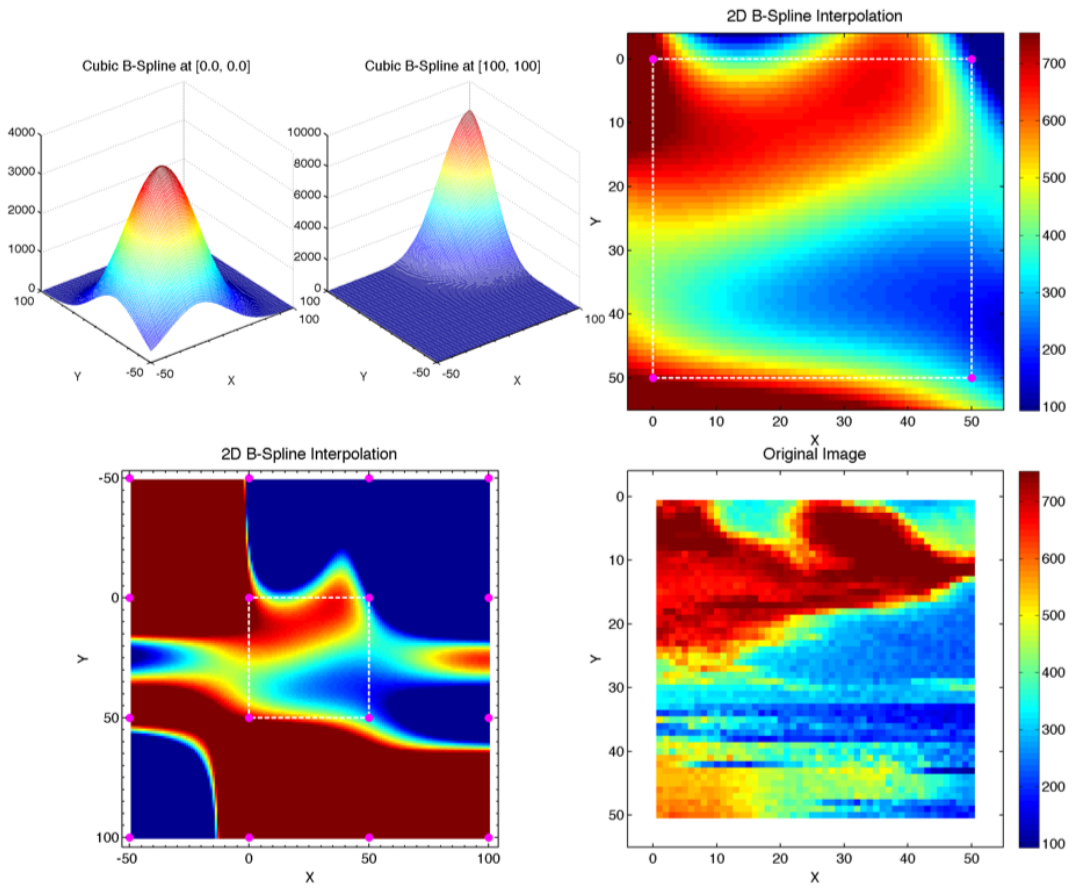


**Figure C.7**: 2D B-spline interpolation. The original 2D function given in Figure C.6 is expressed as the linear combination of 16 2D B-spline functions and their corresponding control points.

Figure C.7 demonstrates a set of 2D B-splines interpolating the original 2D function extracted from Figure C.6. Figure C.7 top left illustrates the shape of two 2D splines whose knots are located at [0, 0] and [100, 100], respectively. The height of each spline represents the color intensity of the original image. Sixteen splines, sixteen control points and nine 2D segments are required to reconstruct the original image (as shown in Figure C.7 bottom left). An internal segment encompassed by white broken lines curve-fits the original image and the interpolation is made up by the linear combination of sixteen control points and sixteen splines. The linear least squares between the original image and interpolation 2D functions are used

to optimize a set of sixteen control points. Figure C.7 top right focuses on the result of interpolation within the internal segment. There are errors between the original image and the interpolation. Several discontinuous features in the original image are smoothed. However the 2,500 original data points in the original image were reduced down to 16 parameters, with limited loss of information.

## C.4 Cubic Hermite Functions in 1D and 2D

There are other types of basis function sets; in this section I present the Hermite basis function. Four pieces of cubic Hermite basis functions are shown in Figure 8A-D and expressed as equation C.7 - C.10 [1, 2].

$$H_0{}^0(t) = 2t^3 - 3t^2 + 1 \tag{C.7}$$

$$H_1{}^0(t) = t^2(3 - 2t) \tag{C.8}$$

$$H_0{}^1(t) = t(t-1)^2 \tag{C.9}$$

$$H_1{}^1(t) = t^2(t-1) \tag{C.10}$$

Four basis functions are functionally divided into two groups; one is $H_0{}^0$ and $H_1{}^0$, and the other is $H_0{}^1$ and $H_1{}^1$. $H_0{}^0$ and $H_1{}^0$ are joined together, comprising a single spline shown in Figure C.8E and sharing a single parameter (nodal parameter: n). $H_0{}^1$ and $H_1{}^1$ are also combined as shown in Figure C.8F and share another nodal parameter. Unlike B-splines, the same parameter is shared over two neighboring elements (segments). The center of each spline is called a node and each node segments the global function into small local elements. $H_0{}^0$ and $H_1{}^0$ are coupled with each of function values positioning at left and right nodes, respectively. $H_0{}^1$ and $H_1{}^1$ are coupled with the first order derivative of the function at respective nodes (C1 continuity).

Figure C.9 in the top row demonstrates that a set of Hermite functions interpolates the Y=1 function which is similar to Figure C.2 and C.3 . There are twelve basis functions and six are in solid lines ($H_0{}^0$ and $H_1{}^0$) and others presented as broken lines ($H_0{}^1$ and $H_1{}^1$). The interpolation function is expressed as equation

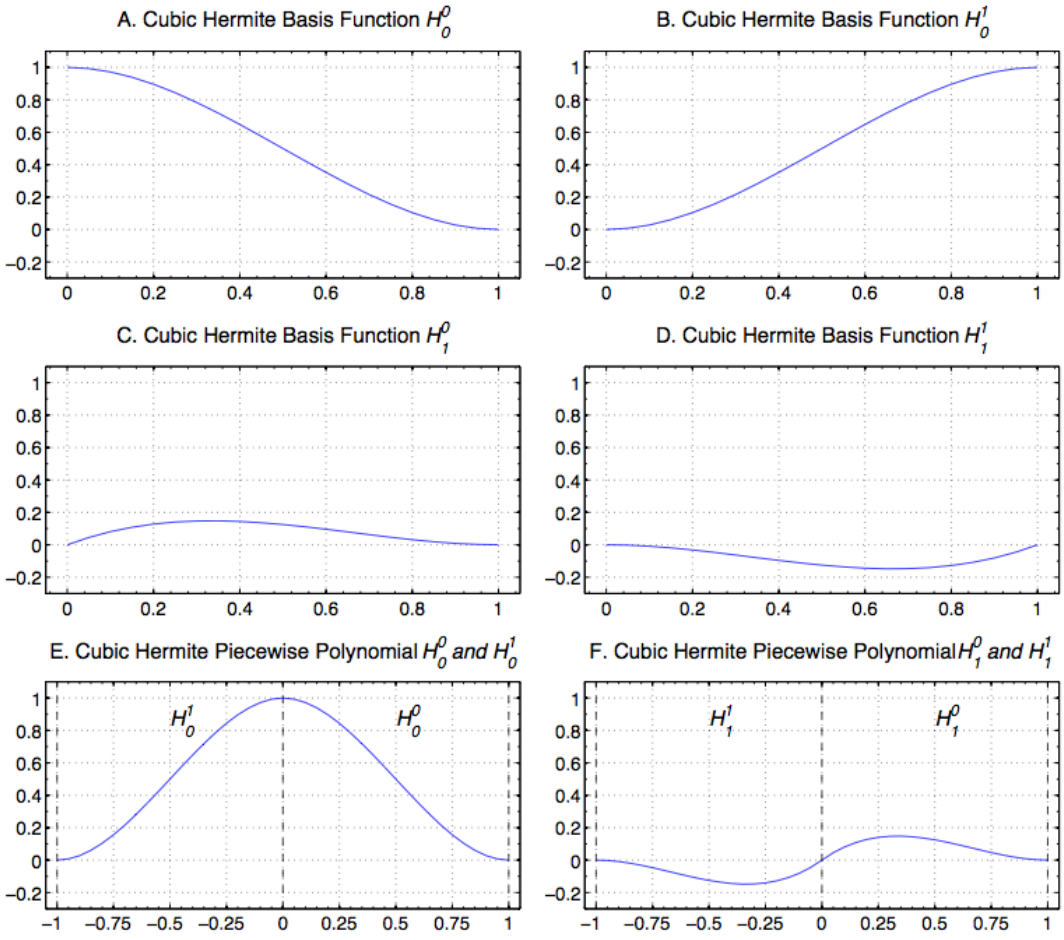


**Figure C.8**: Cubic Hermite basis functions. There are four basis functions (A-D). ${H_0}^0$ and ${H_1}^0$ are combined as well as ${H_0}^1$ and ${H_1}^1$. There are two different spline curves (E and F).

C.11.

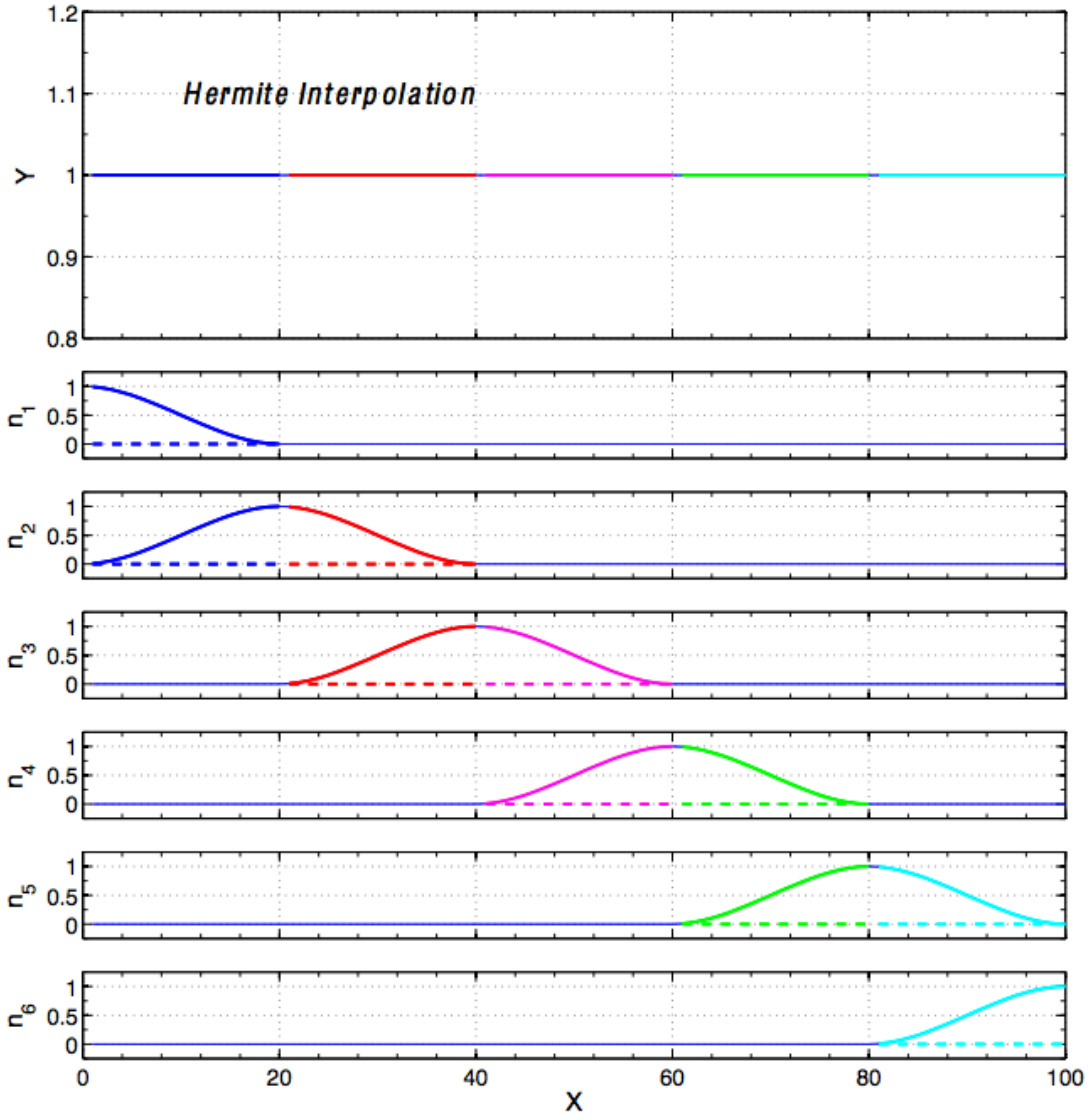


**Figure C.9**: 1D Hermite interpolation 1. A global function (Y = 1) is interpolated by 12 pieces of 1D cubic Hermite splines.

$$\hat{Y}(X) = \sum_{i=1}^{m} n_i H_i(X) \tag{C.11}$$

The six nodal values are all 1 since function values are 1, while the six derivative nodal values are all 0 since first order derivatives are 0 everywhere. The entire function is divided into 5 elements and each element has four sets of

basis functions and each node has 2 parameters. Total of twelve parameters are required to reconstruct the original function over five elements. Figure C.10 shows that the linear combination of cubic Hermite basis functions interpolates Bitcoin trading price chart ($n_1$ = 19.8, $n_2$ = 28.7, $n_3$=48.9, $n_4$ = 116.8, $n_5$ = 117.4, $n_6$ =117.2, $\partial n_1/\partial x = 1.8$, $\partial n_2/\partial x = 13.9$, $\partial n_3/\partial x = 61.9$, $\partial n_4/\partial x = 290.2$, $\partial n_5/\partial x =$ 166.6, and $\partial n_6/\partial x = 107.6$). Compared with B-spline interpolation in Figure C.4 and C.5, the interpolation function in Figure C.10 is qualitatively more flexible and has less error than the B-spline approach. This is because Hermite basis functions use double amount of parameters compared with the B-spline example shown previously.

Figure C.11 shows a 2D image interpolation using 2D cubic Hermite basis functions. The original 2D image is as same as in Figure C.6 right. Four nodes delineate a square on the top of original image. Each node has four parameters; nodal value: $n_i$, first derivative: $\partial n_i/\partial x$, $\partial n_i/\partial y$ and second derivative: $\partial^2 n_i/\partial x \partial y$ so that the total of 16 2D Hermite basis functions and corresponding 16 parameters are required. Figure C.6 left shows all the 16 combinations of the Hermite basis functions and parameters and Figure C.6 top right represents the sum of these 16 2D splines to interpolate the original image.

## C.5 Element refinement

Figure C.12 shows that the adding more parameter and basis function pairs (by the subdivision of the elements) ensures more degrees of freedom and enables to curve-fit the more complex structures in the original 2D function. For instance, the original 2D function contains 50 $\times$ 50 pixelated data points (Figure C.12A), while Figure C.12B approximates the original 2D function using only 14 $\times$ 14 parameters. It should be noted that the cubic Hermite method uses four pairs of basis function and parameter at each node point in 2D curve-fitting, whereas cubic B-spline method uses one pair at each control knot. Therefore, more degrees of freedom are introduced by the subdivision of element grids with Hermite method than with B-spline method.

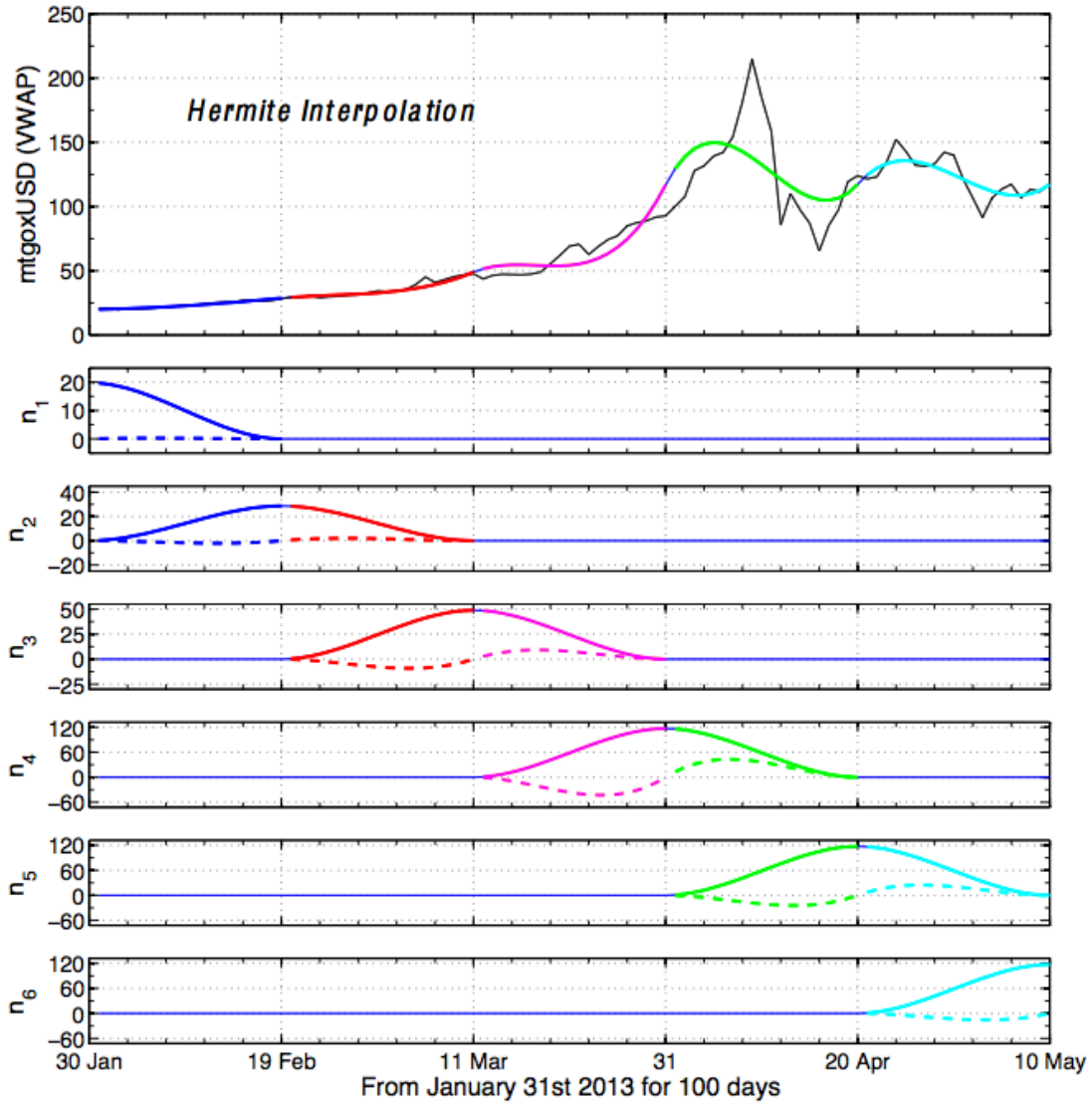


**Figure C.10**: 1D Hermite interpolation 2 (mtgoxUSD(VWAP)). A global function (Bitcoin trading price (mtgoxUSD(VWAP))) is interpolated by 12 pieces of 1D cubic Hermite splines.

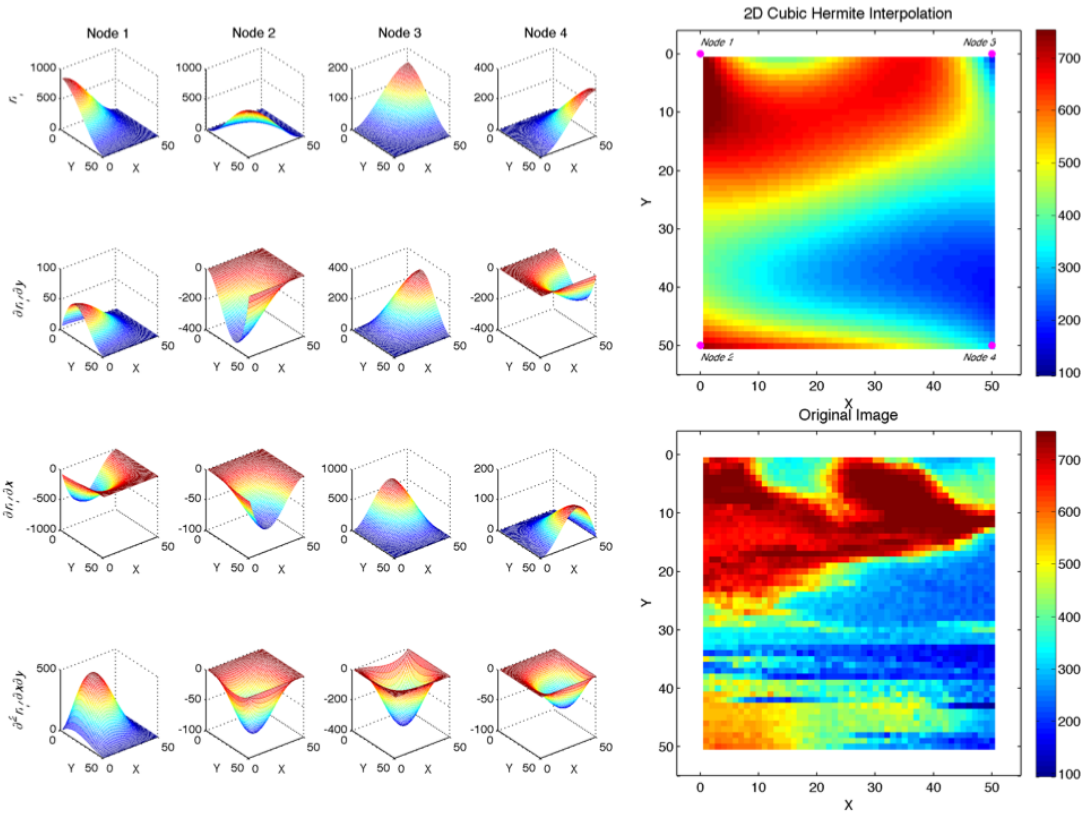


**Figure C.11**: 2D Hermite interpolation. The original 2D function given in Figure C.6 is expressed as the linear combination of 16 2D Hermite functions and their corresponding control points.

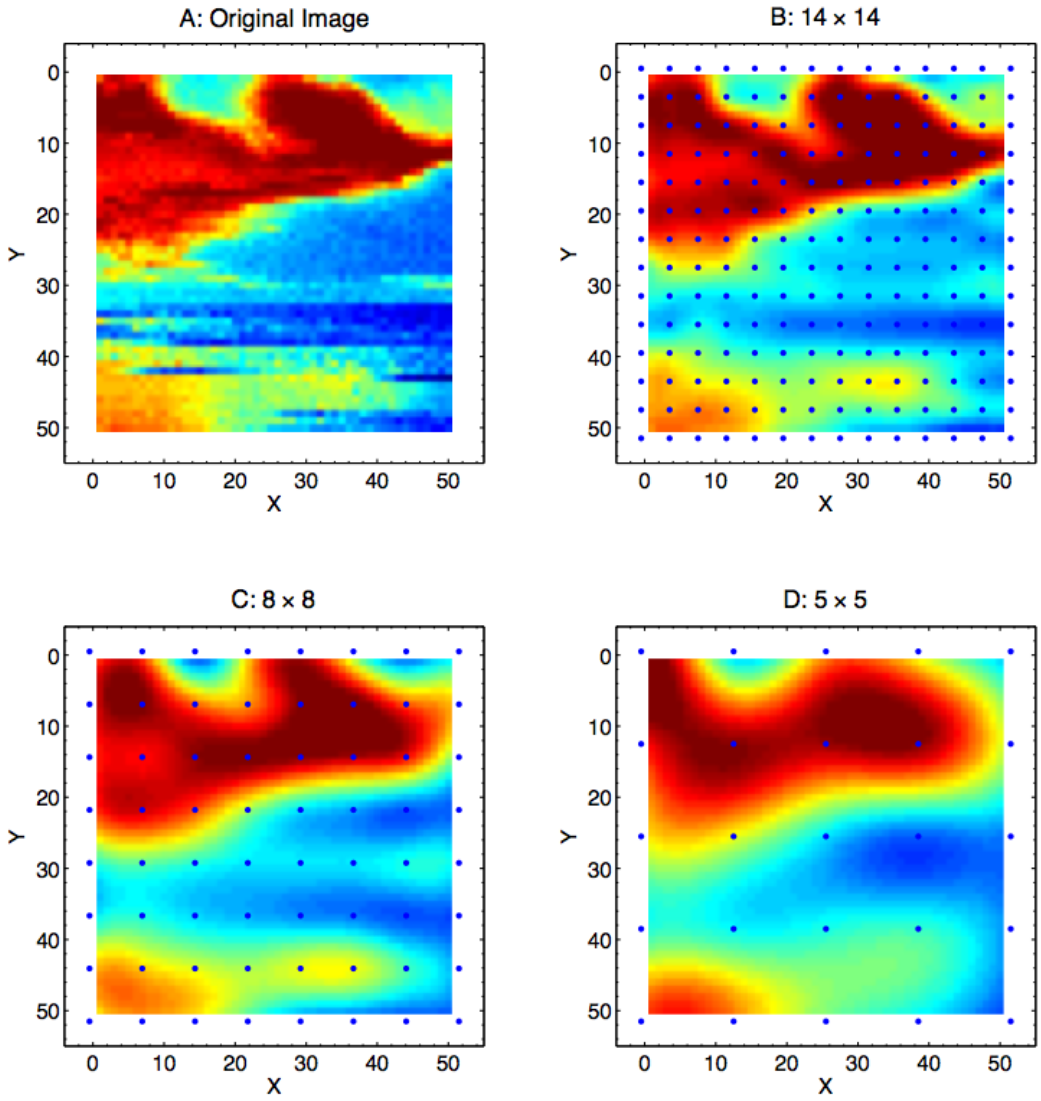


**Figure C.12**: 2D element refinement. The original 2D function given in Figure C.6 is approximated by more parameter and B-spline pairs. Original 2D function (A) is approximated by 14 × 14 (B), 8 × 8 splines (C), and 5 × 5 (D) splines. The subdivision of element grids ensures more degrees of freedom and enables to curve-fit the more complex structure in the original 2D function.

## C.6 2D deformation model using parameterized piecewise polynomials

The methods described above are applied to express spatially heterogeneous deformation. Assuming there is a known transformation from the original coordinates to deformed coordinates. Figure C.13A shows the original Cartesian coordinate system (50 pixels in both X and Y) and red broken lines represent grids every 5 pixels. The deformed curved coordinate system is shown in black grids. Deformed X and Y coordinates are separately shown in Figure C.13B1 and B2, respectively. The color map, which represents the either deformed X or Y coordinates is also considered as a 2D image in the same way as previously shown in Figure C.6, C.7 and .C.11. Cubic basis functions are defined based on the Cartesian coordinate system and each of deformed coordinates is expressed as the linear combination of parameters and polynomials. Figures C.13 C1 and C2 show that the deformed X and Y coordinates are separately interpolated by the corresponding parameter set. Calculated deformed coordinates X and Y are combined to shape a calculated deformed grid shown in black solid lines in Figure C.13D. There are errors (displacement errors) between the original deformed coordinates (Figure C.13A) and calculated deformed coordinates (Figure C.13D). The square root of errors is shown in Figure C.13E in the unit of pixel. Contour lines represent 0.1, 0.4 and 1.6 pixels shift. B-spline basis functions within a single internal segment are used for this demonstration so that the total of 32 ($16 \times 2$) parameters are used to optimize the coordinate transformation. Additional parameters help to reduce the amount of errors.

## C.7 Bibliography

[1] T. J. Arai, C. T. Villongco, M. T. Villongco, S. R. Hopkins, and R. J. Theilmann. Affine transformation registers small scale lung deformation. *Conference proceedings: Annual International Conference of the IEEE Engineering in Medicine and Biology Society. IEEE Engineering in Medicine and Biology Society. Conference*, 2012(1):5298–5301, 2012.

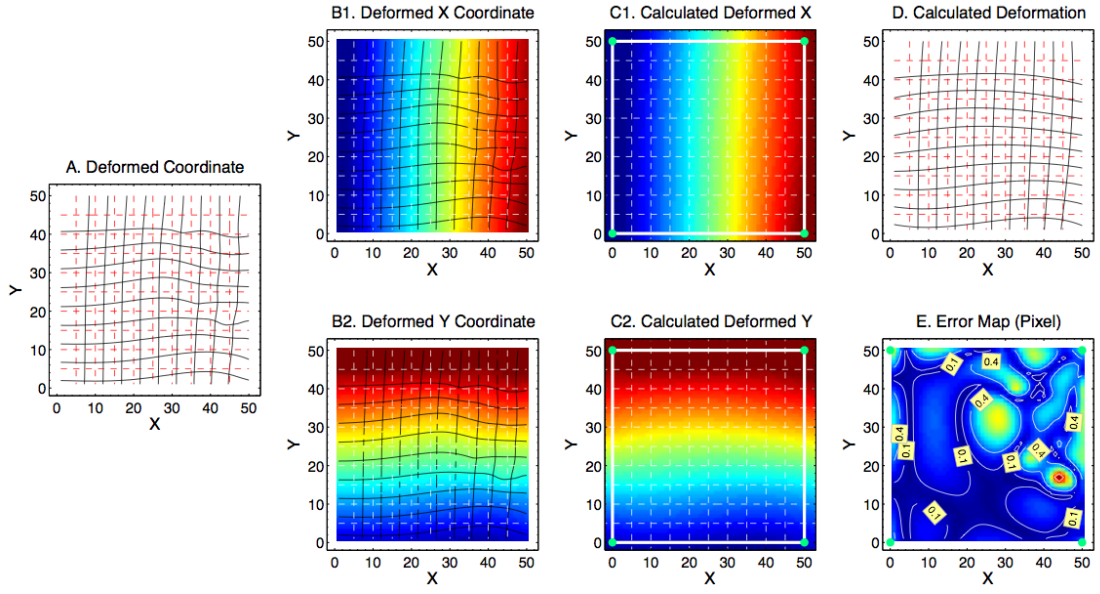


**Figure C.13**: 2D deformation model expressed by parameterized piecewise polynomials. A: Original Cartesian coordinate system and deformed coordinate system expressed by in red and black grids, respectively. B: Deformed coordinate system is dealt separately in X (B1) and Y (B2) axes. Deformed X and Y coordinates are just as the 2D function given in Figure C.6. C: Each of X and Y coordinates are interpolated by the corresponding parameter set. D: Computed deformed coordinate X and Y are combined to shape a calculated deformed grid shown in black solid line. E: Errors (displacement errors) between the original deformed coordinate (A) and calculated deformed coordinate systems (D).

[2] P. M. Nielsen, I. J. Le Grice, B. H. Smaill, and P. J. Hunter. Mathematical model of geometry and fibrous structure of the heart. *The American journal of physiology*, 260(4 Pt 2):H1365–H1378, Apr 1991.

[3] Y. Yin, E. A. Hoffman, and C. L. Lin. Mass preserving nonrigid registration of CT lung images using cubic b-spline. *Medical physics*, 36(9):4213–4222, Sep 2009.